Synthesis and Characterization of Photocatalytically Active [FeFe] Hydrogenase Subsite Models

seit 1558

Dissertation

(kumulativ)

zur Erlangung des akademischen Grades doctor rerum naturalium

(Dr. rer. nat.)

vorgelegt dem Rat der Chemisch-Geowissenschaftlichen Fakultät

der Friedrich-Schiller-Universität Jena

von Dipl.-Chem. Roman Goy

geboren am 02.06.1987 in Eisenach

Gutachter:

1. Prof. Dr. Wolfgang Weigand,

   Friedrich-Schiller-Universität Jena

   Institut für Anorganische und Analytische Chemie

   Humboldtstraße 8

   D-07743 Jena

2. Prof. Dr. Wolfgang Imhof

   Universität Koblenz – Landau

   Institut für Integrierte Naturwissenschaften, Abteilung Chemie

   Universitätsstraße 1

   D- 56070 Koblenz

3. Prof. Dr. Evamarie Hey-Hawkins

   Universität Leipzig

   Institut für Anorganische Chemie

   Linnéstraße 3

   D-04275 Leipzig

Tag der Verteidigung: 10.02.2016

"On the arid lands there will spring up industrial colonies without smoke and without smokestacks; forests of glass tubes will extend over the plains and glass buildings will rise everywhere; inside of these will take place the photochemical processes that hitherto have been the guarded secret of the plants, but that will have been mastered by human industry which will know how to make them bear even more abundant fruit than nature, for nature is not in a hurry and mankind is. And if in a distant future the supply of coal becomes completely exhausted, civilization will not be checked by that, for life and civilization will continue as long as the sun shines!"

Giacomo Luigi Ciamician, *Science* **1912**, *36*, 385-394.

Table of Contents

Abbreviations ..... **vi**

1 List of Publications **1**

2 Documentation of Authorship **2**

2.1 [RG1] A Silicon-Heteroaromatic System as Photosensitizer for Light-Driven Hydrogen Production by Hydrogenase Mimics 2

2.2 [RG2] A Sterically Stabilized Fe^{I}-Fe^{I} Semi-Rotated Conformation of [FeFe] Hydrogenase subsite Model 3

2.3 [RG3] Silicon-Heteroaromatic [FeFe] Hydrogenase Model Complexes: Insight into Protonation, Electrochemical Properties and Molecular Structures 4

2.4 [RG4] Enhanced Photocatalytic Hydrogen Evolution by Silicon-Containing [FeFe] Hydrogenase Models 5

2.5 Declaration 6

3 Introduction **7**

3.1 Hydrogenases 8

3.2 [FeFe] hydrogenase 9

3.3 Redox states of the active site and mechanistic implications 12

3.4 Biomimetic catalysts 15

3.4.1 First generation of [FeFe] hydrogenase mimics 15

3.4.2 Abiological modifications 17

3.4.3 Proton relays and hydride species of [FeFe] hydrogenase models 19

3.4.4 Rotated state species of [FeFe] hydrogenase models 26

3.5 Light Driven hydrogen production by hydrogenase mimics 30

3.5.1 Light harvester covalently linked to the $[Fe_2S_2(CO)_{6-x}(L)_x]$ cluster 33

3.5.2 Non-covalent systems utilizing $[Fe_2S_2(CO)_{6-x}(L)_x]$ clusters as catalyst 37

3.6 Silicon containing model complexes 41

3.6.1 Silicon containing aromatic systems 44

3.7 Motivation 46

4 Publications **48**

4.1 [RG1] 48

A Silicon-Heteroaromatic System as Photosensitizer for Light-Driven Hydrogen Production by Hydrogenase Mimics 48

4.2 [RG2] 69

A Sterically Stabilized Fe^{I}-Fe^{I} Semi-Rotated Conformation of [FeFe] Hydrogenase subsite Model 69

4.3 [RG3] 90

Silicon-Heteroaromatic [FeFe] Hydrogenase Model Complexes: Insight into Protonation, Electrochemical Properties and Molecular Structures 90

4.4 [RG4] 121

Enhanced Photocatalytic Hydrogen Evolution by Silicon-Containing [FeFe] Hydrogenase Models 121

5 Summary **166**

6 Zusammenfassung **171**

7 References **177**

8 Acknowledgements **186**

9 Curriculum Vitae **188**

10 Declaration of authorship/Selbstständigkeitserklärung **191**

Abbreviations

adt	azadithiolate
bdt	benzenedithiolate
bn	benzyl
bpy	bipyridinyl
CpI	[FeFe] hydrogenase from *Clostridium pasteurianum*
CTAB	cetyltrimethylammonium bromide
CV	cyclic voltammetry
Cys	cysteine
DBBN	*2,2'*-dibromo-*1,1'*-binaphtyl
DdHase	[FeFe] hydrogenase from *Desulfovibrio desulfuricans*
dmpe	1,2-bis(dimethylphosphino)ethane
dppv	1,2-bis(diphenylphospino)vinylen
edt	ethanedithiolate
EDTA	ethylenediaminetetraacetic acid
e.g.	exempli gratia
ENDOR	electron nuclear double resonance
EPR	electron paramagnetic resonance
ET	electron transfer
et al.	et alii
Fc^+	ferrocenium
FTIR	fourier transformation infrared
H_2*ase*	hydrogenase
IR	infrared
MPA	3-mercaptopropionic acid
MS	mass spectrometry
NADH	nicotinamide adenine dinucleotide
n-BuLi	*n*-butyllithium
NHE	normal hydrogen electrode
NMR	nuclear magnetic resonance
odt	oxodithiolate
PAA	poly(acrylic acid)
PET	photoinduced electron transfer

pdt	propanedithiolate
ppm	parts per million
ppy	phenylpyridinyl
PS	photosensitizer
r.t.	room temperature
SDS	sodium dodecyl sulfate
sdt	sulfurdithiolate
tert.-BuLi	*tertiary*-butyllithium
TEA	triethylamine
TFA	trifluoroacetic acid
TMEDA	*N,N,N',N'*-tetramethylethane-1,2-diamine
TOF	turn-over frequency
TON	turn-over number

1 List of Publications

[RG1] A Silicon-Heteroaromatic System as Photosensitizer for Light-Driven Hydrogen Production by Hydrogenase Mimics

Roman Goy, Ulf-Peter Apfel, Catherine Elleouet, Daniel Escudero, Martin Elstner, Helmar Görls, Jean Talarmin, Philippe Schollhammer, Leticia González, Wolfgang Weigand

European Journal of Inorganic Chemistry **2013**, 4466-4472.

[RG2] A Sterically Stabilized Fe^{I}-Fe^{I} Semi-Rotated Conformation of [FeFe] Hydrogenase Subsite Model

Roman Goy, Luca Bertini, Catherine Elleouet, Helmar Görls, Giuseppe Zampella, Jean Talarmin, Luca De Gioia, Philippe Schollhammer, Ulf-Peter Apfel, Wolfgang Weigand

Dalton Transactions **2015**, *44*, 1690-1699.

[RG3] Silicon-Heteroaromatic [FeFe] Hydrogenase Model Complexes: Insight into Protonation, Electrochemical Properties and Molecular Structures

Roman Goy, Luca Bertini, Helmar Görls, Giuseppe Zampella, Jean Talarmin, Luca De Gioia, Philippe Schollhammer, Wolfgang Weigand

Chemistry – A European Journal **2015**, *21*, 5061-5073.

[RG4] Enhanced Photocatalytic Hydrogen Evolution by Silicon-Containing [FeFe] Hydrogenase Models

Roman Goy, Luca Bertini, Tobias Rudolph, Martin Schulz, Giuseppe Zampella, Benjamin Dietzek, Felix H. Schacher, Luca De Gioia, Wolfgang Weigand

In preparation

2 Documentation of Authorship

2.1 **[RG1]** A Silicon-Heteroaromatic System as Photosensitizer for Light-Driven Hydrogen Production by Hydrogenase Mimics

Roman Goy[1], Ulf-Peter Apfel[2], Catherine Elleouet[3], Daniel Escudero[4], Martin Elstner[5], Helmar Görls[6], Jean Talarmin[3], Philippe Schollhammer[3], Leticia González[4], Wolfgang Weigand[7]

European Journal of Inorganic Chemistry **2013**, 4466-4472.

Beteiligt an	**Autoren**						
	1	2	3	4	5	6	7
Manuscript preparation	X						
Discussion of the manuscript	X	X					X
Syntheses of compounds	X						
Analytics	X				X		
Cyclic voltammetry			X				
Quantum chemical calculations				X			
X-Ray structure determination						X	
Strategy of research approach		X					X
Strategy of investigations	X						X
Vorschlag Anrechnung Publikationsäquivalente	1,0						

2.2 **[RG2]** A Sterically Stabilized Fe^{I}-Fe^{I} Semi-Rotated Conformation of [FeFe] Hydrogenase subsite Model

Roman Goy[1], Luca Bertini[4], Catherine Elleouet[3], Helmar Görls[5], Giuseppe Zampella[4], Jean Talarmin[3], Luca De Gioia[4], Philippe Schollhammer[3], Ulf-Peter Apfel[2], Wolfgang Weigand[6]

Dalton Transactions **2015**, *44*, 1690-1699.

Beteiligt an	**Autoren**					
	1	2	3	4	5	6
Manuscript preparation	X					
Discussion of the manuscript	X	X	X			X
Syntheses of compounds	X	X				
Analytics	X	X				
Cyclic voltammetry			X			
Quantum chemical calculations				X		
X-Ray structure determination	X				X	
Strategy of research approach	X	X				X
Strategy of investigations	X					X
Vorschlag Anrechnung Publikationsäquivalente	1,0					

2.3 **[RG3]** Silicon-Heteroaromatic [FeFe] Hydrogenase Model Complexes: Insight into Protonation, Electrochemical Properties and Molecular Structures

Roman Goy[1], Luca Bertini[2], Helmar Görls[3], Giuseppe Zampella[2], Jean Talarmin[4], Luca De Gioia[2], Philippe Schollhammer[4], Wolfgang Weigand[5]

Chemistry – A European Journal **2015**, *21*, 5061-5073.

Beteiligt an	**Autoren**				
	1	2	3	4	5
Manuscript preparation	X				
Discussion of the manuscript	X	X		X	X
Syntheses of compounds	X				
Analytics	X				
Cyclic voltammetry	X			X	
Quantum chemical calculations		X			
X-Ray structure determination	X		X		
Strategy of research approach	X				X
Strategy of investigations	X				X
Vorschlag Anrechnung Publikationsäquivalente	1,0				

2.4 **[RG4]** Enhanced Photocatalytic Hydrogen Evolution by Silicon-Containing [FeFe] Hydrogenase Models

Roman Goy[1], Luca Bertini[2], Tobias Rudolph[3], Martin Schulz[4], Giuseppe Zampella[2], Benjamin Dietzek[4], Felix H. Schacher[3], Luca De Gioia[2], Wolfgang Weigand[5]

In preparation

Beteiligt an	**Autoren**				
	1	2	3	4	5
Manuscript preparation	X				
Discussion of the manuscript	X	X			X
Hydrogen evolution experiments	X				
Analytics	X			X	
Preparation of micelle-solutions			X		
Quantum chemical calculations		X			
Strategy of research approach	X				X
Strategy of investigations	X				X
Vorschlag Anrechnung Publikationsäquivalente	1,0				

2.5 Declaration

Erklärung zu den Eigenanteilen des Promovenden sowie der weiterer Doktoranden/Doktorandinnen als Koautoren an den Publikationen und Zweitpublikationsrechten bei einer kumulativen Dissertation.

Für alle in dieser kumulativen Dissertation verwendeten Manuskripte liegen die notwendigen Genehmigungen der Verlage für die Zweitpublikation vor.

Die Ko-Autoren der in dieser kumulativen Dissertation verwendeten Manuskripte sind sowohl über die Nutzung, als auch über die oben angegebenen Eigenanteile informiert und stimmen dem zu.

Ich bin mit der Abfassung der Dissertation als publikationsbasiert, d.h. kumulativ, einverstanden und bestätige die vorstehenden Angaben. Eine entsprechend begründete Befürwortung mit Angabe des wissenschaftlichen Anteils des Doktoranden an den verwendeten Publikationen werde ich parallel an den Rat der Fakultät der Chemisch-Geowissenschaftlichen Fakultät richten.

Dipl.-Chem. Roman Goy Jena, _____

Prof. Dr. Wolfgang Weigand Jena, _____

3 Introduction

The global fossil energy use is estimated to be 400 EJ/a,[1] which is 0.01% of the yearly received solar energy (3,500,000 EJ). The polluting impact of fossil fuels increase the concentration of the greenhouse gas CO_2 in the atmosphere in spring 2013 for the first time to 400 ppm.[2–4] The extensive and adverse consequences for the global climate and enviroment are unclear and not predictable. It is a highly desired endeavor to fundamentally change global energy economics. The exhaust of technical limits for energy production causes huge accidents like in the case of the oil platform "Deepwater Horizon" in 2010[5] or the nuclear power plant accident in "Fukushima I" 2011,[6] whose complications are seriously to handle.

Molecular dihydrogen represents an alternative energy storage for a sustainable energy economy and shows advantageous properties: H_2 is part of the biological cycle and is environmental neutral, the aerobic combustion of hydrogen to water has a high specific energy value (142 $MJkg^{-1}$),[7] combustion produces water as clean emission product[8] and compared to electricity, H_2 is easier to store in large quantities and represents by this an ideal fuel.[9–11] In industry 30 Mt/a hydrogen are already used in a broad scale, *e.g.* in processes like carbon hydrogenation, Haber-Bosch as well as fat hardening or as rocket fuel, cryogen and reducing agent. It is currently generated mainly by transformation of fossil fuels like steam reforming[12,13] and coal gasification.[14]. As mentioned before, the incoming solar radiation is far larger than the total energy consumption. Nonetheless this source is barely utilized. One important reason is that energy is needed at certain times. The arriving solar energy shows a typical daily and seasonal variation, which makes it difficult to realize the time-dependent energy needs. To solve such problems, the sunlight has to be converted into energy storages like hydrogen.

But not only mankind consumes and generates hydrogen, also nature uses an enormous amount of hydrogen in different forms as energy source and transporter.[15] The generation and exhaustion is regulated by enzymes, called hydrogenases.[16] They are very efficient enzymes catalyzing the two-electron reduction equilibrium of protons to dihydrogen (Scheme 1).

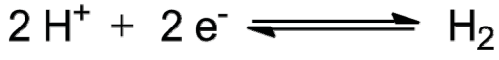

Scheme 1: Two-electron reduction equilibrium of protons and dihydrogen.

One of such microorganisms is *Desulfovibrio desulfuricans*, in which the enzyme [FeFe] hydrogenase was detected and isolated. This enzyme is able to produce 9000 molecules dihydrogen per second.[17] In order to challenge the catalytic efficiency of the natural enzymatic system as well as to utilize light as energy source for proton reduction, it is necessary to create novel catalysts derived from inexpensive metals. To create a catalyst that combines structural features of [FeFe] hydrogenases active site and of a light harvesting molecule will be the focus of this work.

3.1 Hydrogenases

Hydrogenases can be classified according to their metal content into the three different classes [FeFe], [NiFe], and [Fe] hydrogenase enzymes (Table 1). The catalytic processes in the hydrogenases are bidirectional; they act as H_2 uptake as well as H_2 producing enzymes.[18] The [NiFe] hydrogenases are more active for H_2 oxidation and exhibit a [$NiFeS_2$] active site. A subgroup of the [NiFe] hydrogenases are the [NiFeSe] hydrogenases, whereby one cysteine ligand of the nickel atom is substituted by a selenocysteine.[19] The [FeFe] hydrogenases catalyze the reduction of protons to dihydrogen and will be described in detail, because they are the focus of this work. The third class of hydrogenases are the [Fe] H_2ases, whose active site includes just a single Fe^{II} with an unusual coordination sphere.[20–23]

Table 1. Classification of H_2ases.[24]

Classification	Occurrence	Structure	Localization	Function
[NiFe] H_2ase	anaerobic, photosynthetic bacteria, cyanobacteria	heterodimeric, multimeric	cytoplasmic, membrane bound, periplasmic	uptake of H_2
[NiFeSe] H_2ase	sulphate-reducing bacteria, methanogenes	oligomeric	cytoplasmic, membrane-bound	oxidation of H_2

[FeFe] H_2ase	Photosynthetic bacteria, anaerobic fermentative bacteria, cyanobacteria, green algae, protozoan	monomeric, heteromeric	cytoplasmic, membrane bound, periplasmic, chloroplasts, hydrogenosomes	reduction of protons to H_2
[Fe]-H_2ase	methanogenes	monomeric	cytoplasmic	H_2 formation

3.2 [FeFe] hydrogenase

Regarding to their known H_2 generation efficiency (up to 9000 molecules H_2/s) the [FeFe] hydrogenases are interesting targets for biomimetic modeling.[17] As revealed in Table 1, [FeFe] H_2ases are found in anaerobic organisms.[25]. Nicolet *et al.* and Peters *et al.* reported in 1998 and 1999 the topology of the [FeFe] hydrogenases from *Desulfovibrio desulfuricans* (DdHase)[26] and *Clostridium pasteurianum* (CpI), respectively.[27] The periplasmic, heterodimeric DdHase consists of a small and a large subunit, which have molecular weights of approximately 11 kDa and 42 kDa, respectively. The so called "H-cluster" (Figure 1), which represents the catalytic active site of this enzyme, consists of a [4Fe4S] cluster buried deeply in the hydrogenase peptide matrix (Figure 2) and is bridged through a thiolate (Cys382) to a binuclear [2Fe2S] cluster.

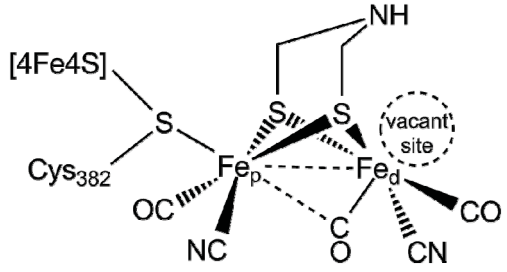

Figure 1: Active site of DdHase.

The two iron atoms of this cluster are bridged by a three-membered dithiolato ligand, which is today known as adt (azadithiolate) bridge,[28,29] and further coordinated by five non-protein and non-sulfur ligands.[30–33] Two of them are cyanide ligands and establish hydrogen bonds with the nitrogen atoms of alanine A109 and isoleucine I204, respectively. The formed hydrogen bonds are highlighted in Figure 2 as dashed lines.[34,35] The other three ligands are carbonyls, of whose two are placed in hydrophobic pockets and the third asymmetrically bridges the two iron atoms. Whereas the coordination sphere of the proximal iron (Fe_p in Figure 1, or Fe2 in Figure 2) is coordinatively saturated, the distal iron possesses a vacant coordination site to which hydrogenic species like a proton, molecular hydrogen or a hydride can bind. Additionally, a lysine K237 is positioned 440 ppm away from the Fe_d and can act as a possible proton distributor during the catalysis (Figure 2).

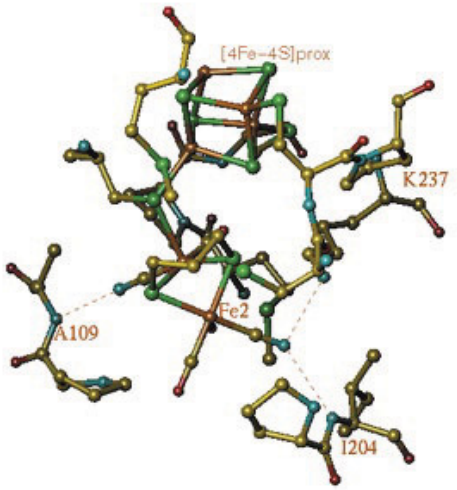

Figure 2: Interactions of the active site of DdHase with the protein. The two cyanide ligands form hydrogen bonds (dashed lines) with the protein (gold: carbon, brown: iron, blue: nitrogen, red: oxygen, green: sulfur).[26]

In addition to the catalytic active "H-cluster", the enzyme is connected to a [4Fe4S] cluster (Figure 1-3) by the Cys382. Two additional [4Fe4S] cluster form the electron pathway from the surface of the protein to the [2Fe2S] cluster.[26,36] In order to prove the substrate access to the active site, DFT calculations of the cavity structure were performed. The calculations afford a unique hydrophobic channel connecting the enzyme surface with the vacant site of the Fe_d from the active site (Figure 3).[26,37] The calculations further suggested that internal protein flexibility is required for the diffusion of the substrate through this channel. The approach of a proton is plausible by a proton pathway of DdHase (Figure 4) running either from

lysine K237 or serine S202 to glutamine E240, three water molecules and glutamine E245, which represents the shortest distance from the molecular surface to the active site.[26] Recent molecular dynamic studies of CpI are consistent with a dominant proton transfer pathway containing mainly amino acid residues rather than water molecules.[38,39]

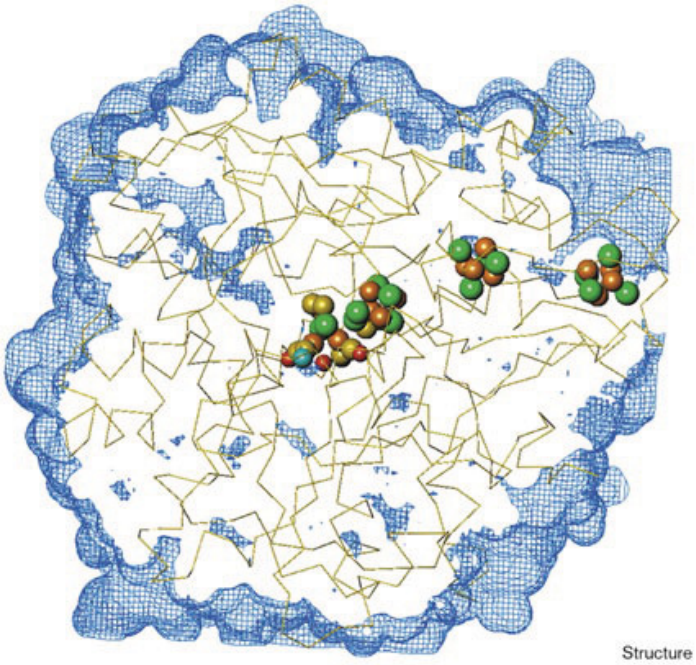

Figure 3: Calculated presentation of the gas access to the active site of a [FeFe] H_2ase with a single channel connecting the vacant coordination site with the molecular surface and the electron pathway through the ferredoxin units.[26]

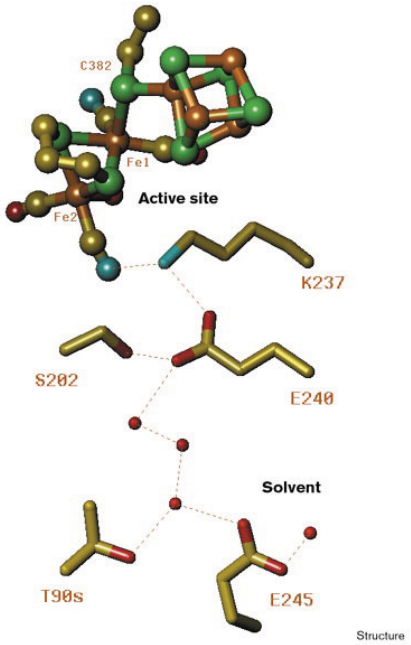

Figure 4: Possible proton pathway in DdHase (hydrogen bonds are depicted as dashed lines, red spheres are water molecules, gold: carbon, brown: iron, blue: nitrogen, red: oxygen, green: sulfur).[26]

3.3 Redox states of the active site and mechanistic implications

As mentioned above the active site contains the [2Fe2S] subsite covalently linked by Cys382 to a [4Fe4S] ferredoxin unit (Figure 1),[28,40,41] which can assume different catalytic active and non-catalytic states, respectively. Until today, seven different redox states of the active site were identified by EPR and Mössbauer spectroscopy as well as FTIR measurements (Figure 5).[36,42–44] Under aerobically conditions the active site exists in a doubly oxidized form, which is named $\mathbf{H_{ox}^{air}}$ and reveals no EPR signal (S = 0). Reduction of $\mathbf{H_{ox}^{air}}$ by a one-electron step (E = -92 mV, against NHE)[45] leads to the transient state, which is called $\mathbf{H_{trans}}$ (rhombic EPR signals are observed (S = ½) at g = 2.06, 1.96 and 1.89).[36] Mössbauer spectroscopy exhibits diamagnetic states for the [2Fe2S] cluster in $\mathbf{H_{ox}^{air}}$ and $\mathbf{H_{trans}}$ (the transferred electron reduces the [4Fe4S] cubane, which is now in a paramagnetic state)[42,46] and DFT calculations for these both states support a $Fe^{II}Fe^{II}$ configuration of the active site.[47,48] One CO ligand is bridged between the two iron atoms and the free coordination site is occupied by an OH-group.[36] Reduction at E = -301 mV (against NHE) leads to an irreversible redox-dependent activation from the $\mathbf{H_{trans}}$ to the catalytic active oxidized $\mathbf{H_{ox}}$ state, which was identified by Mössbauer and ENDOR studies to be now paramagnetic and characterized by a mixed valence $Fe^{I}Fe^{II}$ diiron part (distal Fe^{I} and proximal Fe^{II}).[49–51] Rhombic EPR signals are observed (S = ½) at g = 2.10, 2.04 and 2.00[36] and the [4Fe4S] subcluster is in a diamagnetic state again.[49,50] Furthermore, this species has one CO bridged between the two iron atoms and a free vacant site. Addition of a proton, which bounds at the adt-amine,[43] and reduction leads to the catalytic active reduced $\mathbf{H_{red}}$ state, which is diamagnetic again (S = 0) due to the $Fe^{I}Fe^{I}$ configuration.[43,52–54] The bridged CO ligand shifts toward the distal iron atom and is now in a semi-bridging position.[28] Transfer of a third electron (counted starting from $\mathbf{H_{ox}^{air}}$) results the paramagnetic super reduced state $\mathbf{H_{sred}}$. In this state the [4Fe4S] subcluster is an essential part, because this cubane is singly reduced,[43,45] whereas the binuclear site remains in the $Fe^{I}Fe^{I}$ configuration.[43] The former adt-bound proton in $\mathbf{H_{sred}}$ is now believed to be just associated with the H-cluster and is possibly bound to a nearby amino acid residue instead of the adt-nitrogen atom (“hydride-to-be” proton). Recent studies presume also the presence of iron-hydride bonds in the super-reduced state as a possible intermediate in the catalytic cycle.[55] In a next step a second proton is transferred to

the adt-amine and the “hydride-to-be” proton is bound to the vacant site of the distal iron atom to form a terminal hydride. DFT calculations suggests, that only the second protonation at the adt bridge triggers the electron transfer from the singly reduced $[4Fe4S]^{+}$ cubane to the [2Fe2S] cluster and enables the formation of a hydride, while the [4Fe4S] subcluster and the distal iron atom are oxidized again to $[4Fe4S]^{2+}$ and to the mixed-valance $Fe_p^{I}Fe_d^{II}$ core, respectively.[43,56] In addition, the CO ligand is in a bridging position again. In turn, the formed terminal hydride reacts with the proton available at the adt-amine to produce molecular hydrogen, which leaves the active site to form the $\mathbf{H_{ox}}$ state again.[43]

Since it is known, that [FeFe] hydrogenases are sensitive to inhibition by CO, the active $\mathbf{H_{ox}}$ state can be coordinated by a CO, which occupies the vacant site and leads to the $\mathbf{H_{ox}CO}$ state.[40] For this state (S = ½) an axial EPR signal at g = 2.006, 2.065 is observed.[36,57] A reactivation pathway of the $\mathbf{H_{ox}CO}$ state was identified recently by two consecutive reductions at E = -470 mV and E = -500 mV (against NHE), respectively, which lead directly to the super reduced state $\mathbf{H_{sred}}$.[44] The first reduction at E = -470 mV leads to the intermediary $\mathbf{H_{„red"}CO}$ state, in which the [4Fe4S] ferredoxin unit is singly reduced and the [2Fe2S] cluster remains in a $Fe^{I}Fe^{II}$ configuration. During the second reduction step at E = -500 mV the inhibiting CO leaves the vacant site of the catalytic center and the Fe^{II} is reduced to a Fe^{I}, forming the $Fe^{I}Fe^{I}$ subsite of $\mathbf{H_{sred}}$.[44]

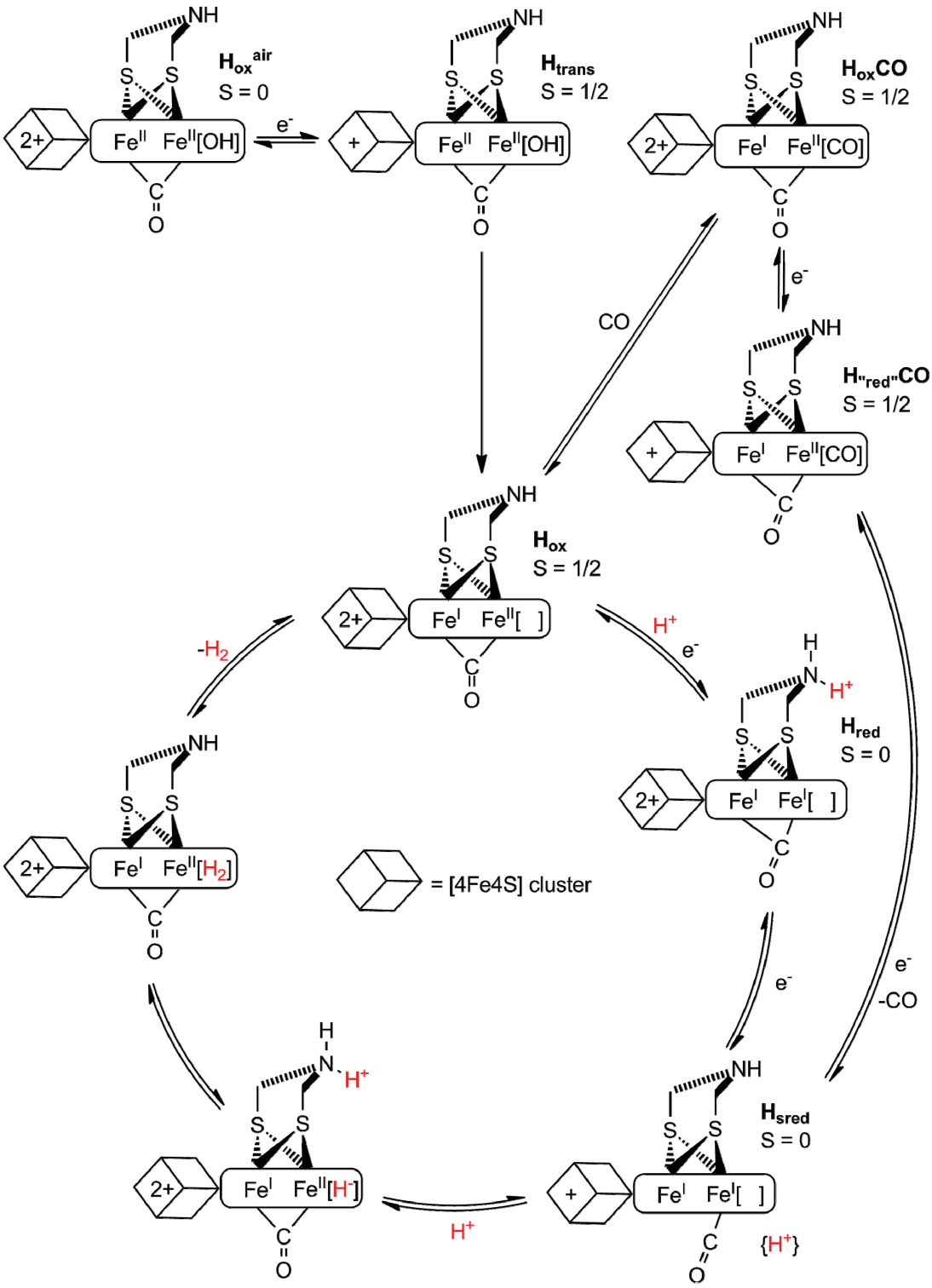

Figure 5: Redox states of the active site and proposed catalytic cycle for [FeFe] H2ase including the possible super reduced state H_{sred} {H^+}.[36,42–44]

3.4 Biomimetic catalysts

3.4.1 First generation of [FeFe] hydrogenase mimics

Figure 6 represents the simplified historical evolution of the iron hydrogenases starting from the CO-mobilized iron sulfide, whose origin lies in FeS_x (x = 1, 2) as proposed by Wächtershäuser[58], Weigand[59] and Darenbourg[60], as the anchestor of the organometallic active site of iron hydrogenases comparing the nature with chemists work. In nature, condensation reactions of atoms and small molecules on the surface of $[Fe_2S_2(CO)_6]$ created first rudimentary organic moieties.[60] Within 4 billion of years the catalyst became internalized within the protein, evolving to be protected from the oxidizing enviroment of a maturing earth and obligatory, resulting in a controlled synthesis of an extraordinary and sophisticated catalytic site.[60]

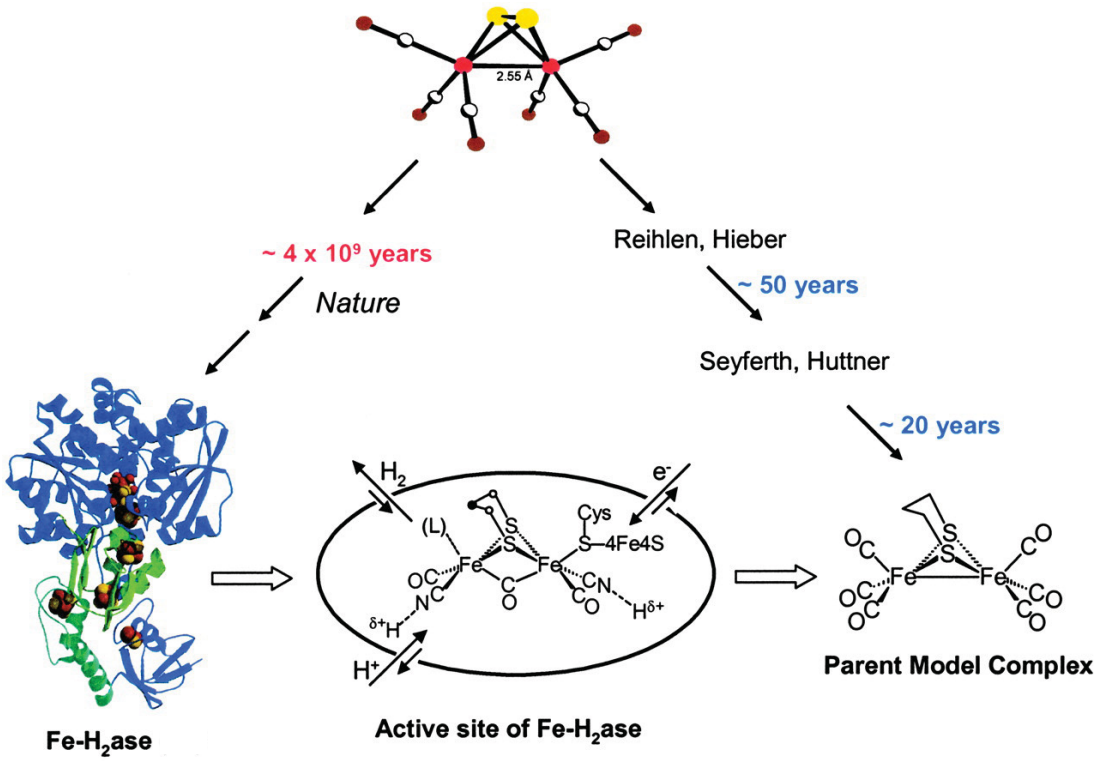

Figure 6: Representation of the evolution of CO-mobilized iron sulfide in nature to yield the active site of [FeFe] hydrogenase and in chemists' laboratories to yield the parent model complex.[60]

In 1929 Reihlen *et al.* reported a dithiolate-alkyl substituted hexacarbonyl diiron system analogous to the structure of the [FeFe] hydrogenases' active site; long before their structure was unveiled.[61] Later on, Hieber *et al.* synthesized the first complex with the general structure $[Fe_2(CO)_6(SR_2)_2]$ by reaction of two equivalents ethanethiol with $Fe_2(CO)_9$ (Scheme 2) to get complex **1**.[62] In the following years Hieber,[62–65] Huttner[66,67] and Seyfarth[68–92] pursued the systematic research on [2Fe2S] low valant complexes (Scheme 2). In 1963, Dahl *et al.* verified the structure of $[Fe_2(CO)_6(SEt_2)_2]$ **1** by X-ray structure analysis.[93] Since the discovery of a hydrogenase enzyme in bacteria in 1931,[94] almost seven decades are required to unveil the structural elements of their active site by Seefeldt *et al.*[27] and Fontecilla-Camps *et al.*[26], and to determine the striking similarity of the [2Fe2S] subsite to the diiron complexes reported years before. [61–93] Inspired from these findings, Pickett, Rauchfuss, and Darenbourg replaced two CO ligands of **2** through two cyanides by reaction of the hexacarbonyl diiron system with two equivalents tetraethyl ammonium cyanide to give the [FeFe] hydrogenase model complex $[Fe_2(CO)_4(CN)_2(\mu\text{-pdt})]^{2-}$ **3** (Scheme 2).[95–97]

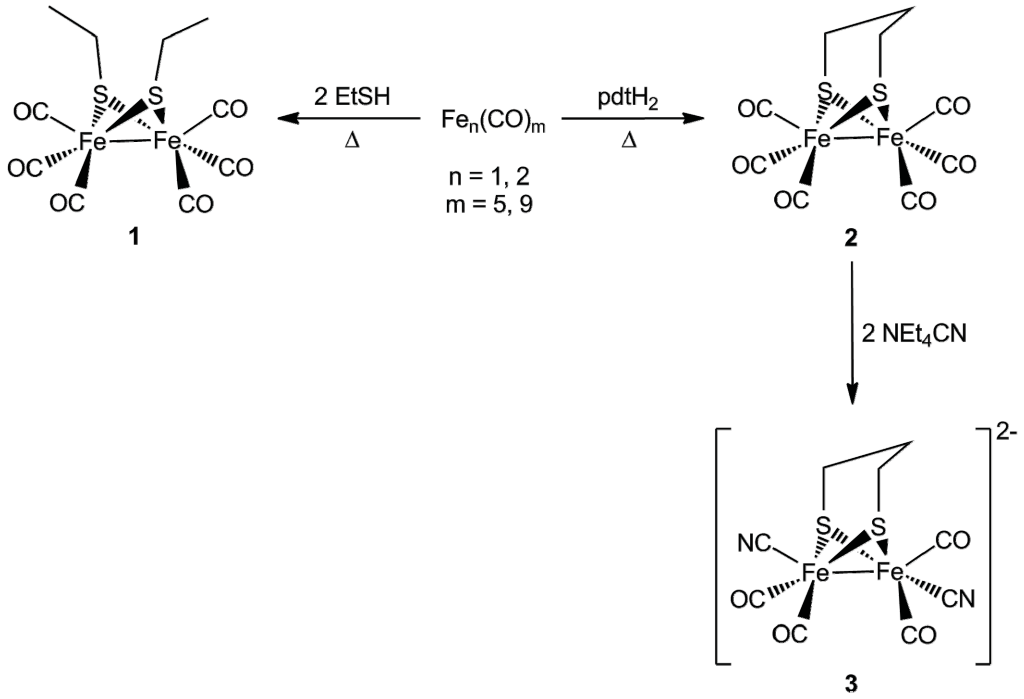

Scheme 2: Synthetic scheme for the preparation of the first diiron model complexes **1**-**3**.

3.4.2 Abiological modifications

In the last 15 years a plenty of compounds were synthesized and investigated.[98] Till the nature of the bridging dithiolato ligand was revealed as an adt bridge, numerous of possibilities in the design of hydrogenase mimics were feasible and led to the preparation of [FeFe] hydrogenase model complexes bearing adt[99], odt[99–101] (oxodithiolato) and sdt[102,103] (sulfurdithiolato) ligands analogues to pdt bridged compounds **4** - **9** (Scheme 3).[104]

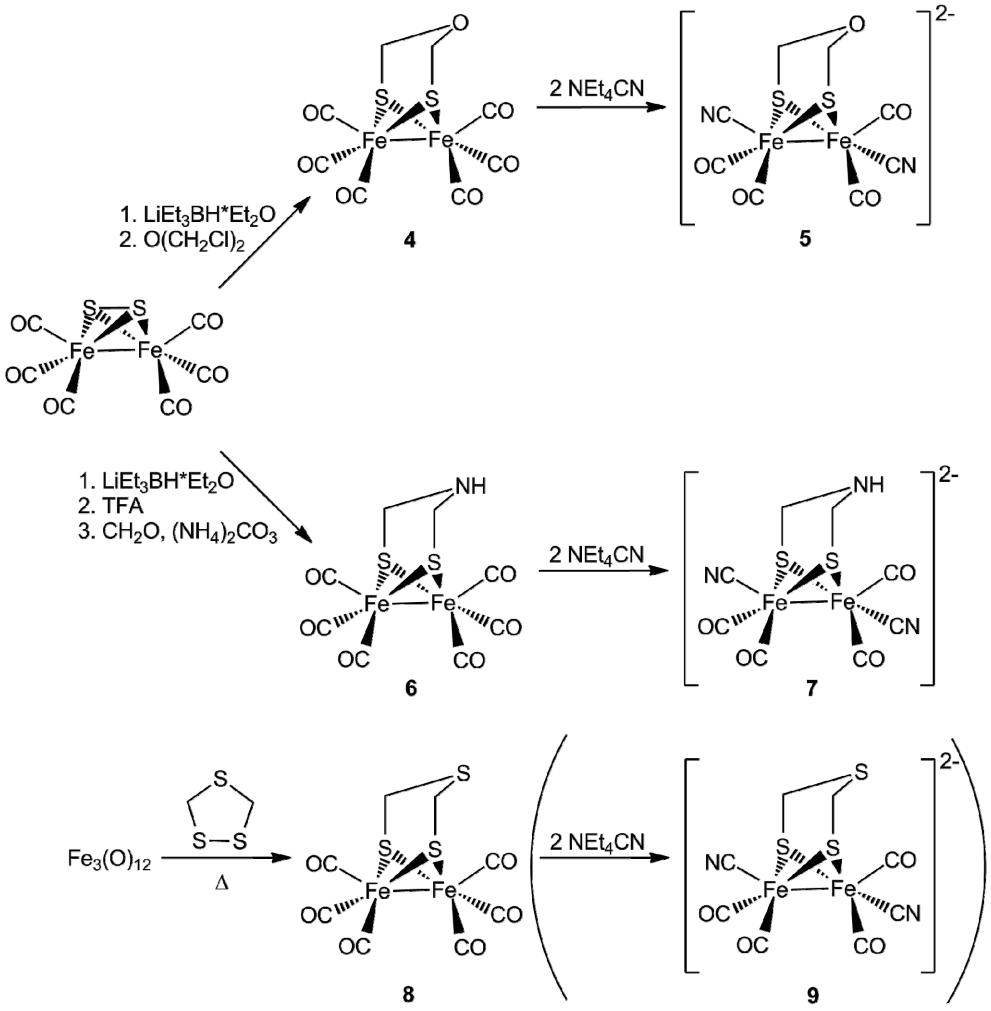

Scheme 3: Synthetic scheme for the preparation of [FeFe] hydrogenase model complexes bearing relevant odt (**4**, **5**), adt (**6**, **7**) and sdt (**8**, **9**) bridges and their cyanide substituted ones.

Till today different bridgehead groups are established and interesting systems possessing novel features have been developed. The effect of bridgehead alteration with atypical elements from the crystallogens (group IV), pnictogens and chalcogens, such as Si,[105–107] Ge, Sn,[108] P[109] and Se,[110,111] were investigated to benefit the

design of future [FeFe] hydrogenase model systems. To overcome some key issues, such as large overpotential requirements for proton reduction, inclusion of suitably substituted aromatic dithiolate bridges are reported, bearing highly substituted benzenedithiolate (bdt) **10**-**14** or quinoxaline **15** shown in Figure 7.[112–114] With an increasing number of electron-withdrawing groups, the potential can be shifted into positive direction by 150 mV with a concurrent decreasing of the catalytic efficiency.

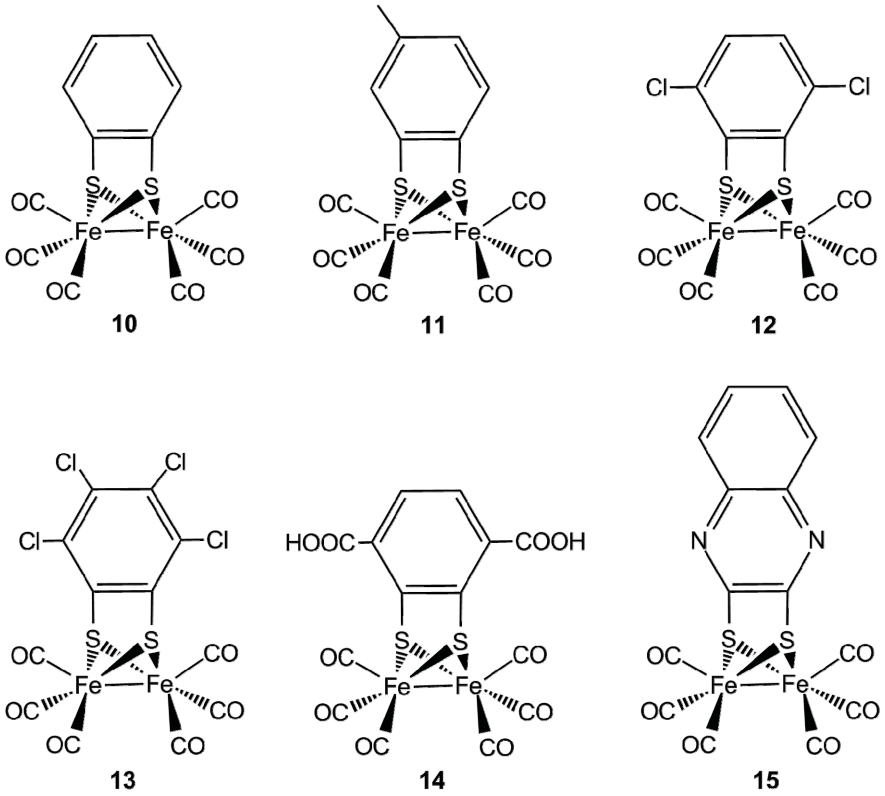

Figure 7: Reported [Fe_2(μ-arenedithiloate)$(CO)_6$]-hydrogenase model systems.[112–114]

To simulate the electron donating properties of the cyanide ligand from natural enzymes, biologically relevant ligands such as thioethers or isocyanides were introduced by CO-exchange, but also abiological groups like phosphines, carbenes and amines were investigated to modify the [2Fe2S] subsite models.[104,115] These alterations will allow the replication of some key aspects of the natural [FeFe] hydrogenase, for example the isolation of a bridging and terminal hydride species, respectively, or of the rotated state conformation, which will be discussed in the next chapters.

3.4.3 Proton relays and hydride species of [FeFe] hydrogenase models

Protonation of the [FeFe] H_2ases active site is believed to occur at the vacant site of the Fe_d in the H_{ox} state. Other possible protonation sites like the Fe-Fe bond, the nitrogen atom of the adt bridge, the cyanide ligands as well as the dithiolate bridge have been suggested to play a crucial role in hydrogenase modeling.[115–120] Initial protonation at the adt bridge in the [FeFe] hydrogenase allow for a proton relay between the amino function and the distal iron atom, which opened a wide range of research possibilities.[121–123]

Such a conceivable proton relay mechanism was published by Rauchfuss *et al.* in 2009 represented in Figure 8.[123] Initially, protonation occurs at the nitrogen atom of the adt-bridge followed by a subsequent relay of this proton to the distal iron atom. At room temperature this relay is ensued by an isomerization of the terminal hydride to the thermodynamically favoured bridging hydride.[123] Although the basicity of the distal iron atom and the adt nitrogen atom with a $pK_a \sim 8$ is comparable,[122] protonation of the amino function is kinetically favoured, even if the basicity of the iron atom is increased by substitution with electron donating groups.[124]

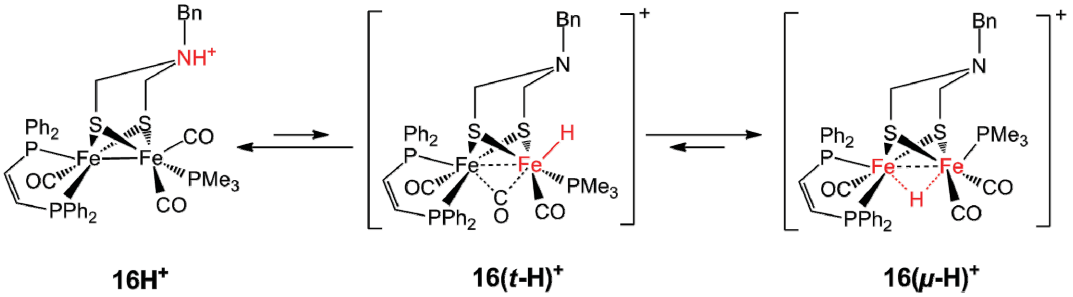

Figure 8: Proton relay mechanism reported by Rauchfuss *et al.* in 2009.[123]

Worth noting Åkermark *et al.* reported on [FeFe] hydrogenase model complexes bearing alkyl or aryl carboxylic acid functions at the adt bridge, which allow the efficient electrocatalytic formation of hydrogen in the presence of small amounts of an additional acid in aqueous solution.[125] Scheme 4 shows the proposed electrocatalytic mechanism for proton reduction for their reported system. After addition of two equivalents TfOH a shift of the reduction peak by 400 mV to more positive values is observed, which is due to the protonation of the amino function

before reduction (**17H$^+$**). Forced by the lowered pH-value related to the added trifluoroacetic acid, the carboxylic acid function transfers its proton to the amino bridge. This is followed by the first electron transfer as well as the transfer of a hydrogen bond from a water molecule to the carboxylate, which allows the relay of the adt-proton to the iron atom to form a rotated state species with a terminal hydride. Protonation of the nitrogen atom of the adt bridge followed by a second electron transfer gives intermediate **17(*t*-H--H$^+$)**, in which the proton can bind to the hydride to form molecular hydrogen.

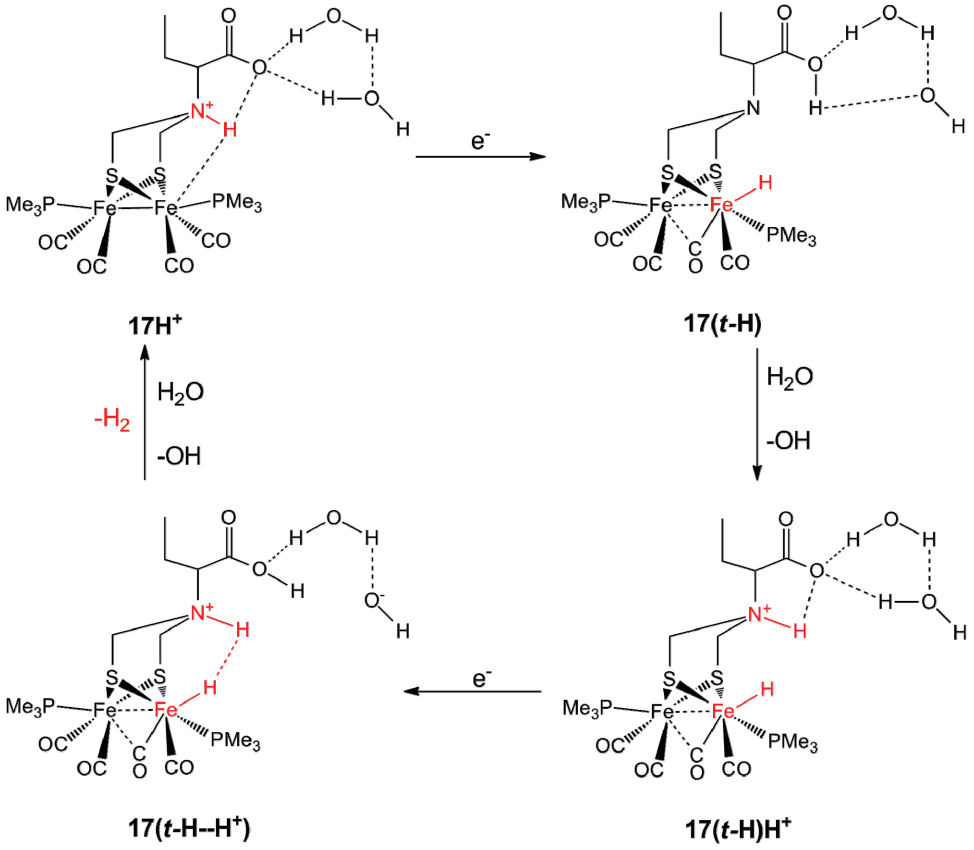

Scheme 4: Proposed electrocatalytic mechanism for proton reduction of carboxylate functionalized [FeFe] hydrogenase mimics (trifluoroacetic acid is omitted for clarity).[125]

The obtained mechanism of Åkermark *et al.*[125] and also previous works suggest, that the twofold exchange of CO by phosphines stabilizes terminal hydrides. These results lead to a new class of [FeFe] hydrogenase model complexes implementing a pendant basic functionality into chelating phosphine ligands. Investigations by Schollhammer,[126] Liu[127] and Sun *et al.*[128] report of such an incorporation of pendant basic functionality into phosphine ligands. Ott *et al.* shows the directional control of the initial protonation site by tuning the amine functionalities of

bisphosphine ligands (Scheme 5). Just small variations within the amine group allow the generation of an ammonium salt (**18**/**18H**$^+$), a μ-hydride species by attack at the Fe-Fe bond (**19**/**19(μ-H)**$^+$) or a protonated dithiolate sulfur species (**20**/**20(*μ*-SH)**$^+$), if the amine group is substituted just by a CH_2 group.[117]

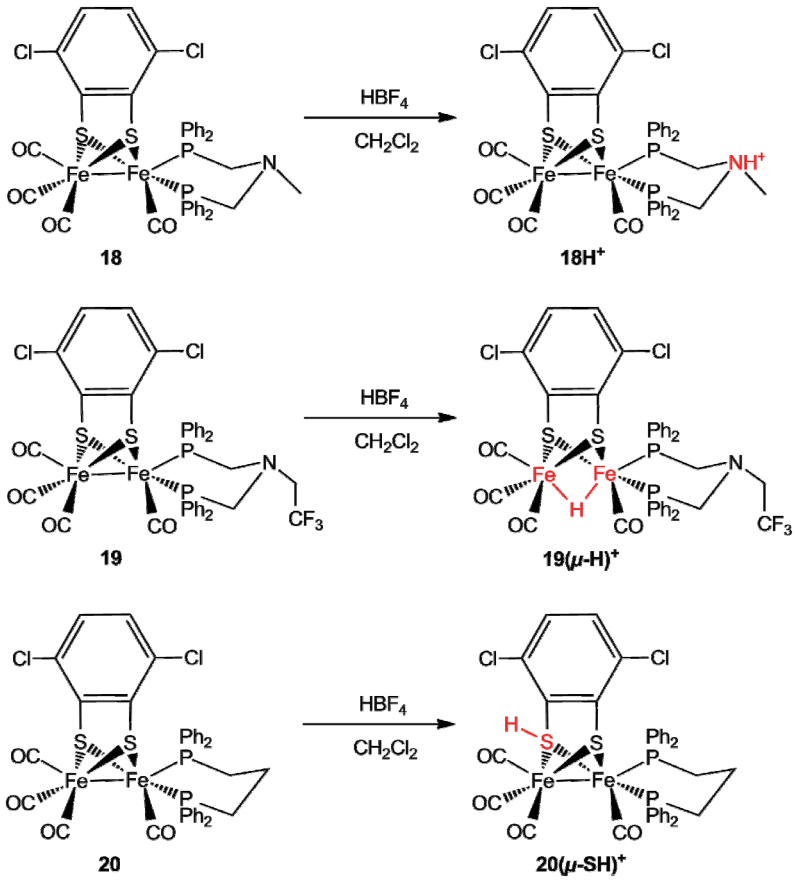

Scheme 5: Directional control of initial protonation by tuning of amine functionalities.[117]

Talarmin *et al.* reported an example for a proton transfer from such an amine function of a bisphosphine ligand in chair conformation to the diiron center. Protonation of $[Fe_2(\mu\text{-pdt})(CO)_4(\{PPh_2CH_2\}NCH_3)]$ with an excess of $HBF_4{\cdot}Et_2O$ in acetone yields the ammonium species $[Fe_2(\mu\text{-pdt})(CO)_4(\{PPh_2CH_2\}HNCH_3)]^+$, whereas no protonation at the diiron center was observed. Dissolving this species in dichloromethane gave the thermodynamically favoured bridging hydride species $[Fe_2(\mu\text{-pdt})(\mu\text{-H})(CO)_4(\{PPh_2CH_2\}NCH_3)]^+$ by a proton relay between the ligand and the diiron center meanwhile the bisphosphine ligand isomerizes from basal-apical to basal-basal.[126]

As **20(μ-SH)**$^+$ demonstrates, not only protonation at nitrogen atoms from an adt bridge or a pendant phosphine ligand allow for a proton relay, but also the μ-sulfur atoms of the dithiolate bridge can be considered as possible basic sites in the catalytic cycle of natural enzymes, which was also suggested by DFT calculations[129] and opened a wide range of research possibilities. To force the kinetically favoured protonation of a μ-sulfur atom, complex **20** combines the substitution of two carbonyl ligands with an electron donating bisphosphine ligand and an electron withdrawing dithiolate bridge. The μ-sulfur protonation was proved indirectly by IR and ^{31}P NMR spectroscopy. After addition of $HBF_4 \cdot Et_2O$ to a dichloromethane solution of complex **20**, a shift of CO stretching modes by 63 cm^{-1} to higher wavenumbers was observed, whereas no signal in the typical hydride region in the ^{1}H NMR could be detected. The ^{31}P NMR spectrum shows one singlet at 9.6 ppm suggesting a rapid proton exchange between the two μ-sulfur atoms. Because of the absence of an amino function like occurring in complexes **18** and **19**, the only remaining basic sites are the μ-sulfur atoms.[117]

Other examples for μ-sulfur protonated complexes were reported recently[130] and further more related examples are shown in Figure 9. Whereas [FeFe] hydrogenase mimic **21**[118] also combines the substitution of two carbonyl ligands with electron donating phosphine ligands and an electron withdrawing dithiolate bridge, compound **22**[107] does not contain any stronger electron donating ligands than carbonyl ligands, but a silicon atom at the bridgehead, which increases the basicity of μ-sulfur atoms and thus forcing a protonation. The absence of stronger electron donating ligands (compared to CO) in **22** is in line with the relatively small shift observed for the carbonyl stretching modes in the IR spectrum by only 30 cm^{-1} after addition of acid.[120]

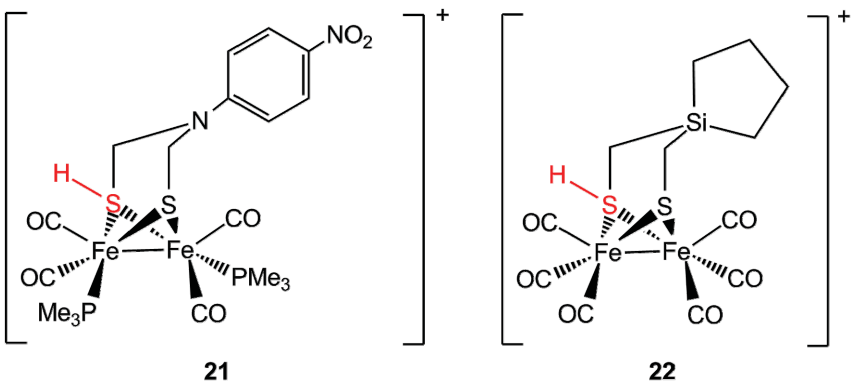

Figure 9: Structure of μ-sulfur protonated species.[107,118]

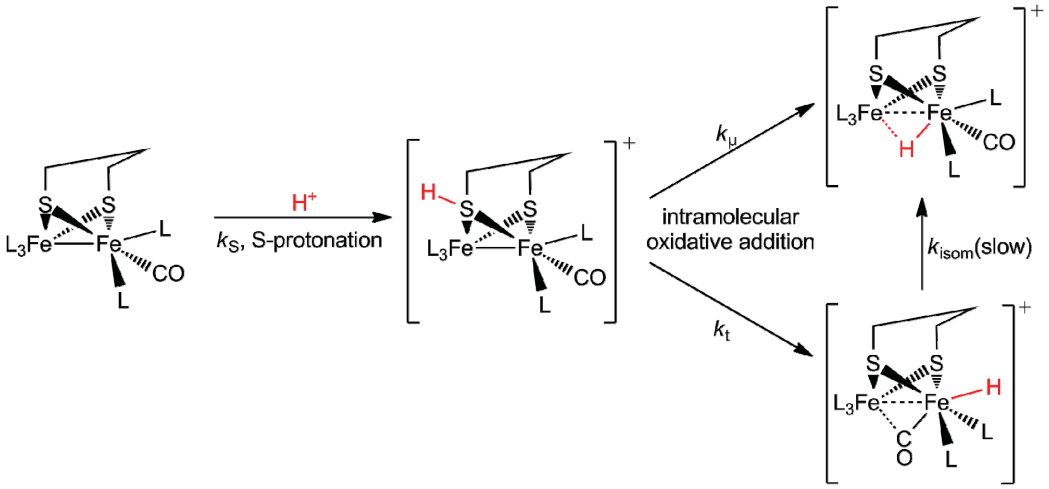

Scheme 6: Proton relay mechanism postulated by Rauchfuss *et al*. in 2012.[116]

In 2012 Rauchfuss *et al*. postulated a proton relay mechanism shown in Scheme 6. They also suggest the μ-sulfur atom as possible protonation site upon addition of acid and assume at the first time that these μ-S-protonated intermediates are involved in the hydride-formation. NMR spectroscopic studies showed that the $[Fe_2(CO)_2(PMe_3)_4\{\mu\text{-}SCH_2)_2\}]$ as well as the $[Fe_2(CO)_2(PMe_3)_4\{\mu\text{-}SCH_2)_2CH_3\}]$ complex form the μ-hydride without proceeding *via* the terminal hydride, although the terminal hydride species of these complexes are known to be stable. The isomerization of the terminal hydride to the μ-hydride species is also reliable with a possible μ-sulfur protonation, because this weakens the Fe-S bonds and thus promoting the rotation at the $FeH(PMe_3)_2$ center.[116]

However, the majority of the reported protonated [FeFe] hydrogenase model complexes resulting in bridging hydride species as the thermodynamically stable form or in a protonation of other functional groups as reported in this chapter. This chemistry is well investigated.[107,115–129] In 2005 Rauchfuss *et al*. reported a molecular structure of a model complex bearing a terminal hydride as well as a structure of the corresponding complex bearing a bridging hydride as shown in Figure 10.[131] Reduction of $[Fe_2(edt)(CO)_2(PMe_3)_4]$ by addition of $LiAlH_4$/$NaBH_4$ at -25 °C to an acetonitrile solution of this complex gave a mixture of the terminal and the bridging hydride species. The structure of the terminal hydride species offers one carbonyl ligand in a bridging position between the two iron atoms.

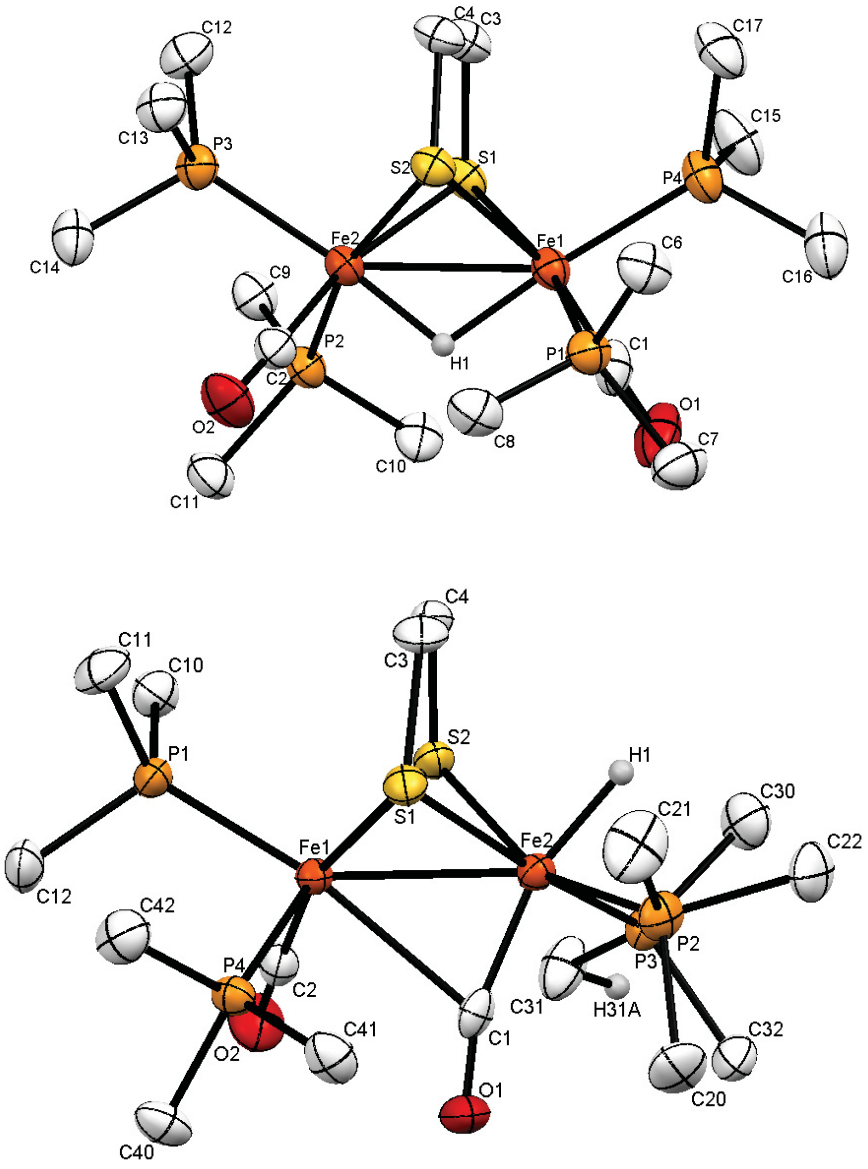

Figure 10: Molecular structures of $[Fe_2(edt)(\mu\text{-}H)(CO)_2(PMe_3)_4]PF_6]$ (top) and $[Fe_2(edt)(\mu\text{-}CO)(H)(CO)(PMe_3)_4]PF_6$ (bottom) with thermal ellipsoids drawn at 50 % probability level. All hydrogen atoms, except the bridging or terminal hydride are omitted for clarity.[131]

In further works Rauchfuss[122], Schollhammer[132]and Hogarth[133] *et al.* reported the detection of ^{1}H NMR signals characteristic of terminally bound hydrides upon protonation of phosphine substituted [FeFe] hydrogenase model complexes. In 2012, Rauchfuss *et al.* finally isolated and characterized a doubly protonated species (Figure 11). Protonation and isolation at low temperatures afford the doubly protonated complex $[Fe_2(\mu\text{-adtH})(CO)_2(H)(dppv)_2]^{2+}$.[134] The molecular structure reveals the terminal hydride at Fe1 and a bridging carbonyl ligand relevant to the catalytic cycle in nature. The distance of the terminal hydride H1 and the equatorial

amino proton H3 of 1.88(7) Å indicate a significant dihydrogen bonding. Upon warming the reaction solution to room temperature, the terminal hydride isomerizes to the thermodynamically favoured bridging hydride species, which was confirmed by ^{1}H NMR.[134] Comparison of terminal hydride with bridging hydride species offers a smaller overpotential under electrocatalytic conditions for the terminal hydride species (150 mV). The turn-over-frequencies during electrochemical reduction in the presence of CF_3COOH in dichloromethane offers a TOF of 5000/s for the $[Fe_2(\mu\text{-adtH})(CO)_2(H)(dppv)_2]^{2+}$ species, whereas the bridging hydride isomer reached just 20/s. These results suggest that the natural enzyme would likely favour such a catalytic intermediate, further evidenced by the fact, that the presence of a pendant base in close proximity to the iron atom kinetically favour terminal hydride species.[104,121,122,135]

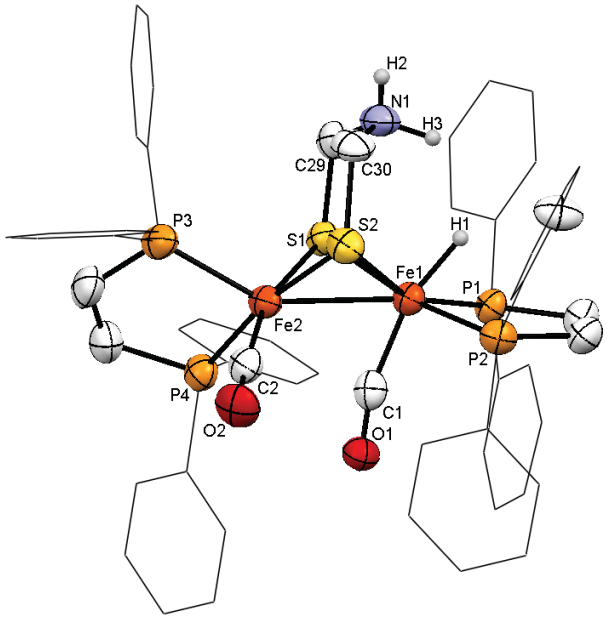

Figure 11: Molecular structure of $[Fe_2(\mu\text{-adtH})(CO)_2(H)(dppv)_2]^{2+}$ with thermal ellipsoids drawn at 50 % probability level. All hydrogen atoms, except the terminal hydride or the ammonia protons are omitted for clarity.[134]

3.4.4 Rotated state species of [FeFe] hydrogenase models

An indispensible criterion for an effective catalysis is the rotated state of the H-cluster in the [FeFe] H_2ase (Figure 1), which was described in detail in chapter 1.2. The limitation of this specific rotated geometry of the [FeFe] hydrogenases' active site is highly challenging as no stabilizing protein environment is present in model compounds. In 2001 Razavet *et al.* synthesized the first assembly of a [$Fe^{I}Fe^{I}$] species containing a bridging carbonyl ligand (Figure 12). Chemical reaction of **23** with two equivalents cyanide in acetonitrile/[K^{+}(18-crown-6)] salt reveals an instable [2Fe3S] dicyanide species **24** with a bridging carbonyl ligand. Comparison of the infrared data with the natural system are in agreement.[136–138]

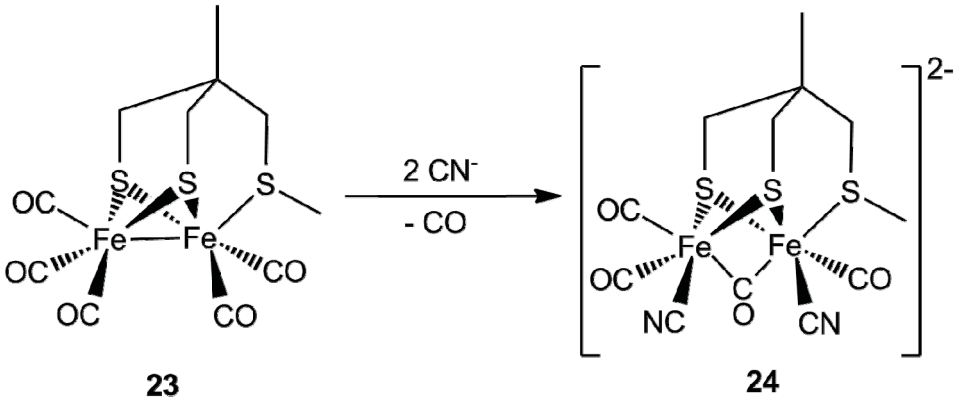

Figure 12: [$Fe^{I}Fe^{I}$] species **24** containing a bridging carbonyl ligand.[136]

In the following years different approaches were reported (Figure 13). An increased stability of the rotated form of [FeFe] hydrogenase mimics could be reached *via* increasing the electron density at the iron centers by multiple substitutions of carbonyl ligands with different nitriles and phosphines like in complexes **25-36**, but were less stable than the previously reported complex **24**.[131,139–141]

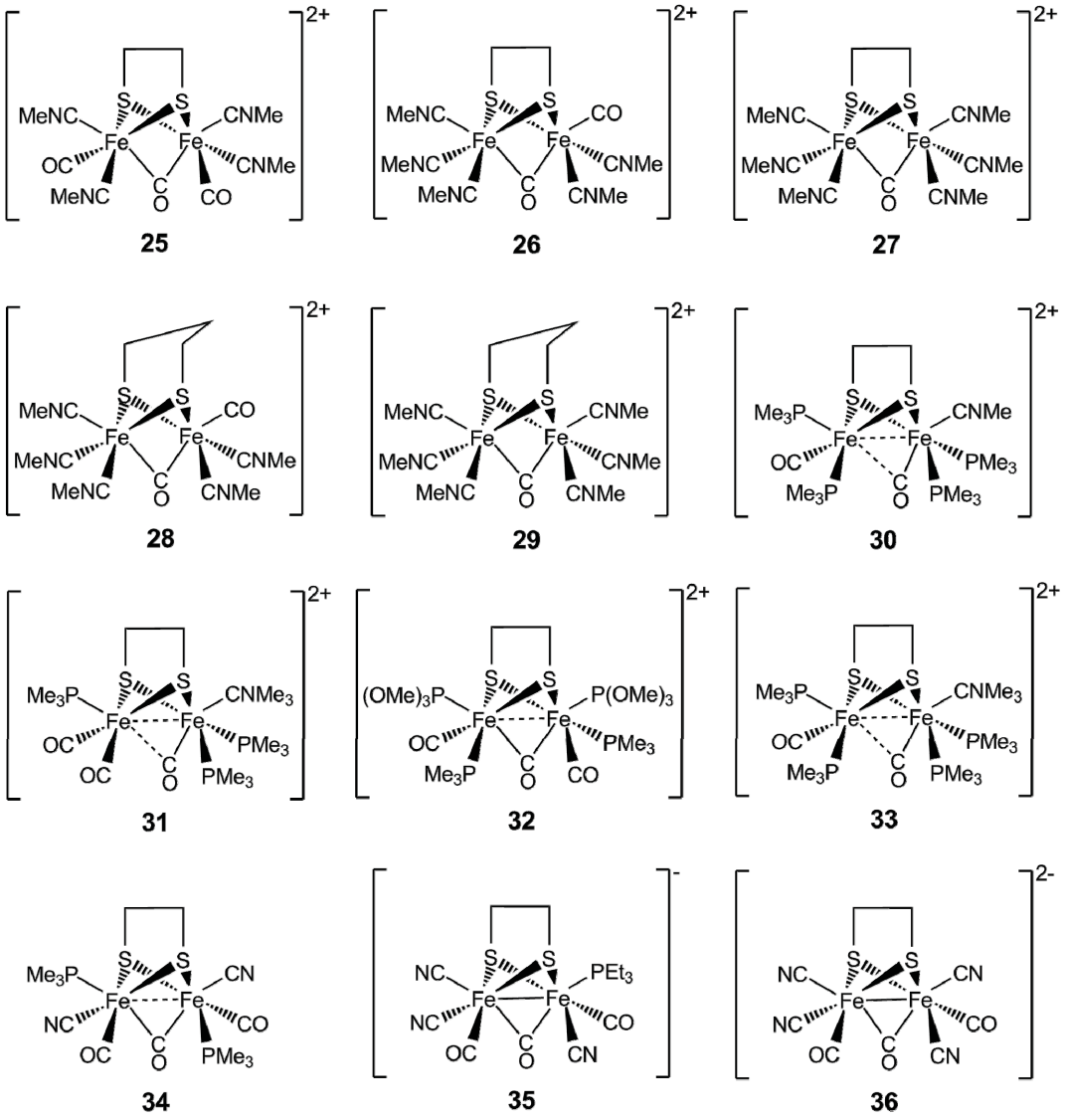

Figure 13: Rotated forms of [FeFe] hydrogenase mimics **25-36**.[131,139–141]

Furthermore, Darenbourg as well as Rauchfuss *et al*. introduced sterically bulk for the stabilization of the rotated state (Figure 14). These complexes possesses sterically bulky dithiolate linker and two or more non-carbonyl ligands like carbenes and diphosphines (**37-40**).[142–145]

Another approach is the isoelectronic replacement of a carbonyl ligand by NO^+ reported first by Rauchfuss *et al*. in 2008. Substitution yielded **41** as a largely rotated structure as the minor isomer (major isomer presents the unrotated form) of the diiron complex.[146] In addition, Darenbourg *et al*. introduced in this NO^+ substituted complexes a sterical bulky dithiolate linker, which results in complexes **42** and

43.[145] These two complexes also revealing the rotated form and compared to compound **41** only exists in this isomeric form.

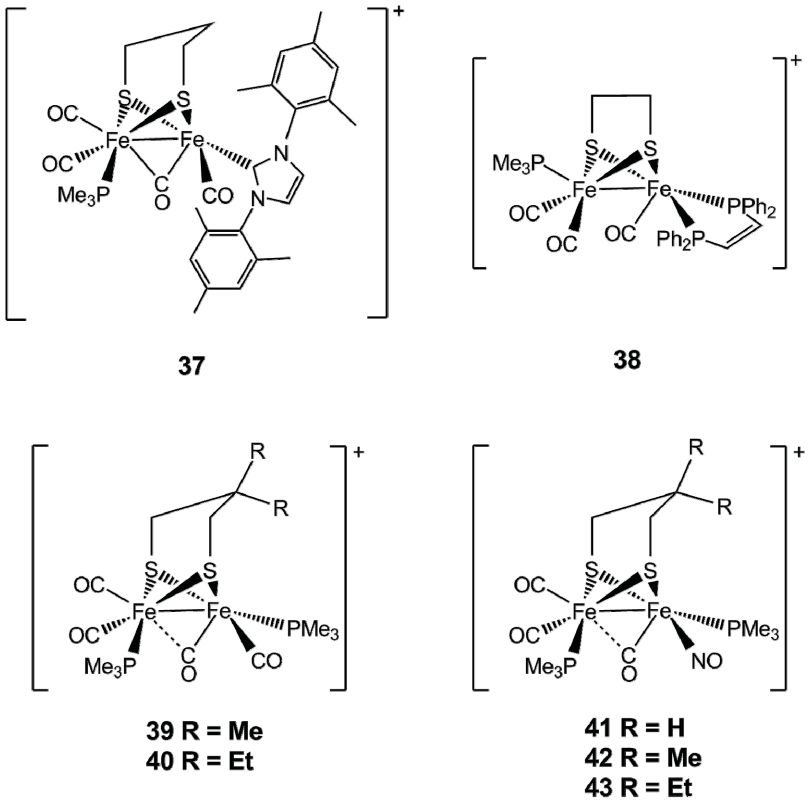

Figure 14: Sterical crowded mixed-valent rotated forms of [FeFe] hydrogenase mimics **37**-**43**.

Sun *et al.* reported a diiron dithiolate complex with a pendant phosphine in the second coordination sphere bound at the nitrogen atom of the adt-bridge (Figure 15). Oxidation of this complex with ferrocenium at -70 °C reveals a $[Fe^{I}Fe^{II}]$ moiety with a bridging carbonyl ligand and the pendant phosphine coordinated to the rotated iron moiety. Further oxidation with ferrocenium yields in a $[Fe^{II}Fe^{II}]$ species and a complete dissociation of the Fe-Fe bond. This work shows, that the dithiolate bridgehead can function not only as a proton transfer relay (in the presence of protons for reduction to hydrogen), but also as an electron donor to stabilize the unsaturated coordination sphere of the Fe^{II} moiety in redox reactions.[147]

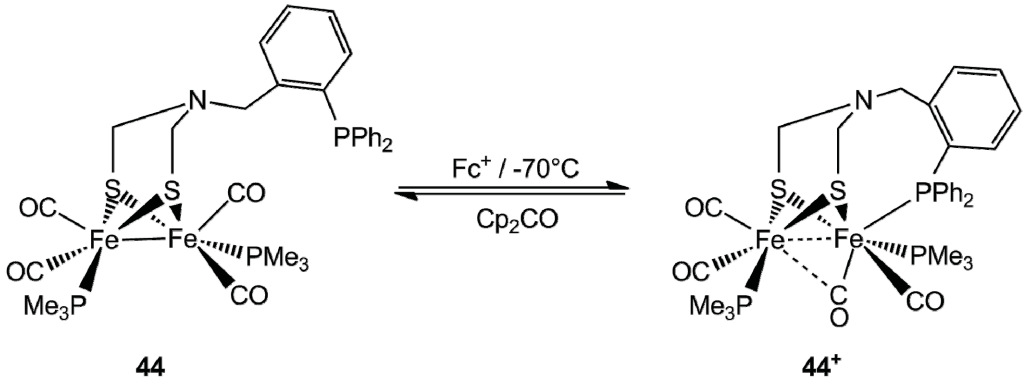

Figure 15: Redox reaction of diiron dithiolate complex **44** revealing a rotated [$Fe^{I}Fe^{II}$] species.[147]

Model complexes comprising a stable [$Fe^{I}Fe^{I}$] moiety in a rotated geometry instead of unstable or mixed-valent species described in this chapter before, are rare. Only very recently, the first examples of [$Fe^{I}Fe^{I}$] H_2ase mimics featuring a fully rotated conformation, $[Fe_2(CO)_4(\kappa^2\text{-dmpe})\{\mu\text{-}(SCH_2)_2N\text{-Bn}\}]$[148,149] **45** and $[Fe_2(CO)_4(\kappa^2\text{-dppv})\{\mu\text{-}(SCH_2)_2CEt_2\}]$[150] **46** were reported simultaneously in 2013 by Schollhammer and Rauchfuss *et al*., respectively (Figure 16). Remarkably, both complexes reveal similar structural features that were reported to be crucial for the stabilization of this particular structure: (a) asymmetrical coordination at the two iron atoms using a bidentate donor ligand (here dmpe and dppv, respectively), (b) a bulky dithiolato bridgehead, which promotes (c) a weak remote agostic Fe···H-C interaction.

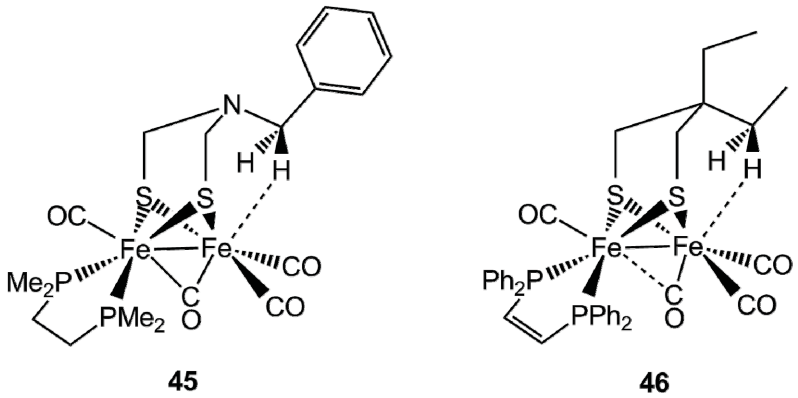

Figure 16: [$Fe^{I}Fe^{I}$] H_2ase mimics of Schollhammer (left)[148] and Rauchfuss *et al.* (right)[150] featuring a fully rotated conformation.

Indeed each of these three factors seems to be crucial for observing, in dithiolate models, a full-rotated geometry, as that existing in the [FeFe] hydrogenase cofactor. To date, when one of these factors is not conformed, only partially or semi-rotated structures of [FeFe] hydrogenase models have been observed.[145] On the other hand, a glance to the rotated state of the natural cofactor reveals that no type of agostic interaction is necessary to obtain the full-rotated geometry. The amino acid residues, which face the [2Fe2S] cluster and the [4Fe4S] cubane, are able to constrain the H-cluster itself in the full-rotated form.[151] Thus in nature, just (a) and (b) of the established factors are necessary, which suggests the importance of a sterical demanding environment around the diiron center of [FeFe] hydrogenase model complexes by dithiolato ligands to force a full-rotated geometry.

Recently, Darensbourg postulated a modified factor (a), in which an electronic asymmetrically substitution at the two iron atoms is necessary to stabilize the rotated species of [FeFe] hydrogenase model complexes using an electrophilic ligand such as NO^+ at one of the iron atoms and a nucleophilic ligand such as PMe_3 at the other iron atom. This tilt of the balance of electrophilicity/nucleophilicity at the 2Fe center creates an optimal electronic asymmetry for catalysis. This thesis is justified by comparison with the active site of the natural enzyme: the distal iron atom (Figure 1) is coordinated just by one good donor ligand (CN^-) and has a CO that can shift into a bridging position representing the electrophilic iron atom. This bridged CO ligand is stabilized by an interaction with the proximal iron atom (Figure 1), which has two good donor ligands (2 CN^-) and the thiolate ligand representing the nucleophilic iron atom of this thesis.[152]

3.5 Light Driven hydrogen production by hydrogenase mimics

A typical photocatalytic active system for hydrogen generation (Figure 17) consists of a photosensitizer, a catalyst, and a sacrificial electron as well as proton donor. To promote an efficient photocatalytic hydrogen evolution, these components should work together in a controlled assembly.[153]

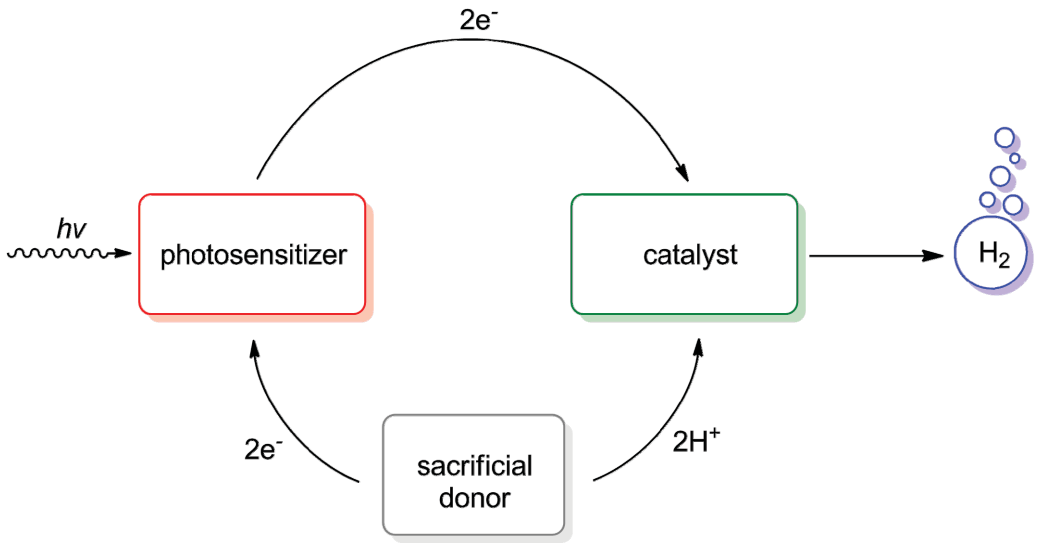

Figure 17: Schematic photocatalytic hydrogen formation.

The photosensitizer serves as light absorber and electron deliverer to the catalyst. Ideal photosensitizers should have large extinction coefficients and absorb photons in the visible light region. They should have a long excited state lifetime and be photostable. Photosensitizers can be bound covalently to the catalytic active center, whereas an intramolecular electron transfer should takes place after photoexcitation of the light harvester. Another possibility is to split the photoactive system and the catalyst into two different molecules, whereas an intermolecular ET should be followed after excitation of the PS to the catalyst molecule. Various photosensitizers involving organic and organometallic chromophores as well as quantum-confined semiconductor nanocrystals (quantum dots) have been developed.[154–161] The commonly used organometallic chromophores are Ru, Ir, or Re complexes, which consist of noble metals and have complicated structures. [114,115,162–169] Typical quantum dots consist of cadmium sulfide as well as environmentally harmful metal compositions like cadmium/tellurium and cadmium/selenium and are sized between 2.5 and 6 nm.[153,170]

A sacrificial electron donor provides electrons to the photooxidized sensitizer, in which an electron hole is generated due to the transfer of an excited electron from the sensitizer to the catalytic center. Typical electron donors involve amines (triethylamine, triethanolamine, NADH or EDTA), alcohols, thiols as well as ascorbic acid.[153,171,172] Under catalytic conditions, these molecules undergo one electron oxidation followed by decomposition pathways, which are highlighted in Scheme 7 for triethylamine and ascorbic acid as examples. As these pathways show,

decomposition produces also protons, which can be a source of H^+ in catalytic hydrogen generation. Triethylamine can provide two electrons and one proton (in non-aqueous solution) compared to ascorbic acid, which can provide two electrons as well as two protons under decomposition.[153,171,172]

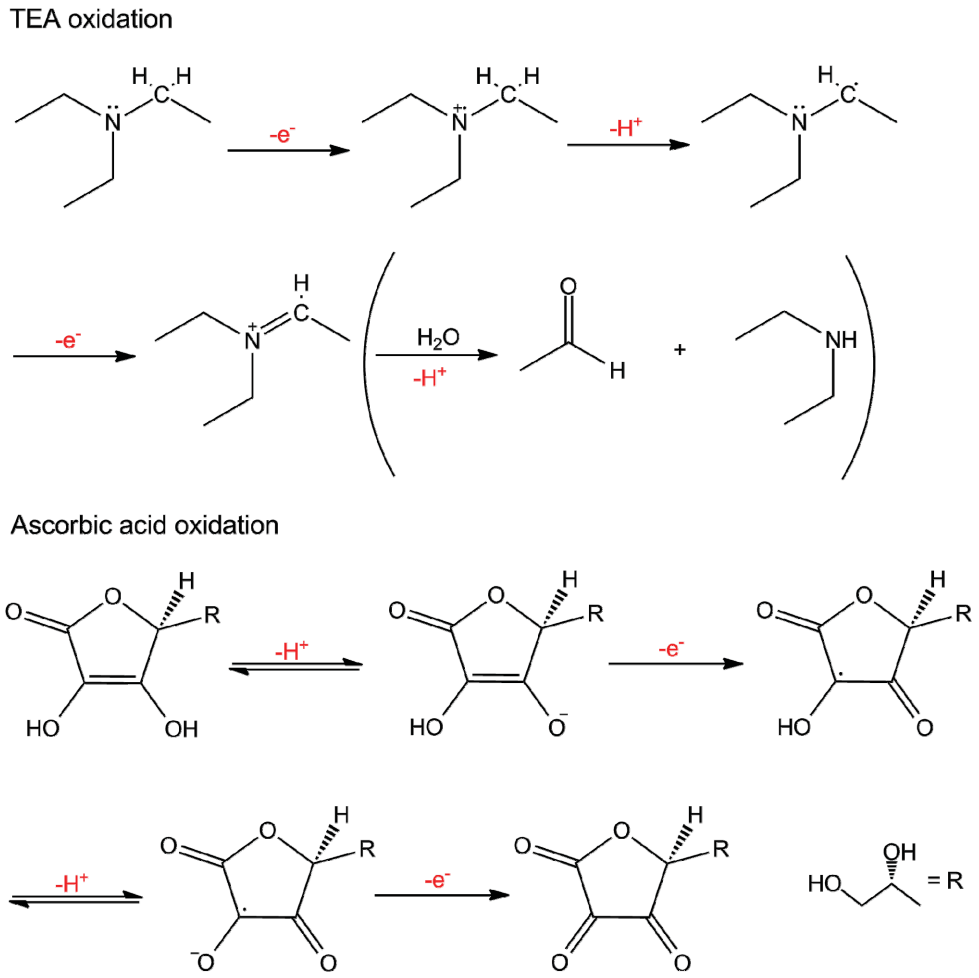

Scheme 7: Decomposition pathways for TEA and ascorbic acid oxidation, respectively.[171,172]

In a photocatalysis, the catalyst accepts electrons from a photoexcited sensitizer, which is called oxidative quenching, or from the photosensitizer radical anion generated from reductive quenching by a sacrificial electron donor. After this first electron transfer step the catalyst begins to generate dihydrogen in the presence of protons.[153] As discussed, an interesting catalyst is the [FeFe] hydrogenase, which is a highly capable systems for H_2 evolution in nature.[173–175] Up to date a wide range of bioinspired model systems for hydrogenases powered by photosensitizers were reported. Approaches like multicomponent systems with commonly used organometallic complexes as photosensitizers containing Ru, Re or Ir with high turn-

over numbers[114,115,162–169] as well as systems, in which the light harvester is covalently linked to the catalytic active site revealing moderate turn-over-numbers (TON < 127) will be discussed.[153,176–179] In detail, complete hybrid artificial photosynthetic systems,[180] dendrimer-based systems,[165], nanophotocathodes,[181] ZnS-nanoparticles[182] or quantum dots[153,183] as light harvester, reaching turn-over numbers up to tens of thousands were reported. Much afford was spent to force a photocatalytic H_2 generation in aqueous solution, thus the hydrophobic catalysts were incorporated in supramolecular systems like, polymers (including peptides and proteins),[153,162,164] micelles,[167,184] cyclodextrins,[185] metal-organic frameworks,[114,186] molecular thieves[168] or hydrogels.[169] Advantages and efficiencies of selected systems will be discussed in the following two chapters.

3.5.1 Light harvester covalently linked to the $[Fe_2S_2(CO)_{6-x}(L)_x]$ cluster

Initial reports on this research field from Sun, Song and Wasielewski *et al*. report about [FeFe] hydrogenase model complexes, in which the mimic of the active site was covalently linked to ruthenium or rhenium containing organometallic complexes or to metal-free organic chromophores like porphyrin as shown in Figure 18. Unfortunately, the electronic interactions between the sensitizer and the [2Fe2S] center investigated for the complexes **47**-**52** were negligible and just TONs < 1 were reached.[187–193]

In the following years, Zhao, Song, Tung and Liu *et al.* reported about different, more or less efficient approaches highlighted in Figure 19.[153,176,178,194,195] The group of Song *et al*. synthesized the first [FeFe] hydrogenase model complex containing a subphthalocyanine macrocycle **54** with strong absorption bands between 500-600 nm. Although the study of the fluorescence properties offered a strong fluorescence of the subphthalocyanine macrocyle quenched by the [2Fe2S] cluster with an efficiency of 94 %, which could be attributed to the intramolecular electron transfer from the macrocycle to the diiron center, no photoinduced hydrogen generation (TON = 0.11 is reported) could be detected after 90 min irradiation. Instead decomposition of **54** was observed due to a less photostability.[194]

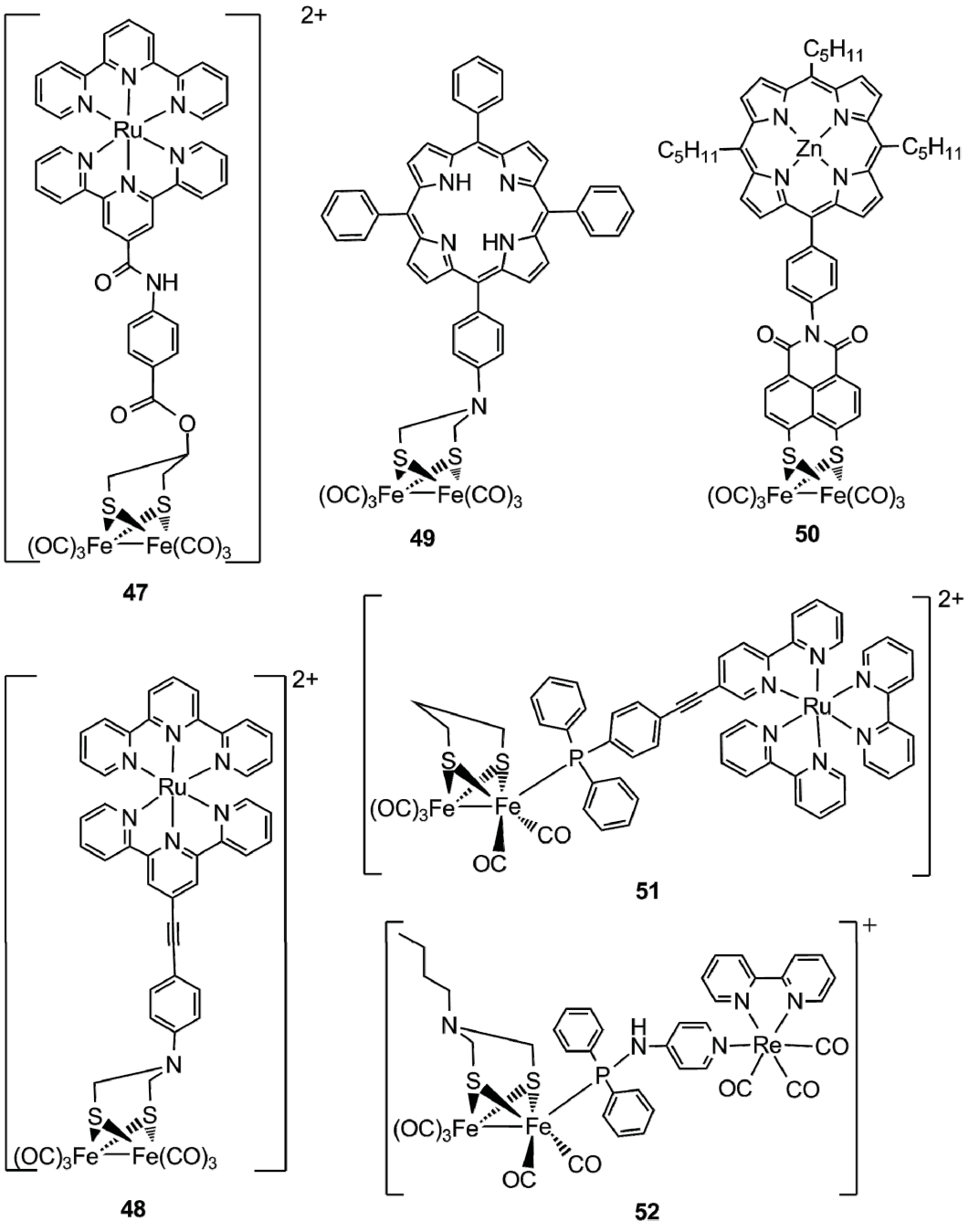

Figure 18: [FeFe] hydrogenase model complexes covalently linked to organometallic photosensitizers.[187–193]

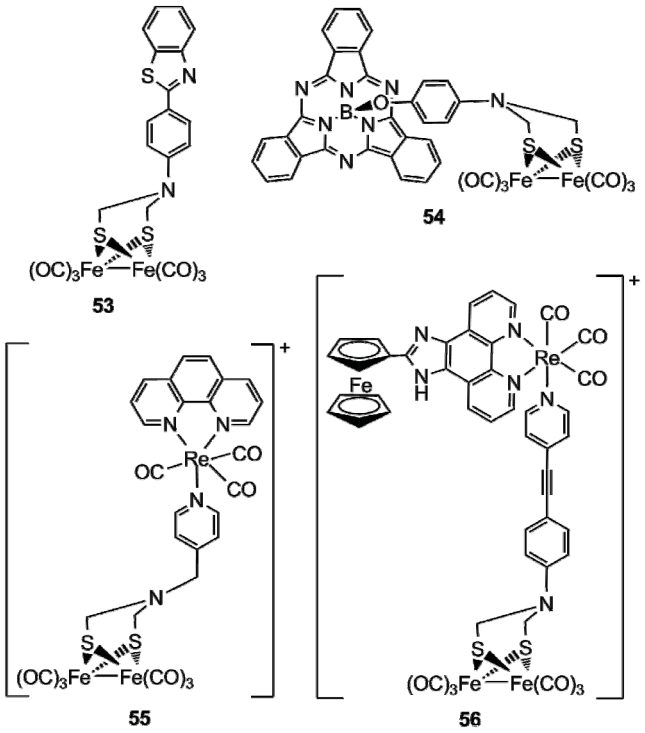

Figure 19: [FeFe] hydrogenase model complexes covalently linked to organometallic photosensitizers as well as organic chromophores.[153,176,178,194,195]

Better results could be obtained for the complexes **53**, **55** and **56**. Liu *et al.* construct a model system, which utilize a Re(I)-containing 10-phenanthroline organometallic complex as light harvester similar to complex **52**, whereas the photosensitizer is linked *via* the dithiolate bridge to the diiron unit instead by a phosphine ligand. Under irradiation with $\lambda > 400$ nm of an acetonitrile solution of **55** using 500 equivalents triethylamine as the sacrificial electron donor offered a TON of 11.8 after 6 h, which was the best value reported to this date.[176] Recently, Gao *et al*. published a photocatalytic [FeFe] hydrogenase mimic **53** with a noble-metal free benzothiazole, linked by the dithiolate bridge to the diiron center, as photosensitizer. Steady-state spectroscopy, electrochemistry as well as laser flash photolysis confirmed an efficient photo-induced ET from the photoexcited benzothiazole to the diiron center generating a $[Fe^{I}Fe^{0}]$ species, which is responsible for the photocatalytic hydrogen evolution. Irradiation with $\lambda > 320$ nm of an acetonitrile solution of **53** in the presence of 40 equivalents ethanethiol as sacrificial electron donor and acetic acid as proton source revealed a TON = 24.2.[178]

Tung *et al.* reported an interesting approach (**56**), in which a ferrocene as a potential electron donor is covalently bound to an Re(I) complex similar to those of

55, also bound by a rigid triad to the dithiolate linker. Compared with other Re(I) utilizing complexes as photosensitizers, a turn-over number of 47 could be reached with **56**, which offers the influence of an electron donor into the dyad to build up a multistep PET chain as a possible strategy.[153,195]

A similar approach comparable with the complexes **51** and **52** were reported by Chen *et al.* in 2012, in which an $[Ir(ppy)_2(bpy)]^+$-photosensitizer was covalently linked to one of the iron atoms by forming an amide bond *via* a phosphine ligand (Figure 20).[177] Compared to the Re and Ru containing complexes **51** and **52**, **57** and **58** show a remarkable hydrogen evolution within 4 hours of irradiation with $\lambda > 400$ nm. Insertion of a sulfur atom into the linker between the catalyst and the photosensitizer in **57** changes the electron distribution in **57** compared to **58** (spectroscopic studies offered a reduced conjugation between the sensitizer and the [2Fe2S] cluster in **57**), causing differences in catalysis experiments. It is proposed, that the insertion of a sulfur atom can prevent the unwanted back electron transfer step to a certain extent. Catalysis experiments under optimized conditions in a acetonitrile-water mixture 9:1 at pH = 10 and a catalyst concentration of 0.2 mM with added 5 % triethylamine afforded a turn-over number of 127 molecules H_2 per molecule catalyst after 4 h for complex **57** and a TON of 82 for complex **58**, indicating the influence of the sulfur atom. Up to date this represents the highest reported turn-over number for covalently linked hydrogenase mimic/sensitizer systems.[177]

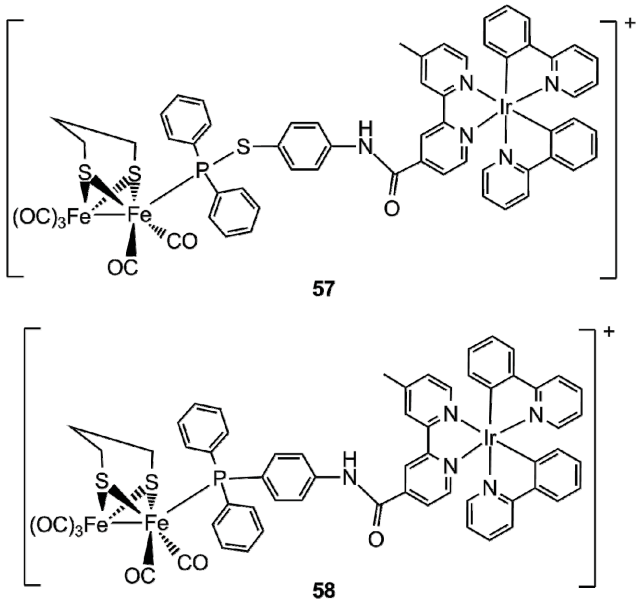

Figure 20: [FeFe] hydrogenase model complexes covalently linked to an Ir photosensitizer.[177]

3.5.2 Non-covalent systems utilizing $[Fe_2S_2(CO)_{6-x}(L)_x]$ clusters as catalyst

Initial reports of Sun *et al.* revealed low turn-over numbers for multi-component photocatalytic hydrogen evolution systems composed of the typical $[Ru(bpy)_3]^{2+}$ as photosensitizer and simple [FeFe] hydrogenase model complexes as catalyst.[115,195,196] Ott *et al.* believe, that these moderate TONs were related due to the instability and irreversibility of the reduced $[Fe^0Fe^I]$ or $[Fe^0Fe^0]$ species offered already by cyclovoltammetric experiments. An important property should be a high stability at different redox states of diiron species.[166]

In 2010 Ott *et al*. reported an example for such a multi-component system utilizing a redox-stable benzene-dithiolate bridged [FeFe] hydrogenase model complex shown in

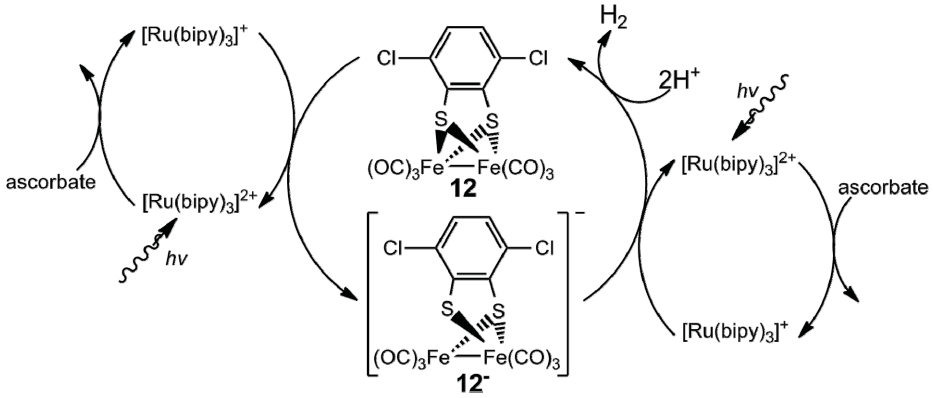

Scheme **8**. After 2.5 h irradiation in the range of 455-850 nm in a DMF/water 1:1 mixture utilizing ascorbic acid as sacrificial donor, a TON of 200 could be reached. For the first time this study has demonstrated, that a [FeFe] hydrogenase mimic could function as an efficient catalyst in photocatalytic hydrogen generation. In the following years a wide range of diiron complexes acting as catalysts in photocatalysis were reported.[166]

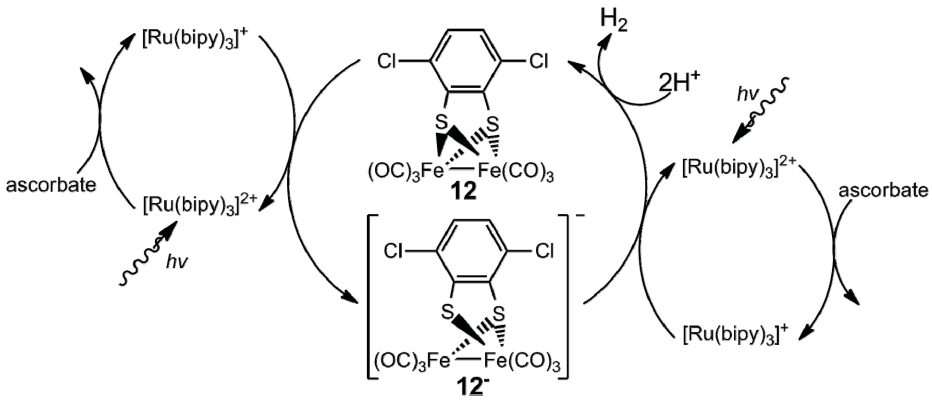

Scheme 8: Photocatalytic hydrogen evolution reported by Ott *et al*. utilizing [Fe_2(μ-benzen-1,2-dithiolat)$(CO)_6$] as catalyst.[166]

Not only a high stability of different redox states of the diiron species is important for a capable catalysis, also an efficient electron transfer from the light harvester to the hydrogen evolution catalyst is crucial to achieve a high-performance artificial photosynthetic system. For this reason, a different approach is to utilize a semiconductor as light harvester. The process of an ET from photoexcited semiconductors to complexes (reverse process takes place in dye-sensitized solar cells DSSCs) is predicted to be fast and may benefit a high efficient photocatalytic system. In the last years, some of these hybrid photoelectrocatalytic systems consisting of a semiconductor as light harvester and a [FeFe] hydrogenase mimic as catalyst were reported.[153,180–183,197–200] Notably is a work of Li *et al.*, who established a noble-metal free, highly efficient and stable photosynthetic system utilizing ZnS nanoparticles (average diameter 50 nm) as light harvester and the simple [$Fe_2(CO)_6${μ-S-Ph-4-NH_2}$_2$] complex as catalyst physically adsorbed at the surface of the nanoparticles. Within 38 h of irradiation by a 300 W Xe lamp without a cut-off filter in a DMF/water 9:1 mixture utilizing ascorbic acid as sacrificial donor a TON of 2607 could be reached, while the catalyst was still active after 38 hours of irradiation. He could show that both, the semiconductor nanoparticles and the [FeFe] hydrogenase mimic, are absolutely necessary for a photocatalytic hydrogen evolution.[180,182]

Furthermore, different n-type II-VI semiconductors like CdSe as well as CdTe, stabilized by 3-mercaptopropionic acid (MPA) in aqueous solution, were used by Wu

et al. revealing extraordinary efficient photoelectrocatalytic systems, whereas three of these systems are highlighted in Figure 21.[153]

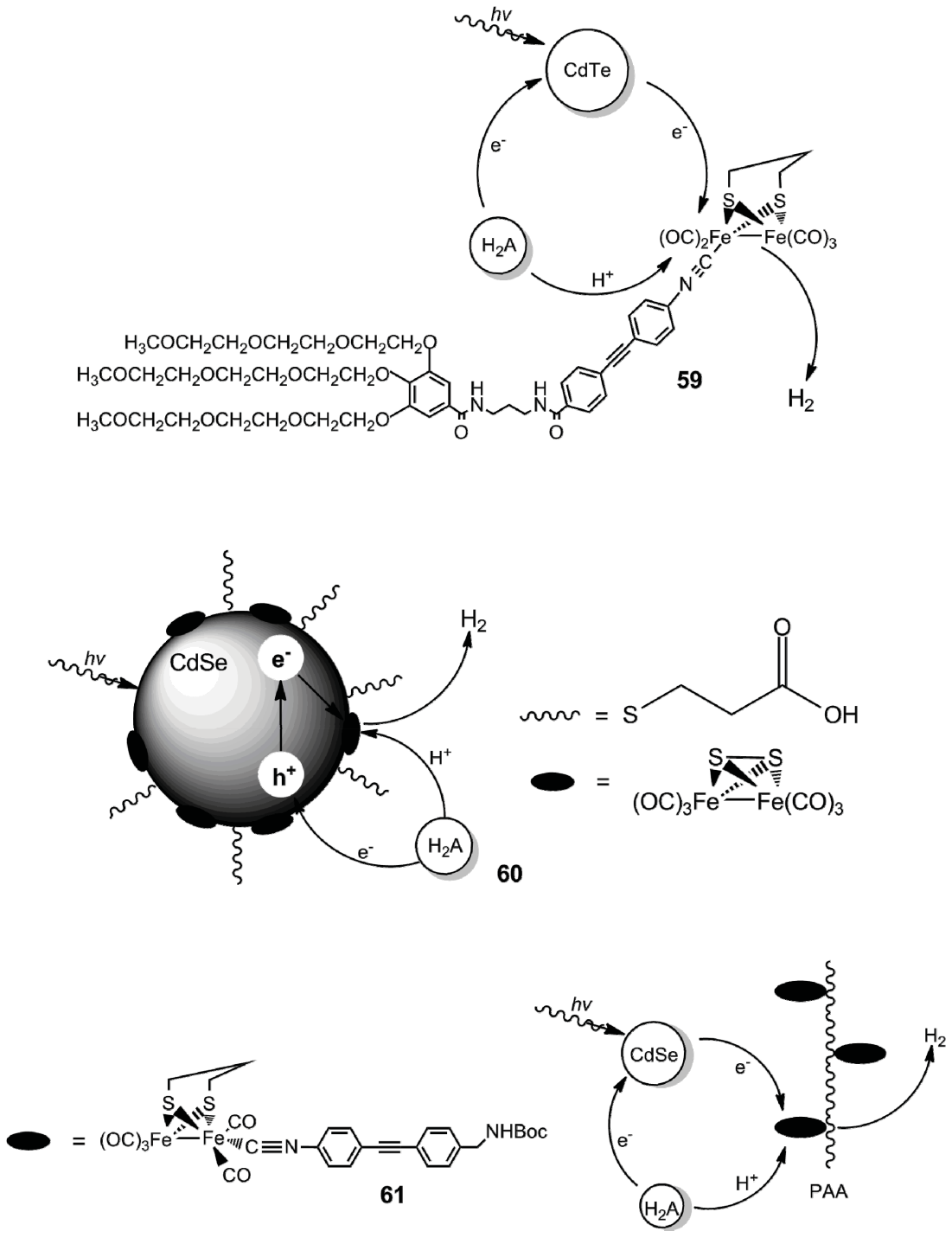

Figure 21: Photoelectrocatalytic systems reported by Wu and coworkers.[153]

Because of the water-solubility of the light-harvesting semiconductors, the [FeFe] hydrogenase model complexes should be also soluble in polar solvents like water. For this reason Wu *et al*. introduced three long hydrophilic ether chains *via* an

isonitrile at one of the iron atoms in **59**. Photocatalytic investigations with ascorbic acid as sacrificial donor offered a TON of up to 505 after 10 h irradiation.[153,183] Much more efficient systems represent assembly **60** and **61**. Surface affinity of CdSe quantum dots allow for an interaction of sulfur atoms by interface-directed surface binding. By this way the simple $[Fe_2S_2(CO)_6]$ cluster could be immobilized as the catalyst on the CdSe surface in assembly **60**. Photogeneration experiments in aqueous solution utilizing ascorbic acid as sacrificial donor revealed a turn-over number of 8,781 with an initial turn-over frequency of 9.9 molecules H_2 per minute in the first 4 hours. The high efficiency of this system is best explained by a fast electron transfer from the photoexcited quantum dots to the catalyst due to their intimate contact in assembly **60**, which could be verified by an efficient luminescence quenching of the CdSe quantum dots upon binding of the $[Fe_2S_2(CO)_6]$ cluster.[153,198]

Another approach of Wu *et al.* is the anchoring of [FeFe] hydrogenase mimic **61** to a poly(acrylic acid) (PAA) chain, thus providing a water soluble catalyst to use MPA-stabilized CdSe quantum dots as photosensitizer and ascorbic acid as donor in photocatalytic experiments. A peptide bond is formed between the carboxyl groups of PAA and an amine group of the mimic **61**, which is introduced by an isonitrile ligand to one of the iron atoms. Another advantage of the carboxyl groups of PAA is the attribute of coordination to cadmium ions, and thus on the surface of the CdSe dots. By this way an intimate assembly of a [FeFe] hydrogenase mimic **61** grafted PAA chains wrapped around the CdSe nanoparticles is formed. Like in assembly **60** an efficient PET occurs in this system and under catalytic conditions a remarkably TON of 27,135 with an initial TOF of 3.6/s could be reached. For this system a quantum yield up to 5 % for photocatalytic hydrogen evolution is calculated.[153,199]

To date the highest reported turn-over number by using [FeFe] H_2ase mimics was reported by Wu *et al*., too. Utilizing a chitosan-confined [FeFe] hydrogenase mimic, a TON up to 52,800 under visible light irradiation could be reached due to an enhanced catalytic stability of 60 hours. Chitosan is a linear polysaccharide composed of *β*-(1,4)-linked D-glucosamine. It contains a high amount of primary amines and hydroxyl groups and bears a polycationic character if it is protonated. By this way chitosan can incorporate [FeFe] hydrogenase complexes mimicking the protein matrix in nature. For the photocatalytic experiment Wu *et al*. selected the simple $[Fe_2(CO)_6\{\mu\text{-}(SCH_2)_2N\text{-}Bn\}]$ complex as the catalyst, MPA-stabilized CdTe

quantum dots as photosensitizer as well as ascorbic acid as donor and added 1.0 g/L chitosan to a methanol/water mixture of 1:3. The influence of the chitosan could be shown by performing the same catalytic experiments without the use of chitosan reaching just a TON 4,160-fold lower. This work sets a new benchmark reaching a turn-over number up to 52,800 and a high stability of the catalytic system of 60 h. The performance of this system clearly demonstrates the importance of an environment surrounding the catalytic [FeFe] hydrogenase mimic suggesting the need to mimic not only the structure but also the biological environment of the active site of [FeFe] hydrogenase.[153,200]

Nevertheless, also other systems are worth to be mentioned. A complicated four-generation dendritic [FeFe] hydrogenase mimic with a deeply buried $[Fe_2S_2(CO)_6]$ cluster is reported by Li *et al*., using $[Ir(ppy)_2(bpy)]^+$ as photosensitizer and a mixture of triethylamine/water as donors. Irradiation with visible light offered a remarkable TON of 22,200 after 8 h with a corresponding initial TOF of 2,775/h. This work supports the suggestion, that the mimicking of the biological enviroment is important to reach efficient hydrogen generation catalysis.[165] Similar approaches were reported by Ghirlanda,[162] Hayashi,[164] Tung,[167] Sun,[185] Feng,[186] Ott[114] and Li[168,169] *et al*. trying to mimic or incorporate hydrophobic [FeFe] hydrogenase model complexes into a microenvironment like peptides[162] and proteins,[164] micelles,[167] cyclodextrins,[185] metal-organic frameworks,[114,186] molecular thieves[168] or hydrogels[169] reaching TONs up to 780 by utilization of Ru, Ir and Re-containing organometallic complexes[114,162,164,167–169] as well as Zn-porphyrin[186] and fluorescein[185] as photosensitizers.

3.6 Silicon containing model complexes

The influence of silicon in organic compounds is well investigated. It is known that the substitution of one or more carbon atoms by silicon atoms influences the chemical, physical as well as biological properties in a extraordinary way.[201–209] Polysilol polymers as well as oligomers are also known and reveal strong light emission and absorption in the longer wavelength region compared to carbon analogues and offer non-linear optical properties.[210–220] These attributes are a result of a different covalent radius and electronegativity of the silicon compared to carbon.

A summary of the electronegativities, covalence radii, average bonding distances and energies can be seen in Table 2. In contrast to the C-C bond, the polarity of the $C^{\delta-}$-$Si^{\delta+}$ bond is changed due to the smaller electronegativity of Si. The covalent radius and bonding distance of C-Si are larger than those for C-C bonds. The stability of the E-C bonds is comparable, supporting the high stability of the Si-C bond. Inspired by these unique features, silicon containing dithiols were used by Weigand *et al*. as ligands for [FeFe] hydrogenase models to investigate their structural and electrochemical properties compared to carbon analogue complexes.[105–107]

Table 2: Comparison between carbon and silicon.[221]

E	electronegativity	Covalent radius [ppm]	Bonding distance E-C [ppm]	Bond energy E-C [kJ/mol]
C	2.5	77	154	358
Si	1.9	117	188	311

It was revealed, that the introduction of a silicon atom in the dithiolate bridge of [FeFe] hydrogenase model complexes influences the electronic and catalytic properties of these complexes. The basicity of the sulfur atoms increases,[107] according to results obtained by Glass *et al.* for tin analogues complexes by a σ(Sn-C)→*3p*(S) filled-filled interaction.[108] This result is conceivable also for the silicon containing complexes as DFT calculations figured out (Figure 22).

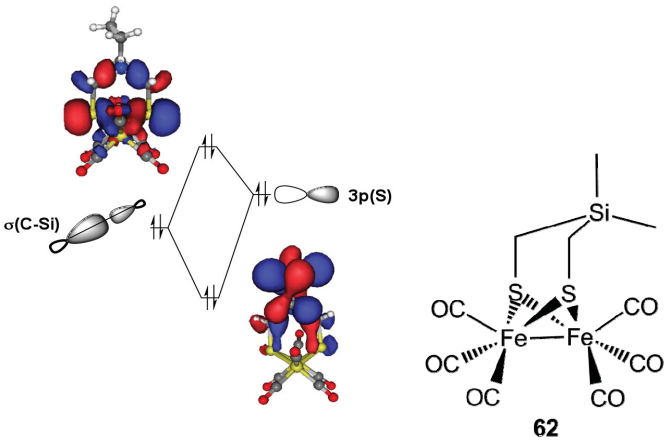

Figure 22: DFT calculated (B3LYP 6-311+G (d, p)) orbital interaction between σ(Si-C) and *3p*(S) for **62** forming the $HOMO^{-1}$ (upper left) and the MO103 (bottom right).[222]

The increased basicity at the μ-S atoms ($HOMO^{-1}$, Figure 22) allow for a kinetically favoured proton interaction with the μ-sulfur atoms instead of the formation of a hydride species as it was observed in IR studies shown in

Figure 23. After addition of 100 equivalents of tetrafluoroboric acid new CO vibrational modes can be observed shifted to higher wavenumbers.

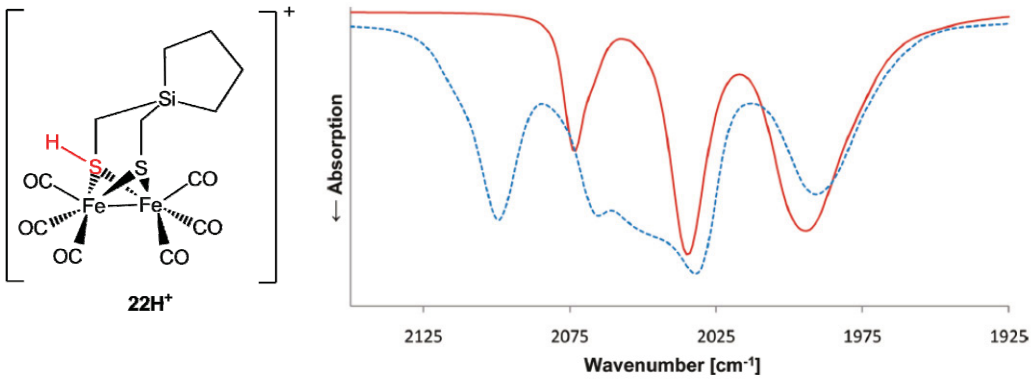

Figure 23: CO vibrational range of the IR spectra of compound **22** without acid (red line) and after addition of 100 equivalents $HBF_4 \cdot Et_2O$ (blue line).[107]

These findings are in contrast to the behavior of related complexes with carbon-based dithiolato ligands. [FeFe] hydrogenase model complex **22** also shows extraordinary electrochemical properties. Substitution of a carbon atom by a silicon atom leads to a compound that is both easier to oxidize and to reduce and dihydrogen development at three different reduction potentials with high activity toward dihydrogen formation is observed in cyclovoltammetric experiments.[105,107]

Furthermore, under reductive conditions complex **22** forms a rotated state species with a carbonyl ligand bridged between the two iron atoms, whereas the iron-iron bond and one of the iron-sulfur bonds are broken. After reduction of **22** with sodium amalgam in acetonitrile, in the IR spectrum an additional vibrational mode at 1725 cm^{-1} is observed suggesting the formation of the rotated state proved by DFT calculations (Figure 24).[107]

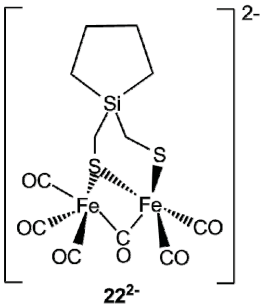

Figure 24: Structure of the doubled reduced [FeFe] H_2ase model complex **22**.[107]

3.6.1 Silicon containing aromatic systems

Silicon containing heteroaromatic systems are well known for their extraordinary properties like low band gaps and non-linear optical properties.[223–234] As already indicated in chapter 3.6, silicon containing molecules differ significantly to their carbon analogues due to different electron negativities, covalence radii, average bonding distances and energies, which demonstrate an example shown in Figure 25. The HOMO of the silole is lowered by -0.440 eV and the LUMO even more by -1.289 eV. This matter can be best described by the interaction between the π^* orbital of the butadiene residue and the σ^* orbital of the silylene residue (Figure 26). Furthermore, the interaction is enforced by the tetrahedral geometry around the silicon atom, whereby the σ^* orbital of the silylene and the π^* orbital of the butadiene residue are parallel to each other. In contrast to the silole, a comparable interaction in cyclopentadiene is rather not possible due to the energetically high σ^*(CH) orbitals.[211,235]

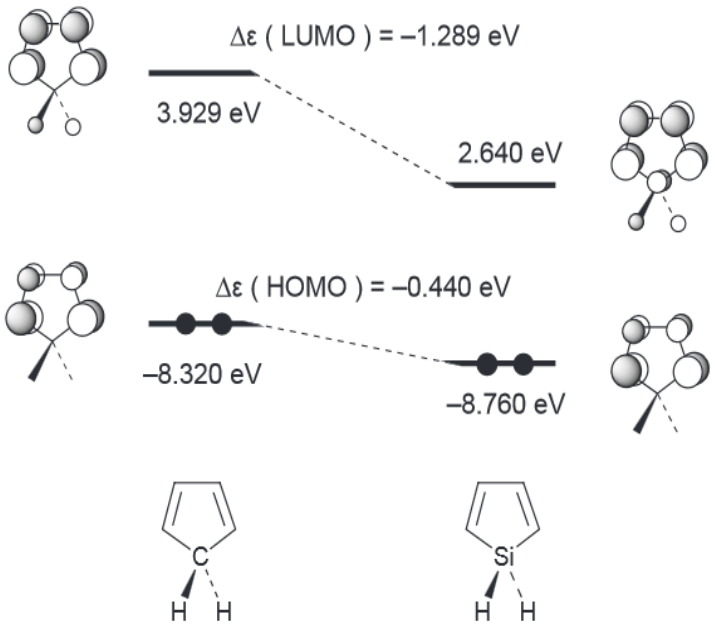

Figure 25: Relative energy levels of the HOMO and LUMO for silole and cyclopentadiene.[235]

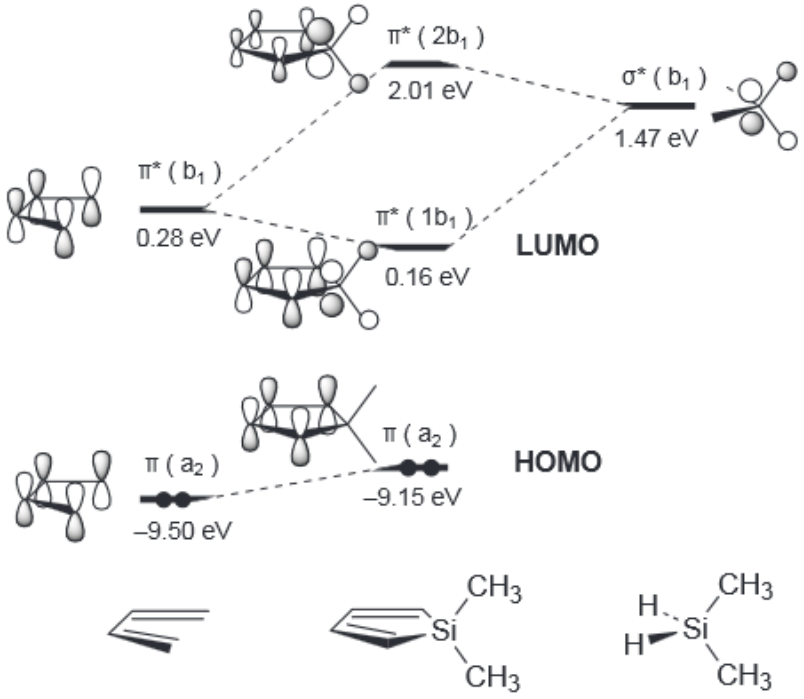

Figure 26: Orbital correlation diagram for 1,1-dimethylsilole.[235]

The reduced energy distance σ^*(b1)/π^*(b1) of the silole orbitals result in both, a bathochromic shift of the absorption and the fluorescence like shown for example **63**/**64** in Figure 27 by an shift of about 60 nm to higher wavenumber by simple silicon substitution.[219,235]

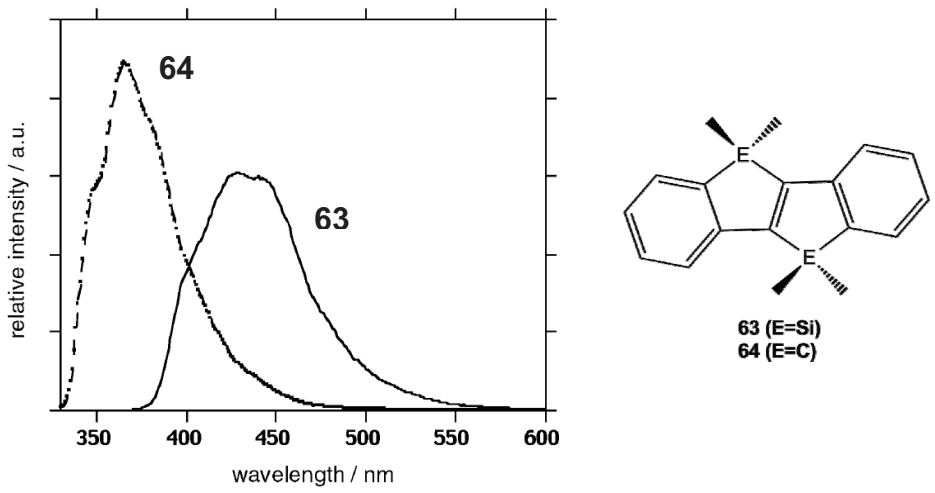

Figure 27: Fluorescence spectra for comparison of compound **63** and **64**.[219]

Since it was shown that the silicon atom can interact with the [2Fe2S] cluster *via* a σ(Si-C)→*3p*(S) filled-filled interaction, fluorescence quenching can be expected, if such silicon containing heteroaromatic system is placed at the bridgehead position of

the dithiolate linker in a [FeFe] hydrogenase model complex (Figure 28). This should allow the establishment of a photocatalytic hydrogen generation mechanism. The short linker and the filled-filled interaction should make such small and compact complexes very attractive for photocatalytically H_2 formation.

3.7 Motivation

As before mentioned in chapter 3.6, silicon containing [FeFe] hydrogenase model complexes show interesting properties as sulfur protonation due to an increased basicity by σ(Si-C)→*3p*(S) filled-filled interaction, reduced overpotential for proton reduction and the formation of a the rotated state under reductive conditions. With these model complexes the generation of H_2 was only possible within electrocatalysis. Therefore, new silicon containing complexes were planned, which combine these unique properties and the possibility of achieving the reduction of the [2Fe2S] cluster by irradiation as explained in chapter 3.5 without the use of expensive noble-metal containing sensitizers or quantum dots. Therefore the photosensitizer should be a silicon containing heteroaromatic system like shown in Figure 28, directly connected to the bridgehead position of the dithiolate linker.

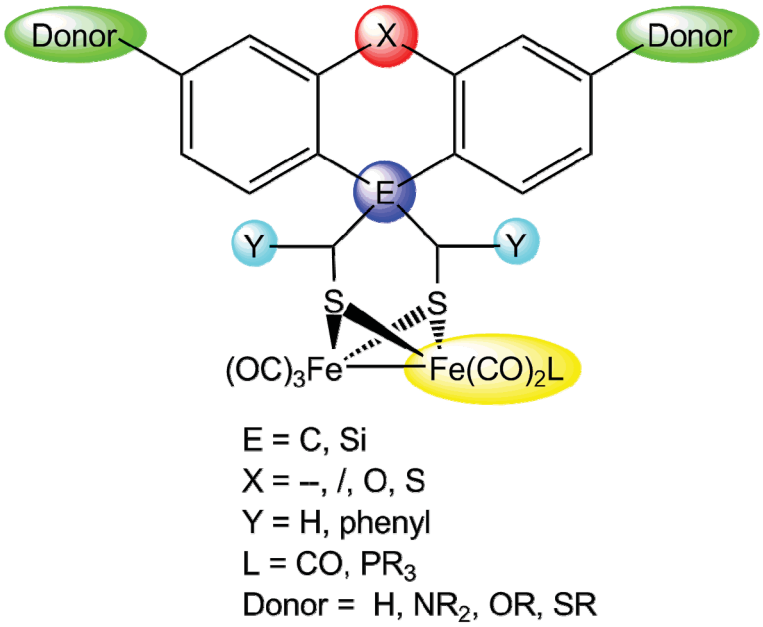

Figure 28: [FeFe] hydrogenase model complex planned in this thesis. The colored shapes show different ways for alteration.

As depicted in Figure 28, the silicon containing complex as well as the carbon analogue shall be synthesized to investigate the influence of the substitution to the optical, electrochemical as well as catalytically properties. Asymmetric CO exchange by mono- and/or bisphosphine ligands should increase the electron density at the diiron center in order to force a better electron support of the catalytic active site. Substitutions at the benzene unit with amines, ethers or thioethers will shift the absorption wavelength to higher wavenumbers due to a higher electron density. Introduction of a phenyl-ring at the Y-position (Figure 28) will increase rigidity and steric bulk of the dithiolate moiety in order to force better fluorescence properties as well as the possible formation of a rotated state.

4 Publications

4.1 **[RG1]**

A Silicon-Heteroaromatic System as Photosensitizer for Light-Driven Hydrogen Production by Hydrogenase Mimics

Roman Goy, Ulf-Peter Apfel, Catherine Elleouet, Daniel Escudero, Martin Elstner, Helmar Görls, Jean Talarmin, Philippe Schollhammer, Leticia González, Wolfgang Weigand

European Journal of Inorganic Chemistry **2013**, 4466-4472.

In this publication a viable synthetic pathway is reported towards a small and compact photocatalytic [FeFe] hydrogenase model complex with a *1*-silafluorene moiety as the photosensitizer directly imbedded into the bridging dithiolate unit. The model complex was fully characterized by NMR and IR spectroscopy, mass spectrometry, elemental analysis, XRD analysis as well as cyclovoltammetry, offering a possible filled-filled interaction between the σ(Si-C)-orbital and the *3p*(S)-orbital and hence, allowing a direct communication between the photosensitizer and the [2Fe2S] cluster. This possible filled-filled interaction was further investigated by DFT calculations. Optical properties of the *1*-silafluorene moiety were investigated as well as the influence to the [2Fe2S] cluster. Fluorescence quenching experiments were performed and allow for the establishment of a photocatalytic hydrogen generation mechanism. Thus, first catalysis experiments were performed to test the principle function of the reported photoactive system, which was confirmed by the photocatalytic H_2 evolution with the highest reported TON (29 after 15 h irradiation) for such small [FeFe] H_2ase model complexes to this date. The elimination of Ir, Pt, Rh or Re containing complexes as photosensitizers makes this design to a powerful platform for the further development of proton reduction catalysts.

EurJIC European Journal of Inorganic Chemistry

ChemPubSoc Europe

FULL PAPER

DOI:10.1002/ejic.201300537

A Silicon-Heteroaromatic System as Photosensitizer for Light-Driven Hydrogen Production by Hydrogenase Mimics

Roman Goy,[a] Ulf-Peter Apfel,[b] Catherine Elleouet,[c] Daniel Escudero,[d] Martin Elstner,[a] Helmar Görls,[a] Jean Talarmin,*[c] Philippe Schollhammer,[c] Leticia González,*[e] and Wolfgang Weigand*[a]

Dedicated to Professor Wolfgang Beck

Keywords: Photocatalysis / Enzyme models / Iron / Sulfur / Silicon / Hydrogenase

The utilization of light and inexpensive catalysts to afford hydrogen represents a huge challenge. Following our interest in silicon-containing [FeFe]-hydrogenase ([FeFe]-H_2ase) mimics, we report a new model approach for a photocatalytic [FeFe]-H_2ase mimic **1**, which contains a 1-silafluorene unit as a photosensitizer. Thereby, the photoactive ligand is linked to the [2Fe2S] cluster through S–CH_2–Si bridges. Photochemical H_2 evolution experiments were performed and revealed a turnover number (TON) of 29. This is the highest reported photocatalytic efficiency for an [FeFe]-H_2ase model complex in which the photosensitizer is covalently linked to the catalytic center.

Introduction

The conversion of light into a storable energy source is a highly desired endeavor. In particular, the photocatalytic reduction of water into hydrogen affords an ideal fuel, which is easy to store in large quantities.[1–3] In addition, the combustion of hydrogen to water has a high specific energy value (142 MJ kg^{-1})[4] and affords no polluting emissions.[5]

Hydrogen is part of the biological cycle and appears as a biological energy source and transporter.[6] Numerous structurally modified and photocatalytically functionalized models have been inspired by the structure of [FeFe]-hydrogenase ([FeFe]-H_2ase). Multicomponent systems containing a surplus of ruthenium photosensitizers or organic fluorophores and [2Fe2S] clusters were investigated and showed moderate H_2 development upon irradiation with light.[7–11] Multiple covalently linked dyads were synthesized with porphyrin or ruthenium units as the photosensitizer.[12–18] These complexes revealed low turnover numbers (TON < 0.15) for H_2 generation.[12–18] To the best of our knowledge, there is only one system containing a rhenium photosensitizer covalently connected to the [2Fe2S] cluster by an azadithiolato linker and it showed significant H_2 development with a turnover number of 11.8.[19] Furthermore, supramolecular assemblies comprising [2Fe2S] model compounds with an InP nanophotocathode,[20] ZnS nanoparticles,[21] multichromophoric hexad self-assemblies,[22] or Mn_2Ru complexes[23] as light-harvesting molecules were reported. Also, micellar systems[24] and dendrimer-based mimics[25] were utilized to allow for photocatalytic H_2 development in aqueous media.

However, water splitting by utilizing light and inexpensive catalysts to afford hydrogen still represents a huge challenge, as most complexes show a lack of reactivity and stability.[26–31]

In continuation of our research on silicon-containing [FeFe]-H_2ase mimics,[32–34] we aimed to synthesize a small, compact, heavy-metal-free, and easily accessible photocatalytic [FeFe] model complex (Scheme 1) by utilizing a silicon-

[a] Institut für Anorganische und Analytische Chemie, Friedrich-Schiller-Universität,
Humboldtstraße 8, 07743 Jena, Germany
Fax: +49-3641-948102
E-mail: wolfgang.weigand@uni-jena.de
Homepage: http://www.uni-jena.de/Prof_W_Weigand.html
[b] Institut für Anorganische Chemie, Ruhr-Universität Bochum, Universitätsstraße 150, 44780 Bochum, Germany
[c] Chimie, Electrochimie Moléculaires et Chimie Analytique, Université de Bretagne Occidentale,
6 Avenue Victor le Gorgeu, CS93837, 29238 Brest cedex 3, France
[d] Max-Planck-Institut für Kohlenforschung, Kaiser-Wilhelm-Platz 1, 45470 Mülheim an der Ruhr, Germany
[e] Institut für Theoretische Chemie, Universität Wien, Währinger Str. 17, 1090 Wien, Austria

Supporting information for this article is available on the WWW under http://dx.doi.org/10.1002/ejic.201300537.

containing heteroaromatic system. Silicon-containing aromatics are well known for their good optical properties such as light-emission and absorption in the longer wavelength area or their electroluminescence properties[35–41] as well as for their interesting physical properties.[42–46]

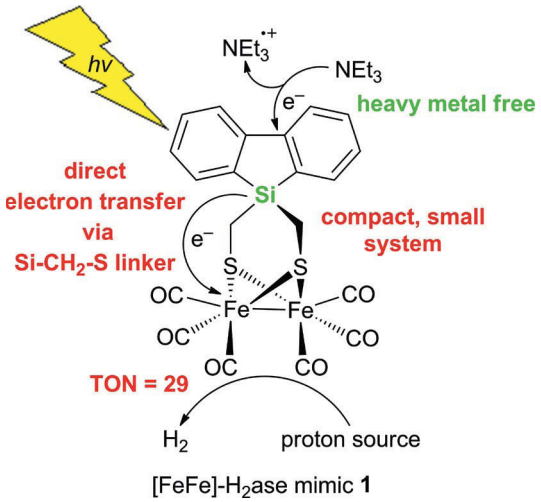

Scheme 1. Schematic representation of the light-driven production of hydrogen by [FeFe]-H_2ase mimic **1**.

Herein, we present a new model approach for a photocatalytic [FeFe]-H_2ase mimic **1**, which contains 1-silafluorene as a photosensitizer. Thereby, the photoactive ligand is linked to the [2Fe2S] cluster through S–CH_2–Si bridges, and the photoactive 1-silafluorene is directly connected with the redox-active iron center (Scheme 1).

Results and Discussion

The 1-silafluorene complex **1** was prepared according to Scheme 2. The reaction of 2,2′-dibromobiphenyl (**2**), *n*-butyllithium, and bis(chloromethyl)dichlorosilane afforded 1,1′-bis(chloromethyl)-1-silafluorene (**3**) as a colorless oil in 70% yield. Subsequent reaction with [(μ-S)$_2$Fe$_2$(CO)$_6$] according to known procedures gave [FeFe]-H_2ase mimic **1** as a red-brown solid in 32% yield and it was characterized by ^{1}H and ^{13}C{^{1}H} NMR spectroscopy, IR spectroscopy, and mass spectrometry.[47]

The molecular structure of **1** (Figure 1, crystal data in Table 1) shows the characteristic [2Fe2S] butterfly core. The Si atom is surrounded in a distorted tetrahedral fashion. Notably, all of the C–Si–C angles [92.2(2)–114.2(3)°] differ significantly from those of an ideal tetrahedron. Additionally, both Si–C–S angles [123.3(3) and 122.9(3)°] are best explained by sp^2 rather than sp^3 hybridization. Similar observations were recently reported for other [2Fe2S(Si)] complexes.[32] Additionally, Glass and co-workers reported a related [2Fe2S(Sn)] complex.[48] Consistent with our observations, enhanced S–C–Sn angles were observed and an interaction between a σ(Sn–C) orbital and a 3p(S) orbital was verified by photoelectron spectroscopy.[48] We assume that the large angle (170.54°) between the planes generated by C1–Si1–C2 and S1–C1C2–S2 is an indicator for an effective

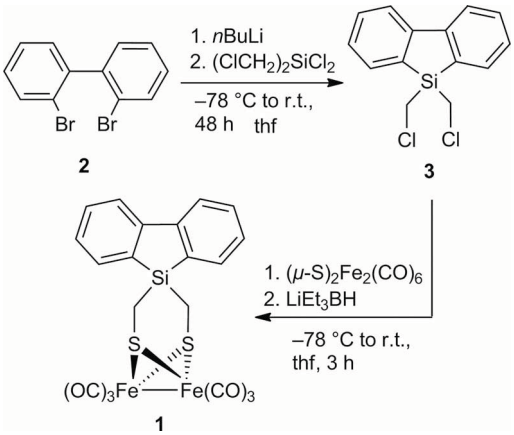

Scheme 2. Reaction pathway towards **1**.

photoelectron transfer between the photosensitizer and the diiron center. A comparable orbital interaction between the σ(Si–C) orbital and a 3p(S) orbital in **1** is, therefore, very likely. A similar interaction is not reported for [$Fe_2(CO)_6$(pdt)] (pdt = propanedithiolate), which shows an angle between the C–C–C and S–CC–S planes of 137.09°.[49] Cyclic voltammetry (CV) experiments at slow-to-moderate scan rates ($0.05 \leq v \leq 1$ V s^{-1}) show that the electrochemical re-

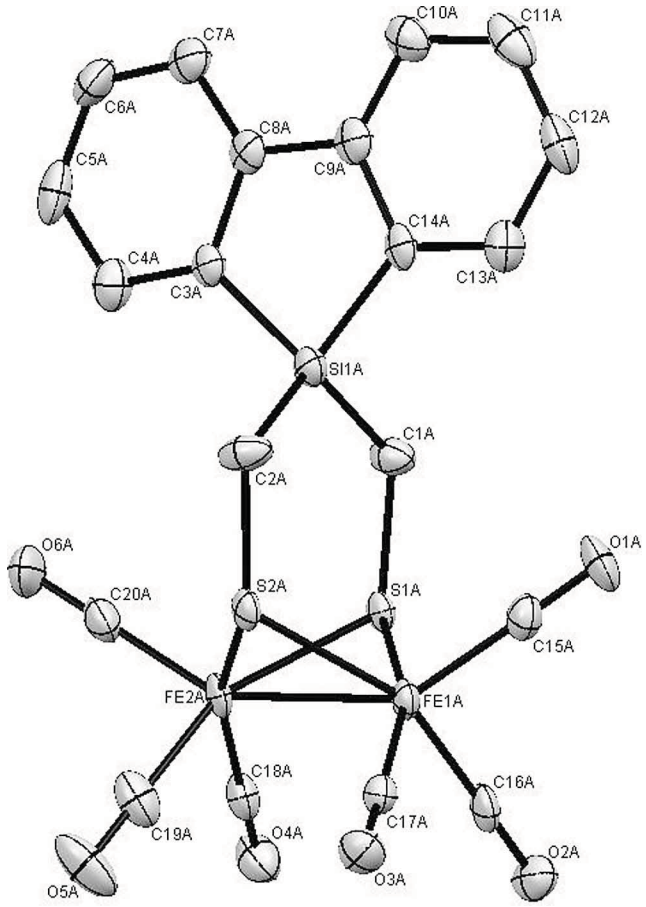

Figure 1. ORTEP view of **1** (ellipsoids at the 50% probability level).

duction of $[Fe_2(CO)_6\{\mu\text{-}SCH_2Si(R)CH_2S\}]$ (**1**) at $E_{1/2}$ = –1.55 V is quasireversible in $CH_2Cl_2/[NBu_4][PF_6]$.[50]

Table 1. Selected bond lengths [Å] and angles [°] for **1**.

Fe(1A)–Fe(2A)	2.5268(10)
Fe(1A)–S(1A)	2.2490(15)
Fe(1A)–S(2A)	2.2563(14)
Fe(2A)–S(1A)	2.2504(15)
Fe(2A)–S(2A)	2.2428(15)
S(1A)–C(1A)	1.817(6)
S(2A)–C(2A)	1.821(6)
C(1A)–Si(1A)	1.880(6)
C(2A)–Si(1A)	1.865(6)
Si(1A)–C(3A)	1.867(6)
Si(1A)–C(14A)	1.864(6)
C(3A)–C(8A)	1.418(8)
C(9A)–C(14A)	1.418(8)
C(8A)–C(9A)	1.481(8)
Fe(1A)–Fe(2A)–S(1A)	55.86(4)
Fe(1A)–Fe(2A)–S(2A)	55.58(4)
Fe(1A)–S(1A)–Fe(2A)	68.33(4)
Fe(1A)–S(2A)–Fe(2A)	68.34(5)
S(1A)-(C1A)–Si(1A)	123.3(3)
S(2A)–C(2A)–Si(1A)	122.9(3)
C(1A)–Si(1A)–C(2A)	112.8(3)
C(3A)–Si(1A)–C(14A)	92.2(2)
C(1A)-Si(1A)–C(3A)	112.9(3)
C(2A)–Si(1A)–C(14A)	112.7(3)
C(3A)–Si(1A)–C(2A)	114.2(3)
C(14A)–Si(1A)–C(1A)	110.5(3)

A comparison of the potentials of the reduction of **1** with those of bis(mercaptomethyl)silane $[(SCH_2)_2Si(Me_2)$; $E_{1/2}$ = –1.52 V],[32] pdt $[S(CH_2)_3S$; $E_{1/2}$ = –1.74 V],[51] and benzenedithiolate (bdt: SC_6H_4S; $E_{1/2}$ = –1.44 V)[52] analogues, which were measured under similar experimental conditions, indicates that the electronic effect exerted by the Si-containing bridge of **1** is intermediate between that of the pdt and the bdt ligands. A comparison of the reduction peak current (i_p^{red}) of **1** with the oxidation peak current (i_p^{ox}) of an equimolar bis-N-heterocyclic carbene (bis-NHC) complex $[Fe_2(CO)_4(\kappa^2\text{-}I_{Me}\text{–}CH_2\text{–}I_{Me})(\mu\text{-pdt})]$ (I_{Me} = 1-methylimidazol-2-ylidene), which was previously shown to undergo a one-electron oxidation, demonstrates that the former involves the transfer of two electrons (Figure S1).[53–55] The single-step two-electron transfer arises from an inversion of the potentials of the individual one-electron reduction processes, $E°_2 - E°_1 > 0$, as already observed for a variety of diiron hexacarbonyl complexes bearing different dithiolate bridges.[32,52,56–60] Typically, a potential inversion is observed when a chemical reaction (most often linked to a structural change) makes the second electron transfer thermodynamically more favorable than the first.[61–65] The structural change can either be concerned with one of the electron transfers[32,52,56–59] or appears as the intervening step of an ECE process.[50,60] In the present case, CV at faster scan rates ($1 \leq v \leq 20$ V s^{-1}) leads to a significant decrease of the current function ($i_p^{red}/v^{1/2}$) for the reduction of **1** (Figures S1 and S2). This strongly suggests that the abovementioned rearrangement, probably involving the cleavage of the Fe–S bond, is the intervening reaction of an $EC_{rev}E$ process (see Scheme 3). This result is in accordance with the observation by Evans and coworkers,[60] and hence an EE mechanism can be discarded.

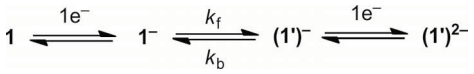

Scheme 3. Proposed $EC_{rev}E$ mechanism.

The UV/Vis absorption spectra of **1** and **3** are shown in Figure 2 for comparison. Time-dependent density functional theory (TD-DFT) calculations have been performed (see computational details in the Supporting Information) to get an insight into the UV/Vis characteristics of **1** and **3**. The theoretical UV/Vis spectra of **1** and **3** are also shown in Figure 2, and the main electronic excited states are highlighted (for a complete description of the main electronic TD-DFT excitations see Table S1). Both compounds have intense absorption bands at 210–242 and 277–290 nm, which are theoretically attributed to π–π* excitations within the 1-silafluorene moiety (for example, see S_2 and S_4 for **3** and S_{33} and S_{56} for **1** in Figure 2 and Table S1). The UV/Vis spectra of **1** and **3** differ in the low-energy regime. Only **1** has a broad band peaking at ca. 330 nm. The states responsible for this band have σ–σ* and d–σ* character and involve the Fe–Fe unit (see S_4 and S_9 in Figure 2 and the orbitals involved in these excitations in Figures S5 and S6). As can be seen in Figure 2, this band is slightly energetically underestimated by the TD-DFT calculations. Obviously, the latter metal-based intense band determines the photophysical and photochemical properties of **1**. Thus, upon excitation of the brighter π–π* band, new deactivation pathways involving the σ–σ*/d–σ* states (either of singlet and triplet character) arise. Hereby, the energy absorbed by the 1-silafluorene chromophore can be transferred in the course of photo-deactivation to the $[(\mu\text{-}S)_2Fe_2(CO)_6]$ catalytic unit. The population of low-lying σ–σ*/d–σ* triplet excited states (owing to strong spin–orbit couplings for Fe) guarantees that the lifetimes of the excited states are increased, and, hence, the quenching of photoluminescence and/or the photochemical hydrogen evolution is favored. Indeed, the lowest triplet excited state is adiabatically only 0.64 eV above the singlet ground state. Furthermore, the lowest triplet excited-state geometry shows longer Fe–Fe distances (see Figure S4). Such active species are then responsible for the catalytic activity of **1**, as the longer Fe–Fe distance allows for the coordination of hydrogen at the Fe–Fe core, and ultimately the H_2 evolution in the photocatalytic center by the coordination of an additional hydrogen atom is favored. The emission spectra of **1** and **3** upon excitation of the π–π* band with an excitation wavelength of 255 nm are shown in Figure 3.

To test whether a photoinduced electron transfer (PET) occurs in this system, the spectral change in the presence of triethylamine was studied. As shown in Figure 3, the emission intensity of **3** decreases upon addition of triethylamine, and the maximum of the emission shifts from 387 to 395 nm (**3** + 150 equiv. NEt_3). The decrease of the emission intensity under these conditions is reasonable as triethyl-

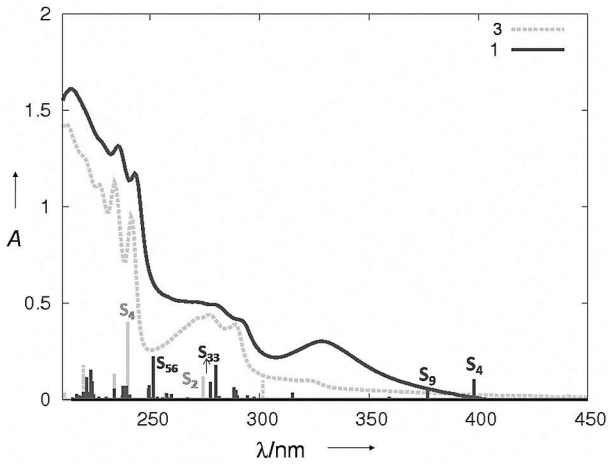

Figure 2. Experimental UV/Vis spectra for **1** and **3** (0.027 mM) in hexane superimposed on the TD-DFT vertical excitations. The main electronic states are highlighted (see Table S1 for assignments).

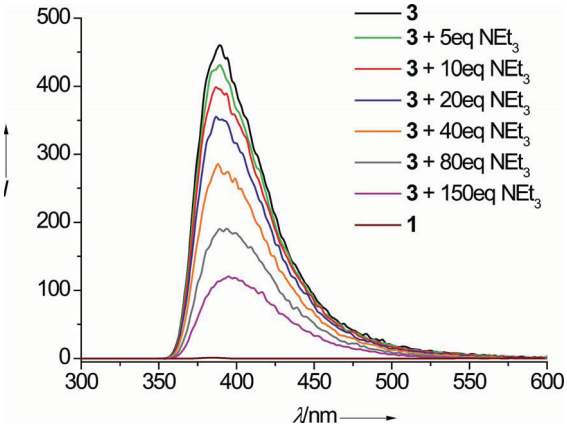

Figure 3. Photoluminescence spectra of **1** (0.27 mM) and **3** (0.092 mM) in acetonitrile in the presence of triethylamine (excitation wavelength 255 nm, K_{SV} = 80.0 ± 2.2 L mol^{-1}, see Figure S7).

amine acts as sacrificial electron donor to fill the hole generated in the π orbital upon photoexcitation. The progressive addition of NEt_3 to the solution of **3** quenched the luminescence with a rate constant K_{SV} of 80.0 ± 2.2 L mol^{-1} (Figure S7). Excitation at the characteristic absorption of both compounds at 255 nm results in a maximal luminescence at 387 nm with a quantum yield of ≤ 0.0003 for **1** and 0.183 ± 0.003 for **3** based on a 0.01 mM pyrene solution (in cyclohexane) as the reference.[66]

Photochemical H_2 evolution experiments were performed by irradiating **1** (0.6 μmol) in the presence of trifluoroacetic acid (TFA, 1 mmol) and triethylamine (1 mmol) in acetonitrile at 254 nm with a 15 W mercury-vapor lamp. Although our experimental set up did not allow us to excite at the absorbance maximum (240 nm), we were able to obtain 17.4 μmol H_2 in the headspace of our reactor after 13 hours irradiation with our system. No further H_2 generation was observed after 13 hours. This amount of H_2 reflects a turnover number (TON) of 29 and a turnover frequency (TOF) of 2.2 h^{-1} (Figure 4) and is the highest reported photocatalytic efficiency for an [FeFe]-H_2ase model complex in which the photosensitizer is covalently linked to the catalytic center. Headspace analysis of a mixture of **1**, Et_3N, and TFA stored in the dark revealed only traces of H_2 and further supports the necessity to photoexcite the complex to achieve catalytic activity. To further substantiate the importance of **1** for the photocatalytic hydrogen generation, an acetonitrile solution containing TFA (1 mmol) and Et_3N (1 mmol) was irradiated (254 nm) for 15 hours in the absence and presence of **3**. In both experiments, no significant generation of H_2 was observed. As reported for $Fe_3(CO)_{12}$ and $Fe_2(CO)_9$, irradiation with UV light in the presence of a photosensitizer can lead to significant CO dissociation and finally to the decomposition of the catalyst.[70,71]

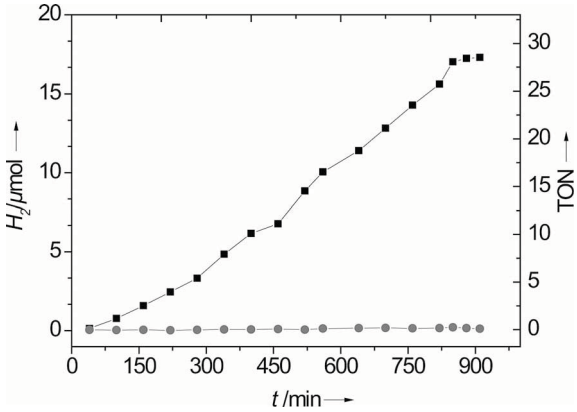

Figure 4. Light-driven hydrogen production by **1** (0.6 μmol, 0.15 mM) in the presence of trifluoroacetic acid (1 mmol, 0.25 M) and triethylamine (1 mmol, 0.25 M) in degassed acetonitrile at 25 °C. H_2 was detected by gas chromatography. Black line: with **1**, grey line: no catalyst.

To test the stability of our system, a solution of **1** was irradiated under the conditions described above and the UV/Vis spectra were recorded (Figures S8 and S9). In the absence of TFA and Et_3N, a new band at 295 nm with a stronger absorbance was observed and overlapped with the band at 330 nm. Further photoexcitation of the solution for a prolonged period of time resulted in stronger absorbance intensities for all bands and a redshift of 30 nm for the band initially observed at ca. 230 nm. After 3 h, a third band was growing in at 340 nm. Additionally, irradiation of the mixture for 15 h resulted in the loss of the characteristic CO resonances in the ^{13}C NMR spectrum of **1**, which indicates dissociation of the CO ligand. This process was further confirmed by IR spectroscopy, which showed no remaining CO bands. These observations indicate that in the absence of a sacrificial electron donor and proton source, irradiation of the complex results in CO dissociation, which finally deactivates the complex for the photocatalytic H_2 generation. Even though catalytic activity was still observed after 13 hours, experiments in the absence of Et_3N and TFA suggested decomposition of **1** after 7.5 hours. Thus, we assume that different PET quenching mechanisms under the catalysis conditions are likely.

To test this hypothesis, we repeated the irradiation experiment in the presence of TFA and Et_3N. The UV/Vis spectrum showed different spectroscopic features than the UV/Vis spectrum of the mixture without sacrificial electron donors and acid. This observation suggests a different reaction pattern in the presence of TFA and Et_3N, which is most likely because of a PET quenching processes (Figure S9). A significant redshift was observed for the band at 250–270 nm. Furthermore, in contrast to the experiments without TFA and Et_3N, the intensity of this band increases considerably faster and visibly results in higher extinction coefficients. After 240 min, a new band at 283 nm with a strong absorbance was observed. An additional band at 295 nm was observed and shifts to 315 nm upon excitation. Contrary to our experiments in the absence of TFA and NEt_3, no band at 340 nm was observed, which further confirms a different reaction pathway.

Conclusions

With the synthesis of **1**, we provide a viable synthetic pathway towards the first photocatalytic model complex of the [FeFe]-H_2ase active site with the photosensitizer directly imbedded into the bridging dithiolate unit. Thus, the photosensitizer is in close proximity to the catalytic [2Fe2S] cluster and allows for an effective electron transfer. In comparison to the influence of phosphanes,[67] cyanides[68] or NHCs,[69] the implementation of the photosensitizer into the bridge revealed only moderate influence on the [2Fe2S] cluster; thus, the fluorophore can be changed without alteration of the mechanism of H_2 formation. The Si–C–S angles from the X-ray-structure are in accordance with sp^2 hybridization of the carbon atom; therefore, a "filled–filled" interaction between the σ(Si–C) orbital and the 3p(S) orbital is favored and, hence, there is direct communication between the photosensitizer and the [2Fe2S] cluster. This behavior was also investigated by DFT calculations and confirmed by the photocatalytic H_2 evolution with the highest reported TON for such a small [FeFe]-H_2ase model complex. Even though photocatalytic systems with higher turnover numbers exist, the elimination of Ir, Pt, Rh, or Re complexes as photosensitizers makes this design a powerful platform for the further development of proton reduction catalysts. However, a precise statement about the nature of the different intermediates during the photocatalytic hydrogen generation cannot be given, and further investigations to discover the mechanism for the H_2 development with **1**, possible degradation pathways, and visible-light-driven catalysis with the presented core structure are currently in progress. This will allow the properties of this platform to be tuned to achieve, for example, excitation with visible light and higher turnover numbers.

Experimental Section

General Procedures: All reactions were performed under a dry nitrogen or argon atmosphere with standard Schlenk techniques. All solvents were dried and distilled according to standard methods prior to use. Et_3BHLi (1.0 M in THF), 1,2-dibromobenzene, and bis(chloromethyl)dichlorosilane are commercially available and were used without further treatment.

Infrared spectra were measured with a Bruker IFS 66 spectrometer (resolution ± 4 cm^{-1}) with the samples dispersed in compressed KBr pellets. Preparative column chromatography was performed with silica gel (Fluka, Kieselgel 60). UV/Vis spectra were recorded with a Specord S600 spectrometer, and fluorescence spectra were recorded with a Perkin–Elmer LS50B spectrometer. ^1H, ^{13}C, and ^{29}Si NMR spectra were obtained with either a BRUKER Avance 200 or Avance 400 spectrometer. Elemental analyses were performed with a Vario EL III CHNS analyzer from Elementar Analysensysteme GmbH. Mass spectra were measured with a FINNIGAN MAT SSQ710 instrument.

Structure Determination: Single crystals suitable for X-ray analysis were mounted on a fiber loop and placed in a cold, gaseous nitrogen stream on a Nonius KappaCCD diffractometer performing ϕ and ω scans at 120(2) K. Diffraction intensities were measured by using graphite-monochromated Mo-K_α radiation (λ = 0.71073 Å). Data were corrected for Lorentz and polarization effects, but not for absorption.[72,73] The structure was solved by direct methods (SHELXS) and refined by full-matrix least-squares techniques against F_0^2 (SHELXL-97).[74] All hydrogen atoms were included at calculated positions with fixed thermal parameters. All non-hydrogen atoms were refined anisotropically.[74]

CCDC-905950 contains the supplementary crystallographic data for this paper. These data can be obtained free of charge from The Cambridge Crystallographic Data Centre via www.ccdc.cam.ac.uk/data_request/cif.

Crystallographic Data of 1: $C_{20}H_{12}Fe_2O_6S_2Si$, M_r = 552.21 g mol^{-1}, red-brown prism, size 0.06 × 0.06 × 0.05 mm, monoclinic, space group $P2_1/c$, a = 13.8679(3), b = 26.8618(7), c = 11.6998(3) Å, β = 92.863(1)°, V = 4352.93(18) Å^3, T = –140 °C, Z = 8, $\rho_{calcd.}$ = 1.685 g cm^{-3}, λ(Mo-K_α) = 0.71073 Å, μ(Mo-K_α) = 16.15 cm^{-1}, F(000) = 2224, 26452 reflections in h(–18/17), k(–34/33), l(–15/15), measured in the range 2.11° ≤ Θ ≤ 27.50°, completeness Θ_{max} = 98.9%, 9877 independent reflections, R_{int} = 0.0915, 8063 reflections with $F_o > 4\sigma(F_o)$, 559 parameters, 0 restraints, $R1_{obs}$ = 0.0756, wR^2_{obs} = 0.1849, $R1_{all}$ = 0.0939, wR^2_{all} = 0.1977, Goodness-of-fit on F^2 = 1.149, largest difference peak and hole: 1.265/–1.016 e Å^{-3}.

Electrochemical Procedures: The electrochemical experiments were conducted under an inert atmosphere of nitrogen or argon. The preparation and purification of the supporting electrolyte ([NBu_4][PF_6]) was performed as described previously.[75] Trifluoromethanesulfonic acid (Aldrich) was used as received. Cyclic voltammetry was performed in a three-electrode cell by using a radiometer potentiostat (PGSTAT 128N or μ-Autolab III) driven by the GPES software. The working electrode consisted of a vitreous carbon disk, which was polished on a felt tissue with alumina, thoroughly rinsed with water, and dried before each CV scan. The Ag/Ag^+ reference electrode was separated from the analyte by a CH_2Cl_2–[NBu_4][PF_6] bridge. All the potentials are reported against the ferrocene–ferrocenium couple; ferrocene was added as an internal standard at the end of the experiments.

Procedure for Photocatalytic H_2 Evolution: Photochemical hydrogen evolution experiments were performed by irradiating an acetonitrile solution of **1** in the presence of trifluoroacetic acid (TFA) and triethylamine at 254 nm with a 15 W mercury-vapor lamp in a quartz glass precision cell at room temperature. Prior to irradiation, the solution was sealed with a septum cap, degassed, and flushed

with dry nitrogen. Hydrogen was detected by gas chromatography by using a calibrated Varian CP-3800 Gas Chromatograph with a thermal conductivity detector and argon as the carrier gas.

Dibromobiphenyl (2):[76] A solution of 1,2-dibromobenzene (21.5 g, 91.1 mmol) dissolved in THF (120 mL) was cooled to –78 °C, and *n*-butyllithium (31.4 mL, 50.24 mmol, 1.6 M in hexane) was added dropwise over a period of 30 min. Within 24 h the reaction mixture was warmed to room temperature and then hydrolyzed at 0 °C by using hydrogen chloride (100 mL, 0.5 M in water). The reaction mixture was extracted with diethyl ether (4 × 50 mL), and the combined organic fractions were dried with sodium sulfate. Evaporation to dryness and crystallization from ethanol afforded colorless crystals (11.1 g, 78%). ^{1}H NMR (200 MHz, CD_2Cl_2): δ = 7.70 (m, 2 H, $CH_{aromatic}$), 7.45–7.24 (m, 6 H, $CH_{aromatic}$) ppm. ^{13}C NMR (50 MHz, $CDCl_3$): δ = 142.09 (C_q), 132.59, 130.96, 129.38, 127.1 ($CH_{aromatic}$), 123.52 (CBr) ppm. MS (DEI): *m*/*z* = 312 $[M]^+$, 232 $[M – Br]^+$, 152 $[M – 2Br]^+$, 76 $[M – C_6H_4Br_2]^+$.

Bis(chloromethyl)-1-silafluorene (3): A solution of 2,2′-dibromobiphenyl (2.0 g, 6.4 mmol) in Et_2O (25 mL) was cooled to –78 °C, and *n*BuLi (1.6 M in hexane, 8.2 mL, 13 mmol) was added. The reaction solution was warmed to room temperature by removing the cooling bath and subsequent stirring overnight. The resulting solution was cooled to –78 °C, and a solution of $Cl_2Si(CH_2Cl)_2$ (1.5 g, 7.6 mmol) in Et_2O (5 mL) was added dropwise. The reaction mixture was stirred at –78 °C for 4 h and at room temperature for an additional 12 h. The mixture was filtered, and the solvents were evaporated by vacuum transfer under an argon atmosphere. The residue was purified by bulb-to-bulb distillation (130 °C/0.11 mbar) to afford **3** as colorless oil (1.24 g, 70%). ^{1}H NMR (200 MHz, $CDCl_3$): δ = 7.85 (t, *J* = 7.6 Hz, 2 H, $CH_{aromatic}$), 7.55 (t, *J* = 7.6 Hz, 2 H, $CH_{aromatic}$), 7.34 (m, 4 H, $CH_{aromatic}$), 3.29 (s, 4 H, CH_2) ppm. ^{13}C NMR (50 MHz, $CDCl_3$): δ = 148.52 (C_q), 134.34 (CH), 131.78 (CH), 131.72 (CSi), 128.06 (CH), 121.15 (CH), 25.29 (CH_2) ppm. ^{29}Si NMR (79.5 MHz, $CDCl_3$): δ = –6.07 ppm. MS (DEI): *m*/*z* = 278 $[M]^+$, 229 $[M – CH_2Cl]^+$, 193 $[M – CH_2Cl_2]^+$, 179 $[M – (CH_2Cl)_2]^+$, 152 $[M – Si(CH_2Cl)_2]^+$. $C_{14}H_{12}Cl_2Si$ (279.24): calcd. C 60.22, H 4.33, Cl 25.39; found C 60.27, H 4.41, Cl 25.10. IR $\tilde{\nu}$ = 3062 (m), 2995 (m), 2933 (m), 2872 (m), 1963 (w), 1928 (w), 1894 (w), 1854 (w), 1820 (w), 1593 (vs), 1483 (m), 1459 (s), 1431 (s), 1384 (s), 1260 (s), 1128 (vs), 1095 (s), 786 (vs), 749 (s) cm^{-1}. UV/Vis (hexane): λ_{max} (logε) = 211.7 (4.72), 233.6 (4.62), 241.2 (4.54), 277.3 (4.21), 289 (4.16), 321.7 (3.56) nm. Emission (hexane): λ_{max} = 386 nm.

[($C_{14}H_{12}SiS_2$)$Fe_2(CO)_6$] (1): A solution of [(μ-S)$_2$$Fe_2(CO)_6$] (62 mg, 0.18 mmol) in THF (10 mL) was cooled to –78 °C, and Et_3BHLi (0.36 mL, 0.36 mmol) was added dropwise. The solution was stirred for 15 min, and 1,1′-bis(chloromethyl)-1-silafluorene (50 mg, 0.18 mmol) was added. The mixture was warmed to room temperature and stirred at this temperature for 16 h. The volatiles were removed under vacuum, and the residue was purified by column chromatography (silica gel) with hexane as eluent. From the major red band, **1** was obtained as a red-brown solid (0.031 g, 32%). ^{1}H NMR (200 MHz, $CDCl_3$): δ = 7.81–7.11 (m, 8 H, $CH_{aromatic}$), 1.89 (s, 4 H, CH_2) ppm. ^{13}C NMR (50 MHz, $CDCl_3$): δ = 205.47 (CO), 145.89 (C_q), 133.21 (CSi), 131.39 (CH), 129.85 (CH), 126.41 (CH), 119.16 (CH), 0.23 ($SiCH_2S$) ppm. MS (DEI): *m*/*z* = 552 $[M]^+$, 496 $[M – Fe]^+$, 468 $[M – Fe(CO)]^+$, 440 $[M – Fe(CO)_2]^+$, 412 $[M – Fe(CO)_3]^+$, 384 $[M – Fe(CO)_4]^+$, 356 $[M – Fe(CO)_5]^+$. $C_{20}H_{12}Fe_2O_6S_2Si$ (552.21): calcd. C 43.50, H 2.19, S 11.61; found C 43.62, H 2.21, S 11.47. IR $\tilde{\nu}$ = 3069 (w), 2925 (m), 2854 (w), 2073 (vs), 2032 (vs), 2001 (vs), 1984 (vs), 1719 (w), 1628 (w), 1594 (w), 1459 (w), 1432 (w), 1260 (w), 1132 (w), 782 (m), 750 (m) cm^{-1}. UV/Vis (hexane): λ_{max} (logε) = 213.4 (4.77), 235.3 (4.69), 242.8 (4.64), 273.9 (4.27), 288.2 (4.19), 328.4 (4.05).

Supporting Information (see footnote on the first page of this article): Electrochemical investigations, computational details, TD-DFT results, emission quenching of **3**, and irradiation of **1**.

Acknowledgments

Financial support for this work was provided by the Deutsche Bundesstiftung Umwelt (to R. G.) and the Studienstiftung des Deutschen Volkes as well as the Alexander-von-Humboldt foundation (to U.-P. A.). The authors thank B. Dietzek, L. Zedler, and J. Popp for discussions and K. Dubnack for experimental support.

[1] L. Schlapbach, A. Züttel, *Nature* **2001**, *414*, 353–358.
[2] C. L. Aardahl, S. D. Rassat, *Int. J. Hydrogen Energy* **2009**, *34*, 6676–6683.
[3] W. Osborn, T. Markmaitree, L. L. Shaw, R. Ren, J. Hu, J. H. Kwak, Z. Yang, *JOM-J. Min. Met. Mater. S.* **2009**, *61*, 45–51.
[4] C. Koroneos, *Int. J. Hydrogen Energy* **2004**, *29*, 1443–1450.
[5] R. Cammack, M. Frey, R. Robson (Eds.), *Hydrogen as a Fuel: Learning from Nature*, Taylor and Francis, London, **2001**.
[6] R. K. Thauer, *Eur. J. Inorg. Chem.* **2011**, 919–921.
[7] Y. Na, J. Pan, M. Wang, L. Sun, *Inorg. Chem.* **2007**, *46*, 3813–3815.
[8] Y. Na, M. Wang, J. Pan, P. Zhang, B. Åkermark, L. Sun, *Inorg. Chem.* **2008**, *47*, 2805–2810.
[9] D. Streich, Y. Astuti, M. Orlandi, L. Schwartz, R. Lomoth, L. Hammarström, S. Ott, *Chem. Eur. J.* **2010**, *16*, 60–63.
[10] W.-N. Cao, F. Wang, H.-Y. Wang, B. Chen, K. Feng, C.-H. Tung, L.-Z. Wu, *Chem. Commun.* **2012**, *48*, 8081–8083.
[11] X. Li, M. Wang, D. Zheng, K. Han, J. Dong, L. Sun, *Energy Environ. Sci.* **2012**, *5*, 8220–8224; T. Yu, Y. Zeng, J. Chen, Y.-Y. Li, G. Yang, Y. Li, *Angew. Chem. Int. Ed.* **2013**, *52*, 5631–5635.
[12] S. Ott, M. Kritikos, B. Åkermark, L. Sun, *Angew. Chem.* **2003**, *115*, 3407; *Angew. Chem. Int. Ed.* **2003**, *42*, 3285–3288.
[13] L.-C. Song, M.-Y. Tang, F.-H. Su, Q.-M. Hu, *Angew. Chem.* **2006**, *118*, 1148; *Angew. Chem. Int. Ed.* **2006**, *45*, 1130–1133.
[14] J. Ekström, M. Abrahamsson, C. Olson, J. Bergquist, F. B. Kaynak, L. Eriksson, L. Sun, H.-C. Becker, B. Akermark, L. Hammarström, S. Ott, *Dalton Trans.* **2006**, 4599–4606.
[15] W.-G. Wang, F. Wang, H.-Y. Wang, G. Si, C.-H. Tung, L.-Z. Wu, *Chem. Asian J.* **2010**, *5*, 1796–1803.
[16] A. P. S. Samuel, D. T. Co, C. L. Stern, M. R. Wasielewski, *J. Am. Chem. Soc.* **2010**, *132*, 8813–8815.
[17] X. Li, M. Wang, S. Zhang, J. Pan, Y. Na, J. Liu, B. Åkermark, L. Sun, *J. Phys. Chem. B* **2008**, *112*, 8198–8202.
[18] A. M. Kluwer, R. Kapre, F. Hartl, M. Lutz, A. L. Spek, A. M. Brouwer, P. W. N. M. van Leeuwen, J. N. H. Reek, *Proc. Natl. Acad. Sci. USA* **2009**, *106*, 10460–10465.
[19] J. Liu, W. Jiang, *Dalton Trans.* **2012**, *41*, 9700–9707.
[20] T. Nann, S. K. Ibrahim, P.-M. Woi, S. Xu, J. Ziegler, C. J. Pickett, *Angew. Chem.* **2010**, *122*, 1618; *Angew. Chem. Int. Ed.* **2010**, *49*, 1574–1577.
[21] F. Wen, X. Wang, L. Huang, G. Ma, J. Yang, C. Li, *ChemSusChem* **2012**, *5*, 849–853.
[22] D. Gust, T. A. Moore, A. L. Moore, *Acc. Chem. Res.* **2009**, *42*, 1890–1898.
[23] A. Magnuson, M. Anderlund, O. Johansson, P. Lindblad, R. Lomoth, T. Polivka, S. Ott, K. Stensjö, S. Styring, V. Sundström, L. Hammarström, *Acc. Chem. Res.* **2009**, *42*, 1899–1909.
[24] H.-Y. Wang, W.-G. Wang, G. Si, F. Wang, C.-H. Tung, L.-Z. Wu, *Langmuir* **2010**, *26*, 9766–9771.
[25] T. Yu, Y. Zeng, J. Chen, Y.-Y. Li, G. Yang, Y. Li, *Angew. Chem. Int. Ed.* **2013**, *52*, 1–6.

[26] W. Lubitz, E. J. Reijerse, J. Messinger, *Energy Environ. Sci.* **2008**, *1*, 15–31.
[27] M. Wang, L. Chen, X. Li, L. Sun, *Dalton Trans.* **2011**, *40*, 12793–12800.
[28] a) M. Wang, Y. Na, M. Gorlov, L. Sun, *Dalton Trans.* **2009**, 6458–6467; b) R. Lomoth, S. Ott, *Dalton Trans.* **2009**, 9952–9959.
[29] M. Wang, L. Sun, *ChemSusChem* **2010**, *3*, 551–554.
[30] L. Sun, B. Akermark, S. Ott, *Coord. Chem. Rev.* **2005**, *249*, 1653–1663.
[31] A. J. Esswein, D. G. Nocera, *Chem. Rev.* **2007**, *107*, 4022–4047.
[32] U.-P. Apfel, D. Troegel, Y. Halpin, S. Tschierlei, U. Uhlemann, H. Görls, M. Schmitt, J. Popp, P. Dunne, M. Venkatesan, M. Coey, M. Rudolph, J. G. Vos, R. Tacke, W. Weigand, *Inorg. Chem.* **2010**, *49*, 10117–10132.
[33] U.-P. Apfel, Y. Halpin, H. Görls, J. G. Vos, W. Wolfgang, *Eur. J. Inorg. Chem.* **2011**, 581–588.
[34] U.-P. Apfel, H. Görls, G. A. N. Felton, D. H. Evans, R. S. Glass, D. L. Lichtenberger, W. Weigand, *Helv. Chim. Acta* **2012**, *95*, 2168–2175.
[35] B. Z. Tang, X. Zhan, G. Yu, P. P. S. Lee, Y. Liu, D. Zhu, *J. Mater. Chem.* **2001**, *11*, 2974–2978.
[36] T. Matsuda, S. Kadowaki, T. Goya, M. Murakami, *Org. Lett.* **2007**, *9*, 133–136.
[37] S. Yamaguchi, K. Tamao, *Chem. Lett.* **2005**, *34*, 2–7.
[38] M. Hissler, *Coord. Chem. Rev.* **2003**, *244*, 1–44.
[39] S. Yamaguchi, C. Xu, T. Okamoto, *Pure Appl. Chem.* **2006**, *78*, 721–730.
[40] G. Yu, S. Yin, Y. Liu, J. Chen, X. Xu, X. Sun, D. Ma, X. Zhan, Q. Peng, Z. Shuai, B. Tang, D. Zhu, W. Fang, Y. Luo, *J. Am. Chem. Soc.* **2005**, *127*, 6335–6346.
[41] K. Tamao, *J. Organomet. Chem.* **2000**, *611*, 5–11.
[42] S. Grigoras, *Synth. Met.* **1992**, *49*, 293–304.
[43] G. Frapper, M. Kertesz, *Organometallics* **1992**, *11*, 3178–3184.
[44] J. Kurti, P. Surjan, M. Kertesz, G. Frapper, *Synth. Met.* **1993**, *57*, 4338–4343.
[45] Y. Yamaguchi, J. Shioya, *Mol. Eng.* **1993**, *2*, 339–347.
[46] Y. Yamaguchi, *Mol. Eng.* **1994**, *3*, 311–320.
[47] L.-C. Song, C.-G. Li, J. Gao, B.-S. Yin, X. Luo, X.-G. Zhang, H.-L. Bao, Q.-M. Hu, *Inorg. Chem.* **2008**, *47*, 4545–4553.
[48] R. S. Glass, N. E. Gruhn, E. Lorance, M. S. Singh, N. Y. T. Stessman, U. I. Zakai, *Inorg. Chem.* **2005**, *44*, 5728–5737.
[49] E. J. Lyon, I. P. Georgakaki, J. H. Reibenspies, M. Y. Darensbourg, *Angew. Chem.* **1999**, *111*, 3373; *Angew. Chem. Int. Ed.* **1999**, *38*, 3178–3180.
[50] The parameters i_p and E_p are the peak current and the peak potential of a redox process, respectively; $E_{1/2} = (E_p^a + E_p^c)/2$; E_p^a and E_p^c are the potentials of the anodic and cathodic peaks of a reversible process; v ($V s^{-1}$) is the scan rate in CV experiments. An ECE process is a chemical reaction (C) between two electron transfer steps (E).
[51] K. Charreteur, M. Kdider, J.-F. Capon, F. Gloaguen, F. Y. Pétillon, P. Schollhammer, J. Talarmin, *Inorg. Chem.* **2010**, *49*, 2496–2501.
[52] J.-F. Capon, F. Gloaguen, P. Schollhammer, J. Talarmin, *J. Electroanal. Chem.* **2004**, *566*, 241–247.
[53] D. Morvan, J.-F. Capon, F. Gloaguen, A. Le Goff, M. Marchivie, F. Michaud, P. Schollhammer, J. Talarmin, J.-J. Yaouanc, R. Pichon, N. Kervarec, *Organometallics* **2007**, *26*, 2042–2052.
[54] D. Chouffai, G. Zampella, J.-F. Capon, L. De Gioia, A. Le Goff, F. Y. Pétillon, P. Schollhammer, J. Talarmin, *Organometallics* **2012**, *31*, 1082–1091.
[55] We made the reasonable assumption that the diffusion coefficient of **1** is close to that of $[Fe_2(CO)_4(\kappa^2\text{-}I_{Me}\text{–}CH_2\text{–}I_{Me})(\mu\text{-pdt})]$.
[56] G. A. N. Felton, A. K. Vannucci, J. Chen, L. T. Lockett, N. Okumura, B. J. Pedro, U. I. Zakai, D. H. Evans, R. S. Glass, D. L. Lichtenberger, *J. Am. Chem. Soc.* **2007**, *129*, 12521–12530.
[57] J. Chen, A. K. Vannucci, C. A. Mebi, N. Okomura, S. C. Borowski, M. Swenson, L. T. Lockett, D. H. Evans, R. S. Glass, D. L. Lichtenberger, *Organometallics* **2010**, *29*, 5330–5340.
[58] J. Windhager, M. Rudolph, S. Bräutigam, H. Görls, W. Weigand, *Eur. J. Inorg. Chem.* **2007**, 2748–2760.
[59] J.-F. Capon, S. Ezzaher, F. Gloaguen, F. Y. Pétillon, P. Schollhammer, J. Talarmin, T. Davin, J. E. McGrady, K. W. Muir, *New J. Chem.* **2007**, *31*, 2052–2064.
[60] G. A. Felton, B. J. Petro, R. S. Glass, D. L. Lichtenberger, D. H. Evans, *J. Am. Chem. Soc.* **2009**, *131*, 11290–11291.
[61] For leading references, see: a) D. H. Evans, *Chem. Rev.* **2008**, *108*, 2113–2144; b) W. E. Geiger, *Prog. Inorg. Chem.* **1985**, *33*, 275–352; c) D. H. Evans, K. M. O'Connell, in: *Electroanalytical Chemistry*, vol. 14 (Ed.: A. J. Bard), Dekker, New York, **1986**, p. 113–207.
[62] D. Urhammer, F. A. Schultz, *J. Phys. Chem. A* **2002**, *106*, 11630–11636.
[63] J. B. Fernandes, L. Q. Zhang, F. A. Schultz, *J. Electroanal. Chem.* **1991**, *297*, 145–161.
[64] D. T. Pierce, W. E. Geiger, *J. Am. Chem. Soc.* **1992**, *114*, 6063–6073, and references cited therein.
[65] A. J. Downard, A. M. Bond, A. J. Clayton, L. R. Hanton, D. A. McMorran, *Inorg. Chem.* **1996**, *35*, 7684–7690.
[66] The quantum yield of pyrene is 0.32, see: I. B. Berlman, *Handbook of Fluorescence Spectra of Aromatic Molecules*, Academic Press, New York, **1971**.
[67] a) X. Zhao, I. P. Georgakaki, M. L. Miller, J. C. Yarbrough, M. Y. Darensbourg, *J. Am. Chem. Soc.* **2001**, *123*, 9710–9711; b) X. Zhao, I. P. Georgakaki, M. L. Miller, R. Mejia-Rodriguez, C.-Y. Chiang, M. Y. Darensbourg, *Inorg. Chem.* **2002**, *41*, 3917–3928; c) D. Chong, I. P. Georgakaki, R. Mejia-Rodriguez, J. Sanabria-Chinchilla, M. P. Soriaga, M. Y. Darensbourg, *Dalton Trans.* **2003**, *21*, 4158–4163; d) R. Mejia-Rodriguez, D. Chong, J. H. Reibenspies, M. P. Soriaga, M. Y. Darensbourg, *J. Am. Chem. Soc.* **2004**, *126*, 12004–12014.
[68] a) F. Gloaguen, J. D. Lawrence, M. Schmidt, S. R. Wilson, T. B. Rauchfuss, *J. Am. Chem. Soc.* **2001**, *123*, 12518–12527; b) J. D. Lawrence, T. B. Rauchfuss, S. R. Wilson, *Inorg. Chem.* **2002**, *41*, 6193–6195; c) J. L. Nehring, D. M. Heinekey, *Inorg. Chem.* **2003**, *42*, 4288–4292.
[69] J.-F. Capon, S. E. Hassnaoui, F. Gloaguen, P. Schollhammer, J. Talarmin, *Organometallics* **2005**, *24*, 2020–2022.
[70] F. Gärtner, A. Boddien, E. Barsch, K. Fumino, S. Losse, H. Junge, D. Hollmann, A. Brückner, R. Ludwig, M. Beller, *Chem. Eur. J.* **2011**, *17*, 6425–6436.
[71] F. Gärtner, B. Sundararaju, A.-E. Surkus, A. Boddien, B. Loges, H. Junge, P. H. Dixneuf, M. Beller, *Angew. Chem.* **2009**, *121*, 10147–10150.
[72] *COLLECT*, Data Collection Software, Nonius B. V., The Netherlands, **1998**.
[73] Z. Otwinowski, W. Minor, *Processing of X-ray Diffraction Data Collected in Oscillation Mode*, in: *Methods in Enzymology*, vol. 276: *Macromolecular Crystallography, Part A* (Eds.: C. W. Carter Jr., R. M. Sweet), *Academic Press*, **1997**.
[74] G. M. Sheldrick, *Acta Crystallogr., Sect. A* **2008**, *64*, 112–122.
[75] J.-F. Capon, F. Gloaguen, P. Schollhammer, J. Talarmin, *J. Electroanal. Chem.* **2004**, *566*, 241–247.
[76] F. R. Leroux, L. Bonnafoux, C. Heiss, F. Colobert, D. A. Lanfranchi, *Adv. Synth. Catal.* **2007**, *349*, 2705–2713.

Received: April 23, 2013
Published Online: July 4, 2013

Eur. J. Inorg. Chem. **2013** · © WILEY-VCH Verlag GmbH & Co. KGaA, 69451 Weinheim, 2013 · ISSN 1099–0682

SUPPORTING INFORMATION

DOI: 10.1002/ejic.201300537
Title: A Silicon-Heteroaromatic System as Photosensitizer for Light-Driven Hydrogen Production by Hydrogenase Mimics
Author(s): Roman Goy, Ulf-Peter Apfel, Catherine Elleouet, Daniel Escudero, Martin Elstner, Helmar Görls, Jean Talarmin,* Philippe Schollhammer, Leticia González,* Wolfgang Weigand*

1 Electrochemical investigations
2 Computational details
3 TD-DFT results
4 Emission quenching of compound **3**
5 Irradiation of compound **1**
6 References

1 Electrochemical investigations

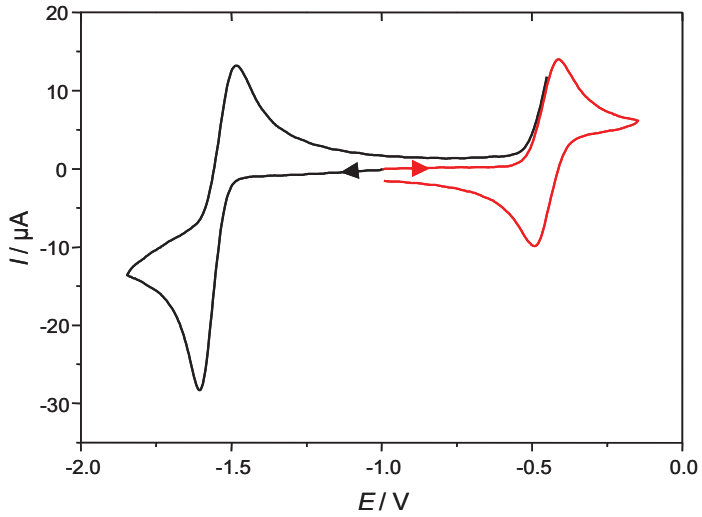

Figure S1: Cyclic voltammetry of **1**, (0.81 mM, black trace) and of $[Fe_2(CO)_4(\kappa^2\text{-}I_{Me}\text{-}CH_2\text{-}I_{Me})(\mu\text{-pdt})]$ (0.83 mM, red trace) in CH_2Cl_2-$[NBu_4][PF_6]$ (vitreous carbon electrode, $v = 0.2$ V s^{-1}; potentials are in V *vs*. Fc^+/Fc).

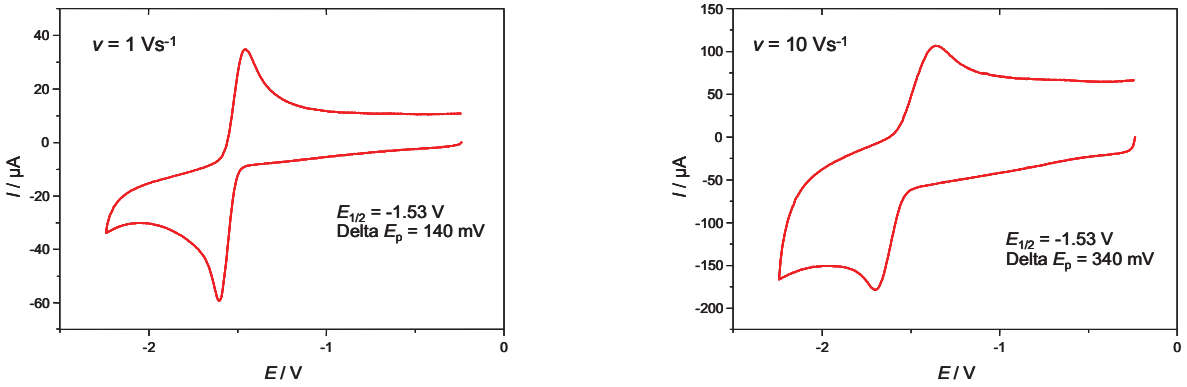

Figure S2: Cyclic voltammetry of **1**, 0.4 mM in CH_2Cl_2-$[NBu_4][PF_6]$ (vitreous carbon electrode, potentials are in V *vs*. Fc^+/Fc).

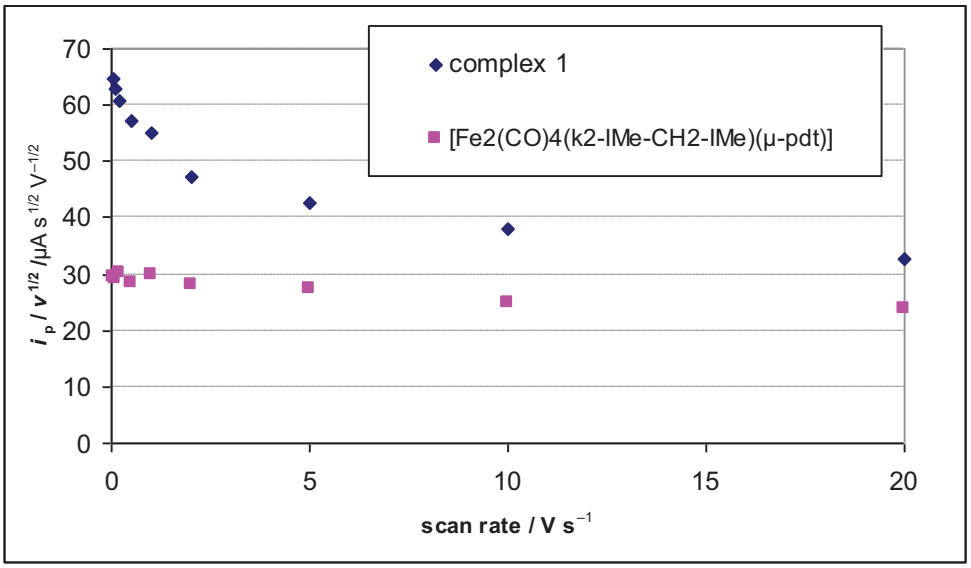

Figure S3: Scan rate dependence of the current for the reduction of **1** (0.81 mM, □) and for the oxidation of $[Fe_2(CO)_4(\kappa^2\text{-}I_{Me}\text{-}CH_2\text{-}I_{Me})(\mu\text{-}pdt)]$ (0.83 mM, □) in CH_2Cl_2-$[NBu_4][PF_6]$ (vitreous carbon electrode).

2 Computational details

All calculations are based on density functional theory (DFT). Both geometry optimizations in the ground (S_0) and lowest triplet (T_1) excited states have been carried out with the hybrid functional B3LYP[1, 2] in combination with the 6-311G* basis set for all atoms. Relativistic effects were included in the Fe atoms using the MDF10 pseudopotential.[3] All the species have been characterized as true minima or transition states of the corresponding hyper-potential energy surfaces *via* a vibrational analysis. In Figure S4 the main geometrical features of complex **1** in its S_0 and T_1 optimized geometries are schematically shown. In Figure S5 and S6 the relevant orbitals involved in the relevant electronic excitations of **1** and **3** are depicted.

To reproduce the measured absorption UV-Vis spectrum, the lowest-lying 130 and 25 vertical singlet electronic excitation energies for **1** and **3**, respectively, were calculated using time-dependent DFT (TD-DFT) at the S_0 optimized geometry using the same functional and basis set employed in the geometry optimizations. Additionally, □SCF-DFT calculations have been performed to obtain the singlet-triplet splitting. Such calculations yield the adiabatic energy difference between the lowest triplet excited state and the ground state at their respective optimized geometries. The TD-DFT and □SCF-DFT calculations were performed in solution using heptane as solvent with the polarization continuum model.[4, 5] We point out here that the solvent employed in the experiments is hexane, which possesses very similar molecular properties as heptane. Therefore, we hardly expect any divergence in the results of our calculations performed in heptane. All the calculations were performed with the Gaussian03 program package.[6]

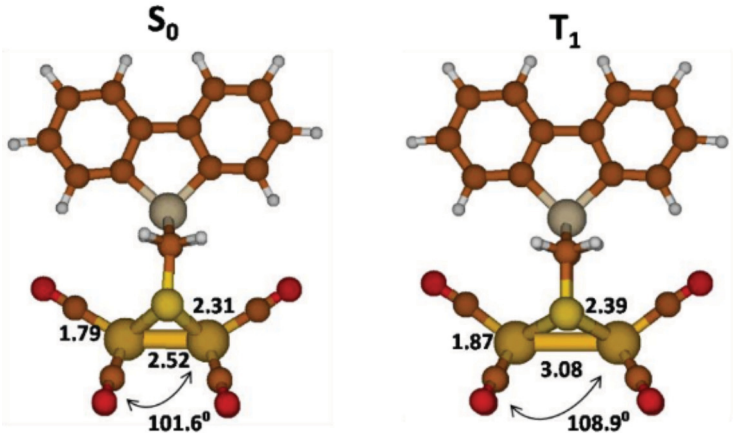

Figure S4. Relevant geometrical parameters of the optimized S_0 and T_1 geometries of complex **1**. Distances in Ångströms and angles in degrees.

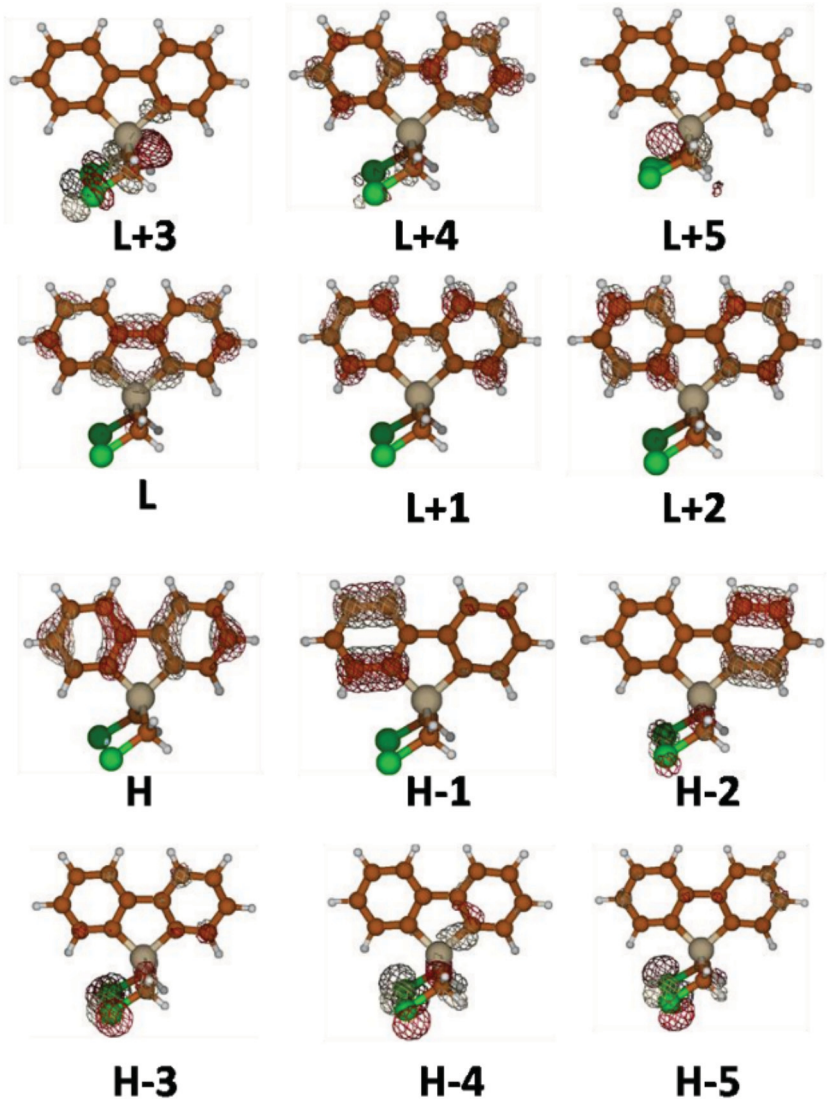

Figure S5. Relevant Kohn-Sham orbitals (B3LYP/6-311G*) for **3**.

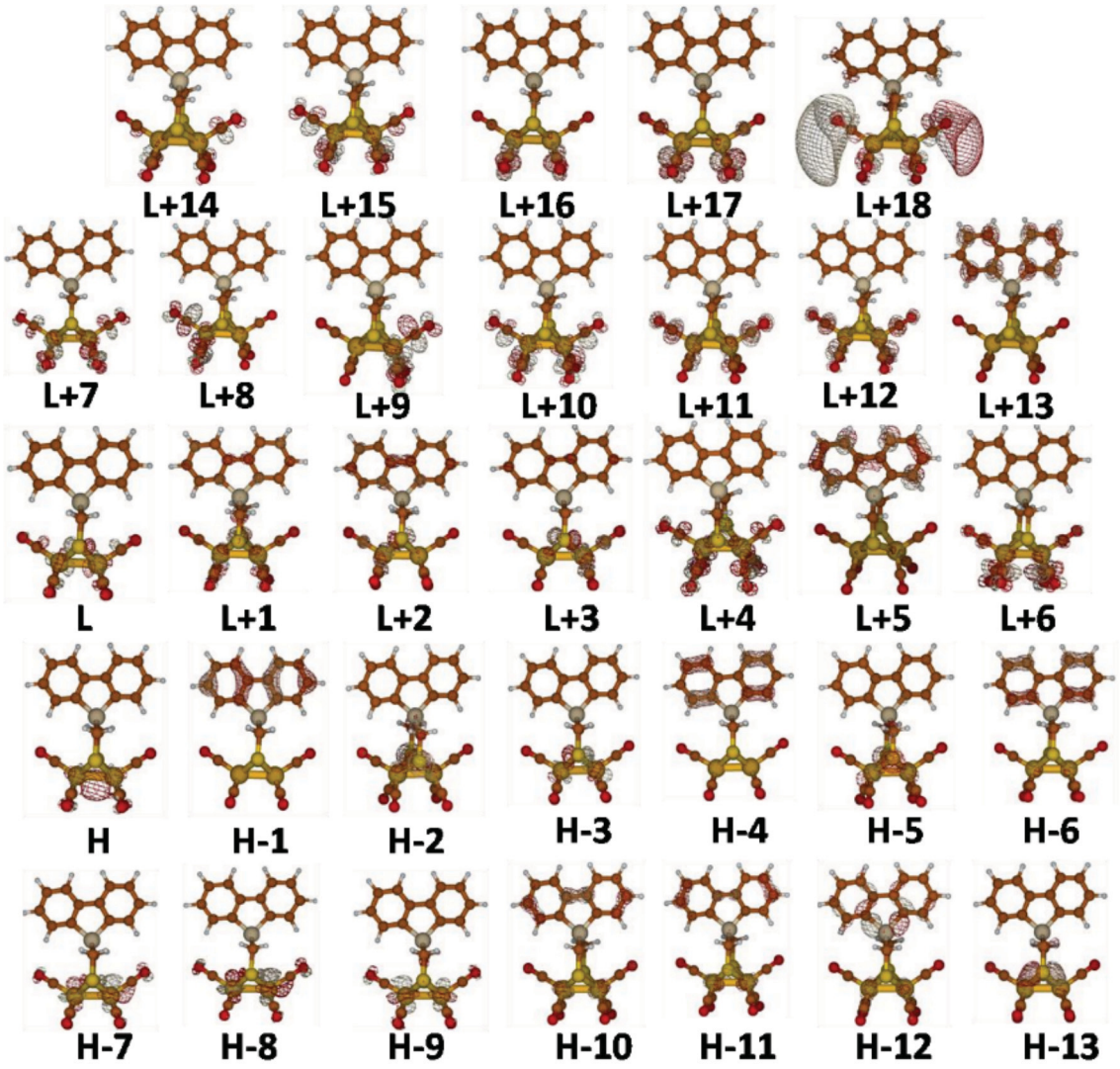

Figure S6. Relevant Kohn-Sham orbitals (B3LYP/6-311G*) for complex **1**.

3 TD-DFT results

Table S1. Main theoretical electronic singlet-singlet transition energies (□*E*) with corresponding oscillator strengths (*f*) and assignment for **1** and **3**. Number in parenthesis correspond to the wavefunction coefficient for the specified transition.

3

State	□*E* /nm	*f*	Assignment[a]
S_1	302	0.107	H→L (0.66) $\pi_{fl} \rightarrow \pi^*_{fl}$
S_2	274	0.130	H→L+1 (0.54) $\pi_{fl} \rightarrow \pi^*_{fl}$
S_4	240	0.440	H-1→L (0.46) $\pi_{fl} \rightarrow \pi^*_{fl}$
S_6	233	0.143	H-3→L (0.39) $n_{Cl} \rightarrow \pi^*_{fl}$ H→L+2 (-0.34) $\pi_{fl} \rightarrow \pi^*_{fl}$
S_9	221	0.045	H-1→L+1 (0.36) $\pi_{fl} \rightarrow \pi^*_{fl}$
S_{10}	219	0.195	H-2→L+1 (0.49) $\pi_{fl} \rightarrow \pi^*_{fl}$
S_{18}	202	0.100	H-3→L+1 (0.47) $n_{Cl} \rightarrow \pi^*_{fl}$

1

State	□*E* /nm	*f*	Assignment[b]
S_1	443	0.004	H-3→L (0.58) $3d_{Fe} \rightarrow$ □*$_{Fe\text{-}Fe}$
S_4	398	0.104	H→L (0.60) □$_{Fe\text{-}Fe}$ → □*$_{Fe\text{-}Fe}$
S_9	377	0.044	H-9→L (0.41) $3d_{Fe} \rightarrow$ □*$_{Fe\text{-}Fe}$
S_{10}	359	0.015	H-5→L (0.39) $n_S \rightarrow$ □*$_{Fe\text{-}Fe}$
S_{19}	315	0.036	H-1→L+1 (0.66) $\pi_{fl} \rightarrow 3d_{Fe} + \pi^*_{fl}$
S_{23}	297	0.015	H→L+8 (0.45) □$_{Fe\text{-}Fe}$ → $\pi^*_{3\text{-}CO}$
S_{24}	295	0.019	H→L+9 (-0.45) □$_{Fe\text{-}Fe}$ → $\pi^*_{3\text{-}CO}$
S_{26}	290	0.022	H→L+6 (0.49) □$_{Fe\text{-}Fe}$ → $\pi^*_{6\text{-}CO}$
S_{27}	289	0.048	H-3→L+4 (0.33) $3d_{Fe} \rightarrow \pi^*_{6\text{-}CO}$
S_{28}	288	0.061	H-1→L+2 (0.66) $\pi_{fl} \rightarrow 3d_{Fe}$
S_{30}	282	0.017	H-1→L+3 (0.68) $\pi_{fl} \rightarrow 3d_{Fe} + n_S$
S_{32}	280	0.178	H-2→L+3 (0.68) $n_S \rightarrow 3d_{Fe} + n_S$
S_{33}	277	0.092	H-1→L+5 (0.68) $\pi_{fl} \rightarrow \pi^*_{fl}$
S_{46}	260	0.027	H-3→L+9 (0.29) $3d_{Fe} \rightarrow \pi^*_{3\text{-}CO}$
S_{48}	258	0.030	H-8→L+4 (0.31) $3d_{Fe} \rightarrow \pi^*_{6\text{-}CO}$
S_{55}	253	0.015	H-7→L+7 (0.31) $3d_{Fe} \rightarrow \pi^*_{3\text{-}CO}$
S_{56}	251	0.222	H-4→L+1 (0.53) $\pi_{fl} \rightarrow 3d_{Fe} + \pi^*_{fl}$
S_{58}	250	0.071	H→L+15 (0.25) □$_{Fe\text{-}Fe}$ → $\pi^*_{6\text{-}CO}$
S_{60}	249	0.025	H-1→L+6 (0.31) $\pi_{fl} \rightarrow \pi^*_{6\text{-}CO}$
S_{61}	249	0.054	H-2→L+5 (0.43) $n_S \rightarrow \pi^*_{fl}$
S_{76}	241	0.025	H-3→L+7 (0.37) $3d_{Fe} \rightarrow \pi^*_{3\text{-}CO}$
S_{77}	239	0.071	H-4→L+2 (0.47) $\pi_{fl} \rightarrow 3d_{Fe}$
S_{78}	239	0.049	H-2→L+11 (0.40) $n_S \rightarrow \pi^*_{4\text{-}CO}$
S_{79}	237	0.071	H-4→L+3 (0.42) $\pi_{fl} \rightarrow 3d_{Fe} + n_S$
S_{84}	234	0.055	H-5→L+7 (0.48) $n_S \rightarrow \pi^*_{6\text{-}CO}$
S_{108}	223	0.094	H-4→L+5 (0.47) $\pi_{fl} \rightarrow \pi^*_{fl}$
S_{110}	223	0.157	H-6→L+5 (0.30) $\pi_{fl} \rightarrow \pi^*_{fl}$ H-6→L+3 (-0.31) $\pi_{fl} \rightarrow 3d_{Fe} + n_S$

S_{114}	222	0.037	H-5→L+10 (0.37) $n_S \rightarrow \pi^*_{6\text{-CO}}$
S_{115}	221	0.116	H-2→L+16 (0.34) $n_S \rightarrow \pi^*_{4\text{-CO}}$
S_{122}	218	0.020	H-8→L+7 (0.53) $3d_{Fe} \rightarrow \pi^*_{3\text{-CO}}$
S_{115}	217	0.026	H-2→L+18 (0.46) $n_S \rightarrow$ Rydberg

[a] The fl subindex denotes the 1-silafluorene moiety. [b] The 3-CO (4-CO, *etc*) subindex denotes a delocalized orbital among 3 (4, *etc*) of the CO ligands (see the involved orbitals in the excitations in Figure S6)

4 Emission quenching of compound 3

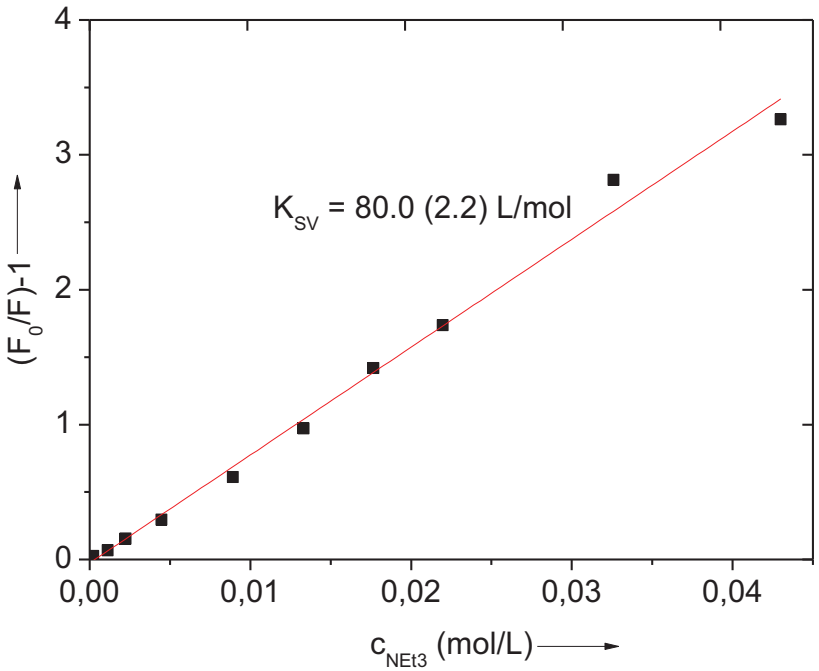

Figure S7: Stern-Volmer plot for the emission quenching of compound **3** by triethylamine.

5 Irradiation of compound 1.

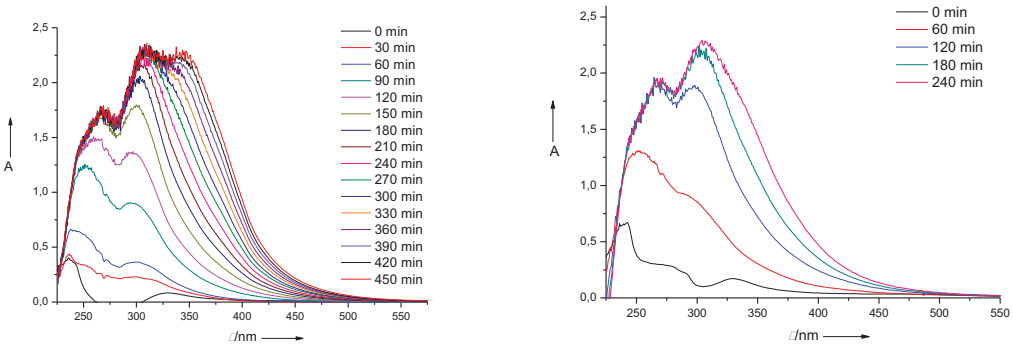

Figure S8: UV-vis spectra for compound **1** in acetonitrile (0.011 mM, left and 0.027 mM, right) and excitation at 254 nm.

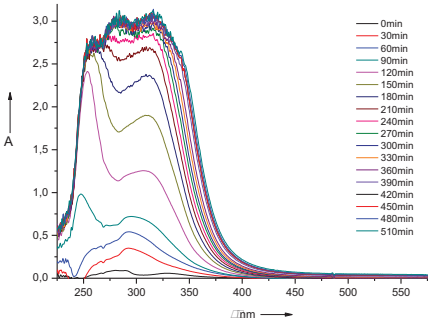

Figure S9: UV-vis spectra for compound **1** (0.011 mM) in the presence of trifluoroacetic acid (0.5 M) and triethylamine (0.5 M) in acetonitrile and excitation at 254 nm.

6 References

[1] A. D. Becke, *J. Chem. Phys.* **1993**, *98*, 5648–5652.

[2] C. T. Lee, W. T. Yang, R. G. Parr, *Phys. Rev. B.* **1988**, *37*, 785–789.

[3] a) M. Dolg, U. Wedig, H. Stoll, H. Preuss, *J. Chem. Phys.* **1987**, *86*, 866-872. b) B. Metz, H. Stoll, M. Dolg. *J. Chem. Phys.* **2000**, *113,* 2563-2569.

[4] M. Cossi, V. Barone, B. Menucci, J. Tomasi, *Chem. Phys. Lett.* **1998**, *286*, 253–260.

[5] B. Menucci, J. Tomasi, *J. Chem. Phys.* **1997**, 106, 5151–5158.

[6] Gaussian 03, Revision C.02, Frisch, M. J.; Trucks, G. W.; Schlegel, H. B.; Scuseria, G. E.; Robb, M. A.; Cheeseman, J. R.; Montgomery, Jr., J. A.; Vreven, T.; Kudin, K. N.; Burant, J. C.; Millam, J. M.; Iyengar, S. S.; Tomasi, J.; Barone, V.; Mennucci, B.; Cossi, M.; Scalmani, G.; Rega, N.; Petersson, G. A.; Nakatsuji, H.; Hada, M.; Ehara, M.; Toyota, K.; Fukuda, R.; Hasegawa, J.; Ishida, M.; Nakajima, T.; Honda, Y.; Kitao, O.; Nakai, H.; Klene, M.; Li, X.; Knox, J. E.; Hratchian, H. P.; Cross, J. B.; Bakken, V.; Adamo, C.; Jaramillo, J.; Gomperts, R.; Stratmann, R. E.; Yazyev, O.; Austin, A. J.; Cammi, R.; Pomelli, C.; Ochterski, J. W.; Ayala, P. Y.; Morokuma, K.; Voth, G. A.; Salvador, P.; Dannenberg, J. J.; Zakrzewski, V. G.; Dapprich, S.; Daniels, A. D.; Strain, M. C.; Farkas, O.; Malick, D. K.; Rabuck, A. D.; Raghavachari, K.; Foresman, J. B.; Ortiz, J. V.; Cui, Q.; Baboul, A. G.; Clifford, S.; Cioslowski, J.; Stefanov, B. B.; Liu, G.; Liashenko, A.; Piskorz, P.; Komaromi, I.; Martin, R. L.; Fox, D. J.; Keith, T.; Al-Laham, M. A.; Peng, C. Y.; Nanayakkara, A.; Challacombe, M.; Gill, P. M. W.; Johnson, B.; Chen, W.; Wong, M. W.; Gonzalez, C.; Pople, J. A.; Gaussian, Inc., Wallingford CT, **2004**.

4.2 **[RG2]**

A Sterically Stabilized Fe^{I}-Fe^{I} Semi-Rotated Conformation of [FeFe] Hydrogenase subsite Model

Roman Goy, Luca Bertini, Catherine Elleouet, Helmar Görls, Giuseppe Zampella, Jean Talarmin, Luca De Gioia, Philippe Schollhammer, Ulf-Peter Apfel, Wolfgang Weigand

Dalton Transactions **2015**, *44*, 1690-1699.

The publication reports on the synthesis of $[Fe_2(CO)_6\{\mu\text{-}(SCHPh)_2SiPh_2\}]$ as an [FeFe] hydrogenase model complex with a sterically demanding silicon containing dithiolate linker. In further experiments, this *all*-CO complex was reacted with one and two equivalents of 1,2-bis(dimethylphosphino)ethane (dmpe), respectively, leading to the three different compounds $[\{Fe_2(CO)_5\{\mu\text{-}(SCHPh)_2SiPh_2\}\}_2(\mu\text{-dmpe})]$, $[Fe_2(CO)_4(\kappa^2\text{-dmpe})\{\mu\text{-}(SCHPh)_2SiPh_2\}]$ and $[Fe_2(CO)_4(\mu\text{-dmpe})\{\mu\text{-}(SCHPh)_2\ SiPh_2\}]$, where two of the carbonyl ligands were replaced by dmpe. These complexes were fully characterized by NMR and IR spectroscopy, mass spectrometry, elemental analysis, XRD analysis as well as cyclovoltammetry. The molecular structure of the $[Fe^{I}Fe^{I}]$ hydrogenase model complex $[Fe_2(CO)_4(\kappa^2\text{-dmpe})\{\mu\text{-}(SCHPh)_2SiPh_2\}]$ revealed that the introduction of the bidendate phosphine dmpe enforces a semi-rotated conformation of the complex in solid state. The identification of this species with its structural features, along with DFT computations, supports the idea that in order to obtain a fully rotated geometry related to the active site of $[Fe^{I}Fe^{I}]$ hydrogenase three factors are important, which were discussed already in chapter 3.4.4: (a) asymmetrical coordination at the two iron atoms using a bidentate donor ligand, here dmpe, (b) a bulky dithiolate bridgehead, which promotes (c) a weak remote agostic $Fe^{\cdots}H\text{-}C$ interaction. Complex $[Fe_2(CO)_4(\kappa^2\text{-dmpe})\{\mu\text{-}(SCHPh)_2SiPh_2\}]$ represents the example with the highest degree of rotation so far reported for $[Fe^{I}Fe^{I}]$ hydrogenase models without any agostic interactions ($Fe^{\cdots}H\text{-}C$)[145] and enabling new approaches for the design of dithiolate bridgeheads to achieve a full-rotated geometry related to the active site of [FeFe] hydrogenases without any type of H-bond interaction.

Dalton Transactions

PAPER

View Article Online
View Journal | View Issue

Cite this: *Dalton Trans.*, 2015, **44**, 1690

A sterically stabilized Fe^{I}–Fe^{I} semi-rotated conformation of [FeFe] hydrogenase subsite model†

Roman Goy,[a] Luca Bertini,*[b] Catherine Elleouet,[c] Helmar Görls,[a] Giuseppe Zampella,[b] Jean Talarmin,[c] Luca De Gioia,*[b] Philippe Schollhammer,*[c] Ulf-Peter Apfel*[d] and Wolfgang Weigand*[a,e]

Received 20th October 2014,
Accepted 17th November 2014

DOI: 10.1039/c4dt03223c

www.rsc.org/dalton

The [FeFe] hydrogenase is a highly sophisticated enzyme for the synthesis of hydrogen *via* a biological route. The *rotated state* of the H-cluster in the [$Fe^{I}Fe^{I}$] form was found to be an indispensable criteria for an effective catalysis. Mimicking the specific rotated geometry of the [FeFe] hydrogenase active site is highly challenging as no protein stabilization is present in model compounds. In order to simulate the sterically demanding environment of the nature's active site, the sterically crowded *meso*-bis(benzylthio)-diphenylsilane (**2**) was utilized as dithiolate linker in an [2Fe2S] model complex. The reaction of the obtained hexacarbonyl complex **3** with 1,2-bis(dimethylphosphino)ethane (dmpe) results three different products depending on the amount of dmpe used in this reaction: [{$Fe_2(CO)_5$(μ-$(SCHPh)_2SiPh_2$)}$_2$-(μ-dmpe)] (**4**), [$Fe_2(CO)_5$(κ^2-dmpe){μ-$(SCHPh)_2SiPh_2$}] (**5**) and [$Fe_2(CO)_5$(μ-dmpe){μ-$(SCHPh)_2SiPh_2$}] (**6**). Interestingly, the molecular structure of compound **5** shows a [FeFe] subsite comprising a semi-rotated conformation, which was fully characterized as well as the other isomers **4** and **6** by elemental analysis, IR and NMR spectroscopy, X-ray diffraction analysis (XRD) and DFT calculations. The herein reported model complex is the first example so far reported for [$Fe^{I}Fe^{I}$] hydrogenase model complex showing a semi-rotated geometry without the need of stabilization *via* agostic interactions (Fe···H–C).

Introduction

[FeFe] hydrogenases are the most efficient proton reducing catalysts and enable the generation of dihydrogen in nature.[1–3] Numerous structural as well as functional studies on [2Fe2S] as well as their homologous [2Fe2E] (E = Se, Te) complexes as [FeFe]-H_2ase mimics were performed for a better understanding of its active site.[4–18] As independently reported by Peters as well as Fontecilla-Camps *et al.*, the active site of this enzyme contains a $[2Fe]_H$ subsite covalently linked by a cysteine bridge to a [4Fe4S] ferredoxin cluster (Fig. 1).[19–21] The diiron center is best described as rotated state that possesses a square pyramid geometry at one iron atom (Fe_d, Fig. 1) and is inverted with respect to the geometry of the other moiety (Fe_p, Fig. 1).[22] This causes a free coordination site at the apical site of the distal iron moiety (Fe_d), where protons and molecular hydrogen are proposed to bind during the catalytic process of production and uptake of H_2. Mimicking of this specific geometry in synthetic [FeFe]-H_2ase models is highly challenging and only specific states of the H_2-formation mechanism are accessible.[23–26] Mechanistic details of the natural process were intensively investigated by Lubitz *et al.* with EPR spectroscopy and helped synthetic chemists in targeting specific intermediates.[22,27–29] Especially, the rotated state was found to be an indispensable criteria for active compounds[22] and for the formation of stabilized terminal hydrides. Notably, although Happe, Lubitz and Fontecave *et al.* showed the

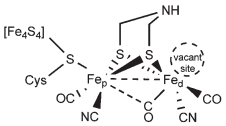

Fig. 1 Active site of [FeFe]-Hydrogenase with the vacant site located at the distal iron (Fe_d).

[a]*Institut für Anorganische und Analytische Chemie, Friedrich-Schiller-Universität, Humboldtstraße 8, 07743 Jena, Germany. E-mail: wolfgang.weigand@uni-jena.de*
[b]*Department of Biotechnology and Biosciences, University of Milano-Bicocca, 20126 Milan, Italy. E-mail: luca.bertini@unimib.it, luca.degioia@unimib.it*
[c]*University of Brest, CNRS, UMR 6521, Chimie, Electrochimie Moléculaires et Chimie Analytique, CS 93837, 29238 Brest-Cedex 3, France. E-mail: Philippe.Schollhammer@univ-brest.fr*
[d]*Inorganic Chemistry I/Bioinorganic Chemistry, Ruhr-Universität Bochum, Universitätsstraße 150, 44780 Bochum, Germany. E-mail: ulf.apfel@rub.de*
[e]*Jena Center for Soft Matter (JCSM), Philosophenweg 7, 07743 Jena, Germany*
†Electronic supplementary information (ESI) available. CCDC 1028097–1028100 and 1028773. For ESI and crystallographic data in CIF or other electronic format see DOI: 10.1039/c4dt03223c

successful incorporation of artificial aminodithiolato derived model complexes into the protein environment with full activity towards H_2 generation, these complexes do show a different chemistry under electrocatalytic conditions.[30,31] Although spectroscopic data pointing towards formation of rotated states in oxidized and reduced model compounds was reported,[10,32] Darensbourg *et al.* were the first to provide structural evidence for a mixed-valent [$Fe^{I}Fe^{II}$] complex with a rotated geometry.[14] Model complexes comprising a [$Fe^{I}Fe^{I}$] moiety with such a rotated geometry are rare. Only very recently, the first examples of [$Fe^{I}Fe^{I}$]-H_2ase mimics featuring a fully rotated conformation, [$Fe_2(CO)_4(\kappa^2$-dmpe){μ-$(SCH_2)_2$-N-Bn}][23] (Bn = Benzyl) and [$Fe_2(CO)_4(\kappa^2$-dppv){μ-$(SCH_2)_2$-CEt_2}][24] were reported simultaneously. Remarkably, both complexes reveal similar structural features that were reported to be crucial for the stabilization of this particular structure, *i.e.* an asymmetrical disubstituted diiron center, a bulky dithiolate bridge and an intramolecular remote agostic interaction.

Inspired by these new findings and in continuation of our research on silicon containing [FeFe] hydrogenase model complexes, we investigated the reactivity of 1,2-bis(dimethylphosphino)ethane (dmpe) with diiron derivatives featuring sterically demanding silicon bridges.[32–35] Silicon species thereby have numerous advantages as the starting materials, R_2SiCl_2 are commercially available in great variety and can be easily modified at the central silicon position. Herein, we report the synthesis and the molecular structure of a [$Fe^{I}Fe^{I}$] model complex having a strongly distorted conformation. In contrast to [$Fe_2(CO)_4(\kappa^2$-dmpe){μ-$(SCH_2)_2$N-Bn}][23] and [$Fe_2(CO)_4(\kappa^2$-dppv){μ-$(SCH_2)_2CEt_2$}],[24] no intramolecular remote agostic interaction is observed and required. The identification of this species with its structural features along with DFT computations corroborates the theory[23,24,36] that in contrast to earlier reports the simultaneous presence of the three proposed structural factors (asymmetrical coordination at the two Fe atoms, bulky size of the dithiolate bridgehead, weak remote agostic interaction Fe···H–C) to obtain partially or semi-rotated structures of diiron(I) dithiolates[14] is not mandatory. However, each of the three factors is crucial for observing full-rotated geometry at a single Fe atom, as that present in the [FeFe] hydrogenase cofactor.

Results and discussion

In order to enforce an inverted geometry and to avoid "flipping" of the S-to-S linker in [2Fe2S]-clusters, the sterically crowded dithiol *meso*-bis(benzylthio)diphenylsilane was synthesized according to Scheme 1 in a modified procedure described by Zubieta *et al.*[37] Dichlorodiphenylsilane was reacted with benzylmercaptan in the presence of *n*-butyllithium, whereas compound **1** was generated. *In situ* treatment of **1** with *tert*-butyllithium induces a double Wittig-rearrangement affording **2** as a mixture of the *d*-, *l*- and *meso*-forms. Crystallization from hexane exclusively yields the *meso*-form as the major product in 61% yield. Since compound **2** is not described in literature, its absolute configuration was established by single crystal X-ray analyses, as depicted in Fig. S1.† Reaction of [$Fe_3(CO)_{12}$] and *meso*-bis(benzylthio)diphenylsilane **2** in refluxing toluene afforded the corresponding [$Fe_2(CO)_6$-{μ-$(SCHPh)_2SiPh_2$}] (**3**) within one hour in 64% yield (Scheme 1). Complex **3** was characterized by ^{1}H, $^{13}C\{^1H\}$, HSQC, ^{1}H,^{1}H-COSY NMR spectroscopy, as well as by elemental analysis and mass spectrometry. Crystals suitable for single crystal X-ray analysis were obtained by cooling an acetonitrile solution of **3** to −20 °C. Complex **3** exhibits a typical [2Fe2S] core with a "butterfly arrangement", whereas the geometry around each iron atoms can be best described as a distorted square pyramidal supplemented by a Fe–Fe single bond (Fig. S2†). As reported for analogous complexes with a silane – as well as tin-functionalized dithiolate bridge the bond angles S–C–Si deviate strongly from the ideal angle of 109.45° (see values in Fig. S2†).[32–35,38]

Since it has recently been shown that the introduction of a bulky S-to-S linker together with an asymmetrical substitution with a bidentate phosphine could favor a "rotated state",[23,24] complex **3** was reacted with 1,2-bis(dimethylphosphino)ethane (dmpe) (Scheme 2). This reaction was performed in refluxing THF for 20 minutes and afforded three different products, [{$Fe_2(CO)_5${μ-$(SCHPh)_2SiPh_2$}}$_2$(μ-dmpe)] (**4**), [$Fe_2(CO)_5(\kappa^2$-dmpe)-{μ-$(SCHPh)_2SiPh_2$}] (**5**), [$Fe_2(CO)_5$(μ-dmpe){μ-$(SCHPh)_2SiPh_2$}] (**6**). The yields of each compound strongly depend on the reaction conditions (see Scheme 2 and experimental part). If one equivalent dmpe based on complex **3** is used in this reaction, compound **4** is observed as the main product in 17% yield, whereas **6** can be obtained in 3% yield and the chelated isomer **5** just in traces, observed as light purple band at the silica column chromatography of the crude product. Switching to two equivalents of dmpe based on complex **3** changes the yields dramatically. Isomer **6** is now observed as the main product with 35% and complex **5** with 7% yield. Compound **4** can just be obtained in traces, to be observed as a light red band at the column. Elongation of the reaction time decreases the yield of complex **5** to nearly 0%. All compounds were characterized by elemental analysis, IR, NMR spectroscopy and X-ray diffraction analysis (XRD). Red crystals of **4** and **6** suit-

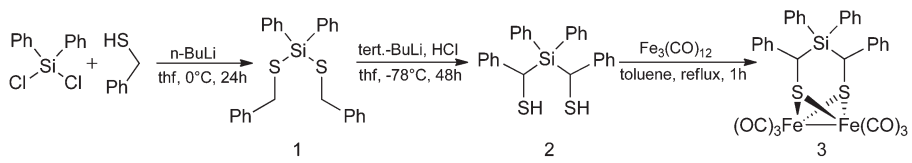

Scheme 1 Synthesis of *meso*-bis(benzylthio)diphenylsilane *via* double Wittig-rearrangement and complexation to afford **3**.

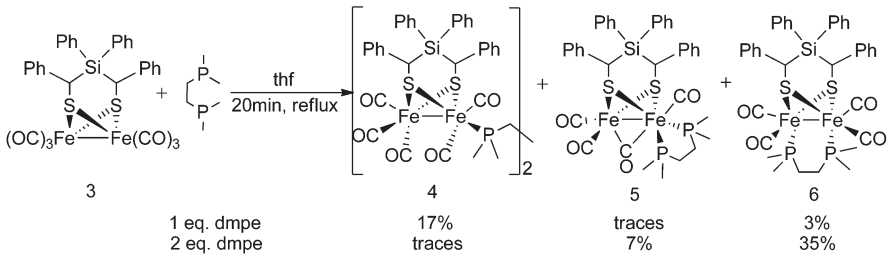

Scheme 2 Synthesis of dmpe-substituted complexes **4**, **5** and **6** in refluxing THF.

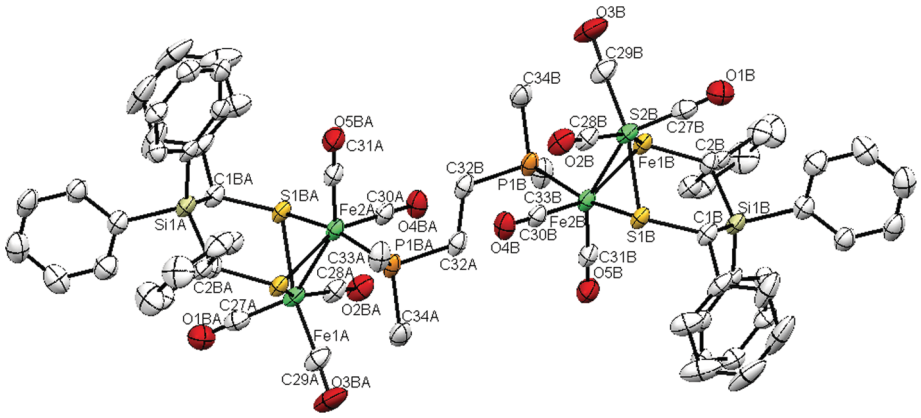

Fig. 2 Molecular structure of compound **4**, which is reduced to one of two independent dimer molecules in the unit cell with an inversion center localized at the C32A–C32B-bond. Hydrogens are omitted for clarity. Selected bond lengths [Å] and angles [°]: Fe1B–Fe2B 2.5526(12), Fe2B–P1B 2.2377(15), P1B–C32B 1.837(6), C32B–C32A 1.531(12), Fe1B–Fe2B–P1B 109.61(6), P1B–C32B–C32A 114.6(5).

able for XRD analysis were obtained by evaporation of a hexane solution at 20 °C (Fig. 2 and 3 right, respectively). Purple crystals of **5** were obtained by slow diffusion of *n*-pentane into a solution of **5** in toluene at 8 °C (Fig. 3 left).

Two crystallographically independent molecules of compound **4** are found in the triclinic unit cell. The molecular structure of **4** reveals that this species features two $\{Fe_2(CO)_5\{\mu\text{-}(SCHPh)_2SiPh_2\}_2\}$ moieties bridged by a dmpe ligand with an inversion center localized at the C32A–C32B-bond. Molecular structures of analogous compounds have been already reported.[36,39,40] It is, however, worth noting that in the case of **4** the phosphorus atoms of the diphosphine are bound in basal position while in other reported molecular structures an apical binding mode is observed.[9,39,40] Complexes **5** and **6** are two structural isomers that differ by the coordination mode of the bidentate ligand dmpe. The structure of **6** is very similar to those reported for analogous complexes.[36,40,41] As it is shown in Fig. 3, the structure reveals an eclipsed structure in the solid state unlike compound **5** and the dmpe is bridged in a dibasal position. The sterically bulky *meso*-bis(benzylthio)-diphenylsilane induces a slight distortion around the two iron atoms evidenced by a significant difference between the two angles C19–Fe2–Fe1 (145.52°) and C16–Fe1–Fe2 (157.15). The IR spectrum of **6** (Fig. 4) shows a typical set of four carbonyl bands at 1987 (s), 1950 (vs), 1917 (s) and 1899 cm^{-1} (m), which are similar to those in other reported complexes with such symmetry.[42–47] The $^{31}P\{^1H\}$ NMR spectrum reveals two singlets at 38.70 ppm and 32.58 ppm for the bridging dmpe ligand caused by the asymmetry of the complex. The ^1H NMR spectrum displays the expected signal group for a symmetrically bridged dmpe ligand.

Compound **5** features a semi-rotated coordination environment with a strongly distorted square pyramidal edge-shared $\{FeS_2(CO)_3\}$ group with respect to the $\{FeS_2(CO)P_2\}$ moiety. This coordination mode is locked and stabilized by a CO ligand in semi-bridging position. A close inspection of the molecular structure of **5** reveals that its conformation cannot be considered as fully rotated and should be better described as a trigonal bipyramid centered at Fe. An Addison τ parameter (the difference between S2–Fe1–C29 and S1–Fe1–C28 divided by 60) of 0.49 indicates that the structure of **5** is best described as an intermediate of a square-pyramidal and a trigonal bipyramidal geometry.[48] In contrast to the diiron complexes $[Fe_2(CO)_4(\kappa^2\text{-dmpe})\{\mu\text{-}(SCH_2)_2NBn\}]$ and $[Fe_2(CO)_4(\kappa^2\text{-dppv})\{\mu\text{-}(SCH_2)_2CEt_2\}]$, in which an Fe–H agostic interaction (2.750 Å)[23] was evidenced as a major structural feature for stabilizing a rotated structure,[24] compound **5** lacks such an agostic interaction. In complex **5** a Fe···H interatomic distance of 3.184 Å between the semi-rotated iron atom Fe1 and the closest hydrogen atom H20A is observed, that belongs to a phenyl ring bound to silicon (Fig. 3). However, this interatomic distance is too long to be considered as a Fe···H agostic inter-

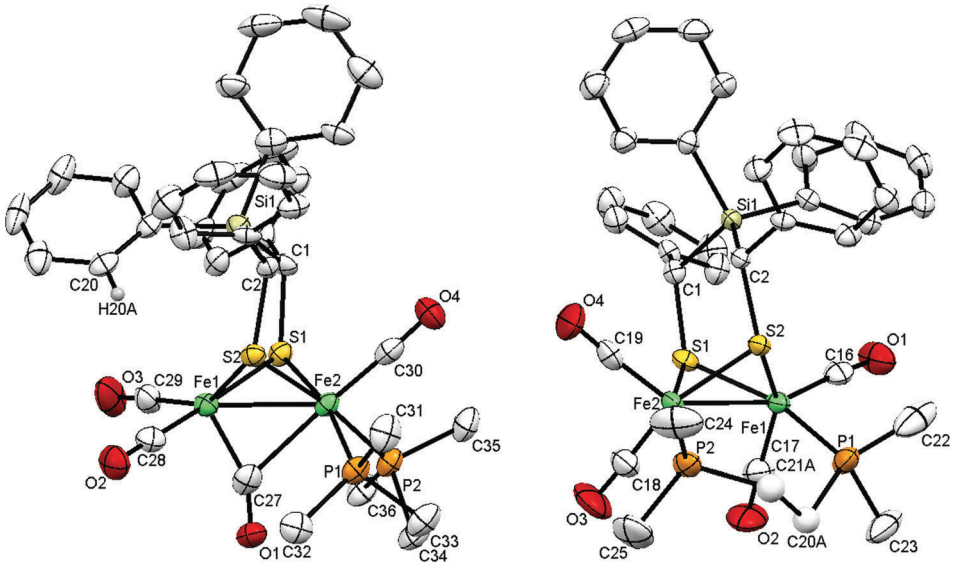

Fig. 3 Molecular structures of chelated isomer **5** (left) and bridged isomer **6** (right). Selected bond lengths [Å] and angles [°]: **5**: Fe1–Fe2 2.5450(15), Fe1–C27 1.789(9), Fe2–C27 2.379(9), Fe1–H20A 3.176. **6**: Fe1–Fe2 2.5238(7), Fe1–P1 2.2101(11), Fe2–P2 2.2174(11), Fe1–P1–C20A 118.9(2), Fe2–P2–C21A 117.7(3).

action and even as an Fe···H electrostatic interaction.[49] The IR spectra of compound **5** are shown in Fig. 4. In the IR spectrum recorded in the solid state a band at 1801 cm^{-1} indicates a bridging CO ligand constrained by crystal packing, while an unrotated conformation of **5** prevails in CH_2Cl_2 solution due to conformational freedom (CH_2Cl_2 was chosen due to the moderate solubility in more or less polar solvents), as only a weak bridging CO ligand stretch can be recognized at 1801 cm^{-1}. A typical set of carbonyl bands at 2007 (s), 1937 (s), 1903 (s) and 1801 cm^{-1} (m) is observed in solution, which are similar to those already reported for $[Fe_2(CO)_4(\kappa^2\text{-dmpe})\{\mu\text{-}(SCH_2)_2\text{-NBn}\}]$.[23] The $^{31}P\{^1H\}$ NMR spectrum reveals just one singlet at 63.13 ppm for the dmpe ligand, which indicates a dibasal coordination. The ^1H NMR spectrum displays the expected signal group for such a dmpe ligand substitution; a ^{13}C NMR spectrum could not be recorded due to poor resolution.

In order to rationalize experimental results, DFT calculations were performed and focused on the relative stability of $\mathbf{5}_{\mathbf{unrot}}$, $\mathbf{5}_{\mathbf{semirot}}$ and **6** (hereafter the subscript rot, semirot and unrot indicate the rotated, semirotated and non rotated isomers, respectively). The geometry optimizations at BP86/TZVP gas-phase level were carried out using molecular structures as starting point and converged $\mathbf{5}_{\mathbf{semirot}}$ to the fully rotated form $\mathbf{5}_{\mathbf{rot}}$. Complex $\mathbf{5}_{\mathbf{rot}}$ is 1.1 kcal mol^{-1} higher in energy as compared to **6**, which is also reflected in the yields of the reaction with dmpe (7% for **5** and 35% for **6**). The $\mathbf{5}_{\mathbf{unrot}}$ isomer as a transition state is 3.4 kcal mol^{-1} higher in energy. Upon optimization, the structure of **6** does not change significantly (Fe–Fe distance from 2.523 Å (XRD) to 2.563 Å (DFT); C–Fe–Fe–C dihedral angle from 23.8° (XRD) to 10.4° degree (DFT)). The optimized structure of $\mathbf{5}_{\mathbf{rot}}$ is much more interesting (Fig. 5) as it features a fully rotated state (dihedral angle from 87.1° to 106.3° degree; shorter Fe–μC distance from 2.385 Å to 2.201 Å) with a more symmetrical shape. The Fe···H interatomic distance of the hypothetical agostic interaction decreases to 2.903 Å (−0.281 Å compared to the molecular structure). These two structural features might suggest either that the interaction among the molecules in the crystal prevents the complete rotation of the $Fe(CO)_3$ group in $\mathbf{5}_{\mathbf{semirot}}$ or, in the light of experimental observations in solution (loss of rotated form) even the opposite effect, namely that removal of packing forces causes the rearrangement from $\mathbf{5}_{\mathbf{semirot}}$ to $\mathbf{5}_{\mathbf{unrot}}$. Moreover, the rotation allows a small rearrangement of the Si bidentate ligand and therefore the approaching of the iron and hydrogen atoms.

Starting from $\mathbf{5}_{\mathbf{unrot}}$ in CH_2Cl_2 solution the optimization converged to $\mathbf{5}_{\mathbf{rot}}$, as well as in the case of B3LYP and BP86/D3 dispersion corrected levels of theory. At BP86/D3 level, the $\mathbf{5}_{\mathbf{unrot}}$ form is not a stationary point on the PES (potential energy surface) and the geometry optimization converges to $\mathbf{5}_{\mathbf{rot}}$. In Table 1 are reported the $\mathbf{5}_{\mathbf{unrot}}/\mathbf{5}_{\mathbf{rot}}$ energy differences.

A closer inspection of the geometry optimization energy profile starting from the $\mathbf{5}_{\mathbf{unrot}}$ structure puts in evidence of a semirotated transition state structure similar to $\mathbf{5}_{\mathbf{semirot}}$ whose energy lies in the middle between $\mathbf{5}_{\mathbf{unrot}}$ and $\mathbf{5}_{\mathbf{rot}}$ (Fig. 6). In the calculated $\mathbf{5}_{\mathbf{semirot}}$ structure the C–Fe–Fe–C dihedral angle is 72.2°. Depending on the nature of the ligands, in the all-terminal CO form of hydrogenase model complexes this dihedral angle is small or even zero while in the rotated form this angle is at least larger than 90°. For example the simple $[Fe_2(CO)_6(\mu\text{-pdt})]$ (pdt = $S_2C_3H_6$; propane-1,3-dithiolato) complex exhibits a dihedral angle of 0° in the all-terminal CO form and this angle became 96° in the corresponding rotated form.[50,51] In **5** and **6** the dihedral angles are determined as 87.1° and 23.8°, respectively.

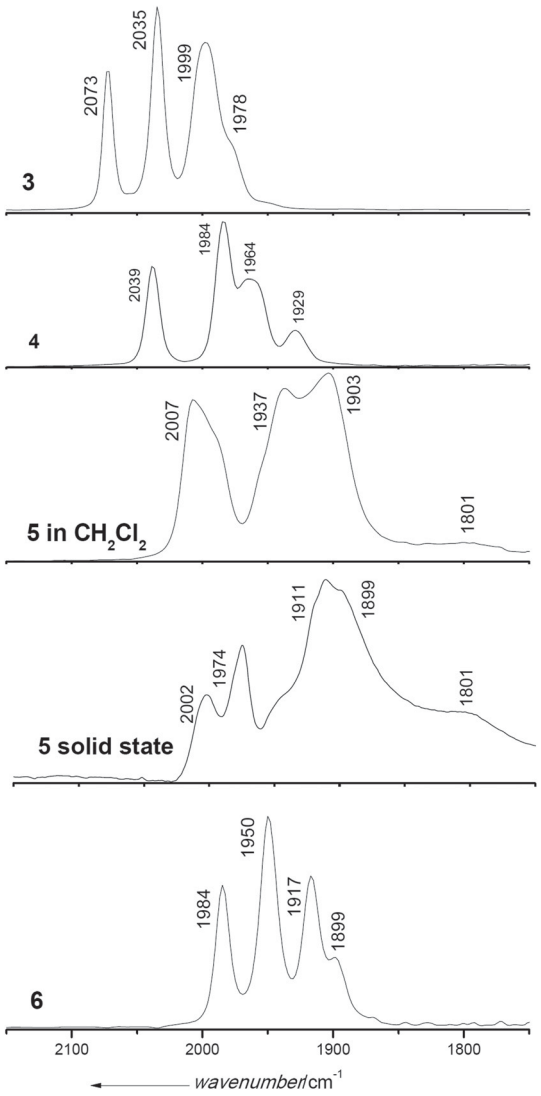

Fig. 4 FTIR spectra of the carbonyl stretching region for compounds **3**, **4**, **5** in CH_2Cl_2 and solid state and **6**.

A summary of the experimental IR spectra in CH_2Cl_2, solid state and the computed CO stretching mode frequencies for $\mathbf{5_{unrot}}$, $\mathbf{5_{semirot}}$ and $\mathbf{5_{rot}}$ are shown in Table 2. On average, the computed IR spectra for $\mathbf{5_{semirot}}$ and $\mathbf{5_{unrot}}$ are both in reasonable agreement with the experimental spectrum from CH_2Cl_2 solution, while the formation of $\mathbf{5_{rot}}$ can be ruled out.

These results highlight a discrepancy between experimental observations and topology of the DFT potential energy surface. To shed some light on such issue, we consider a number of simplified models of molecular systems under investigation. The idea is to probe the effect of each factor (*i.e.* bridgehead type/size and donor *vs.* acceptor coordination to a single Fe) separately. Therefore, starting from $[Fe_2(CO)_6(\mu\text{-pdt})]$ complex, we first substituted the two terminal equatorial CO with the dmpe ligand and then the propane dithiolato by the silicon based ligand. The $[Fe_2(CO)_6(\mu\text{-pdt})]$ complex has an all terminal energy minimum structure, while the rotated form $\mathbf{pdt_{rot}}$ is a transition state (free energy barrier 11.2 kcal mol^{-1}). As aforementioned, the structure of $[Fe_2(CO)_4(\kappa^2\text{-dmpe})(\mu\text{-pdt})]$ (**7**) has been considered (Fig. 7),[52] in which the silicon based pendant ligand, present in the original species **5**, is substituted with a propane dithiolato bridge. The rotation of the $Fe(CO)_3$ group is triggered by the dmpe ligand and the lowest energy isomer of **7** has one semi-bridging CO ligand ($\mathbf{7_{semirot}}$), while fully rotated and fully unrotated isomers $\mathbf{7_{rot}}$ and $\mathbf{7_{unrot}}$ are slightly higher in energy. The energy difference among the three isomers suggests that PES of **7** is extremely flat and this makes the case very complicated. Indeed the X-ray crystal structure of this species shows a full unrotated (eclipsed) geometry of diiron cluster;[52] our computations suggest that also other isomers might be energy accessible. The coordination around the Fe atom of the lowest energy isomer is similar to that of the $\mathbf{5_{semirot}}$. In this case the C–Fe–Fe–C dihedral angle is 50.2° (Fig. 8).

$\mathbf{7_{semirot}}$ was figured out as the most stable isomer at different levels of theory (except for COSMO computation in implicit CH_2Cl_2 solvent). In Table 3 are summarized the various results obtained.

The second simplified model, considered to investigate the effect of the bulk of the dithiolate bridgehead, is complex **3** and its rotated structure $\mathbf{3_{rot}}$, both sketched in Fig. 9. At the BP86 gas-phase level, the all terminal CO isomer $\mathbf{3_{unrot}}$ is the most stable form and the rotated isomer $\mathbf{3_{rot}}$ is a transition state 5.2 kcal mol^{-1} higher in energy. Compared with $[Fe_2(CO)_6(\mu\text{-pdt})]$ species, for which the energy difference between rotated and unrotated form is 8.8 kcal mol^{-1}, the same difference for complex **3** decreases by 3.6 kcal mol^{-1}.

Based purely upon DFT computations for simplified $\mathbf{pdt_{rot}}$ and $\mathbf{7_{rot}}$ models, we conclude that the dmpe ligand provides a large contribution toward stabilization of the rotated/semi-rotated form, while the bridgehead bulk/size plays an apparently minor role (although a measurable one).

In the crystal structure of **5** the distance from the Fe1 atom, which is in a semi-rotated environment, to the closest aromatic CH bond is too long to be considered even a remote agostic or anagostic interaction, *i.e.* endowed of purely electrostatic character (unlike stronger agostic interactions, having "2-electron-3-centers" character).[53,54] This is in close agreement with recent works suggesting that without a subtle stabilizing effect arising from a remote agostic interaction established intramolecularly, the full-rotated geometry is not favoured and semirotated structures, like in **5**, are observed.[23,24,36] Nevertheless, since DFT optimization of **5** (see Fig. 5 and preceding discussion) has shown a shortening of the interatomic Fe···H–C distance down to about 2.9 Å (*i.e.*, the upper limit reported for distances associated with anagostic interactions),[53] we have investigated computationally the effect(s) of the solvent (acetonitrile, implicit model) and of the dispersion (within DFT-D3 empirical dispersion correction for DFT calculations)[55] on the Fe···H–C distance. In Fig. 10 are reported the values of the Fe···H distance and of the Fe···H–C angle upon variation of the level of theory. If implicit solvatation is considered, the Fe···H distance decreases by 0.061 Å while the decrease is only

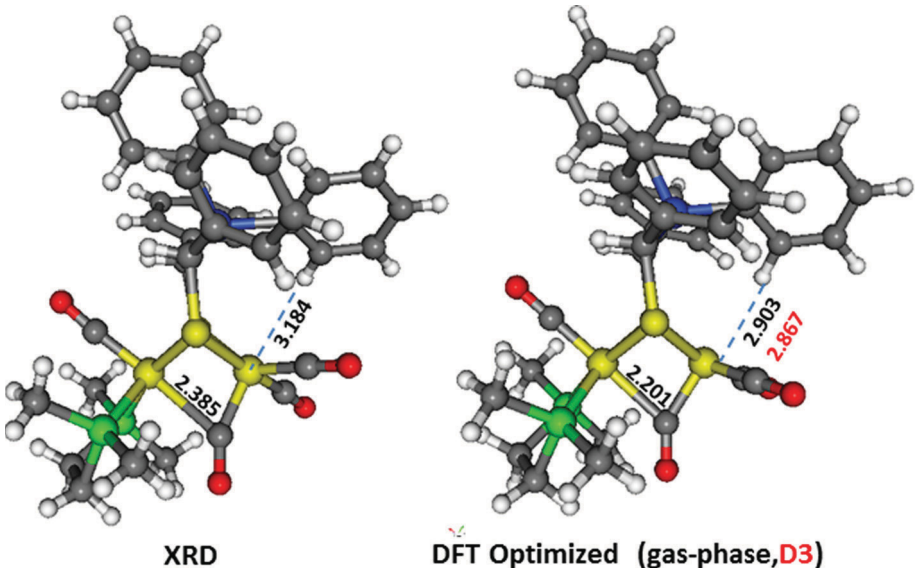

Fig. 5 Comparison of XRD molecular structure and DFT geometry optimized structures at BP86/TZVP gas-phase and D3 dispersion corrected (in red) level for complex **5**. Distances in Å.

Table 1 Total energy differences (in kcal mol^{-1}) between $\mathbf{5}_{unrot}$ and $\mathbf{5}_{rot}$ isomers as a function of the computational level

	BP86/gas-phase	BP86/CH_2Cl_2	BP86/D3	B3LYP/gas-phase
$\mathbf{5}_{unrot}$	+3.4	+5.2	→$\mathbf{5}_{rot}$	+3.9
$\mathbf{5}_{rot}$	0.0	0.0	0.0	0.0

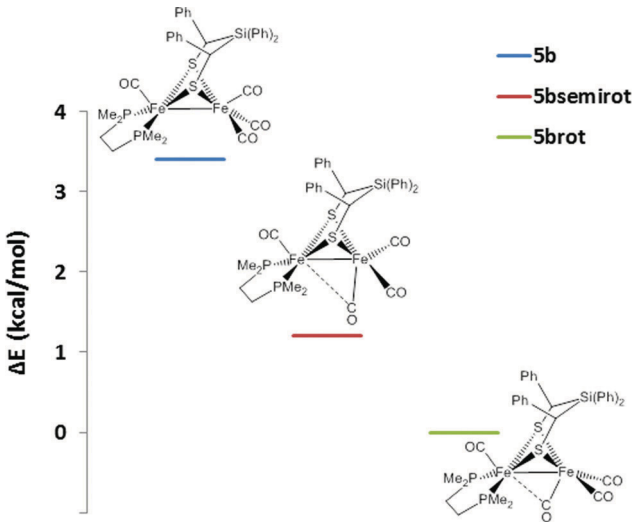

Fig. 6 Total energy differences (in kcal mol^{-1}) between $\mathbf{5}_{unrot}$, $\mathbf{5}_{semirot}$ and $\mathbf{5}_{rot}$.

0.024 Å when taking into account the dispersion. These results confirm that dispersion and solvent inclusion in the computational model do not alter significantly the original result obtained in gas phase conditions. They further suggest that, although an evident shortening of the Fe···H–C distance is observed in silico respect to the molecular structure (possibly due to neglecting packing force by the computational model) yet such value is still very close to the upper limit for agostic interactions. This also indicates that the boundaries between semi-rotated and full rotated structures may be governed by a weak but crucial effect.[23,24,36]

Table 2 Experimental and BP86/TZVP gas-phase computed CO stretching mode frequencies in cm^{-1} (theoretical intensities in km mol^{-1})

IR exp. (CH_2Cl_2 solution)	IR exp. (solid)	$\mathbf{5}_{unrot}$	$\mathbf{5}_{semirot}$	$\mathbf{5}_{rot}$
	1801			1778 (630)
1903	1910	1885 (498)	1903 (752)	1903 (491)
1937	1943	1944 (518)	1904 (391)	1940 (541)
1989	1974	1953 (632)	1953 (612)	1989 (909)
2008	2002	2008 (925)	2000 (788)	

Electrochemical studies of 3, 5 and 6

The cyclic voltammetry of **3** shows a quasi-reversible reduction at $E_{1/2}^{red} = -1.57$ V in CH_2Cl_2-[NBu_4][PF_6], (Fig. 11), at $E_{1/2}^{red1} = -1.43$ V in MeCN-[NBu_4][PF_6]. The comparison of the reduction potential of **3** with that of a Si-containing hexacarbonyl analogue ($E_{1/2}^{red} = -1.55$ V),[35] measured under identical experimental conditions in CH_2Cl_2-[NBu_4][PF_6], indicates that the electronic effects of the two Si-containing bridges are similar. Moreover, the scan rate dependence of the current function ($i_p^{red}/\nu^{1/2}$ C) of **3** follows the same trend as for the [$Fe_2(CO)_6${μ-(SCH_2)$_2$R}] (R = 1-silafluorenyl, $C_{12}H_8Si$) complex (ESI, Fig. S1†), which suggests that both compounds reduce according to similar mechanisms.[35] Thus, at slow scan rates, the reduction involves the transfer of two electrons according to the ECE process shown in Scheme 3.

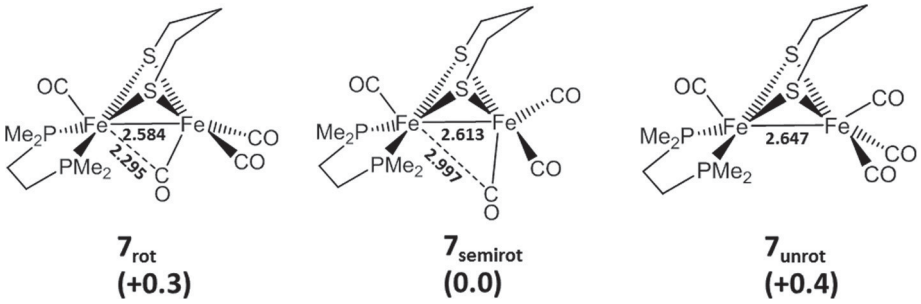

Fig. 7 DFT structures and energies of $[Fe_2(CO)_4](\kappa^2\text{-dmpe})\{\mu\text{-pdt}\}]$ isomers $\mathbf{7}_{rot}$, $\mathbf{7}_{semirot}$ and $\mathbf{7}_{unrot}$. Distances in Å, energy differences in kcal mol^{-1} with respect to $\mathbf{7}_{semirot}$.

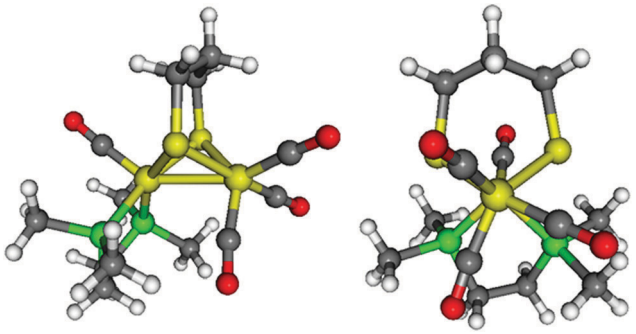

Fig. 8 DFT structure of $\mathbf{7}_{semirot}$. On the right is evidenced the partial rotation of the $Fe(CO)_3$ group with respect to the Fe(dmpe)CO group.

Table 3 Total energy differences (in kcal mol^{-1}) between $\mathbf{7}_{rot}$ and $\mathbf{7}_{semirot}$ as a function of the computational level

	BP86/ gas-phase	BP86/ CH_2Cl_2	BP86/ D3	B3LYP/ gas-phase
$\mathbf{7}_{rot}$	+0.3	0.0	+1.4	+1.1
$\mathbf{7}_{semirot}$	0.0	+0.8	0.0	0.0

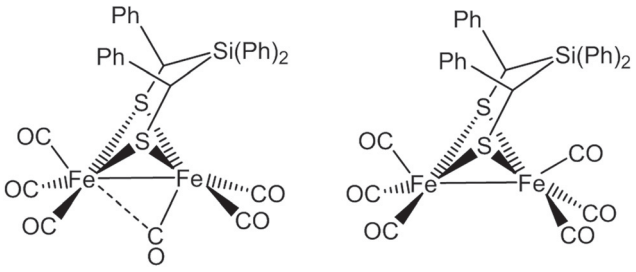

Fig. 9 Complex **3** (right) with its simplified considered rotated structure $\mathbf{3}_{rot}$ (left).

Upon raising the scan rate, the intervening chemical step is suppressed and the current measured at fast scan rates corresponds to the transfer of a single electron (ESI, Fig. S1†) at $E_{1/2}$ = −1.57 V (Fig. 11, ν = 5 V s^{-1}). The reduction of related diiron dithiolate complexes, either in a single two-electron EE process,[16,56–61] or according to an ECE mechanism generally results in the cleavage of a Fe–S bond and the shift of a CO group from a terminal to a bridging position.[32,35,62–68] In the present case, the large peak separation (ΔE_p) of the reduction at fast scan rates suggests that it is not entirely reversible electrochemically, so that some structure change might take place concomitantly with the electron transfer step.[63]

As expected, and in accordance with the IR data, the substitution of two COs by the dmpe ligand into the hexacarbonyl complex **3** shifts the reduction potential to more negative values, respectively 0.63 and 0.74 V for the chelated complex **5** (E_p^{red1} = −2.21 V in CH_2Cl_2-$[NBu_4][PF_6]$) and the bridged complex **6** (E_p^{red1} = −2.32 V in CH_2Cl_2-$[NBu_4][PF_6]$) (ESI, Fig. S2†).

Recently, it has been demonstrated that the electrochemical reduction of $[Fe_2(CO)_4(\kappa^2\text{-dmpe})\{\mu\text{-}(SCH_2)_2NBn\}]$,[36] as that of other chelated compounds $[Fe_2(CO)_4(\kappa^2\text{-dppe})(\mu\text{-}SCH_2XCH_2S)]$ (X = CH_2; N-^{i}Pr; N-Bn; N-$CH_2CH_2OCH_3$),[41] gives rise to an electron-transfer catalyzed (ETC) isomerisation to the bridged analogue. In the case of **5**, no ETC process could be detected. Indeed, while **6** reduces at E_p^{red1} = −2.14 V in MeCN-$[NBu_4][PF_6]$ (ESI, Fig. S3†), the irreversible reduction of **5** at E_p^{red1} = −2.00 V is followed by a second reduction at E_p^{red2} = −2.30 V, which indicates that the reduction of **5** does not generate the complex **6**. In contrast to the occurrence of an ETC isomerisation when the dmpe ligand is associated to the propanedithiolate bridge,[41] no such process is observed for **5**, which possesses a dithiolate Si-bridge. The way the S-to-S link may hinder the migration of one end of the diphosphine ligand from a metal center to the other is not presently understood.

Conclusion

In summary, we report on the reaction of complex **3** with one and two equivalents of dmpe, respectively, leading to the three different compounds **4**, **5** and **6**. The complexes were characterized by X-ray diffraction. The molecular structure of the $[Fe^IFe^I]$ hydrogenase model complex **5** shows that the introduction of the bidendate phosphine dmpe enforces a semi-rotated

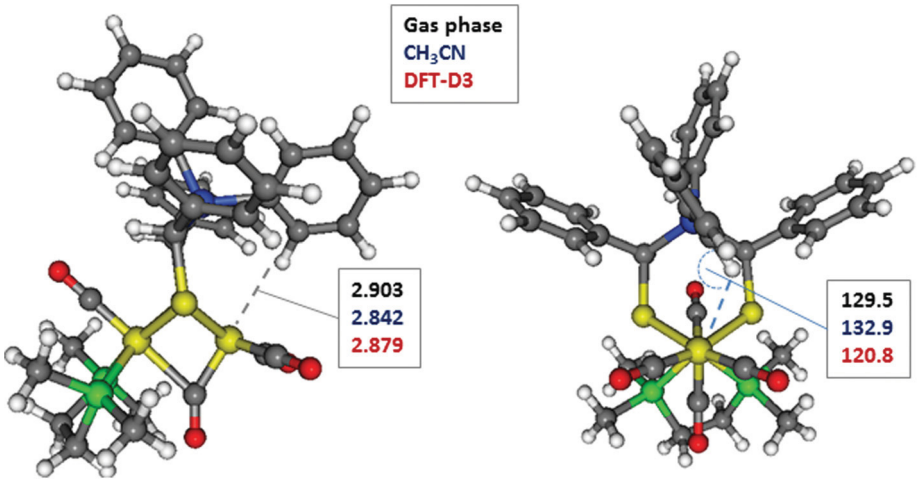

Fig. 10 Values observed computationally of the Fe···H distance (Å) and the Fe···H–C angle (°) upon variation of the level of theory for complex **5** (in black gas-phase level, in blue implicit CH_3CN COSMO solvatation, in red DFT using D3 dispersion correction).

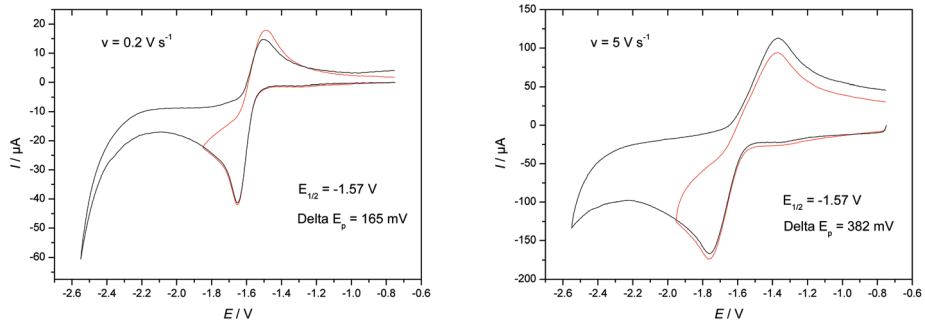

Fig. 11 Cyclic voltammetry of **3**, 0.9 mM in CH_2Cl_2-$[NBu_4][PF_6]$ (potentials are in V *vs.* Fc^+/Fc).

$$3 \underset{}{\overset{1e^-}{\rightleftharpoons}} 3^- \underset{k_b}{\overset{k_f}{\rightleftharpoons}} (3')^- \overset{1e^-}{\rightleftharpoons} (3')^{2-}$$

E1 = -1.57 V E2 ; E2 - E1 > 0

Scheme 3 Proposed ECE mechanism for the reduction of **3**.

conformation in solid state. The identification of this species with its structural features, along with DFT computations, supports the idea that in order to obtain a fully rotated geometry related to the active site of $[Fe^IFe^I]$ hydrogenase three factors are important: (a) asymmetrical coordination at the two iron atoms using a bidentate donor ligand, here dmpe, (b) a bulky dithiolato bridgehead, which promotes (c) a weak remote agostic Fe···H–C interaction. Indeed each of these three factors seems to be crucial for observing, in dithiolate models, a full-rotated geometry, as that existing in the [FeFe] hydrogenase cofactor. To date, when one of these factors is not conformed, only partially or semi-rotated structures of [FeFe] hydrogenase models like complex **5** have been observed.[14] On the other hand, a glance to the rotated state of the natural cofactor reveals that no type of agostic interaction is necessary to obtain the full-rotated geometry. The amino acid residues, which face the [2Fe2S] cluster and the [4Fe4S] cubane, are able to constrain the H-cluster itself in the full-rotated form.[69] Thus in nature, just (a) and (b) of the established factors are necessary, which suggests the importance of a sterical demanding environment around the diiron center of [FeFe] hydrogenase model complexes by dithiolato ligands to force a full-rotated geometry. With the herein reported complex **5**, we could show an example with the highest degree of rotation so far reported for $[Fe^IFe^I]$ hydrogenase models without any agostic interactions (Fe···H–C)[14] and enabling new approaches for the design of dithiolato bridgeheads to achieve a full-rotated geometry related to the active site of [Fe–Fe] hydrogenases without any type of H-bond interaction.

Acknowledgements

Financial support for this work was provided by the Deutsche Bundesstiftung Umwelt (to R. Goy) and the Studienstiftung des Deutschen Volkes, the Alexander-von-Humboldt foundation as well as the Fonds of the Chemical Industry (to U.-P. Apfel). We are grateful to Dr. F. Michaud for crystallographic measurements. The Centre National de la Recherche Scientifique (CNRS), the University of Brest and the University of Milano Bicocca are acknowledged for financial support.

Notes and references

1 C. Madden, M. D. Vaughn, I. Díez-Pérez, K. A. Brown, P. W. King, D. Gust, A. L. Moore and T. A. Moore, *J. Am. Chem. Soc.*, 2012, **134**, 1577–1582.
2 D. J. Evans and C. J. Pickett, *Chem. Soc. Rev.*, 2003, **32**, 268–275.
3 A. Volbeda and J. Fontecillacamps, *Coord. Chem. Rev.*, 2005, **249**, 1609–1619.
4 T. Liu and M. Y. Darensbourg, *J. Am. Chem. Soc.*, 2007, **129**, 7008–7009.
5 M. L. Singleton, N. Bhuvanesh, J. H. Reibenspies and M. Y. Darensbourg, *Angew. Chem., Int. Ed.*, 2008, **120**, 9634–9637.
6 M. L. Singleton, R. M. Jenkins, C. L. Klemashevich and M. Y. Darensbourg, *C. R. Chim.*, 2008, **11**, 861–874.
7 M. L. Singleton, N. Bhuvanesh, J. H. Reibenspies and M. Y. Darensbourg, *Angew. Chem., Int. Ed.*, 2008, **47**, 9492–9495.
8 J.-F. Capon, F. Gloaguen, F. Y. Pétillon, P. Schollhammer and J. Talarmin, *Coord. Chem. Rev.*, 2009, **253**, 1476–1494.
9 M. K. Harb, J. Windhager, A. Daraosheh, H. Görls, L. T. Lockett, N. Okumura, D. H. Evans, R. S. Glass, D. L. Lichtenberger, M. El-khateeb and W. Weigand, *Eur. J. Inorg. Chem.*, 2009, 3414–3420.
10 M. K. Harb, U.-P. Apfel, J. Kübel, H. Görls, G. A. N. Felton, T. Sakamoto, D. H. Evans, R. S. Glass, D. L. Lichtenberger, M. El-khateeb and W. Weigand, *Organometallics*, 2009, **28**, 6666–6675.
11 C. Tard and C. J. Pickett, *Chem. Rev.*, 2009, **109**, 2245–2274.
12 M. Y. Darensbourg and W. Weigand, *Eur. J. Inorg. Chem.*, 2011, 994–1004.
13 S. Tschierlei, S. Ott and R. Lomoth, *Energy Environ. Sci.*, 2011, **4**, 2340–2352.
14 C.-H. Hsieh, Ö. F. Erdem, S. D. Harman, M. L. Singleton, E. Reijerse, W. Lubitz, C. V. Popescu, J. H. Reibenspies, S. M. Brothers, M. B. Hall and M. Y. Darensbourg, *J. Am. Chem. Soc.*, 2012, **134**, 13089–13102.
15 N. Wang, M. Wang, L. Chen and L. Sun, *Dalton Trans.*, 2013, **42**, 12059–12071.
16 R. Trautwein, L. R. Almazahreh, H. Görls and W. Weigand, *Z. Anorg. Allg. Chem.*, 2013, **639**, 1512–1519.
17 T. R. Simmons, G. Berggren, M. Bacchi, M. Fontecave and V. Artero, *Coord. Chem. Rev.*, 2014, **270–271**, 127–150.
18 D. Zheng, M. Wang, L. Chen, N. Wang and L. Sun, *Inorg. Chem.*, 2014, **53**, 1555–1561.
19 B. J. Lemon and J. W. Peters, *Biochemistry*, 1999, **38**, 12969–12973.
20 A. S. Pandey, T. V. Harris, L. J. Giles, J. W. Peters and R. K. Szilagyi, *J. Am. Chem. Soc.*, 2008, **130**, 4533–4540.
21 Y. Nicolet, A. L. de Lacey, X. Vernède, V. M. Fernandez, E. C. Hatchikian and J. C. Fontecilla-Camps, *J. Am. Chem. Soc.*, 2001, **123**, 1596–1601.
22 A. L. De Lacey, V. M. Fernández, M. Rousset and R. Cammack, *Chem. Rev.*, 2007, **107**, 4304–4330.
23 S. Munery, J.-F. Capon, L. De Gioia, C. Elleouet, C. Greco, F. Y. Pétillon, P. Schollhammer, J. Talarmin and G. Zampella, *Chem. – Eur. J.*, 2013, **19**, 15458–15461.
24 W. Wang, T. B. Rauchfuss, C. E. Moore, A. L. Rheingold, L. De Gioia and G. Zampella, *Chem. – Eur. J.*, 2013, **19**, 15476–15479.
25 D. J. Crouthers, J. A. Denny, R. D. Bethel, D. G. Munoz and M. Y. Darensbourg, *Organometallics*, 2014, **33**, 4747–4755.
26 D. Zheng, M. Wang, L. Chen, N. Wang, M. Cheng and L. Sun, *Chem. Commun.*, 2014, **50**, 9255–9258.
27 A. Silakov, E. J. Reijerse, S. P. J. Albracht, E. C. Hatchikian and W. Lubitz, *J. Am. Chem. Soc.*, 2007, **129**, 11447–11458.
28 A. Adamska, A. Silakov, C. Lambertz, O. Rüdiger, T. Happe, E. Reijerse and W. Lubitz, *Angew. Chem., Int. Ed.*, 2012, **51**, 11458–11462.
29 A. Adamska-Venkatesh, D. Krawietz, J. Siebel, K. Weber, T. Happe, E. Reijerse and W. Lubitz, *J. Am. Chem. Soc.*, 2014, **136**, 11339–11346.
30 J. Esselborn, C. Lambertz, A. Adamska-Venkatesh, T. Simmons, G. Berggren, J. Noth, J. Siebel, A. Hemschemeier, V. Artero, E. Reijerse, M. Fontecave, W. Lubitz and T. Happe, *Nat. Chem. Biol.*, 2013, **9**, 607–609.
31 G. Berggren, A. Adamska, C. Lambertz, T. R. Simmons, J. Esselborn, M. Atta, S. Gambarelli, J.-M. Mouesca, E. Reijerse, W. Lubitz, T. Happe, V. Artero and M. Fontecave, *Nature*, 2013, **499**, 66–69.
32 U.-P. Apfel, D. Troegel, Y. Halpin, S. Tschierlei, U. Uhlemann, H. Görls, M. Schmitt, J. Popp, P. Dunne, M. Venkatesan, M. Coey, M. Rudolph, J. G. Vos, R. Tacke and W. Weigand, *Inorg. Chem.*, 2010, **49**, 10117–10132.
33 U.-P. Apfel, H. Görls, G. A. N. Felton, D. H. Evans, R. S. Glass, D. L. Lichtenberger and W. Weigand, *Helv. Chim. Acta*, 2012, **95**, 2168–2175.
34 U.-P. Apfel, Y. Halpin, H. Görls, J. G. Vos and W. Weigand, *Eur. J. Inorg. Chem.*, 2011, **2011**, 581–588.
35 R. Goy, U.-P. Apfel, C. Elleouet, D. Escudero, M. Elstner, H. Görls, J. Talarmin, P. Schollhammer, L. González and W. Weigand, *Eur. J. Inorg. Chem.*, 2013, 4466–4472.
36 L. De Gioia, C. Elleouet, S. Munery, F. Y. Pétillon, P. Schollhammer, J. Talarmin and G. Zampella, *Eur. J. Inorg. Chem.*, 2014, 3456–3461.
37 J. Zubieta, E. Block, G. Ofori-Okai and K. Tang, *Inorg. Chem.*, 1990, **29**, 4595–4597.
38 R. S. Glass, N. E. Gruhn, E. Lorance, M. S. Singh, N. Y. T. Stessman and U. I. Zakai, *Inorg. Chem.*, 2005, **44**, 5728–5737.
39 W. Gao, J. Ekström, J. Liu, C. Chen, L. Eriksson, L. Weng, B. Åkermark and L. Sun, *Inorg. Chem.*, 2007, **46**, 1981–1991.
40 J.-F. Capon, F. Gloaguen, F. Y. Pétillon, P. Schollhammer and J. Talarmin, *Eur. J. Inorg. Chem.*, 2008, 4671–4681.
41 S. Ezzaher, J.-F. Capon, F. Gloaguen, F. Y. Pétillon, P. Schollhammer and J. Talarmin, *Inorg. Chem.*, 2007, **46**, 9863–9872.
42 F. I. Adam, G. Hogarth and I. Richards, *J. Organomet. Chem.*, 2007, **692**, 3957–3968.

43 A. Tsuboyama, K. Kuge, M. Furugori, S. Okada, M. Hoshino and K. Ueno, *Inorg. Chem.*, 2007, **46**, 1992–2001.
44 F. I. Adam, G. Hogarth, S. E. Kabir and I. Richards, *C. R. Chim.*, 2008, **11**, 890–905.
45 N. Wang, M. Wang, T. Liu, P. Li, T. Zhang, M. Y. Darensbourg and L. Sun, *Inorg. Chem.*, 2008, **47**, 6948–6955.
46 S. Ghosh, G. Hogarth, N. Hollingsworth, K. B. Holt, I. Richards, M. G. Richmond, B. E. Sanchez and D. Unwin, *Dalton Trans.*, 2013, **42**, 6775–6792.
47 S. Ghosh, G. Hogarth, N. Hollingsworth, K. B. Holt, S. E. Kabir and B. E. Sanchez, *Chem. Commun.*, 2014, **50**, 945–947.
48 A. W. Addison, T. N. Rao, J. Reedijk, J. van Rijn and G. C. Verschoor, *J. Chem. Soc., Dalton Trans.*, 1984, 1349–1356.
49 M. Brookhart, M. L. H. Green and G. Parkin, *Proc. Natl. Acad. Sci. U. S. A.*, 2007, **104**, 6908–6914.
50 E. J. Lyon, I. P. Georgakaki, J. H. Reibenspies and M. Y. Darensbourg, *J. Am. Chem. Soc.*, 2001, **123**, 3268–3278.
51 L. Bertini, C. Greco, P. Fantucci and L. De Gioia, *Int. J. Quantum Chem.*, 2014, 1–11.
52 S. Ezzaher, J.-F. Capon, F. Gloaguen, N. Kervarec, F. Y. Pétillon, R. Pichon, P. Schollhammer and J. Talarmin, *C. R. Chim.*, 2008, **11**, 906–914.
53 D. Braga, F. Grepioni, E. Tedesco, K. Biradha and G. R. Desiraju, *Organometallics*, 1997, **16**, 1846–1856.
54 M. G. Derry Holaday, G. Tarafdar, A. Kumar, M. L. P. Reddy and A. Srinivasan, *Dalton Trans.*, 2014, **43**, 7699–7703.
55 S. Grimme, *J. Comput. Chem.*, 2004, **25**, 1463–1473.
56 D. T. Pierce and W. E. Geiger, *J. Am. Chem. Soc.*, 1992, **114**, 6063–6073.
57 F. A. Schultz, *J. Solid State Electrochem.*, 2011, **15**, 1833–1843.
58 R. L. Lord, F. A. Schultz and M.-H. Baik, *Inorg. Chem.*, 2010, **49**, 4611–4619.
59 D. Uhrhammer and F. A. Schultz, *J. Phys. Chem. A*, 2002, **106**, 11630–11636.
60 J. B. Fernandes, L. Q. Zhang and F. A. Schultz, *J. Electroanal. Chem. Interfacial Electrochem.*, 1991, **297**, 145–161.
61 D. H. Evans, *Chem. Rev.*, 2008, **108**, 2113–2144.
62 J.-F. Capon, F. Gloaguen, P. Schollhammer and J. Talarmin, *J. Electroanal. Chem.*, 2004, **566**, 241–247.
63 G. A. N. Felton, A. K. Vannucci, J. Chen, L. T. Lockett, N. Okumura, B. J. Petro, U. I. Zakai, D. H. Evans, R. S. Glass and D. L. Lichtenberger, *J. Am. Chem. Soc.*, 2007, **129**, 12521–12530.
64 J. Windhager, M. Rudolph, S. Bräutigam, H. Görls and W. Weigand, *Eur. J. Inorg. Chem.*, 2007, 2748–2760.
65 J.-F. Capon, S. Ezzaher, F. Gloaguen, F. Y. Pétillon, P. Schollhammer, J. Talarmin, T. J. Davin, J. E. McGrady and K. W. Muir, *New J. Chem.*, 2007, **31**, 2052–2064.
66 G. A. N. Felton, B. J. Petro, R. S. Glass, D. L. Lichtenberger and D. H. Evans, *J. Am. Chem. Soc.*, 2009, **131**, 11290–11291.
67 E. S. Donovan, G. S. Nichol and G. A. N. Felton, *J. Organomet. Chem.*, 2013, **726**, 9–13.
68 It must be noted that the uncompensated solution resistance certainly contributes to the large ΔE_p at fast scan rates.
69 A. R. Finkelmann, M. T. Stiebritz and M. Reiher, *Chem. Sci.*, 2014, **5**, 215–221.

A Sterically Stabilized Fe^{I}-Fe^{I} Semi-Rotated Conformation of [FeFe] Hydrogenase Subsite Model

Roman Goy, Luca Bertini, Catherine Elleouet, Helmar Görls, Giuseppe Zampella, Jean Talarmin, Luca De Gioia, Philippe Schollhammer, Ulf-Peter Apfel, Wolfgang Weigand

General Procedures: All reactions were performed under a dry nitrogen or argon atmosphere with standard Schlenk techniques. All solvents were dried and distilled according to standard methods prior to use. Infrared spectra were recorded with a Bruker Vertex 70 spectrometer. Preparative column chromatography was performed with silica gel (Fluka, Kieselgel 60). ^{1}H, ^{13}C, ^{31}P and ^{29}Si NMR spectra were obtained with either a BRUKER Avance 200, Avance 400 spectrometer or a Bruker AMX 400 spectrometer. Elemental analyses were performed with a Vario EL III CHNS analyzer from Elementar Analysensysteme GmbH. Mass spectra were measured with a FINNIGAN MAT SSQ710 instrument.

Structure Determinations: The intensity data for the compounds **2**, **3**, **4** and **5** were collected on a Nonius KappaCCD diffractometer using graphite-monochromated Mo-K_α radiation. Data were corrected for Lorentz and polarization effects; absorption was taken into account on a semi-empirical basis using multiple-scans[1-3] Measurements for compound **6** were carried out on an Oxford Diffraction X-Calibur-2 CDD diffractometer equipped with a jet cooler device. Graphite-monochromated Mo-K_α radiation (λ = 0.71073 Å) was used in this experiment. The structure was solved and refined by standard procedures.[4-6]

The structures were solved by direct methods (SHELXS[7]) and refined by full-matrix least squares techniques against Fo^2 (SHELXL-97 [26]). The hydrogen atoms bounded to the thiole-groups of **2** were located by difference Fourier synthesis and refined isotropically. All other hydrogen atoms were included at calculated positions with fixed thermal parameters. All non-disordered, non-hydrogen atoms were refined anisotropically.[7] Crystallographic data as well as structure solution and refinement details are summarized in Table S1.

Supporting Information available: Crystallographic data (excluding structure factors) has been deposited with the Cambridge Crystallographic Data Centre as supplementary publication CCDC-1028097 for **2**, CCDC-1028098 for **3**, CCDC-1028099 for **4**, CCDC-1028100 for **5** and CCDC-1028773 for **6**. Copies of the data can be obtained free of charge on application to CCDC, 12 Union Road, Cambridge CB2 1EZ, UK [E- mail: deposit@ccdc.cam.ac.uk].

Electrochemical Procedures: The electrochemical experiments were conducted under an inert atmosphere of nitrogen or argon. The preparation and purification of the supporting electrolyte ([NBu_4][PF_6]) was performed as described previously.[34] Cyclic voltammetry was performed in a three-electrode cell by using a radiometer potentiostat (PGSTAT 128N or μ-Autolab III) driven by the GPES software. The working electrode consisted of a vitreous carbon disk, which was polished on a felt tissue with alumina, thoroughly rinsed with water, and dried before each CV scan. The Ag/Ag^+ reference electrode was separated from the analyte by a CH_2Cl_2 – [NBu_4][PF_6] bridge. All the potentials are reported against the ferrocenium-ferrocene–couple; ferrocene was added as an internal standard at the end of the experiments.

Synthesis of Bis(benzylthio)diphenylsilane (2)

Benzylmercaptane (10 g, 0.08 mol) was dissolved in 100 mL THF and cooled to 0°C. Subsequently, 32.2 ml (0.08 mol) *n*-butyllithium (2.5 mol/L in hexane) were added dropwise. To this mixture, 10.1 g (0.04 mol) diphenyldichlorsilan were added slowly and the solution was stirred for additional 24 hours at room temperature, whereupon a white precipitate was formed. Afterwards the solution was cooled to -78°C and 50 mL (0.08 mol) *tert*-butyllithium (1.6 mol/L in pentane) was added. After 24 hours, the orange suspension was cooled to 0°C and acidified with 2N HCl to pH = 4. The organic solvents were removed under reduced pressure and the residue extracted three times with 100 mL of dichloromethane. The combined organic fractions were extracted with water, dried with sodium sulfate and evaporated to dryness. Crystallization from hexane afforded 10.5 g (61%) of **2** as white solid. Anal. calc. for $C_{26}H_{24}S_2Si$: C, 72.9 %; H, 5.6 %; S, 14.9 %. Found: C, 72.4 %; H, 5.7 %; S, 14.6 %. ^{1}H NMR (400 M*Hz*, $CDCl_3$, ppm): δ = 7.58-6.98 (20H, m, C$H_{aromatic}$), 3.89 (2H, d, J = 9.6 Hz, C*H*), 1.87 (2H, d, J = 9.6 Hz, S*H*). ^{13}C NMR (100 M*Hz*, $CDCl_3$, ppm): δ =141.7, 137.6, 130.6, 130.3, 128.7, 127.9, 127.7, 127.2, 126.1 (*C*$H_{aromatic}$), 26.4 (*C*H). *m*/*z* (DEI): 428 (M^+).

Synthesis of [$Fe_2(CO)_6$]{μ-$(SCHPh)_2SiPh_2$}] (3)

Bis(benzylthio)diphenylsilane (**2**) (200 mg, 0.47 mmol) and $Fe_3(CO)_{12}$ (239 mg, 0.47 mmol) were dissolved in 50 mL of toluene and stirred under reflux for one hour. Evaporation, purification via column chromatography (dichloromethane: hexane = 1:8) afforded 97 mg (64%) of a red crystalline solid. Anal. calc. for $C_{32}H_{22}S_2SiFe_2O_6$ + 0.9 hexane: C, 57.3 %; H, 4.4 %; S, 8.2 %. Found: C, 57.7 %; H, 4.0 %; S, 8.3 %. ^{1}H NMR (200 M*Hz*, $CDCl_3$, ppm): δ = 7.35 (20H, m, C$H_{aromatic}$), 3.59 (2H, s, C*H*). ^{13}C NMR (50 M*Hz*, $CDCl_3$, ppm): δ = 207.5, 206.7 (CO), 50 139.7, 139.0, 135.3, 133.7, 130.6, 130.2, 128.4, 128.1, 127.4, 126.4, 125.6 (*C*$H_{aromatic}$), 34.4 (*C*H). *m*/*z* (DEI): 706 (M^+), 650 (M-2CO), 622 (M-3CO), 594 (M-4CO), 566 (M-5CO), 538 (M-6CO). ν_{max}/cm^{-1} (CH_2Cl_2): 2073 (s), 2035 (s), 1999 (s), 1978 (s).

Synthesis of [{$Fe_2(CO)_5${μ-$(SCHPh)_2SiPh_2$}$_2$(μ-dmpe)] (4), [$Fe_2(CO)_5$(κ^2-dmpe){μ-$(SCHPh)_2SiPh_2$}] (5),. [$Fe_2(CO)_5$(μ-dmpe){μ-$(SCHPh)_2SiPh_2$}] (6).

Method A: A solution of [$Fe_2(CO)_6$){μ-$(SCHPh)_2SiPh_2$}] **3** (0.2 g, 0.28 mmol) and dmpe (0,049 mL, 0.283 mmol) in 50 mL of THF was refluxed for 25 min. After evaporation of the solvent, the residue was purified by column chromatography with a dichloromethane/hexane mixture, which afforded a red solution of **4** as first phase and a deep red solution of **6** as second phase. Compound **4** (40 mg, 19%) and **6** (7 mg, 3%) were obtained as red solids.

Method B: In a known procedure, a solution of [$Fe_2(CO)_6$){μ-$(SCHPh)_2SiPh_2$}] **3** (0.5 g, 0.71 mmol) and dmpe (0,24 mL, 1.42 mmol) in 100 mL of THF was refluxed for 25 min. After evaporation of the solvent, the residue was purified by column chromatography with dichloromethane/hexane mixture, which afforded red-purple solution of **5** as first phase and a deep red solution of **6** as second phase. Compound **5** (40 mg, 7%) was obtained as purple solid and **6** (199 mg, 35%) as red solid.

4: Anal. calc. for $C_{68}H_{60}S_2Si_2Fe_4O_{10}P_2$ + 1.0 hexane: C, 55.79 %; H, 4.68 %; S, 8.05 %. Found: C, 55.74 %; H, 4.46 %; S, 8.06 %. ^{1}H NMR (400 M*Hz*, $CDCl_3$, ppm): δ = 7.34-7.06 (40H, m, C$H_{aromatic}$), 3.63 (4H, m, C*H*), 1.99 (4H, s, CH_2), 1.48 (12H, m, CH_3). **^{31}P NMR** (161.9 M*Hz*, $CDCl_3$, ppm): δ = 36.87. ν_{max}/cm^{-1} (CH_2Cl_2): 2039 (m), 1984 (s), 1964 (m), 1929 (w).

5: Anal. calc. for $C_{36}H_{38}S_2SiFe_2O_4P_2$: C, 54.01 %; H, 4.78 %; S, 8.01 %. Found: C, 53.42 %; H, 4.87 %; S, 7.96 %. ^{1}H NMR (400 M*Hz*, $CDCl_3$, ppm): δ = 7.36-7.00 (20H, m, C$H_{aromatic}$), 3.80 (2H, m, C*H*), 1.98 (2H, m, CH_2), 1.86 (2H, m, CH_2), 1.57 (6H, m, CH_3), 1.27 (6H, m, CH_3). ^{31}P NMR (161.9 M*Hz*, $CDCl_3$, ppm): δ = 63.87. *m*/*z* (DEI) 800 (M^+), 744 (M-2CO), 716 (M-3CO), 688 (M-4CO). *m*/*z* (DEI): 800 (M^+), 744 (M-2CO), 688 (M-4CO). ν_{max}(CH_2Cl_2)/cm^{-1}: 2007, 1937, 1903. ν_{max}(solid state)/cm^{-1}: 2002 (s), 1974 (s), 1911 (s), 1899 (s), 1801 (w).

6: Anal. calc. for $C_{36}H_{38}S_2SiFe_2O_4P_2$ + 0.33 hexane: C, 55.02 %; H, 5.22 %; S, 7.73 %. Found: C, 55.04 %; H, 5.19 %; S, 7.73 %. ^{1}H NMR (400 M*Hz*, CD_2Cl_2, ppm): δ = 7.25-7.03 (20H, m, C$H_{aromatic}$), 3.68 (1H, s, C*H*), 3.47 (1H, m, C*H*) 1.93 (4H, m, CH_2), 1.57 (12H, m, CH_3). ^{31}P NMR (161.9 M*Hz*, CD_2Cl_2, ppm): δ = 38.69, 32.58. *m*/*z* (DEI): 800 (M^+), 744 (M-2CO). ν_{max}(CH_2Cl_2)/cm^{-1}: 1984 (m), 1950 (s), 1917 (m), 1899 (w).

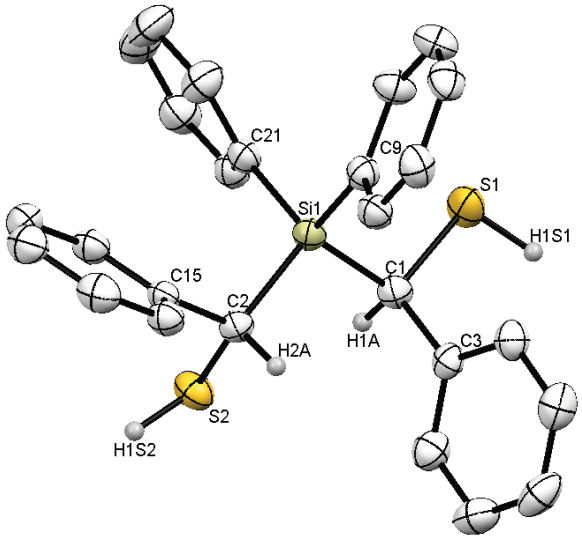

Fig. S1: Molecular structure of compound **2**. Aromatic hydrogens are omitted for clarity. Selected bond lengths [Å] and angles [°]: **2**: Si1-C1 1.899(2), Si1-C2 1.910(2), Si1-C9 1.867(2), Si1-C21 1.870(2), C1-S1 1.840(2), C2-S2 1.837(2), C1-Si1-C2 105.85(9), C1-Si1-C9 111.35(9), C2-Si1-C9 109.13(9), C2-Si1-C21 111.59(9).

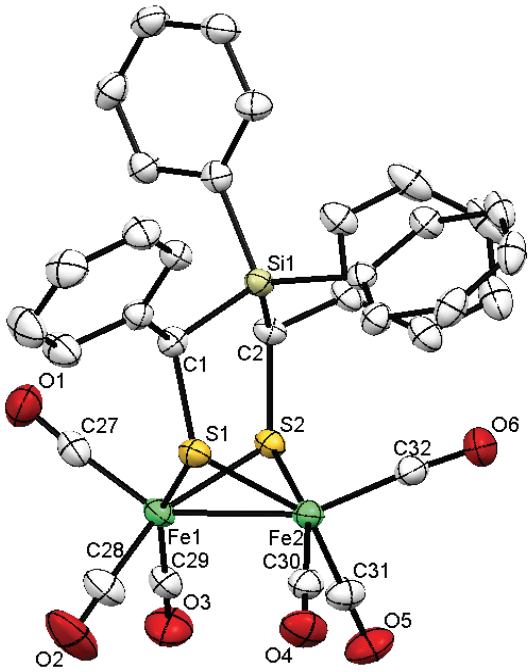

Fig. S2: Molecular structure of complex **3**. Aromatic hydrogens are omitted for clarity. Selected bond lengths [Å] and angles [°]: **3**: Fe1-Fe2 2.5123(6), Si1-C1-S1 113.06(15), Si1-C2-S2 120.21(14). C1-Si1-C2 105.63(12).

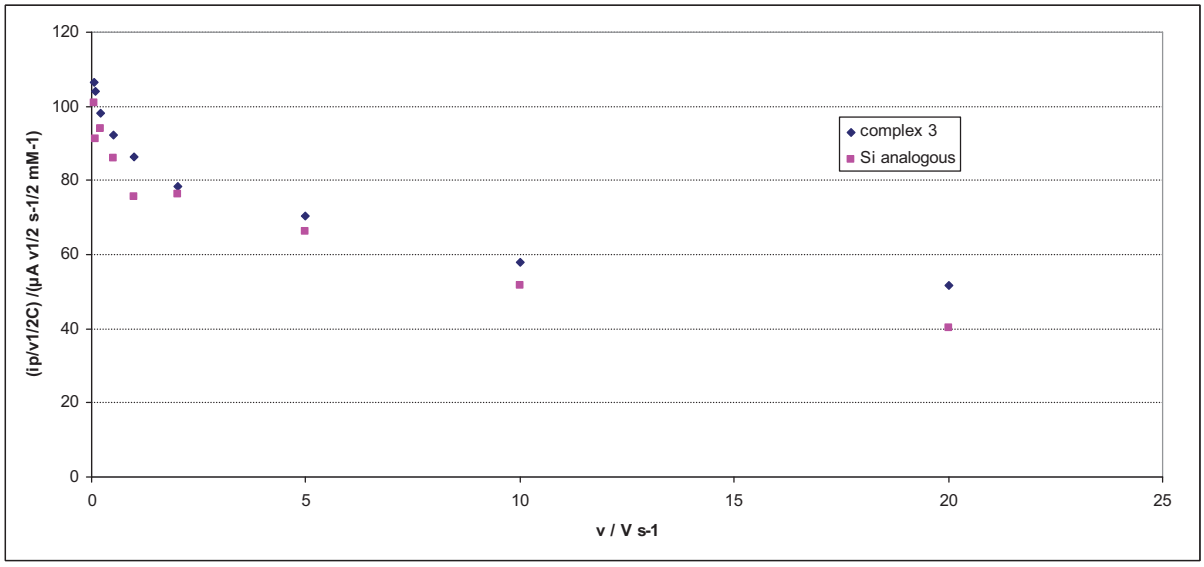

Figure S3 : Scan rate dependence of the current function ($i_p^{red}/ v^{1/2} C$) for the reduction of $[Fe_2(CO)_6\{\mu\text{-}(SCH_2)_2R\}]$ (R = 1-silafluorenyl, $C_{12}H_8Si$) (0.34 mM, 🕘) and for the reduction of **3** (0.91 mM, 🕘) in CH_2Cl_2-$[NBu_4][PF_6]$ (potentials are in V vs Fc^+/Fc).

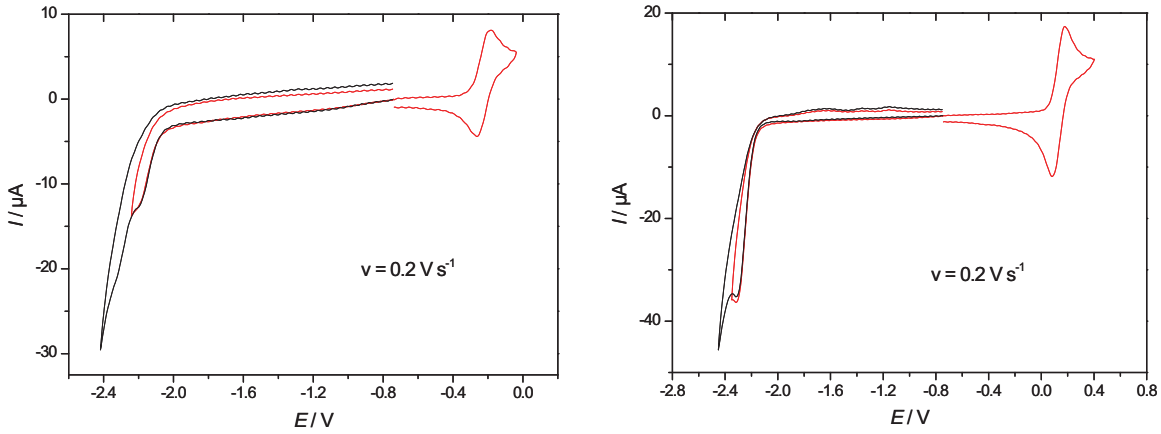

Figure S4: Cyclic voltammetry of **5**, 0.52 mM (left) and **6**, 0.71 mM (right) in CH_2Cl_2-$[NBu_4][PF_6]$ (v = 0.2 V s^{-1}; potentials are in V vs Fc^+/Fc).

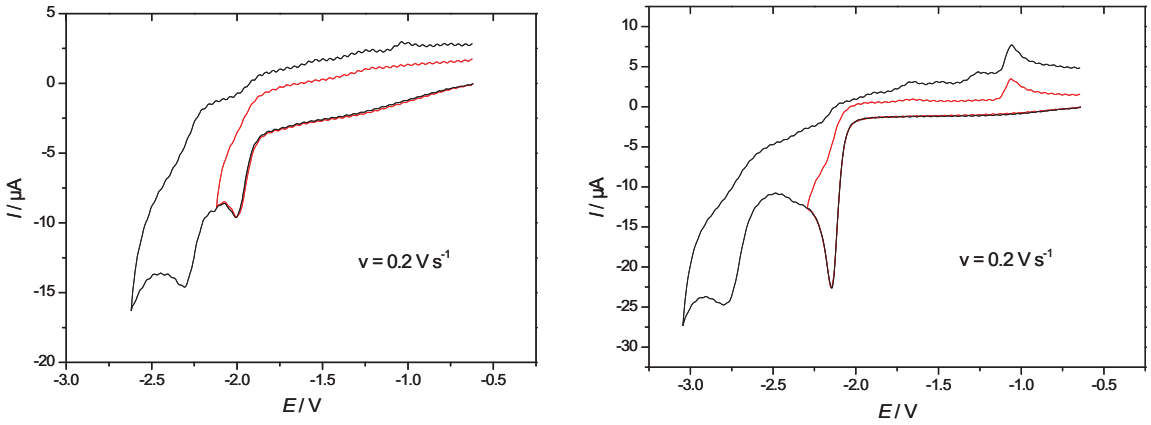

Figure S5 Cyclic voltammetry of **5**, 0.40 mM (left) and **6**, 0.44 mM (right) in MeCN-[NBu_4][PF_6] (v = 0.2 V s^{-1}; potentials are in V vs Fc^+/Fc).

Table S1: Crystal data and refinement details for the X-ray structure determinations of the compounds **2 - 6.**

Compound	**2**	**3**	**4**	**5**	**6**
formula	$C_{26}H_{24}S_2Si$	$C_{32}H_{22}Fe_2O_6S_2Si$	$C_{68}H_{60}Fe_4O_{10}P_2SSi_2$, $2H_2O$	$C_{36}H_{38}Fe_2O_4P_2S_2Si$	$C_{36}H_{38}Fe_2O_4P_2S_2Si$
fw ($g \cdot mol^{-1}$)	428.66	706.41	1542.95	800.51	800.51
T/°C	-90(2)	-90(2)	-140(2)	-140(2)	-103(2)
crystal system	monoclinic	monoclinic	triclinic	monoclinic	monoclinic
space group	P 2_1/n	P 2_1	P $\bar{1}$	P 2_1/n	P 2_1/c
a/ Å	12.5725(7)	8.9705(2)	11.1625(2)	9.4944(5)	11.4702(5)
b/ Å	10.0053(3)	13.1314(5)	17.4213(5)	28.8784(16)	11.9426(5)
c/ Å	18.5969(9)	12.9610(5)	19.7848(5)	13.4812(7)	29.2444(14)
α/°	90	90	98.998(2)	90	90
β/°	105.747(2)	92.088(2)	100.977(2)	91.570(3)	94.382(4)
γ/°	90	90	102.728(2)	90	90
V/Å^3	2251.54(18)	1525.73(9)	3604.34(15)	3694.9(3)	3994.3(3)
Z	4	2	2	4	4
ρ ($g \cdot cm^{-3}$)	1.265	1.538	1.422	1.439	1.472
μ (cm^{-1})	3	11.71	10.4	10.55	11.13
measured data	14761	10977	21863	27814	30116
data with I > 2σ(I)	3153	5518	12708	4716	8162
unique data (R_{int})	5130/0.0732	6369/0.0316	15488/0.0293	6956/0.0898	8162/0.0604
wR_2 (all data, on F^2)[a)]	0.1074	0.0714	0.1582	0.1849	0.1068
R_1 ($I > 2\sigma(I)$) [a)]	0.0455	0.0328	0.0776	0.0919	0.0482
S [b)]	0.973	1.017	1.281	1.116	0.938
Res. dens./e·Å^{-3}	0.540/-0.252	0.296/-0.248	1.393/-0.490	0.703/-0.518	0.858/-0.630
Flack-parameter	-	-0.030(11)	-	-	-
absorpt method	multi-scan	multi-scan	multi-scan	multi-scan	Multi-scan
absorpt corr $T_{min}/_{max}$	0.7235/0.7640	0.6892/0.7464	0.6270/0.7456	0.5927/0.7456	0.8509/0.8969
CCDC No.	1028097	1028098	1028099	1028100	1028773

[a)] Definition of the *R* indices: $R_1 = (\Sigma \,||F_o| - |F_c||)/\Sigma |F_o|$; $wR_2 = \{\Sigma[w(F_o^2-F_c^2)^2]/\Sigma[w(F_o^2)^2]\}^{1/2}$ with $w^{-1} = \sigma^2(F_o^2) + (aP)^2+bP$; $P = [2F_c^2 + Max(F_O^2]/3$;
[b)] $s = \{\Sigma[w(F_o^2-F_c^2)^2]/(N_o-N_p)\}^{1/2}$

Notes and references

1. COLLECT, Data Collection Software; Nonius B.V., Netherlands, **1998**.
2. „Processing of X-Ray Diffraction Data Collected in Oscillation Mode“:Otwinowski, Z.; Minor, W. in Carter, C. W.; Sweet, R. M. (eds.): *Methods in Enzymology, Vol. 276, Macromolecular Crystallography, Part A*, pp. 307-326, Academic Press **1997**.
3. SADABS 2.10, Bruker-AXS inc., 2002, Madison, WI, U.S.A
4. Sheldrick, G.M. *Acta Cryst.Sec.***2008**, *A64*, 112-122.
5. Altomare, A.; Cascarano, G.; Giacovazzo, C.; Guagliardi, A. *J.Appl.Cryst.***1993**, *26*, 343-350.
6. Farrugia, L.J. *J.Appl.Cryst.***1999**, *32*, 837-838.
7. Sheldrick, G. M. *Acta Cryst.* (2008). **A64**, 112-122.

4.3 **[RG3]**

Silicon-Heteroaromatic [FeFe] Hydrogenase Model Complexes: Insight into Protonation, Electrochemical Properties and Molecular Structures

Roman Goy[1], Luca Bertini[2], Helmar Görls[3], Giuseppe Zampella[2], Jean Talarmin[4], Luca De Gioia[2], Philippe Schollhammer[4], Wolfgang Weigand[5]

Chemistry – A European Journal **2015**, *21*, 5061-5073.

In this publication the synthesis and comprehensive characterization of a series of [FeFe] hydrogenase model complexes were discussed in detail. Four different complexes containing bulky Si-heteroaromatic systems (the *1*-silafluorene, *10,10'*-phenoxsilane and *10,10'*-phenothiasilane system) and the carbon analogue *9*-fluorene system at the dithiolate moiety as photosensitizers, were investigated, respectively. CO substitution was performed with the *all*-CO model complexes to afford their *mono*-PPh_3 substituted derivatives. Cyclic voltammetry experiments offered, that the $[Fe_2S_2(CO)_5PPh_3]$ complexes are not very stable under reductive conditions (PPh_3 cleavage). Nevertheless, the PPh_3 ligand increases the steric hindrance in proximity of the Fe-Fe bond region to favor different protonation sites and concomitantly increase the basicity of the diiron cluster. Extensive CV experiments with followed IR spectroscopy offered the μ-S atoms in these complexes as possible protonation sites. Advanced theoretical calculations are in line with these protonation experiments and further elucidate the different structural characteristics of the complex series by the different sterical bulk of the dithiolate bridgeheads. This further clarify that no orbital-based features of the complex series are at the origin of the structural differences. In particular it was shown that small changes in the (hetero)-aromatic system can cause large differences in the molecular structures. Unfortunately, *mono*-PPh_3 substituted derivatives can now be precluded from the use as photocatalysts, because it is not clear, which is the catalytic active species after the cleavage of the PPh_3 ligand. Because of the high amount of results discussed, photocatalytic hydrogen evolution experiments were not performed within this work.

ChemPubSoc Europe

DOI: 10.1002/chem.201406087

CHEMISTRY A European Journal Full Paper

Enzyme Models

Silicon–Heteroaromatic [FeFe] Hydrogenase Model Complexes: Insight into Protonation, Electrochemical Properties, and Molecular Structures

Roman Goy,[a] Luca Bertini,*[b] Helmar Görls,[a] Luca De Gioia,[b] Jean Talarmin,*[c] Giuseppe Zampella,*[b] Philippe Schollhammer,*[c] and Wolfgang Weigand*[a, d]

Dedicated to Professor Christian Robl on the occasion of his 60th birthday

Abstract: To learn from Nature how to create an efficient hydrogen-producing catalyst, much attention has been paid to the investigation of structural and functional biomimics of the active site of [FeFe]-hydrogenase. To understand their catalytic activities, the μ-S atoms of the dithiolate bridge have been considered as possible basic sites during the catalytic processes. For this reason, a series of [FeFe]-H_2ase mimics have been synthesized and characterized. Different [FeFe]-hydrogenase model complexes containing bulky Si–heteroaromatic systems or fluorene directly attached to the dithiolate moiety as well as their mono-PPh_3-substituted derivatives have been prepared and investigated in detail by spectroscopic, electrochemical, X-ray diffraction, and computational methods. The assembly of the herein reported series of complexes shows that the μ-S atoms can be a favored basic site in the catalytic process. Small changes in the (hetero)-aromatic system of the dithiolate moiety are responsible for large differences in their structures. This was elucidated in detail by DFT calculations, which were consistent with the experimental results.

Introduction

Since the structure of the active site of [FeFe]-hydrogenase was determined, much consideration has been paid to the characterization of structurally and functionally modified model complexes.[1–15] In the course of this, one of the challenging issues is to elucidate the mechanism of the catalytic hydrogen production by figuring out which heteroatom of the diiron substrate might act as a favorable internal basic site in the cleavage of dihydrogen.[9,16–19] The protonation of model complexes bearing a pdt- or adt-bridge (pdt = 1,3-propanedithiolato, adt = 2-azapropanedithiolato), especially their highly substituted analogues at the FeFe center, and their catalytic properties for electrochemical proton reduction are well studied.[17–25] In this context, the μ-S atoms of the dithiolate bridge have been considered as possible basic sites in the catalytic reaction that could hold the proton that combines with the hydride, or accept the proton during the heterolytic formation and cleavage of dihydrogen, respectively.[18,19,24,26,27] Examples for protonation of the thiolato sulfur atoms in model complexes are, however, limited to very few examples.[18,19,24,26–28]

Since we reported on the μ-S-protonation of a silicon-containing [FeFe]-hydrogenase model complex,[28] as well as on photocatalytic proton reduction by using a complex containing a bulky Si-heteroaromatic system at the dithiolate moiety, we were interested to have a more detailed insight into the protophilic properties of the photocatalytically active [2Fe2S(Si)] complexes for a better comprehension of mechanistic processes.[29]

In continuation of our research on silicon-containing [FeFe]-H_2ase mimics,[28–32] a series of complexes (Scheme 1) containing different substituents L (L = CO, PPh_3) as well as different heteroatoms X (X = C, Si) and Y (Y = O, S), respectively, in the heteroaromatic moiety, were prepared. Investigation of their protonation processes was developed in the presence of

[a] R. Goy, Dr. H. Görls, Prof. Dr. W. Weigand
Institut für Anorganische und Analytische Chemie
Friedrich-Schiller-Universität
Humboldtstraße 8, 07743 Jena (Germany)
Fax: (+49) 3641-948102
E-mail: wolfgang.weigand@uni-jena.de

[b] Dr. L. Bertini, Prof. Dr. L. De Gioia, Dr. G. Zampella
Department of Biotechnology and Biosciences
University of Milano-Bicocca
20126 Milan (Italy)
E-mail: luca.bertini@unimib.it
giuseppe.zampella@unimib.it
Homepage: http://www.unimib.it

[c] Dr. J. Talarmin, Prof. Dr. P. Schollhammer
Chimie, Electrochimie Moléculaires et Chimie Analytique
Université de Bretagne Occidentale
6 Avenue Victor le Gorgeu
CS93837, 29238 Brest cedex 3 (France)
E-mail: jean.talarmin@univ-brest.fr
philippe.schollhammer@univ-brest.fr
Homepage: http://www.univ-brest.fr

[d] Prof. Dr. W. Weigand
Jena Center for Soft Matter (JCSM)
Philosophenweg 7, 07743 Jena (Germany)

Supporting information for this article is available on the WWW under http://dx.doi.org/10.1002/chem.201406087.

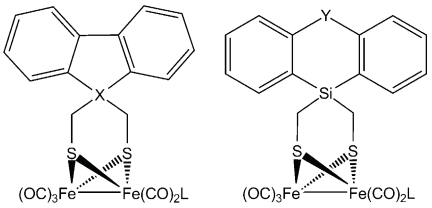

3 X= Si, L=CO
3a X= Si, L=PPh_3
7 X= C, L=CO
7a X= C, L=PPh_3
9 Y= O, L=CO
9a Y= O, L=PPh_3
12 Y= S, L=CO
12a Y= S, L=PPh_3

Scheme 1. Prepared [FeFe]-hydrogenase model complexes.

different amounts of several acids like trifluoroacetic acid (TFA), triflic acid (TfOH), and tetrafluoroboric acid (HBF_4) by spectroscopic (IR, NMR) and electrochemical (cyclic voltammetry) techniques, as well as computational studies.

Results and Discussion

The compounds were prepared according to Scheme 2, whereas the synthesis of **3** was already described.[29] To afford the carbon analogue complex **7**, fluorene was treated with paraformaldehyde and NaOEt[33] and the resulting 9,9′-bis(hydroxymethyl)fluorene was tosylated to get **5**. Subsequent reaction with $Na_2S{\cdot}9H_2O$ and sulfur according to Eliel et al.[34] yielded the spiro(1,2-dithiolane-4,9′-fluorene) as a yellow solid. The treatment of **6** with $[Fe_3(CO)_{12}]$ in THF heated at reflux gave the [FeFe]-H_2ase mimic **7** as a red-crystalline solid. Bis(2-bromophenyl)sulfane was synthesized according to Li et al. by treatment of 1-bromo-2-iodobenzene with $Na_2S{\cdot}9H_2O$, CuI, and K_2CO_3.[35] In a similar reaction, 10,10′-bis(chloromethyl)-phenoxsilane **8** and 10,10′-bis(chloromethyl)phenothiasilane **11** were obtained by the treatment of diphenyl ether and **10** with *n*-BuLi and bis(chloromethyl)dichlorsilan, respectively. Subsequent treatment of **8** and **11** with $[Fe_2(CO)_6(\mu\text{-}S_2)]$ according to known procedures gave the [FeFe]-H_2ase mimics **9** and **12**. To prepare the mono-substituted compounds **3a**, **7a**, **9a**, and **12a**, complexes **3**, **7**, **9**, and **12** were dissolved in anhydrous acetonitrile and treated with trimethylamine *N*-oxide and PPh_3. Column chromatography afforded **3a**, **7a**, **9a**, and **12a** as dark-red solids in good yields. All compounds were characterized by using IR, ^1H, $^{13}C\{^1H\}$, $^{31}P\{^1H\}$, and ^{29}Si NMR spectroscopy, MS, and HRMS, as well as elemental analysis, cyclic voltammetry, and X-ray diffraction analysis (Figure 1).

The molecular structures of **3** and **7** have been studied by XRD experiments (Figure 1) and DFT geometry optimizations (BP86/TZVP, gas phase) (Table 1); they show a characteristic [2Fe2S] butterfly core. As reported before, the silicon atom in **3** exhibits a typical tetrahedral geometry. It is worth noting that the structure of **3** is more symmetric (almost C_{2v}) than that of its carbon analogue **7**. The structure of **3** is best described as a half-chair conformation adopted by the bridging dithiolato ligand, which is very similar to that proposed for the transition state involved in the FeS_2C_3 six-membered ring chair/boat flipping process operative in $[Fe_2(CO)_6(\mu\text{-pdt})]$.[36] The replacement of the silafluorene by a fluorene group induces a more usual conformation of the bridging dithiolato ligand, which corresponds to the energy minimum structure of $[Fe_2(CO)_6(\mu\text{-pdt})]$.[37] The main structural features of the complexes **3** and **7** are reported in Table 1, together with those of $[Fe_2(CO)_6(\mu\text{-pdt})]$ for comparison.[37,38]

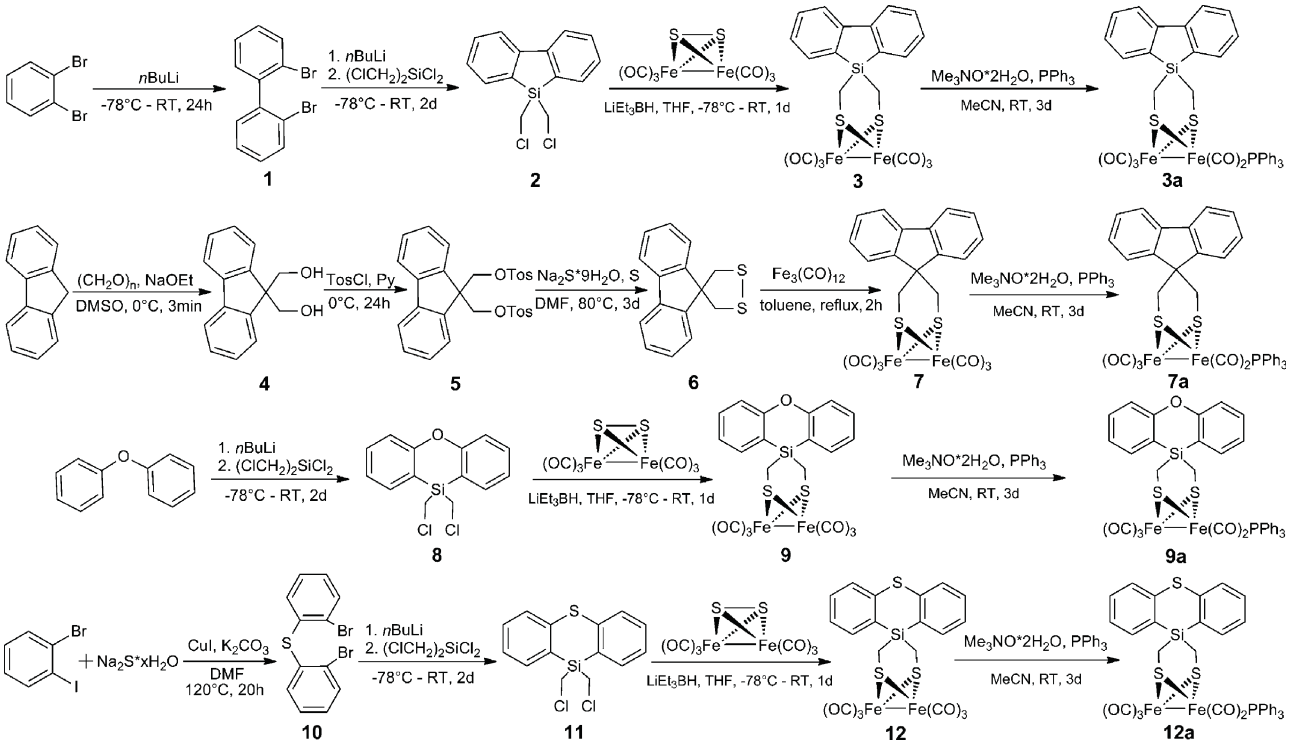

Scheme 2. Synthetic pathways for compounds **1**–**12a**.[29]

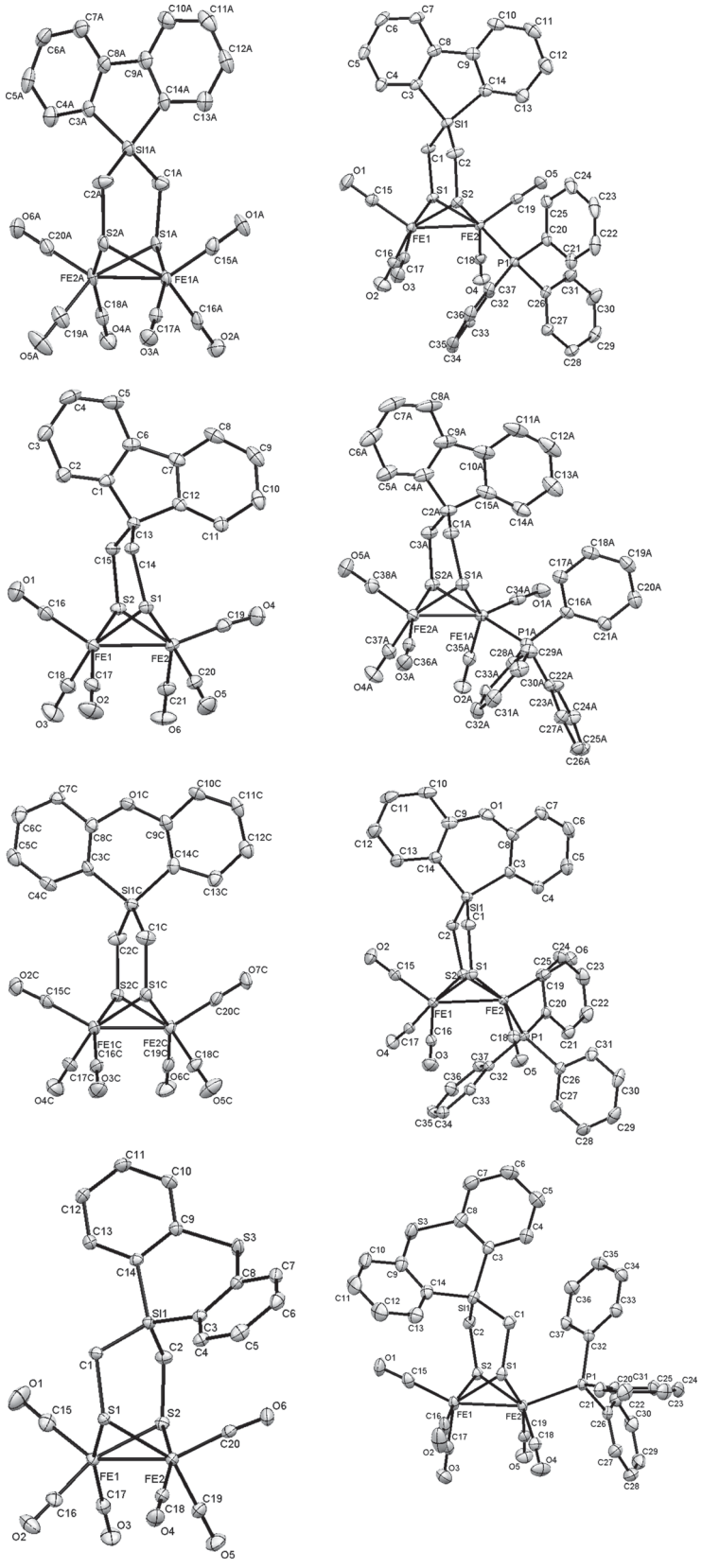

Figure 1. ORTEP views of **3**/**3a** (first row), **7**/**7a** (second row), **9**/**9a** (third row), and **12**/**12a** (fourth row). Ellipsoids at the 50% probability level.[29] Hydrogen atoms are omitted for clarity. Selected bond lengths and angles are listed in the Supporting Information.

In particular, δ is the dihedral angle C-Fe-Fe-C that defines the rotation of one $[Fe(CO)_3]$ group with respect to the other (see a view down the Fe–Fe bond axis of molecular structures in the Supporting Information, Figures S1 and S2), whereas the two S-C-X-C dihedral angles (X = Si, C) indicate the distortion of the dithiolato ligand. In the case of $[Fe_2(CO)_6(\mu\text{-pdt})]$, considered as a reference, the S-C-C-C dihedral angle is determined as 127.2° in the energy minimum structure, whereas the angle is 180° in the half-twist conformation (transition state of the chair/boat flipping).

In **3**, the two S-C-Si-C dihedral angles are close to 180°, as expected for a half-chair conformation, and a slight distortion between the two iron groups is observed ($\delta = 10.6°$). In **7**, the two torsion angles S-C-C-C are closer to those observed in $[Fe_2(CO)_6(\mu\text{-pdt})]$, but the distortion between the two iron moieties is larger ($\delta = 21.5°$). In this case, the coordination of one CO ligand that belongs to the slightly rotated $[Fe(CO)_3]$ fragment acquires a slight tendency to have a semi-bridging character. This fact can be also visualized by the H···O contacts among the hydrogen atoms of the phenyl rings and the closest oxygen atoms of the apical CO ligands (Figure 2). In **7** the aromatic system is tilted toward the slightly rotated $[Fe(CO)_3]$ group and one hydrogen atom of the phenyl ring results close to an axially coordinated CO ligand. On the basis of the H–CO overlap orbital population, it can be excluded that such contact might represent a weak bonding interaction.

To disclose the origin of the different structural feature observed in **3** versus **7**, truncated models of these derivatives have also been optimized through DFT (see Figure 2; silole and cyclopentadiene (cp) replace silafluorene and fluorene, respectively). Notably, in the simplified silole and cp models, the resulting structures are similar, that is, they both display the tilted dithiolate bridgehead. Therefore, DFT calculations suggest that the larger bulk of silafluorene system with respect to the simpler silole ring is one of the key effects to understand the structural features of **3** and **7**. Since the structure of the dithiolate group in **3** resembles the transition state associated with "flipping" of the propanedithiolato ligand in simple biomimetic models, we have compared the structure and the energy of the transition state associated to the dithiolate flipping in $[Fe_2(CO)_6(\mu\text{-pdt})]$ and in the corresponding model, in which a silyl-functionalized dithiolate group replaces pdt (see Figure 3).

It turned out that the energy of the transition state decreases from 9.3[37] to 3.2 kcal mol^{-1} going from the C to the Si derivative. Therefore, it can be concluded, that in **3** the best way to relax the steric clash between silafluorene and the CO ligand im-

Table 1. XRD and DFT geometry parameters for complexes **3**, **7**, and for the simple model $[Fe_2(CO)_6(\mu\text{-pdt})]$. Bond lengths [Å] and angles [°].

		$[Fe_2(CO)_6(\mu\text{-pdt})]$	**3**	**7**
Fe–Fe	XRD	2.510	2.527	2.500
	DFT	2.542	2.553	2.531
δ	XRD	0.0	10.6	21.5
	DFT	0.0	3.3	47.7
S-C-X-C	XRD	137.1	167.9	148.5
			173.4	143.0
	DFT	127.2	173.0	151.2
			174.7	151.3
H···O	XRD	2.900	2.755	2.942
			2.633	2.429[a]/2.674
	DFT	2.855	2.837	2.761
			2.599	2.277[a]/2.485

[a] This interatomic distance refers to the H···C contact between the hydrogen atom of the phenyl ring and the carbon atom of the apical CO ligand (Figure 2)

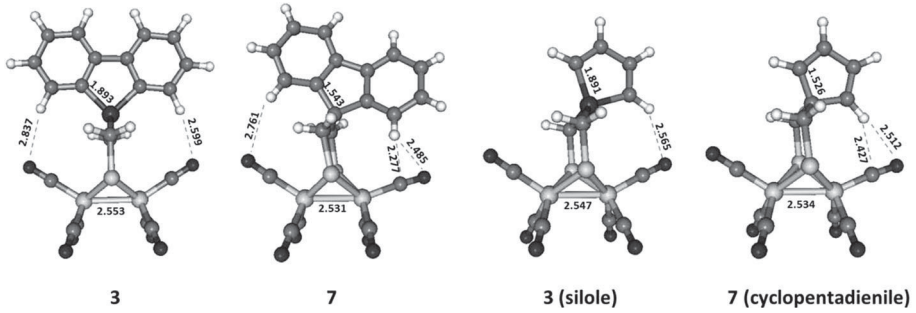

Figure 2. Left: DFT-optimized structure of the complexes **3** and **7**; Right: Calculated structures of the silole and cyclopentadiene analogues of **3** and **7**. The possible H···C and H···O interactions are evidenced (bond lengths in Å).

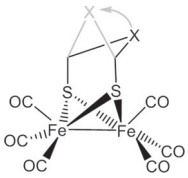

Figure 3. Flipping coordinate of the bidentate ligand. The energy barrier decreases from 9.3 ($X = CH_2$) to 3.2 kcal mol^{-1} ($X = SiH_2$).

plies planarization of the dithiolate moiety, whereas in **7** it is energetically more favorable to adopt a conformation in which the fluorene ring interacts with one of the $[Fe(CO)_3]$ moieties.

The ultimate reason underlying the different steric bulk must be ascribed to longer C–Si bonds in **3** (1.9 Å on average) versus C–C bonds in **7** (1.5 Å) making the Si-functionalized dithiolate bridge bulkier than its carbon analogue. This entails that in **3**, a significant rotation of one $[Fe(CO)_3]$ moiety (generally disfavored in all-CO synthetic systems at the Fe(I)Fe(I) state, except when peculiar structure requirements are fulfilled)[10,11] should be observed and allow a facile accommodation of the bulky group arising from the typically chair conformation of the Fe-$S_2(CH_2)_2$-Si six-membered ring. This difference in the bulkiness of the carbon and silicon-functionalized dithiolate bridge is consistent with the observation that the fluorene ring lies closer to the Fe_2S_2 core inducing a partial rotation of the $[Fe(CO)_3]$ moiety that reduces steric hindrance. In the case of the silafluorene derivative **3**, the ring is equidistant from both apical CO ligands preventing the formation of an unstable semi-rotated form. Considering the simplified silole derivative, the distance of the silole ring from the apical CO ligand is far enough to prevent any distortion of the Fe_2S_2 core and to restore the typical orientation normally observed for the bridging dithiolate.

An analysis of the stereo-electronic structures of **3** and **7** has been also performed (see the Supporting Information, Figure S3) to settle whether other factors contribute to the different orientation of the (hetero)-aromatic group with respect to the Fe_2S_2 core in silicon versus carbon systems. In particular, the interest has been focused on the MOs involved in the C–Si–C and C–C–C unit, because the (hetero)-aromatic group is directly linked either to the –Si– atom or to the inner –C– atom. The shapes of the HOMO−1, HOMO, and LUMO computed for the two complexes **3** and **7** are similar and reported in Figure S3 (see the Supporting Information). The HOMO represents the one-node π-system of the phenyl rings, the LUMO is the Fe–Fe-σ*-orbital, and the corresponding Fe–Fe-σ-orbital bonding is the HOMO−1. The HOMO/LUMO gap of **3** is around 0.00116 hartree (0.032 eV) lower than that of **7**. It is interesting to note that the HOMO and LUMO of **3** are completely localized, whereas in **7** the same MOs are more delocalized. In Table S1 (see the Supporting Information) the corresponding frontier MO energies are reported for **3** and **7**. To check the hypothesis of an increased sp^2 character of the C–Si–C bonding as reported before,[29] we focused on the zero-node type MOs. Either for **3** or for **7**, two low-energy MOs were found, characterized by the zero-node combination of the p orbitals. In Figure S4 (see the Supporting Information), we reported the shapes of the four MOs computed at the same isosurface value (0.02 au). The C-X-C (X = C, Si) moiety orbital contribution due to the "in-phase" p atomic orbitals perpendicular to the C-X-C plane are evidenced. Either for **3** or **7**, this contribution is conjugated with the (hetero)-aromatic π-system and the d-orbital contributions are always negligible. However, the most important point is that the shape and the electron density population of the MOs of interest in the two derivatives are not so different as to be able to justify even only a partial sp^2-character of the silicon atom (of course already absent in the carbon-based moiety). These results corroborate the hypothesis based on the analysis proposed above that the steric hindrance of the (hetero)-aromatic group in the silicon species is bigger than that in the carbon analogue to the extent that the silicon bridgehead takes on an orientation such as to minimize intramolecular repulsion with both apical ligands of the diiron cluster.

DFT results obtained for **3** and **7** also hold for complexes **9** and **12**. In this case, the main differences between **9** and **12** are essentially due to the different conformation of the inner ring in the two systems. This difference reflects the conformation of the whole three-ring system: Whereas the phenoxsilane complex features a quasi-planar three-ring conformation, which makes **9** very similar to **3**, the phenothiasilane derivative **12** has a butterfly (bent) conformation, which allows one of the outer phenyl rings to be accommodated farther from apical CO ligands than the outer phenyl rings of **9**. This entails that **12** can be observed in the typical chair-conformation of the six-membered dithiolate ring, although a small distortion on the $[Fe(CO)_3]$ moiety is visible (see the Supporting Information, Figure S2). Derivatives such as **3** and **9**, showing a full (or quasi) planar disposition of the three-ring moiety, must adopt an orientation placing phenyl rings as far as possible from the apical CO, which is less energy costly than inducing rotation of the $[Fe(CO)_3]$ moiety. In Table 2, the main geometry parameters are reported resulting from comparison of the XRD versus DFT data. Again, when the three-ring groups are modeled by simpler single-rings (deleting the phenyl rings, see on the right Figure 4), the structures of the two resulting systems are similar, which confirms the steric nature of the different disposition observed for the two derivatives **9** and **12**.

Table 2. XRD and DFT geometry parameters for complexes **9** and **12**. Bond lengths [Å] and angles [°].

		3	**7**
Fe–Fe	XRD	2.513	2.512
	DFT	2.545	2.543
δ	XRD	1.9	19.9
	DFT	1.3	19.7
S-C-X-C	XRD	172.8	137.7
		172.6	147.4
	DFT	178.8	146.6
		178.2	155.3
H···O	XRD	2.462	4.191
		2.633	3.077[a]/3.387
	DFT	2.497	3.807
		2.494	3.170[a]/3.276

[a] This interatomic distance refers to the H···C contact between the hydrogen atom of the phenyl ring and the carbon atom of the apical CO ligand (Figure 4)

Crystallographic structures of **3a**, **7a**, and **9a** show a basal orientation of PPh_3, which is expected to bear steric bump with the cumbersome three-cyclic system (see the aforementioned considerations). The values of the S-C-X-C dihedral angles for **9**/**9a** and **12**/**12a** differ by only a few degrees, showing that the substitution with PPh_3 has no significant effect on the conformation of the heteroaromatic ligands. The energy difference between the apical and basal dispositions of PPh_3 in both **9a** and **12a** were computed (the latter being the only one derivative showing an apical orientation (even though distorted) of the PPh_3 at the solid state).

As expected (Figure 5), the apical PPh_3-substituted isomer is less stable in **9a** than the basal isomer by 2.0 kcal mol^{-1}. Curiously, for **12a** DFT (gas phase) predicts a slight (0.8 kcal mol^{-1}) preference for the basal isomer over the one observed in the crystal structure, probably suggesting that packing forces might help stabilize the apical disposition of the PPh_3.

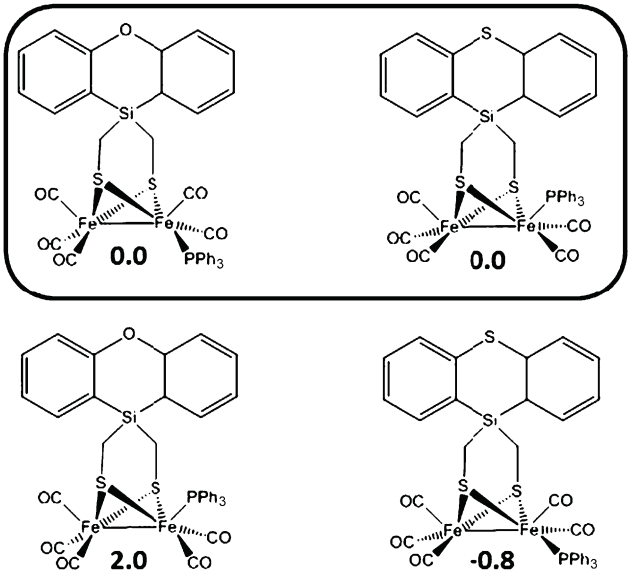

Figure 5. Relative stability [kcal mol^{-1}] of basal versus apical dispositions of PPh_3 in **9a** (left) and **12a** (right).

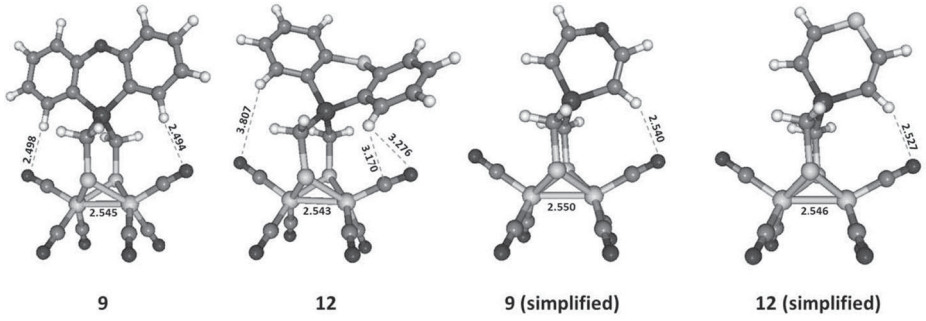

Figure 4. DFT structures of **9** and **12** and the corresponding simplified derivatives. Bond lengths in Å.

Electrochemistry for 7, 9, and 12

Cyclic voltammetry (CV) at slow to moderate scan rates for complexes **9** and **12** ($0.05\ V\,s^{-1} \leq v \leq 1\ V\,s^{-1}$) shows that the electrochemical reduction at $E_{1/2} = -1.56$ V is quasi-reversible in $CH_2Cl_2/[NBu_4][PF_6]$ (Figure 6) and similar to the already known complex **3** ($E_{1/2} = -1.55$ V).[29]

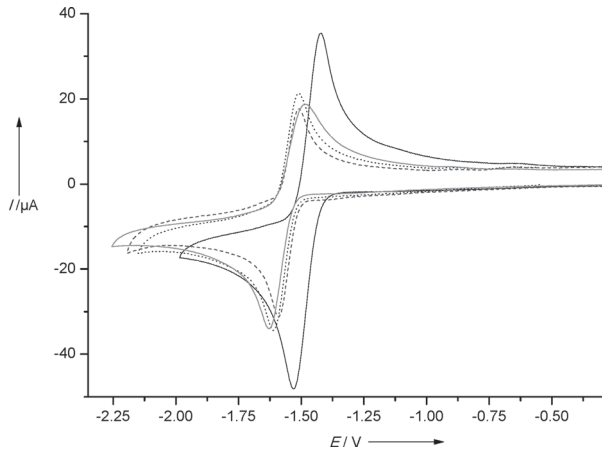

Figure 6. Cyclic voltammogram of **3** (gray, 0.380 mM), **7** (black, 0.503 mM), **9** (– – –, 0.493 mM), and **12** (••••, 0.736 mM) in $CH_2Cl_2/[NBu_4][PF_6]$ (vitreous carbon electrode; 0.5 $V s^{-1}$; potentials are vs. Fc^+/Fc).

Compared to this, the quasi-reversible electrochemical reduction of **7** with $E_{1/2} = -1.48$ V is close to that from benzene dithiolate (bdt)[39] and the effect of the Si atom is a shift of the potential of 70–80 mV to more negative values. Although we observed unexplained differences in the normalized peak currents (i_p^{red}/c; c = concentration of complex) of complexes **7**, **9**, and **12** (Figure 6), the comparison of the shapes of the corresponding CVs to that of equimolar **3**, which was previously shown to undergo a single step two-electron reduction, suggest that the same type of mechanism is at work for all these compounds. Single step two-electron reductions arise from an inversion of the potentials of the individual one-electron reduction processes.[29,39–44] Typically, a potential inversion is observed when a chemical reaction (most often a structure change) makes the second electron transfer thermodynamically more favorable than the first. In the case of the bdt and adt complexes, the single step two-electron transfer was shown by theoretical investigations to result from the cleavage of a Fe–S bond and the shift of a CO group from a terminal to a bridging position.[28,40,43] Such a rearrangement may reasonably be envisaged for the complexes **9** and **12** as well.

Cyclic voltammetry at faster scan rates results in a substantial increase of the peak-to-peak separation and a significant decrease of the current function ($i_p^{red}/v^{1/2}$) for the reduction. The change in ΔE_p is indicative of slow kinetics of the heterogeneous electron transfers.[45–50] Further, the scan rate dependence of the current function could arise from either an EE or an $EC_{rev}E$ mechanism. This finding suggests a transition between a two-electron transfer process at low v and a one-electron transfer at fast scan rates. On this basis, the occurrence of the above-mentioned rearrangement as the intervening reaction of an $EC_{rev}E$ process rather than concomitantly with one of the electron transfer steps of an EE mechanism cannot be ruled out.[44]

The electrochemical behaviour of complex **12** (**9**) in CH_2Cl_2-$[NBu_4][PF_6]$ with added CF_3COOH is illustrated in Figure 7. Addition of the first equivalent of acid shows an initial shift of the reduction peak of the complex from −1.60

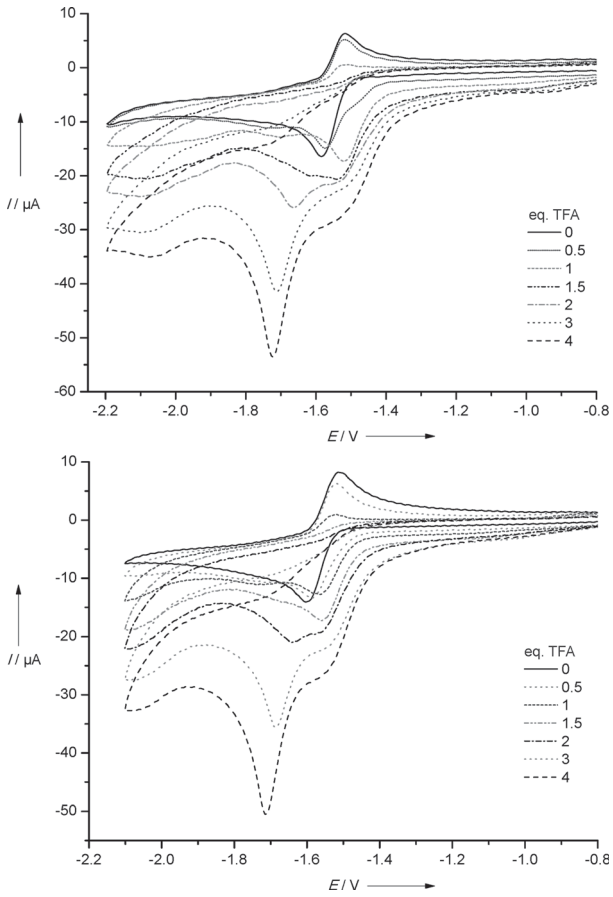

Figure 7. Cyclic voltammetry of **9** (0.493 mM, top) and **12** (0.565 mM, bottom) with added TFA in $CH_2Cl_2/[NBu_4][PF_6]$ (vitreous carbon electrode; 0.2 $V s^{-1}$; potentials are vs. Fc^+/Fc).

(−1.59 V) to −1.56 V (−1.52 V) due to the protonation of the dianion to generate $[Fe^IFe^IH]^-$. Upon further additions of acid, the peak at −1.56 V (−1.52 V) is not increasing, if the change in the baseline is considered, whereas a new reduction around −1.64 V (−1.66 V) is observed and shifts to more negative potential with increasing concentration of the added acid (Figure 7). The acid dependence of the CV of **9** and **12** is very similar, also to that previously observed for the pdt complex and the reduction in the presence of CF_3COOH can be described as shown in Scheme 3.[51,52] The first reduction ob-

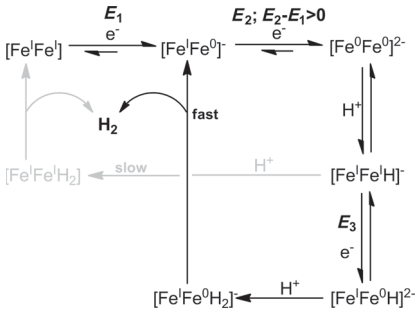

Scheme 3. Proposed electrocatalytic mechanism for the proton reduction by **9** and **12**.

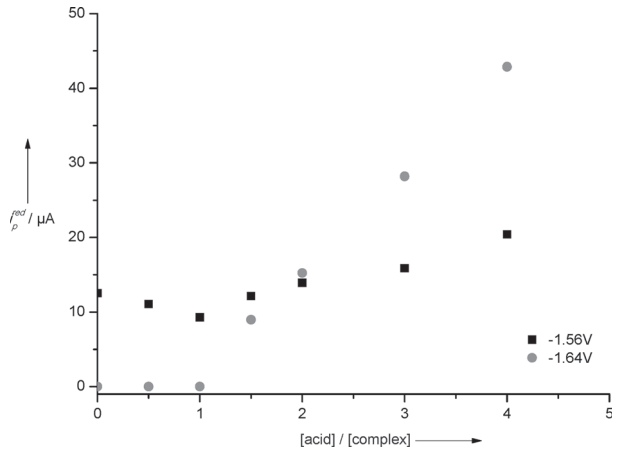

Figure 8. Dependence of the peak currents of the reduction of **12** (0.57 mM) upon the number of added equivalents of CF_3COOH in CH_2Cl_2/$[NBu_4][PF_6]$ (peak current measured by CV, $\nu = 0.2\ V\,s^{-1}$,vitreous carbon electrode).

served in acidic medium comprises the electron transfers at E_1 and E_2, and the weaker acid-dependence of the peak than E_3 indicates a rather inefficient proton reduction process, limited by an acid-independent, very slow reaction, probably the release of H_2 (Scheme 3, slow process, gray).[51–57] The release of H_2 is facilitated by the transfer of a supplementary electron at a more negative potential (potential E_3, fast process, see also Figure 8), as reported for several electrocatalytic proton-reduction processes involving diiron compounds.[40,58,59]

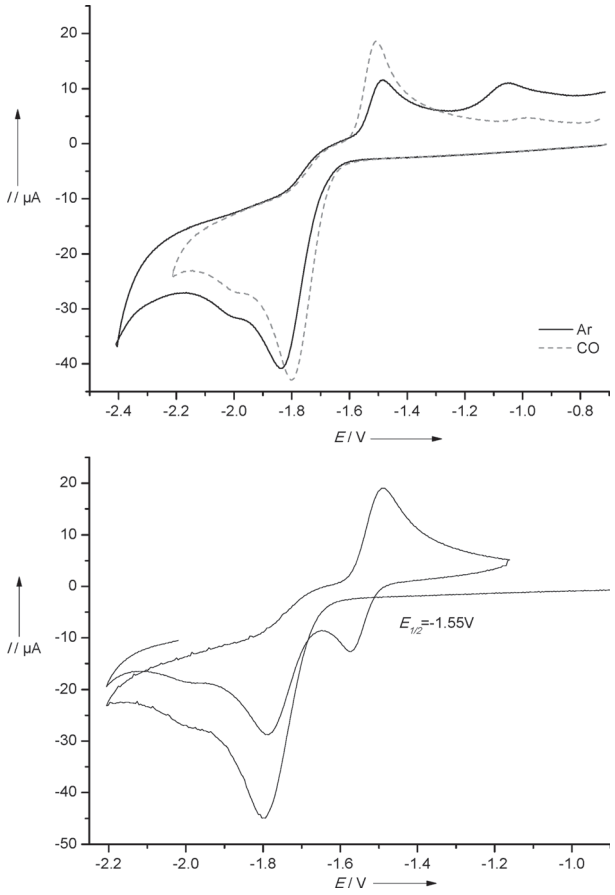

Figure 9. Cyclic voltammogram of **3a** (0.865 mM) under argon and CO (top) and reverse under CO (bottom) in CH_2Cl_2/$[NBu_4][PF_6]$ (vitreous carbon electrode; $0.5\ V\,s^{-1}$; potentials are vs. Fc^+/Fc).

Electrochemistry and Protonation for 3a, 7a, 9a, and 12a

Cyclic voltammetry at slow to moderate scan rates ($0.05\ V\,s^{-1} \leq \nu \leq 1\ V\,s^{-1}$) shows that the electrochemical reduction of **3a** at $E_1 = -1.81$ V is irreversible in CH_2Cl_2/$[NBu_4][PF_6]$ (Figure 9). Comparison of the potentials of the observed re-oxidations of **3a** ($E_{ox} = -1.51$ V) and **3** ($E_{ox} = -1.50$ V) measured under similar experimental conditions indicates the elimination of the PPh_3 ligand and the formation of the hexacarbonyl complex immediately, which was consequently oxidized. At faster scan rates ($2.0\ V\,s^{-1} \leq \nu \leq 20.0\ V\,s^{-1}$) a substantial increase of the peak-to-peak separation of the electrochemical reduction of **3a** at E_1 ($E_{1/2} = -1.79$ V) can be observed, as expected for slow electron-transfer kinetics (and to the effects of uncompensated solution resistance). The increased chemical reversibility of this reduction at faster scan rates is due to the fact that the shorter time scale limits the extent of the chemical reaction. To verify these results, the cyclic voltammetry experiments were carried out under CO atmosphere. Comparison of both atmospheres (Figure 9) at a scan rate of $0.5\ V\,s^{-1}$ shows an increase of E_{ox} for the re-oxidation of the species formed from **3a** and a shift of $E_1 \approx 40$ mV less negative under CO. Also, at faster scan rates ($2.0\ V\,s^{-1} \leq \nu \leq 20.0\ V\,s^{-1}$) under CO, the reversibility of the electrochemical reduction of **3a** at E_1 increases not as much as under argon. Related to this, a reverse scan under CO atmosphere showed a new reduction potential at $E_{red} = -1.58$ V, which indicates also the immediate formation of **3** (Figure 9, bottom). This is representative also for the complexes **7a**, **9a**, and **12a** (see the Supporting Information, Figure S5–S7).

The electrochemical behaviour of **3a** in CH_2Cl_2/$[NBu_4][PF_6]$ in the presence of increasing amounts of triflic acid is illustrated in Figure 10. Addition of the first equivalent of the acid shifts the reduction peak of the complex from −1.81 to −1.72 V. Upon further additions of acid, the peak at −1.72 V increases and shifts to more negative potential, whereas a new reduction around −2.02 V is observed, which shifts to more negative potential with increasing concentration of the added acid (Figure 10). After addition of 6 equivalents of triflic acid a new reduction is observed at −1.70 V. Based on the first reduction of **3a** at −1.81 V, the new reduction is shifted 110 mV to a more positive value, which can be attributed to a protonation of **3a** before reduction. Compared to the mono-PPh_3-substituted pdt complex, such an interaction has not been reported.[60] To verify these results, different experiments were carried out.

At the top of Figure 10, the IR spectra are shown for complex **3a** (0.53 mM in dichloromethane, ——) and for complex $\mathbf{3aH^+}$ with added 40 equivalents of triflic acid (– – –). After addition of triflic acid, an average shift of $79\ cm^{-1}$ to higher wavenumbers is observed for all three CO bands. This range of shift is predicted to be a μ-S protonation.[18,19,24,26–28] The intensities of the CO bands decrease because the solubility in di-

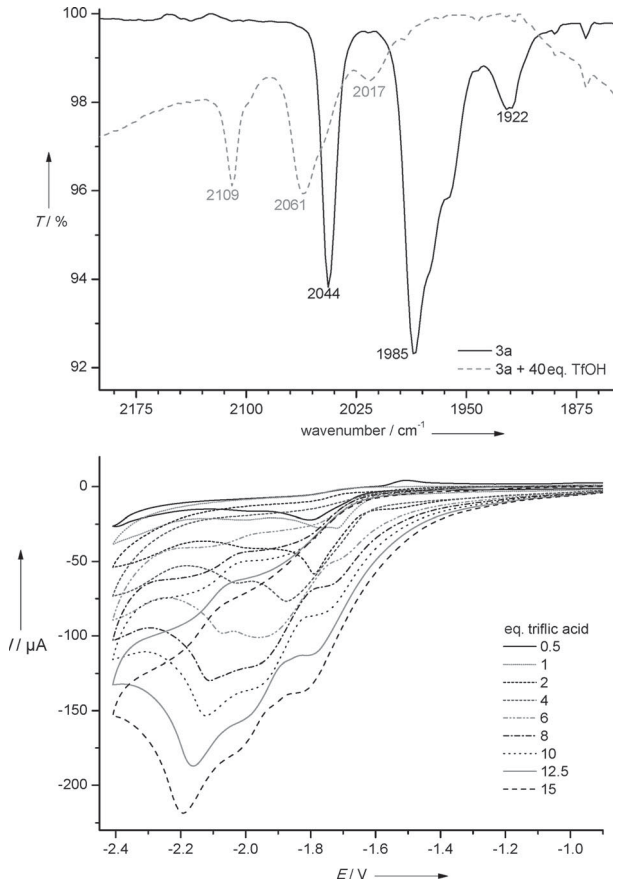

Figure 10. Bottom: Cyclic voltammetry of **3a** (0.865 mM) in CH_2Cl_2/[NBu_4][PF_6] (vitreous carbon electrode; 0.2 $V s^{-1}$; potentials are vs. Fc^+/Fc). Top: Spectra of **3a** without and with 40 equiv TfOH.

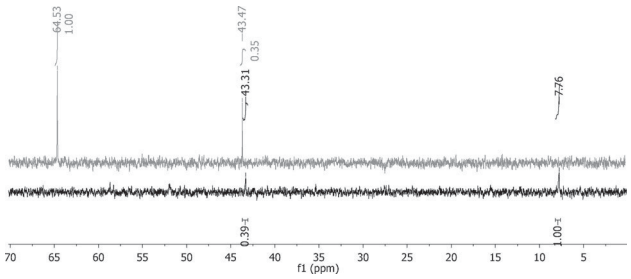

Figure 11. $^{31}P\{^1H\}$ NMR spectra of **3a** (5.2 mg in CD_2Cl_2, top gray line) and with added 40 equiv of TfOH (bottom black line).

chloromethane of the protonated complex **3aH$^+$** is less than that for **3a**; an orange paste was observed at the walls of the Schlenk tube, but also decomposition cannot be ruled out. The CO bands for the deprotonated form **3a** could not be recovered with a close intensity compared to **3aH$^+$** after addition of NEt_3, but were detected between other bands. Decomposition has to be assumed after deprotonation.

Furthermore, $^{31}P\{^1H\}$ NMR experiments were carried out, which are shown in Figure 11. The gray line shows the ^{31}P NMR spectrum of complex **3a**. The signal at $\delta = 64.5$ ppm corresponds to the phosphorus atom of the PPh_3 group and the signal at $\delta = 43.47$ ppm reveals $SPPh_3$ as impurity. After addition of 40 equivalents of triflic acid (black line) the signal at $\delta = 64.5$ ppm completely disappeared and a new signal arises at $\delta = 7.8$ ppm. The range of the signal and the highfield shift of $\delta = 56.8$ ppm suggest **3aH$^+$** with a protonation at the μ-S atom next to the PPh_3-substituted iron, regarding the work of Sun et al.[24]

Compared to **3a** and **7a**, compounds **9a** and **12a** showed a new reduction peak after the addition of equivalents of acid (see the Supporting Information, Figures S8 and S9). For **7a**, the new reduction is observed at −1.68 V and thus shifted 140 mV to a more positive value, which can be attributed also to a protonation of **7a** before reduction. In contrast to experiments performed with **3a**, after addition of 200 equiv TFA to a solution of complex **7a**, no μ-S-atom protonation can be observed in the IR spectrum (see the Supporting Information, Figure S10, bottom), just decomposition with time. After addition of 100 equiv TfOH to a solution of complex **7a** (see the Supporting Information, Figure S10, top), new CO bands comparable to those observed in the IR spectrum of **3a** are observed at 2088 and 2021 cm^{-1} (average shift of 38 cm^{-1} to higher wavenumbers), but new absorption bands also arise, which are typical for decomposition of those compounds. For these results, we can assume a μ-S protonation, which is, however, unstable and is followed immediately by decomposition. The same results are observed for **9a** and **12a** (see the Supporting Information, Figure S9, bottom). The results obtained for **3a** by CV experiments are in general analogous to those observed for **7a**, **9a**, and **12a** (see the Supporting Information, Figures S5–S9), but only **3a** forms the stable protonated form **3aH$^+$**, which can be detected by IR and NMR spectroscopic measurements.

With the aim of understanding the experimental results and to collect additional information about factors affecting the stability of **3aH$^+$**, DFT calculations were performed. The speciation study of protonated isomers of **3a** highlights an important result, which confirms the μ-S atoms as favored protona-

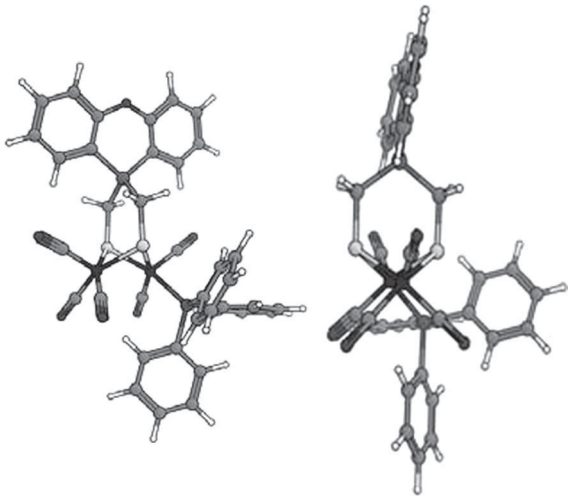

Figure 12. Steric hindrance affecting the region of the Fe–Fe bond caused by a phenyl ring of the basal PPh_3 in **9a**. Left: Side view. Right: View from the ideal Fe–Fe bond axis. Fe–Fe bond is omitted.

tion sites in these diiron compounds. Indeed, once excluding direct protonation at the Fe–Fe region (thermodynamically favored site by 14 kcal mol^{-1} with respect to the μ-S protonated form) due to a supposedly unfavorable kinetics[6,8,17,18] resulting from the occlusion of Fe–Fe by one of the phenyl rings of the basal PPh_3 ligand (Figure 12),[61] dithiolate sulfur atoms show nearly the same proton affinity as that observed for the terminal diiron site. This result is very different compared to published data on the proton speciation of analogous $(PR_3)_4$–diiron dithiolates (see the Supporting Information of ref. [18]), in which a large difference in proton affinities (of iron vs. sulfur sites) emerged. In the complexes described by Rauchfuss et al.,[18] the protonated sulfur isomer is far higher in energy compared with the isomer protonated at a single Fe (although also in that case transient sulfur protonation was proposed).

In principle, the different relative basicity of sulfur and iron atoms in **3a** and $(PR_3)_4$–diiron dithiolates might depend on the different number of phosphine ligands and/or on the presence of a silicon atom and therefore also on the planar conformation of the dithiolate group in **3a**, if the molecular structure of **3a** in the solid state is assumed. To evaluate the relative importance of these factors, we have also computed sulfur and iron proton affinity in **7a** (which differs from **3a** for the presence of a carbon atom in the dithiolate bridge and for the conformation of the latter). The computed sulfur and iron proton affinities in **3a** differ by 0.8 kcal mol^{-1}, whereas in **7a** this difference increases to 3.1 kcal mol^{-1}, indicating that the presence of the Si atom in the dithiolate bridge increases the basicity of the μ-S atoms by about 2.3 kcal mol^{-1} (the same proton affinity for simplified **3a** system becomes 3.8 kcal mol^{-1}, indicating a small effect of the pendant ligand conformation). Even though this effect is far from negligible, the number of phosphine ligands turned out to be more important in tuning the relative basicity of sulfur and iron atoms. In fact, in $(PR_3)_4$– versus PR_3–diiron derivatives, such as those reported by Rauchfuss et al., the corresponding energy difference is larger than 20 kcal mol^{-1}.[18]

Note that **9a**, which has been observed experimentally to behave differently from **3a** (i.e., it tends to decompose), also shows a relatively favorable affinity of sulfur atoms towards protons. It cannot be excluded that also in this case a transient sulfur protonation might occur, followed by events that cannot be simulated by available computational techniques. The formation of the Fe–Fe bridging hydride by rearrangement of terminal H or S–H isomers cannot be ruled out.[17,18]

Subsequently, the reaction energy profile for the sulfur protonation of **3a** by triflic acid has been studied by DFT. To do that, simulations have been performed featuring different values of the ratio $(CF_3SO_3H)_x$/**3a**, since it was verified that a simple one-to-one modeling cannot yield the expected protonation event, namely, the single molecule of triflic acid cannot release the proton to the sulfur atom. This is likely to reflect the experimental observations, indicating the need of a large excess of acid versus **3a** is required to obtain protonation. The value of "*x*" has been sampled choosing only some values (3, 4, and 7), due to the high computational requirements necessary to perform a systematic variation of "*x*", especially when transition-state structures are searched (Table 3).

Table 3. Thermodynamic and kinetic parameters associated with **3a** protonation at the sulfur atom by a variable amount of triflic acid (*x* = number of triflic acid molecules).

x	$\Delta E^{\ddagger}$	ΔE
1	–	–
3	1.9	1.7
4	1.3	1.0
7	0.1	−8.0

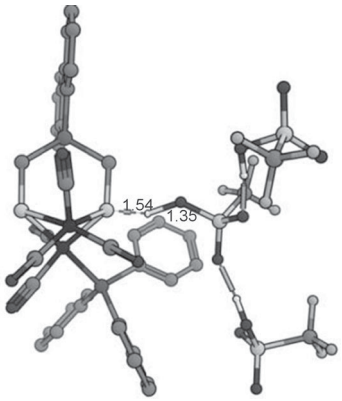

Figure 13. Transition-state structure associated with the protonation reaction of **3a** in the *x* = 3 case.

The hydrogen bonds formed by the excess of acid molecules with the one that actually releases the proton to the sulfur atom are evidently necessary to tune properly the real acid–base tendency of the conjugate couple $CF_3SO_3H/CF_3SO_3^-$ (Figure 13).

The formation of triflic clusters is also compatible with the use of a nonprotic solvent (CH_2Cl_2). Entropic effects have not been estimated in this case. Nonetheless, since reactants (and products) were modeled as van der Waals complexes (therefore already including a certain degree of associative character of bimolecular system acid **3a**, compared to the infinite separation), it can be conceived that the further entropy loss occurring in the transition state is very limited, when using such reference point. The more relevant observation, which

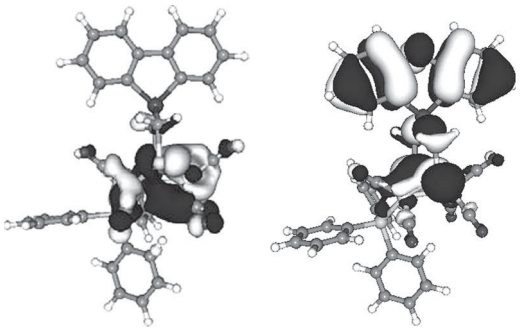

Figure 14. HOMO−1 of **3a** (left) and **9a** (right). Isosurface at 0.05 au.

can be made on data reported in Table 3, is that independently of the ratio $(CF_3SO_3H)_x$/**3a**, the reaction features extremely fast kinetics, perfectly in line with the experiments. Furthermore, when looking at thermodynamics, a sort of direct proportionality emerges between the number of acid molecules and the relative stability of products versus reactants.

To ascertain if the different behavior of **3a** versus **9a** in the presence of excess acid is possibly based on different stereoelectronic structures of the two derivatives, we performed a comparative FMO (frontier molecular orbital) analysis of the two derivatives **3a** and **9a** (Figure 14). Unfortunately, this comparison did not help us to elucidate the intimate reason underlying the different behavior of the two diiron compounds once put in acid solution.

Conclusion

Within this work, a series of [FeFe]-H_2ase mimics were synthesized and characterized. Different complexes containing bulky Si-heteroaromatic systems or the carbon analogue at the dithiolate moiety (bridgehead) were investigated, as well as their mono-PPh_3-substituted derivatives. The complexes, which contain a PPh_3 ligand at one of the iron atoms, are not very stable in CV experiments under reductive conditions, but this ligand increases the steric hindrance in the proximity of the Fe–Fe bond region to favor other protonation sites and concomitantly increase the basicity of the diiron cluster. Theoretical calculations fit with the experimental results, which show that the μ-S atoms of the dithiolate moiety are possible protonation sites. The different structural characteristics of the complex series are best explained by the different sterical bulk of the dithiolate bridgeheads, which was elucidated in detail by DFT calculations. These further clarify that no orbital-based feature of the complex series is at the origin of the structural differences. In particular, it was shown that small changes in the (hetero)-aromatic system result in large differences in the structures.

Further steps of this research will entail the investigation of optical properties as well as the possibility of photocatalytic hydrogen evolution by the complexes herein investigated.

Experimental Section

General procedures

All reactions were performed under a dry nitrogen or argon atmosphere with standard Schlenk techniques. All solvents were dried and distilled according to standard methods prior to use. Li[Et_3BH] (1.0 m in THF), 1,2-dibromobenzene, and bis(chloromethyl)dichlorosilane are commercially available and were used without further treatment or synthesized to known procedures.[62] Infrared spectra were recorded by a Nicolet Nexus Fourier transform and by a Bruker Vertex 70 spectrometer. Preparative column chromatography was performed with silica gel (Fluka, Kieselgel 60). ^1H, ^{13}C, ^{31}P, and ^{29}Si NMR spectra were obtained with either a Bruker Avance 200 or Avance 400 spectrometer. Elemental analyses were performed with a Vario EL III CHNS analyzer from Elementar Analysensysteme GmbH. Mass spectra were measured with a Finnigan MAT SSQ710 instrument.

Structure determination

The intensity data for the compounds **3a**, **7a**, **9**, **9a**, **12**, and **12a** were collected on a Nonius KappaCCD diffractometer using graphite-monochromated $Mo_{K\alpha}$ radiation. Data were corrected for Lorentz and polarization effects; absorption was taken into account on a semi-empirical basis using multiple-scans.[63–65] Measurements for compound **7** were carried out on an Oxford Diffraction X-Calibur-2 CDD diffractometer equipped with a jet cooler device. Graphite-monochromated $Mo_{K\alpha}$ radiation ($\lambda = 0.71073$ Å) was used in this experiment. The structures were solved by direct methods (SHELXS)[66] and refined by full-matrix least squares techniques against Fo^2 (SHELXL-97).[66] The hydrogen atoms of **9** were included at calculated positions with fixed thermal parameters. All other hydrogen atoms were located by difference Fourier synthesis and refined isotropically. All non-disordered, non-hydrogen atoms were refined anisotropically.[66] Crystallographic data as well as structure solution and refinement details are summarized in the Supporting Information, Tables S2 and S3.

Supporting Information available

Crystallographic data (excluding structure factors) has been deposited with the Cambridge Crystallographic Data Centre as supplementary publication CCDC-1028091 for **3a**, CCDC-1028775 for **7**, CCDC-1028092 for **7a**, CCDC-1028093 for **9**, CCDC-1028094 for **9a**, CCDC-1028095 for **12**, and CCDC-1028096 for **12a**. These data can be obtained free of charge from The Cambridge Crystallographic Data Centre via www.ccdc.cam.ac.uk/data_request/cif.

Electrochemical procedures

The electrochemical experiments were conducted under an inert atmosphere of nitrogen or argon. The preparation and purification of the supporting electrolyte ([NBu_4][PF_6]) was performed as described previously. Trifluoromethanesulfonic acid and trifluoroacetic acid (Aldrich) were used as received. Cyclic voltammetry was performed in a three-electrode cell by using a radiometer potentiostat (PGSTAT 128N or μ-Autolab III) driven by the GPES software. The working electrode consisted of a vitreous carbon disk, which was polished on a felt tissue with alumina, thoroughly rinsed with water, and dried before each CV scan. The Ag/Ag^+ reference electrode was separated from the analyte by a CH_2Cl_2/[NBu_4][PF_6] bridge. All potentials are reported against the ferrocene/ferrocenium couple; ferrocene was added as an internal standard at the end of the experiments.

Syntheses

Spiro(1,2-dithiolane-4,9-fluorene) (6): A mixture of 9,9′-bis(tosylmethyl)fluorene (3 g, 5.6 mmol), $Na_2S{\cdot}9H_2O$ (1.35 g, 5,6 mmol), and sulfur (0.18 g, 5,6 mmol) was dissolved in anhydrous DMF (20 mL) and was stirred for three days at 80 °C. The reaction mixture was cooled down to room temperature and poured into water (200 mL) and crushed ice. The mixture was extracted three times with dichloromethane (20 mL). The aqueous phase was acidified with conc. HCl and extracted again three times with dichloromethane (20 mL). The combined organic phases were washed with water and dried with sodium sulfate. After evaporation to dryness the crude product was purified by column chromatography (silica gel) with hexane/dichloromethane (2:1) as eluent to afford the product as a pale-yellow solid (1.01 g, 70%) . ^1H NMR (400 MHz, CD_2Cl_2): $\delta = 7.45$ (m, 4H, $CH_{aromatic}$), 7.42 (m, 4H, $CH_{aromatic}$), 3.51 ppm (s, 4H, CH_2); ^{13}C NMR (75 MHz, CD_2Cl_2): $\delta = 149.79$ (C_q), 139.00 (C_q),

128.48 (*C*H), 128.36 (*C*H), 124.19 (*C*H), 120.24 (*C*H), 62.81 (C_{spiro}), 52.21 ppm (CCH_2S); IR: $\tilde{\nu}$ = 3049 (w), 2926 (w), 1437 (m), 1411 (m), 1307 (w), 1223 (w), 1100 (w), 1035 (w), 951 (w), 770 (m), 737 (s), 556 cm^{-1} (m); MS (DEI): *m/z* = 256 $[M]^+$, 191 $[M-S_2H]^+$, 178 $[M-S_2CH_2]^+$; HRMS calcd for $C_{15}H_{12}S_2$: 256.037280; found: 256.038045.

10,10′-Bis(chloromethyl)-phenoxsilane (8): A solution of diphenyl ether (0.56 g, 3.3 mmol) in THF (15 mL) was cooled to −30 °C, and *n*-BuLi (1.6 M in hexane, 6.2 mL, 9.9 mmol) was added. The reaction solution was warmed to room temperature by removing the cooling bath and subsequently stirring overnight. The resulting solution was cooled to −78 °C, and a solution of $Cl_2Si(CH_2Cl)_2$ (0.75 g, 3.8 mmol) in THF (10 mL) was added dropwise. The reaction mixture was stirred at −78 °C for 2 h and at room temperature overnight. The mixture was filtered, and the solvents were evaporated by vacuum transfer under a nitrogen atmosphere. The residue was purified by bulb-to-bulb distillation (155 °C/0.25 mbar) to afford **8** as white crystalline solid (0.66 g, 68%). ^{1}H NMR (400 MHz, CD_2Cl_2): δ = 7.81 (d, 2H, $CH_{aromatic}$, *J* = 7.7 Hz), 7.57 (t, 2H, $CH_{aromatic}$, *J* = 7.7 Hz), 7.27 (d, 2H, $CH_{aromatic}$, *J* = 8.4 Hz), 7.23 (t, 2H, $CH_{aromatic}$, *J* = 7.3 Hz), 3.36 ppm (s, 4H, CH_2); ^{13}C NMR (100 MHz, CD_2Cl_2): δ = 160.64 (C_qO), 134.85 (CH), 133.23 (CH), 123.18 (CH), 118.71 (CH), 112.22 (CSi), 26.86 ppm ($SiCH_2S$); ^{29}Si NMR (120 MHz, $CDCl_3$): δ = −32.71 ppm; IR: $\tilde{\nu}$ = 3064 (w), 3014 (w), 2968 (w), 2934 (w), 2861 (w), 1737 (m), 1592 (m), 1572 (w), 1461 (w), 1438 (m), 1419 (s), 1375 (m), 1304 (m), 1266 (s), 1216 (s), 1166 (m), 1155 (m), 1128 (m), 1101 (w), 1074 (m), 1030 (w), 885 (m), 850 (w), 789 (m), 745 (s), 727 (s), 708 (m), 670 (m), 643 (m), 612 cm^{-1} (m); MS (DEI): *m/z* = 294 $[M]^+$, 245 $[M-CH_2Cl]^+$, 197 $[M-CH_2Cl_2]^+$, 183 $[M-O(CH_2Cl)_2]^+$; elemental analysis calcd (%) for $C_{14}H_{12}SiCl_2O$: C 56.95, H 4.10, Cl 24.02; found: C 59.20, H 4.43, Cl 21.23.

10,10′-Bis(chloromethyl)-phenothiasilane (11): A solution of bis(2-bromophenyl)sulfane (0.87 g, 2.5 mmol) in Et_2O (10 mL) was added dropwise to a solution of *n*-BuLi (3.5 M in hexane, 1.4 mL, 5 mmol) in hexane (5 mL) at 0 °C. The reaction solution was warmed to room temperature, heated at reflux for four hours and subsequently stirred overnight. The resulting solution was cooled to −78 °C and added dropwise to a solution of $Cl_2Si(CH_2Cl)_2$ (0.5 g, 2.5 mmol) in Et_2O (25 mL). The reaction mixture was stirred at −78 °C for 2 h and then at room temperature overnight. The mixture was filtered, and the solvents were evaporated by vacuum transfer under a nitrogen atmosphere. The residue was purified by bulb-to-bulb distillation (145 °C/0.15 mbar) to afford **11** as white crystalline solid (0.42 g, 53%). ^{1}H NMR (400 MHz, CD_2Cl_2): δ = 7.82 (d, 2H, $CH_{aromatic}$, *J* = 7.3 Hz), 7.54 (d, 2H, $CH_{aromatic}$, *J* = 7.8 Hz), 7.45 (t, 2H, $CH_{aromatic}$, *J* = 7.5 Hz), 7.37 (t, 2H, $CH_{aromatic}$, *J* = 7.3 Hz), 3.42 ppm (s, 4H, CH_2); ^{13}C NMR (100 MHz, CD_2Cl_2): δ = 143.08 (C_qS); 135.39 (CH); 131.10 (CH); 127.92 (CH); 127.33 (C_qSi); 126.48 (CH); 24.70 ppm ($SiCH_2S$); ^{29}Si NMR (120 MHz, $CDCl_3$): δ = −23.36 ppm; IR: $\tilde{\nu}$ = 3052 (w), 2929 (w), 1575 (m), 1446 (m), 1415 (m), 1385 (m), 1255 (m), 1133 (s), 1108 (s), 1046 (s), 745 (s), 658 (s), 609 cm^{-1} (s); MS (DEI): *m/z* = 310 $[M]^+$, 275 $[M-Cl]^+$, 261 $[M-CH_2Cl]^+$; HRMS: *m/z* calcd for $C_{14}H_{12}SiCl_2S$: 309.980608; found: 309.980940.

$[Fe_2\{S_2C_{15}H_{12}\}(CO)_6]$ (7): In toluene (75 mL), spiro(1,2-dithiolane-4,9-fluorene) **6** (200 mg, 0.78 mmol), and $[Fe_3(CO)_{12}]$ (393 mg, 0.78 mmol) were dissolved and stirred under reflux for 2 h. After evaporation to dryness the crude product was purified by column chromatography (silica gel) with hexane/dichloromethane (3:1) as eluent to afford the product as a red crystalline solid (155 mg, 39%). ^{1}H NMR (600 MHz, CD_2Cl_2): δ = 7.87 (d, 2H, $CH_{aromatic}$, *J* = 6.6 Hz), 7.65 (d, 2H, $CH_{aromatic}$, *J* = 6.0 Hz), 7.37 (m, 4H, $CH_{aromatic}$), 2.76 ppm (s, 4H, CH_2); ^{13}C NMR (150 MHz, CD_2Cl_2): δ = 208.33 (CO), 152.21 (C_q), 139.27 (C_q), 128.79 (CH), 127.92 (CH), 125.21 (CH), 120.47 (CH), 49.68 (C_{spiro}), 30.15 ppm ($SiCH_2S$); IR: $\tilde{\nu}$ = 2075 (m), 2034 (s), 2003 (m), 1990 (m), 1976 cm^{-1} (w); MS (DEI): *m/z* = 536 $[M]^+$, 508 $[M-(CO)]^+$, 480 $[M-(CO)_2]^+$, 452 $[M-(CO)_3]^+$, 424 $[M-(CO)_4]^+$, 396 $[M-(CO)_5]^+$, 368 $[M-(CO)_6]^+$; elemental analysis calcd (%) for $C_{15}H_{12}Fe_2S_2(CO)_6$: C 47.04, H 2.26, S 11.96; found: C 47.25, H 2.26, S 11.99.

General complexation (9, 12): A solution of $[Fe_2(CO)_6(\mu\text{-}S)_2]$ (1 mmol) in THF (50 mL) was cooled to −78 °C, and Et_3BHLi (2 mmol) was added dropwise. The solution was stirred for 15 min, and 10,10′-bis(chloromethyl) compound (1 mmol) was added. The mixture was warmed to room temperature and stirred at this temperature for 16 h. The volatiles were removed under vacuum, and the residue was purified by column chromatography (silica gel) with hexane/dichloromethane (10:1) as eluent.

$[Fe_2\{S_2C_{14}H_{12}OSi\}(CO)_6]$ (9): Orange solid, yield 32.5%. ^{1}H NMR (200 MHz, CD_2Cl_2): δ = 7.81–7.42 (m, 4H, $CH_{aromatic}$), 7.27–7.16 (m, 4H, $CH_{aromatic}$), 3.35 ppm (s, 4H, CH_2); ^{13}C NMR (50 MHz, CD_2Cl_2): δ = 207.83 (CO), 160.67 (C_qO), 134.91 (CH), 131.39 (CH), 133.29 (CH), 123.19 (CH), 118.73 (CH), 112.21 (C_qSi), 26.79 ppm ($SiCH_2S$); IR: $\tilde{\nu}$ = 2086 (m), 2074 (m), 2031 (m), 2000 (m), 1973 (m), 1953 cm^{-1} (m); MS (DEI): *m/z* = 568 $[M]^+$, 540 $[M-Fe(CO)]^+$, 512 $[M-Fe(CO)_2]^+$, 484 $[M-Fe(CO)_3]^+$, 456 $[M-Fe(CO)_4]^+$, 428 $[M-Fe(CO)_5]^+$; elemental analysis calcd (%) for $C_{14}H_{12}OSiFe_2S_2(CO)_6$ + 1/6 hexane: C 43.32, H 2.42, S 11.01; found: C 43.30, H 2.15, S 10.96.

$[Fe_2S_2\{C_{14}H_{12}SSi\}(CO)_6]$ (12): Red solid, yield 37%. ^{1}H NMR (600 MHz, CD_2Cl_2): δ = 7.52–7.46 (m, 4H, $CH_{aromatic}$); 7.28–7.24 (m, 4H, $CH_{aromatic}$), 1.99 ppm (s, 4H, CH_2); ^{13}C NMR (150 MHz, CD_2Cl_2): δ = 205.53 (CO), 140.61 (C_qS), 132.82 (CH), 131.16 (C_qSi), 128.14 (CH), 127.14 (CH), 124.91 (CH), 22.57 ppm ($SiCH_2S$); IR: $\tilde{\nu}$ = 2074 (m), 2035 (s), 1999 cm^{-1} (m); MS (DEI): *m/z* = 584 $[M]^+$, 556 $[M-Fe(CO)]^+$, 528 $[M-Fe(CO)_2]^+$, 500 $[M-Fe(CO)_3]^+$; elemental analysis calcd (%) for $C_{14}H_{12}SSiFe_2S_2(CO)_6$: C 41.11, H 2.07, S 16.46; found: C 41.25, H 2.02, S 16.66.

Replacement of CO by PPh_3 (3a, 7a, 9a, and 12a): The hexacarbonyl complex (**3**, **7**, **9**, and **12**) was dissolved in anhydrous acetonitrile (20 mL). Me_3NO (1 equiv) was added to result a dark-red/brown solution within 20 min. Subsequently, PPh_3 (1 equiv) was added, and the reaction mixture was stirred at room temperature for 3 d. Evaporation to dryness afforded the crude product, which was purified by column chromatography of (silica gel) with hexane/dichloromethane as eluent.

$[Fe_2S_2\{C_{14}H_{12}Si\}(CO)_5PPh_3]$ (3a): Dark-red solid, yield 38%. ^{1}H NMR (400 MHz, CD_2Cl_2): δ = 7.74–7.11 (m, 23H, $CH_{aromatic}$), 1.79 ppm (m, 4H, CH_2); ^{13}C NMR (100 MHz, CD_2Cl_2): δ = 209.90 (CO), 147.93 (C_q), 136.40 (C_q), 135.37 (d, C_qP, *J* = 42 Hz), 134.21 (d, CH, *J* = 10 Hz), 133.91 (CH), 131.35 (CH), 131.30 (CH), 130.73 (d, CH, *J* = 2 Hz), 128.83 (d, CH, *J* = 10 Hz), 128.36 (CH), 128.27 (CH), 121.10 (CH), 121.06 (CH), 4.15 ppm ($SiCH_2S$); ^{29}Si NMR (120 MHz, CD_2Cl_2): δ = −9.32 ppm; ^{31}P NMR (80 MHz, CD_2Cl_2): δ = 67.88 ppm; IR: $\tilde{\nu}$ = 2044 (m), 1986 (s), 1976 (m), 1962 (w), 1923 cm^{-1} (w); MS (DEI): *m/z* = 496 $[M-PPh_3(CO)]^+$, 468 $[M-PPh_3(CO)_2]^+$, 412 $[M-PPh_3(CO)_4]^+$, 384 $[M-PPh_3(CO)_5]^+$; elemental analysis calcd (%) for $C_{14}H_{12}SiFe_2S_2(CO)_5PPh_3$ + 1/4 hexane: C 57.23, H 3.80, S 7.94; found: C 56.97, H 3.79, S 7.79.

$[Fe_2S_2\{C_{15}H_{12}\}(CO)_5PPh_3]$ (7a): Dark-red crystalline solid, yield 62%. ^{1}H NMR (600 MHz, CD_2Cl_2): δ = 7.72–7.25 (m, 23H, $CH_{aromatic}$), 2.66 ppm (s, 4H, CH_2); ^{13}C NMR (150 MHz, CD_2Cl_2): δ = 215.06 (CO), 214.90 (CO), 210.07 (CO), 152.82 (C_q), 139.04 (C_q), 134.85 (C_qP), 133.77 (CH), 130.41(CH), 128.56 (CH), 127.97 (CH), 127.25 (CH), 126.13 (CH), 124.97 (CH), 119.71 (CH), 49.94 (C_{spiro}), 30.22 ppm ($SiCH_2S$); ^{31}P NMR (160 MHz, CD_2Cl_2): δ = 63.83 ppm; IR: $\tilde{\nu}$ = 2046 (m), 1986 (s), 1973 (m), 1959 (w), 1922 cm^{-1} (w); MS (DEI): *m/z* =

664 $[M-Ph(CO)]^+$, 608 $[M-Ph(CO)_3]^+$, 580 $[M-Ph(CO)_4]^+$, 480 $[M-PPh_3(CO)]^+$; elemental analysis calcd (%) for $C_{15}H_{12}Fe_2S_2(CO)_5PPh_3$: C 59.24, H 3.53, S, 8.32; found: C 58.70, H 3.89, S 8.47.

$[Fe_2\{S_2C_{14}H_{12}SiO\}(CO)_5PPh_3]$ (9a): Dark-red solid, yield 37%. ^{1}H NMR (400 MHz, CD_2Cl_2): $\delta = 7.70–7.11$ (m, 23H, $CH_{aromatic}$), 4.19 ppm (m, 4H, CH_2); ^{13}C NMR (100 MHz, CD_2Cl_2): $\delta = 209.47$ (CO), 160.09 (C_qO), 134.99, 134.57, 133.72, 131.74, 130.39, 128.53, 123.02, 118.40, 118.04, 68.36 ppm ($SiCH_2S$); ^{31}P NMR (160 MHz, CD_2Cl_2): $\delta =$ 63.22 ppm; IR: $\tilde{\nu} = 2045$ (m), 1987 (s), 1923 cm^{-1} (w); MS (DEI): *m/z* = 802 $[M]^+$, 746 $[M-(CO)_2]^+$, 692 $[M-(CO)_4]^+$, 662 $[M-(CO)_5]^+$, 512 $[M-PPh_3(CO)]^+$, 484 $[M-PPh_3(CO)_2]^+$, 456 $[M-PPh_3(CO)_3]^+$, 428 $[M-PPh_3(CO)_4]^+$, 400 $[M-PPh_3(CO)_5]^+$; elemental analysis calcd (%) for $C_{14}H_{12}SiOFe_2S_2(CO)_5PPh_3$: C 55.38, H 3.39, S 7.99; found: C 55.47, H 3.44, S 7.98.

$[Fe_2S_2\{C_{14}H_{12}SiS\}(CO)_5PPh_3]$ (12a): Dark-red solid, yield 24%. ^{1}H NMR (400 MHz, CD_2Cl_2): $\delta = 7.81–7.30$ (m, 23H, $CH_{aromatic}$), 2.06 ppm (d, 4H, CH_2, $J = 16$ Hz); ^{13}C NMR (100 MHz, CD_2Cl_2): $\delta =$ 214.06 (CO), 209.69 (CO), 142.94, 142.44, 136.69, 135.74 (d, C_qP, $J =$ 40 Hz), 135.08, 134.20, 134.10, 133.90 (d, CH, $J = 10$ Hz), 130.72 (d, CH, $J = 2$ Hz), 129.89, 129.61, 129.07 (d, CH, $J = 10$ Hz), 126.84, 126.58, 1.44 ppm ($SiCH_2S$); ^{31}P NMR (162 MHz, CD_2Cl_2): $\delta =$ 63.42 ppm; IR: $\tilde{\nu} = 2046$ (s), 1988 (s), 1935 cm^{-1} (w); MS (DEI): *m/z* = 762 $[M-(CO)_2]^+$, 734 $[M-(CO)_3]^+$, 706 $[M-(CO)_4]^+$, 528 $[M-PPh_3(CO)]^+$, 500 $[M-PPh_3(CO)_2]^+$; *m/z* calcd (%) for $C_{14}H_{12}SiSFe_2S_2(CO)_5PPh_3$ + 1/2 hexane: C 55.76, H 3.98, S, 11.16; found: C 55.74; H 3.91, S 11.30.

Computational methods

Computations were performed using pure GGA BP86 functional. The Resolution of Identity (RI) technique was adopted for pure functionals in order to save CPU time. Basis sets of triple-ζ plus polarization split valence quality (TZVP) were adopted for all atoms in the complex. All computations presented were carried out using the TURBOMOL suite of programs.[67] DFT grid size was set to standard m3 value. Ground state geometry optimizations were carried out with convergence criteria fixed to 10^{-6} hartree for the energy and 0.001 hartree $bohr^{-1}$ for the gradient norm vector.

Acknowledgements

Financial support for this work was provided by the Deutsche Bundesstiftung Umwelt (to R.G.). We gratefully acknowledge the DAAD for the procope project for financial support. We are grateful to Dr. F. Michaud for crystallographic measurements. The Centre National de la Recherche Scientifique (CNRS), the University of Brest, and the University of Milano Biccoca are acknowledged for financial support.

Keywords: density functional calculations · enzyme models · hydrogen · protonation · sulfur

[1] Y. Nicolet, A. L. de Lacey, X. Vernède, V. M. Fernandez, E. C. Hatchikian, J. C. Fontecilla-Camps, *J. Am. Chem. Soc.* **2001**, *123*, 1596–1601.
[2] J. W. Peters, W. N. Lanzilotta, B. J. Lemon, L. C. Seefeldt, *Science* **1998**, *282*, 1853–1858.
[3] Y. Higuchi, H. Ogata, K. Miki, N. Yasuoka, T. Yagi, *Structure* **1999**, *7*, 549–556.
[4] H.-J. Fan, M. B. Hall, *J. Am. Chem. Soc.* **2001**, *123*, 3828–3829.
[5] A. Volbeda, J. C. Fontecilla-Camps, *Dalton Trans.* **2003**, 4030–4038.
[6] A. Adamska, A. Silakov, C. Lambertz, O. Rüdiger, T. Happe, E. Reijerse, W. Lubitz, *Angew. Chem. Int. Ed.* **2012**, *51*, 11458–11462; *Angew. Chem.* **2012**, *124*, 11624–11629.
[7] B. Ginovska-Pangovska, M.-H. Ho, J. C. Linehan, Y. Cheng, M. Dupuis, S. Raugei, W. J. Shaw, *Biochim. Biophys. Acta Bioenerg.* **2014**, *1837*, 131–138.
[8] A. R. Finkelmann, M. T. Stiebritz, M. Reiher, *Chem. Sci.* **2014**, *5*, 215–221.
[9] B. E. Barton, M. T. Olsen, T. B. Rauchfuss, *J. Am. Chem. Soc.* **2008**, *130*, 16834–16835.
[10] W. Wang, T. B. Rauchfuss, C. E. Moore, A. L. Rheingold, L. De Gioia, G. Zampella, *Chem. Eur. J.* **2013**, *19*, 15476–15479.
[11] S. Munery, J.-F. Capon, L. De Gioia, C. Elleouet, C. Greco, F. Y. Pétillon, P. Schollhammer, J. Talarmin, G. Zampella, *Chem. Eur. J.* **2013**, *19*, 15458–15461.
[12] D. Zheng, M. Wang, L. Chen, N. Wang, L. Sun, *Inorg. Chem.* **2014**, *53*, 1555–1561.
[13] T. R. Simmons, G. Berggren, M. Bacchi, M. Fontecave, V. Artero, *Coord. Chem. Rev.* **2014**, *270–271*, 127–150.
[14] T. Happe, A. Hemschemeier, *Trends Biotechnol.* **2014**, *32*, 170–176.
[15] V. Fourmond, C. Greco, K. Sybirna, C. Baffert, P.-H. Wang, P. Ezanno, M. Montefiori, M. Bruschi, I. Meynial-Salles, P. Soucaille, J. Blumberger, H. Bottin, L. De Gioia, C. Leger, *Nat. Chem.* **2014**, *6*, 336–342.
[16] S. Ezzaher, J.-F. Capon, F. Gloaguen, F. Y. Pétillon, P. Schollhammer, J. Talarmin, N. Kervarec, *Inorg. Chem.* **2009**, *48*, 2–4.
[17] M. E. Carroll, B. E. Barton, T. B. Rauchfuss, P. J. Carroll, *J. Am. Chem. Soc.* **2012**, *134*, 18843–18852.
[18] R. Zaffaroni, T. B. Rauchfuss, D. L. Gray, L. De Gioia, G. Zampella, *J. Am. Chem. Soc.* **2012**, *134*, 19260–19269.
[19] S. Tschierlei, S. Ott, R. Lomoth, *Energy Environ. Sci.* **2011**, *4*, 2340–2352.
[20] M.-H. Chiang, Y.-C. Liu, S.-T. Yang, G.-H. Lee, *Inorg. Chem.* **2009**, *48*, 7604–7612.
[21] A. Jablonskytė, J. A. Wright, C. J. Pickett, *Dalton Trans.* **2010**, *39*, 3026–3034.
[22] G. Eilers, L. Schwartz, M. Stein, G. Zampella, L. de Gioia, S. Ott, R. Lomoth, *Chem. Eur. J.* **2007**, *13*, 7075–7084.
[23] S. Ezzaher, A. Gogoll, C. Bruhn, S. Ott, *Chem. Commun.* **2010**, *46*, 5775–5777.
[24] W. Dong, M. Wang, X. Liu, K. Jin, G. Li, F. Wang, L. Sun, *Chem. Commun.* **2006**, 305–307.
[25] F. Wang, M. Wang, X. Liu, K. Jin, W. Dong, L. Sun, *Dalton Trans.* **2007**, 3812–3819.
[26] D. Sellmann, M. Geck, M. Moll, *J. Am. Chem. Soc.* **1991**, *113*, 5259–5264.
[27] X. Zhao, C.-Y. Chiang, M. L. Miller, M. V. Rampersad, M. Y. Darensbourg, *J. Am. Chem. Soc.* **2003**, *125*, 518–524.
[28] U.-P. Apfel, D. Troegel, Y. Halpin, S. Tschierlei, U. Uhlemann, H. Görls, M. Schmitt, J. Popp, P. Dunne, M. Venkatesan, M. Coey, M. Rudolph, J. G. Vos, R. Tacke, W. Weigand, *Inorg. Chem.* **2010**, *49*, 10117–10132.
[29] R. Goy, U.-P. Apfel, C. Elleouet, D. Escudero, M. Elstner, H. Görls, J. Talarmin, P. Schollhammer, L. González, W. Weigand, *Eur. J. Inorg. Chem.* **2013**, 4466–4472.
[30] U.-P. Apfel, Y. Halpin, H. Görls, J. G. Vos, W. Weigand, *Eur. J. Inorg. Chem.* **2011**, 581–588.
[31] U.-P. Apfel, H. Görls, G. A. N. Felton, D. H. Evans, R. S. Glass, D. L. Lichtenberger, W. Weigand, *Helv. Chim. Acta* **2012**, *95*, 2168–2175.
[32] R. Goy, L. Bertini, C. Elleouet, H. Görls, G. Zampella, J. Talarmin, L. De Gioia, P. Schollhammer, U.-P. Apfel, W. Weigand, *Dalton Trans.* **2014**, *44*, 1690–1699.
[33] B. Wesslén, E. J. Vellan, B. Werdinius, H. Corrodi, G. Eriksson, R. Blinc, S. Pausak, L. Ehrenberg, J. Dumanović, *Acta Chem. Scand.* **1967**, *21*, 718–720.
[34] E. L. Eliel, V. S. Rao, S. Smith, R. O. Hutchins, *J. Org. Chem.* **1975**, *40*, 524–526.
[35] Y. Li, C. Nie, H. Wang, X. Li, F. Verpoort, C. Duan, *Eur. J. Org. Chem.* **2011**, 7331–7338.
[36] D. J. Crouthers, J. A. Denny, R. D. Bethel, D. G. Munoz, M. Y. Darensbourg, *Organometallics* **2014**, *33*, 4747–4755.
[37] L. Bertini, C. Greco, L. De Gioia, P. Fantucci, *J. Phys. Chem. A* **2009**, *113*, 5657–5670.
[38] E. J. Lyon, I. P. Georgakaki, J. H. Reibenspies, M. Y. Darensbourg, *Angew. Chem. Int. Ed.* **1999**, *38*, 3178–3180; *Angew. Chem.* **1999**, *111*, 3373–3376.

[39] J.-F. Capon, F. Gloaguen, P. Schollhammer, J. Talarmin, *J. Electroanal. Chem.* **2004**, *566*, 241 – 247.
[40] G. A. N. Felton, A. K. Vannucci, J. Chen, L. T. Lockett, N. Okumura, B. J. Petro, U. I. Zakai, D. H. Evans, R. S. Glass, D. L. Lichtenberger, *J. Am. Chem. Soc.* **2007**, *129*, 12521 – 12530.
[41] J. Chen, A. K. Vannucci, C. A. Mebi, N. Okumura, S. C. Borowski, M. Swenson, L. T. Lockett, D. H. Evans, R. S. Glass, D. L. Lichtenberger, *Organometallics* **2010**, *29*, 5330 – 5340.
[42] J. Windhager, M. Rudolph, S. Bräutigam, H. Görls, W. Weigand, *Eur. J. Inorg. Chem.* **2007**, 2748 – 2760.
[43] J.-F. Capon, S. Ezzaher, F. Gloaguen, F. Y. Pétillon, P. Schollhammer, J. Talarmin, T. J. Davin, J. E. McGrady, K. W. Muir, *New J. Chem.* **2007**, *31*, 2052 – 2064.
[44] G. A. N. Felton, B. J. Petro, R. S. Glass, D. L. Lichtenberger, D. H. Evans, *J. Am. Chem. Soc.* **2009**, *131*, 11290 – 11291.
[45] D. H. Evans, *Chem. Rev.* **2008**, *108*, 2113 – 2144.
[46] W. E. Geiger in *Prog. Inorg. Chem.* (Ed.: S. J. Lippard), Wiley, Hoboken, **1985**, pp. 275 – 352.
[47] D. Uhrhammer, F. A. Schultz, *J. Phys. Chem. A* **2002**, *106*, 11630 – 11636.
[48] J. B. Fernandes, L. Q. Zhang, F. A. Schultz, *J. Electroanal. Chem. Interfacial Electrochem.* **1991**, *297*, 145 – 161.
[49] D. T. Pierce, W. E. Geiger, *J. Am. Chem. Soc.* **1992**, *114*, 6063 – 6073.
[50] A. J. Downard, A. M. Bond, A. J. Clayton, L. R. Hanton, D. A. McMorran, *Inorg. Chem.* **1996**, *35*, 7684 – 7690.
[51] S. J. Borg, T. Behrsing, S. P. Best, M. Razavet, X. Liu, C. J. Pickett, *J. Am. Chem. Soc.* **2004**, *126*, 16988 – 16999.
[52] M. H. Cheah, S. P. Best, *Eur. J. Inorg. Chem.* **2011**, 1128 – 1137.
[53] A. M. Appel, D. L. DuBois, M. R. DuBois, *J. Am. Chem. Soc.* **2005**, *127*, 12717 – 12726.
[54] G. M. Jacobsen, J. Y. Yang, B. Twamley, A. D. Wilson, R. M. Bullock, M. R. DuBois, D. L. DuBois, *Energy Environ. Sci.* **2008**, *1*, 167 – 174.
[55] A. Prejzner-Morawska, *Folia Morphol.* **1978**, *37*, 103 – 112.
[56] U. J. Kilgore, J. A. S. Roberts, D. H. Pool, A. M. Appel, M. P. Stewart, M. R. DuBois, W. G. Dougherty, W. S. Kassel, R. M. Bullock, D. L. DuBois, *J. Am. Chem. Soc.* **2011**, *133*, 5861 – 5872.
[57] B. Keita, S. Floquet, J.-F. Lemonnier, E. Cadot, A. Kachmar, M. Benard, M.-M. Rohmer, L. Nadjo, *J. Phys. Chem. C* **2008**, *112*, 1109 – 1114.
[58] R. Trautwein, L. R. Almazahreh, H. Görls, W. Weigand, *Z. Anorg. Allg. Chem.* **2013**, *639*, 1512 – 1519.
[59] C. Greco, G. Zampella, L. Bertini, M. Bruschi, P. Fantucci, L. De Gioia, *Inorg. Chem.* **2007**, *46*, 108 – 116.
[60] P. Li, M. Wang, C. He, G. Li, X. Liu, C. Chen, B. Åkermark, L. Sun, *Eur. J. Inorg. Chem.* **2005**, 2506 – 2513.
[61] G. Zampella, P. Fantucci, L. D. Gioia, *J. Am. Chem. Soc.* **2009**, *131*, 10909 – 10917.
[62] J. O. Daiss, K. A. Barth, C. Burschka, P. Hey, R. Ilg, K. Klemm, I. Richter, S. A. Wagner, R. Tacke, *Organometallics* **2004**, *23*, 5193 – 5197.
[63] COLLECT, Data Collection Software; Nonius B. V., Netherlands, **1998**.
[64] Processing of X-Ray Diffraction Data Collected in Oscillation Mode": *Methods in Enzymology, Vol. 276, Macromolecular Crystallography, Part A* (Eds.: Z. Otwinowski, W. Minor, C. W. Carter, R. M. Sweet), Academic Press, New York, **1997**, pp. 307 – 326.
[65] SADABS 2.10, Bruker-AXS inc., **2002**, Madison, WI, U.S.A.
[66] G. M. Sheldrick, *Acta Crystallogr. Sect. A* **2008**, *64*, 112 – 122.
[67] R. Ahlrichs, M. Bar, M. Haser, H. Horn, C. Kolmel, *Chem. Phys. Lett.* **1989**, *162*, 165 – 169.

Received: November 13, 2014
Published online on February 17, 2015

CHEMISTRY
A European Journal

Supporting Information

Silicon–Heteroaromatic [FeFe] Hydrogenase Model Complexes: Insight into Protonation, Electrochemical Properties, and Molecular Structures

Roman Goy,[a] Luca Bertini,*[b] Helmar Görls,[a] Luca De Gioia,[b] Jean Talarmin,*[c] Giuseppe Zampella,*[b] Philippe Schollhammer,*[c] and Wolfgang Weigand*[a, d]

chem_201406087_sm_miscellaneous_information.pdf

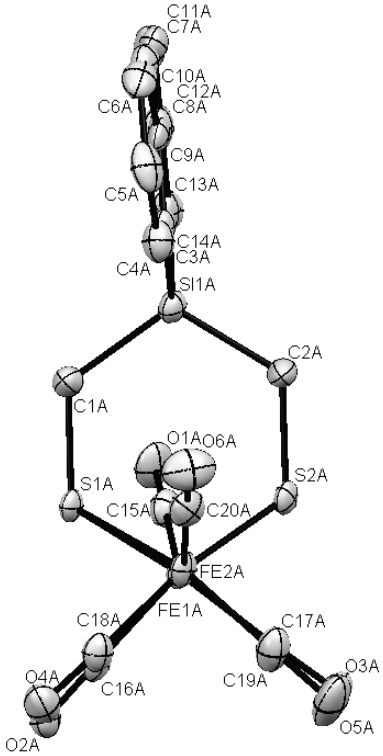

3

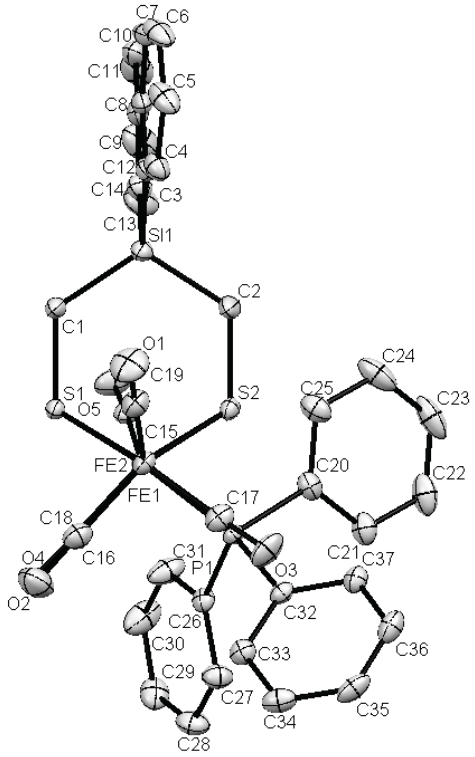

3a

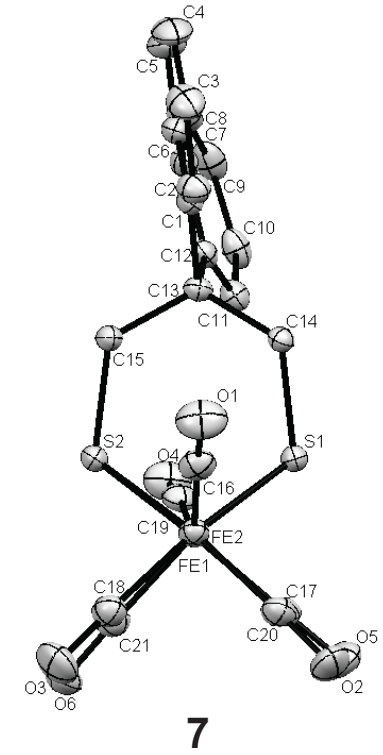

7

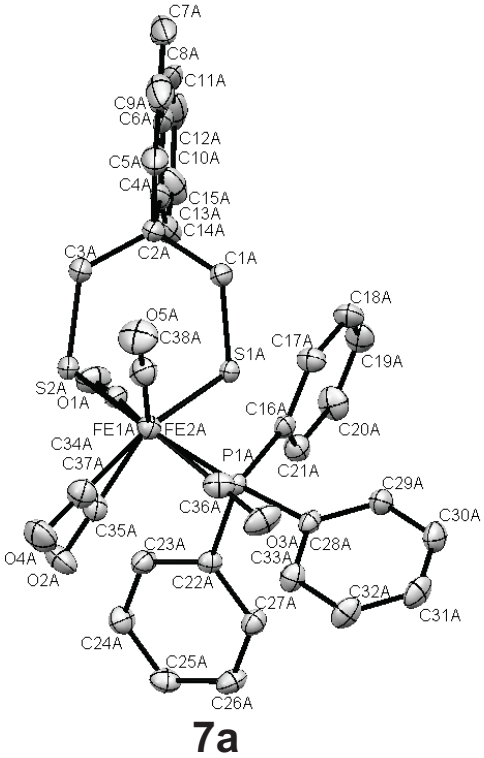

7a

Figure S1: Ortep views down the Fe-Fe bond of **3/3a** (first row) and **7/7a** (second row). Ellipsoids at the 50 % probability level. Hydrogens are omitted for clarity.

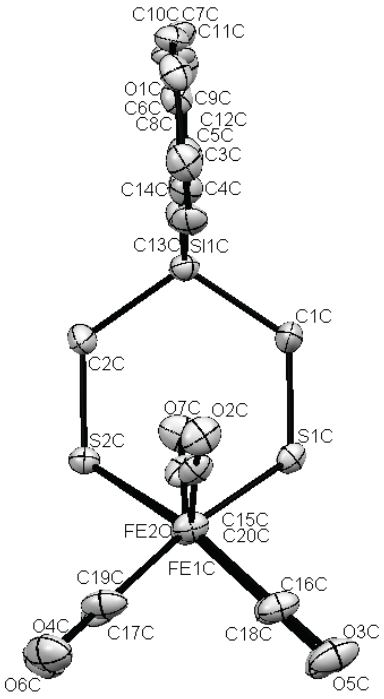

9

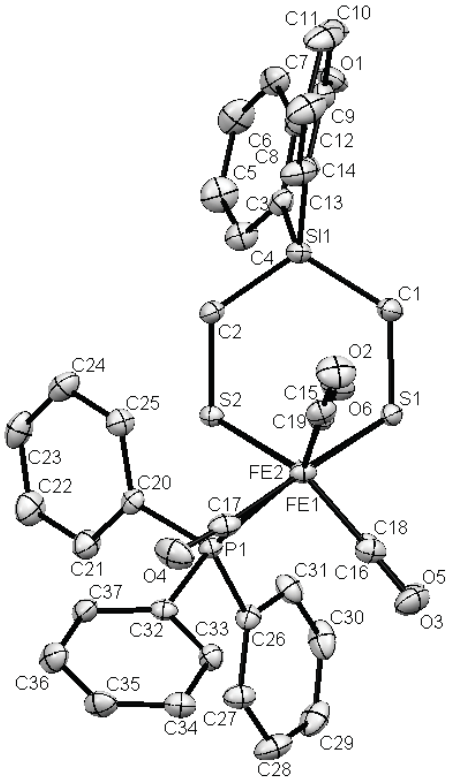

9a

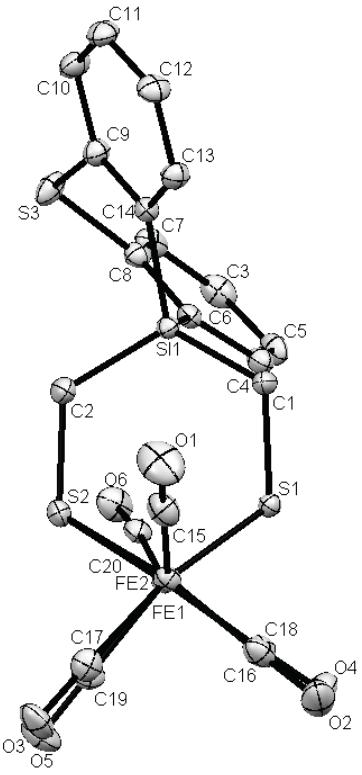

12

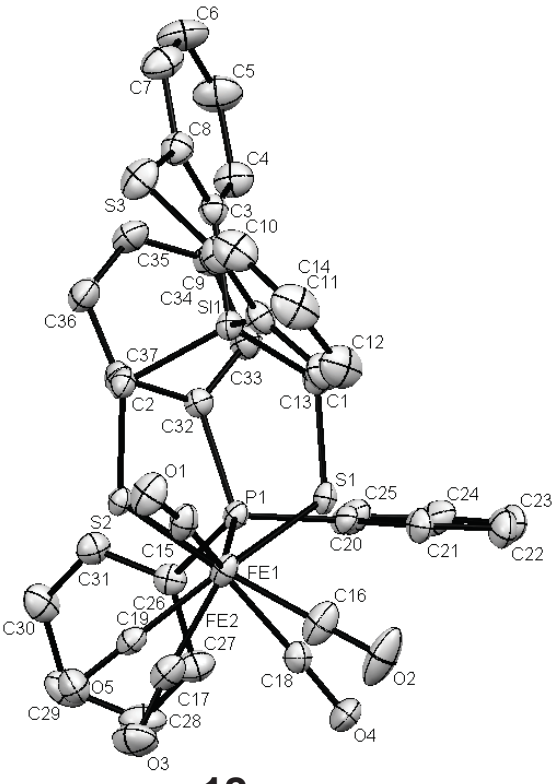

12a

Figure S2: Ortep views down the Fe-Fe bond of **9/9a** (first row) and **12/12a** (second row). Ellipsoids at the 50 % probability level. Hydrogens are omitted for clarity.

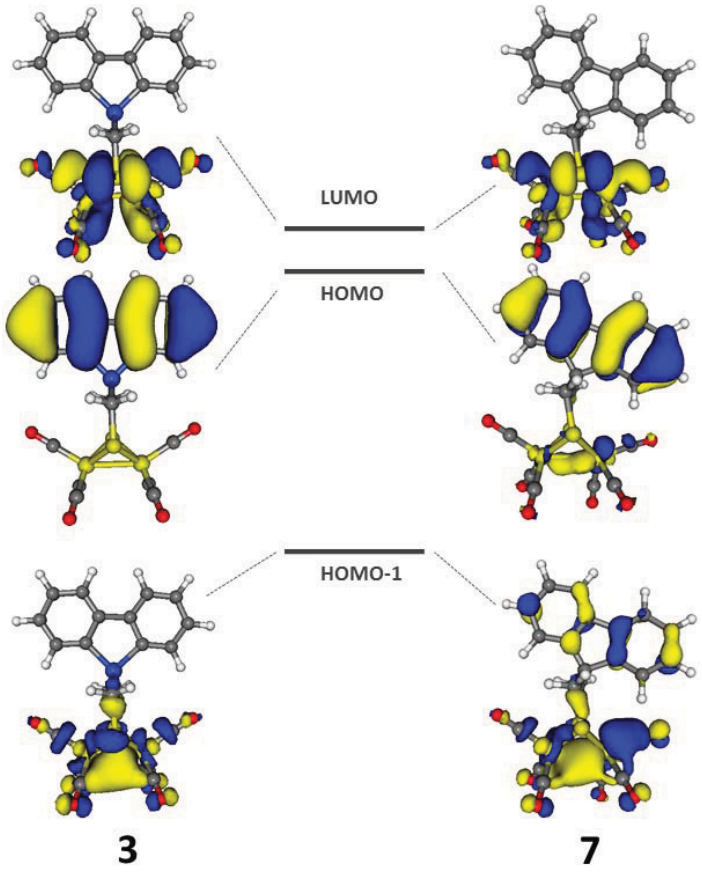

FigureS3. HOMO-1, HOMO and LUMO isosurface plots computed at 0.03 au, in **3** and **7**.

Table S1. **3** and **7** frontier MO eigenvalues and HOMO-LUMO gap (in hartree).

	3		**7**	
H-4	135a	-0.23615	131a	-0.24033
H-3	136a	-0.23035	132a	-0.23518
H-2	137a	-0.22649	133a	-0.22878
H-1	138a	-0.2229	134a	-0.21885
HOMO	139a	-0.21801	135a	-0.21794
LUMO	140a	-0.13198	136a	-0.13075
L+1	141a	-0.11462	137a	-0.11715
L+2	142a	-0.10887	138a	-0.11194
L+3	143a	-0.09458	139a	-0.08872
L+4	144a	-0.08581	140a	-0.08307
L+5	145a	-0.08004	141a	-0.07673
H/L gap		**0.08603**		**0.08719**

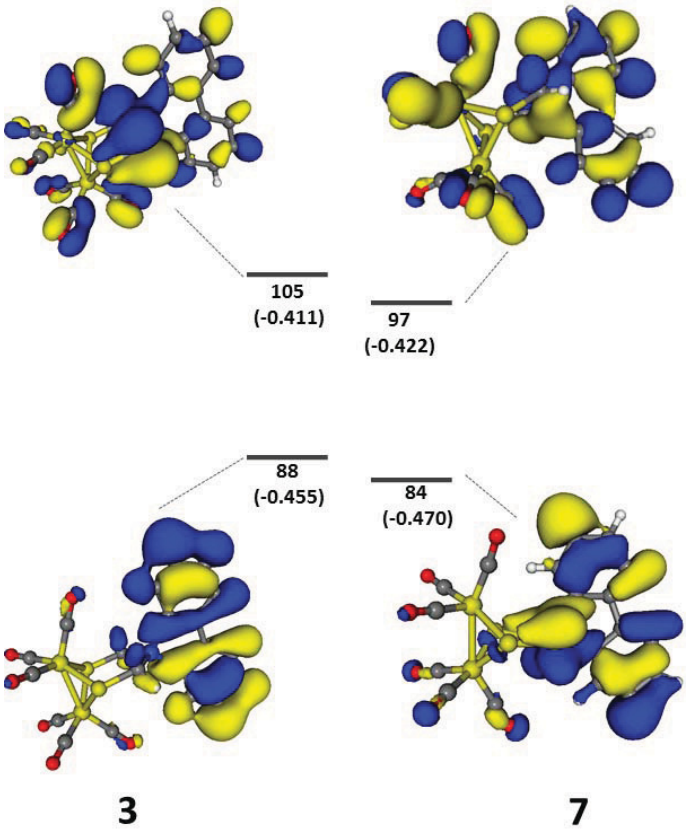

Figure S4. 3 and **7** isosurface plots of the MO involved in the C-X-C bonding (computed at 0.03 au) that resemble the zero-node π-MO of the allyl group. The MO eigenvalues are reported in hartree.

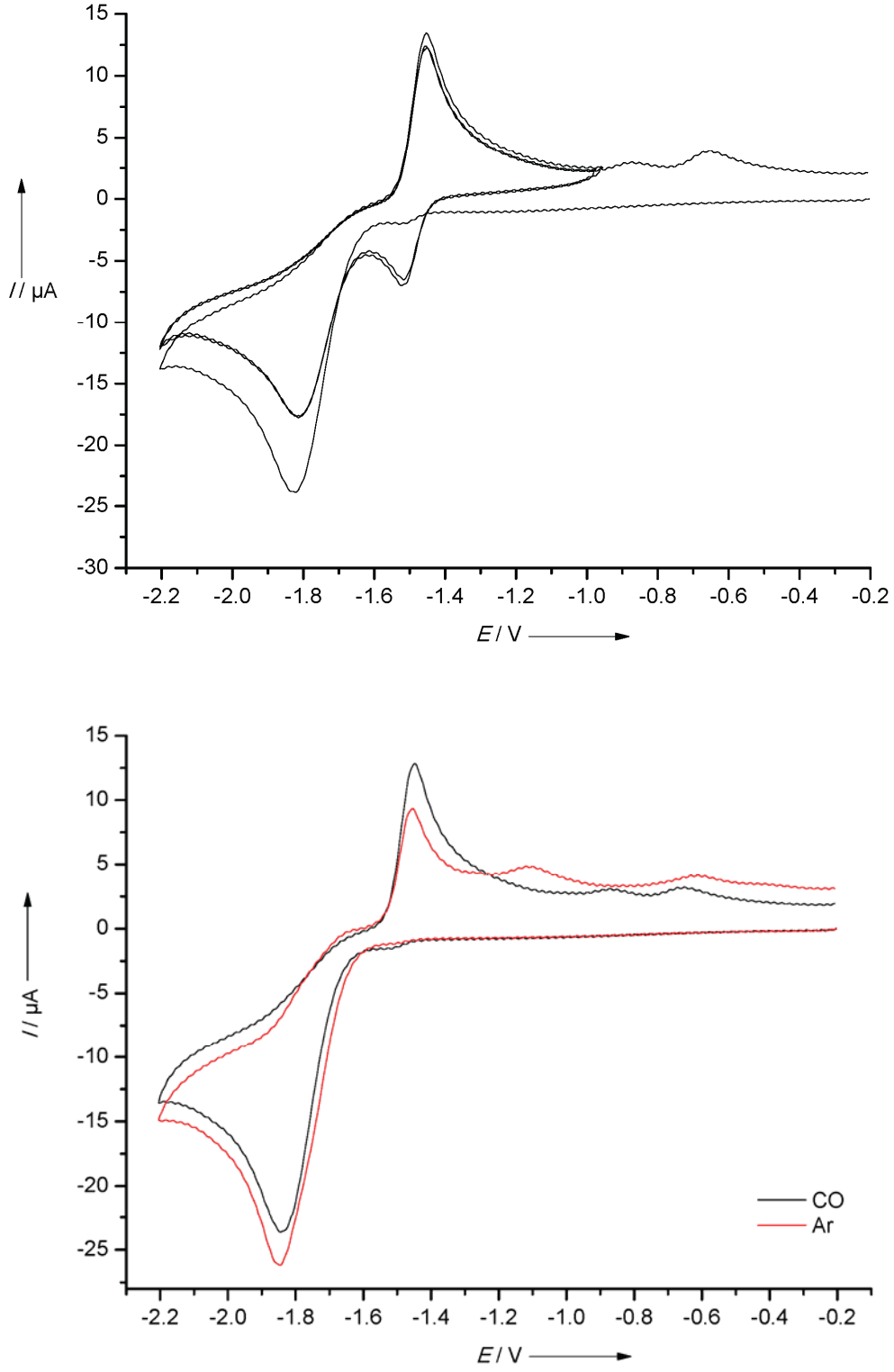

Figure S5. Cyclic voltammograms of **7a** (0.727 mM) under argon and CO (bottom) and reverse under CO (top) in CH_2Cl_2-[NBu_4][PF_6] (vitreous carbon electrode; 0.2 V/s; potentials are vs. Fc^+/Fc).

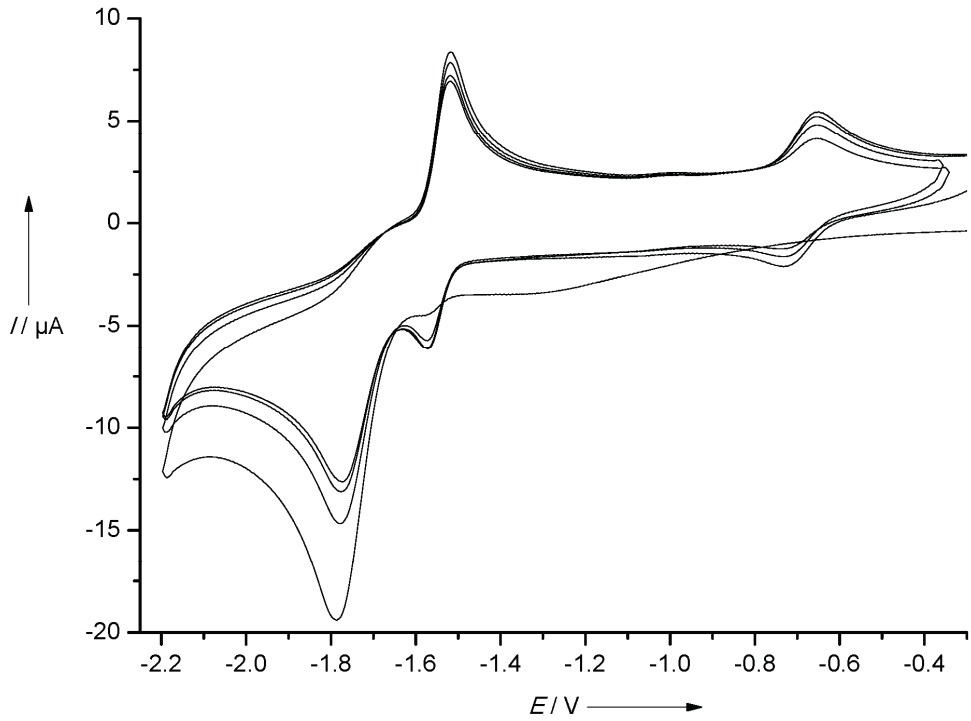

Figure S6. Cyclic voltammogram of **9a** (0.499 mM) reverse under CO in CH_2Cl_2-[NBu_4][PF_6] (vitreous carbon electrode; 0.5 V/s; potentials are vs. Fc^+/Fc).

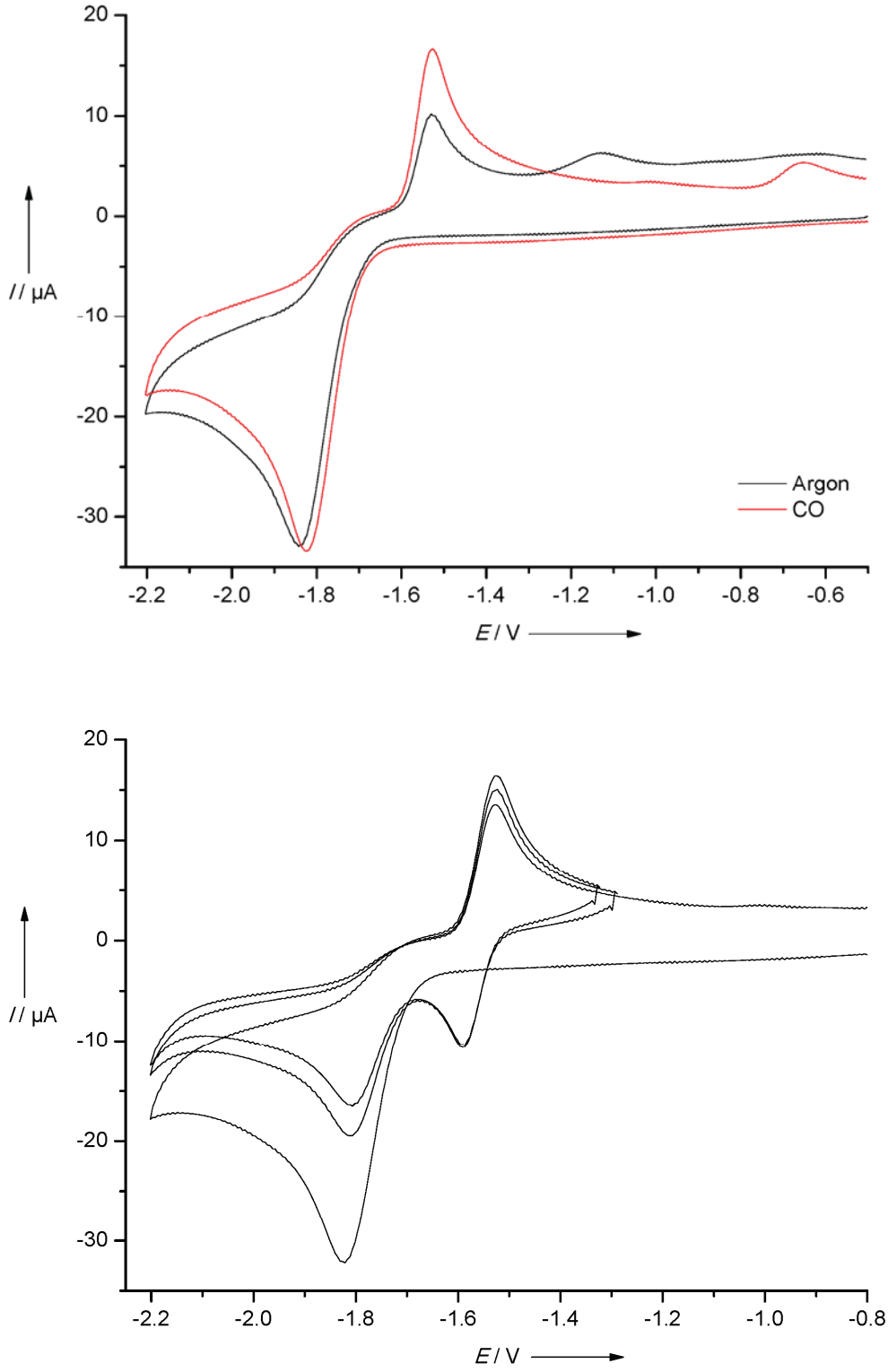

Figure S7. Cyclic voltammograms of **12a** (0.465 mM) under argon and CO (top) and reverse under CO (bottom) in CH_2Cl_2-$[NBu_4][PF_6]$ (vitreous carbon electrode; 0.5 V/s; potentials are vs. Fc^+/Fc).

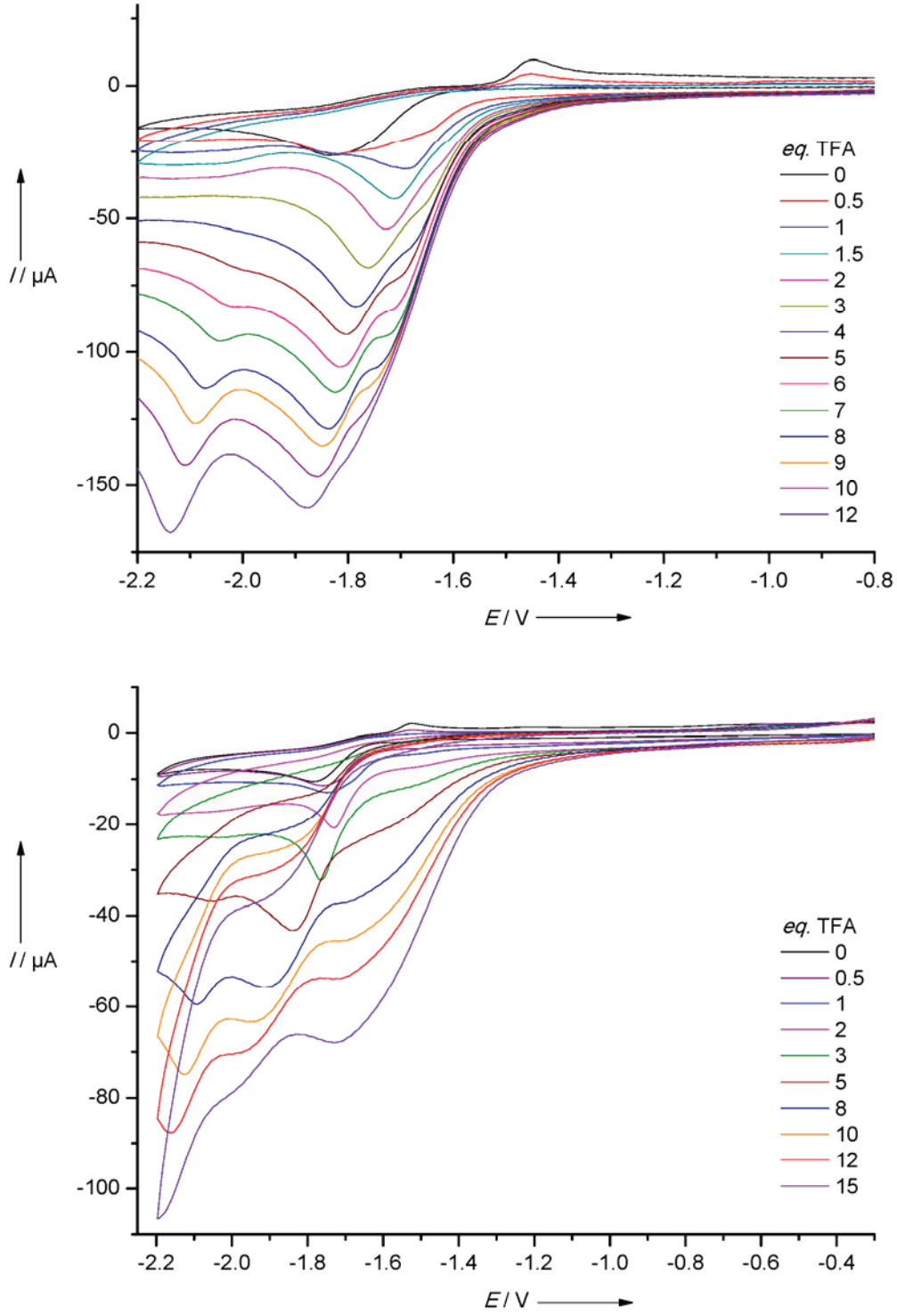

Figure S8: Cyclic voltammograms of **7a** (0.78mM, top) and **9a** (0.499mM, bottom) in CH_2Cl_2-$[NBu_4][PF_6]$ (vitreous carbon electrode; 0.2V/s; potentials are vs Fc^+/Fc).

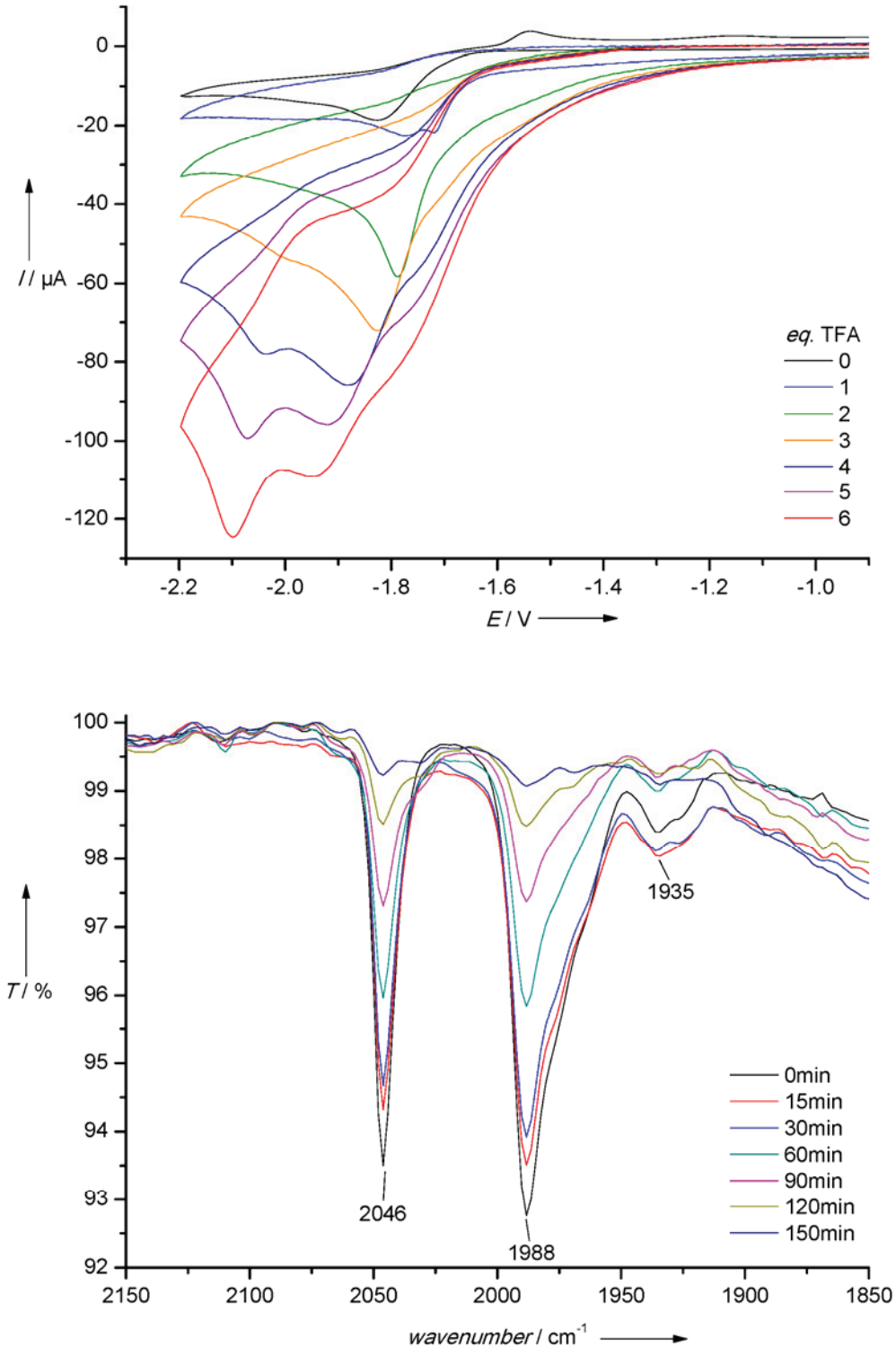

Figure S9: Cyclic voltammograms of **12a** (0.49 mM) in CH_2Cl_2-$[NBu_4][PF_6]$ (vitreous carbon electrode; 0.2 V/s; potentials are vs. Fc^+/Fc) (top). IR-spectrum with added 200 eq. TfOH (bottom).

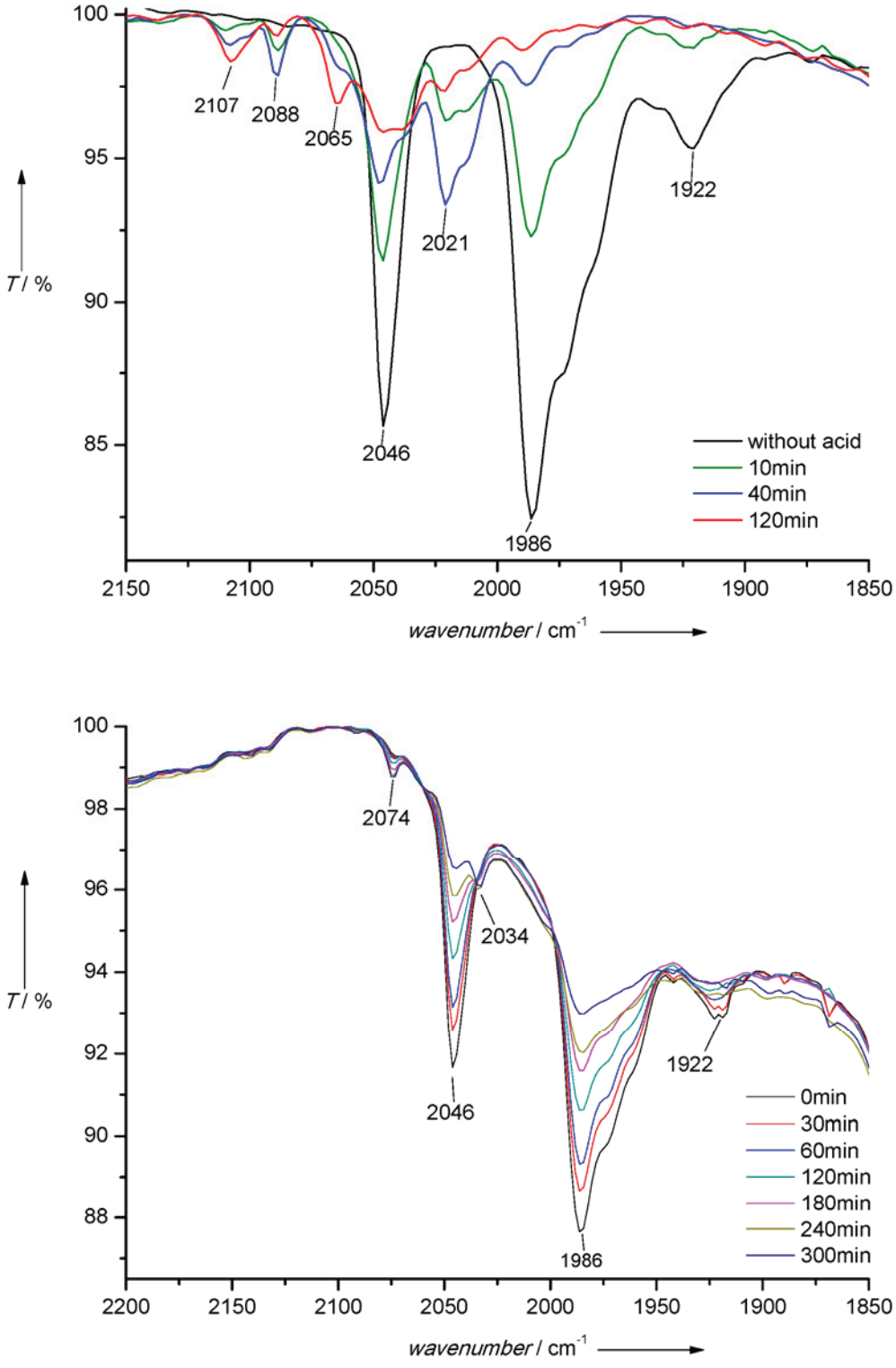

Figure S10: IR-spectra of **7a** (0.39 mM) in CH_2Cl_2 with 100 eq. of TfOH (top); with added 200 eq. TFA (bottom).

Table S2: Crystal data and refinement details for the X-ray structure determinations of the compounds **3a, 7,** and **7a.**

Compound	**3a**	**7**	**7a**
formula	$C_{37}H_{27}Fe_2O_5PS_2Si$	$C_{21}H_{12}Fe_2O_6S_2$	$C_{38}H_{27}Fe_2O_5PS_2$
fw ($g \cdot mol^{-1}$)	786.47	536.13	770.39
T/°C	-140(2)	-103(2)	-140(2)
crystal system	orthorhombic	monoclinic	monoclinic
space group	P b c a	P 2_1/c	P 2_1/n
a/ Å	25.0807(5)	9.6658(2)	9.9316(1)
b/ Å	10.4192(2)	21.6449(5	20.9550(3)
c/ Å	27.1868(5)	10.3379(2)	32.7228(5)
α/°	90	90	90
β/°	90	102.943(2)	91.899(1)
γ/°	90	90	90
V/Å^3	7104.5(2)	2107.90(8)	6806.42(16)
Z	8	4	8
ρ ($g \cdot cm^{-3}$)	1.471	1.689	1.504
μ (cm^{-1})	10.55	16.11	10.66
measured data	42018	21103	46686
data with I > 2σ(I)	7596	6368	14511
unique data (R_{int})	8118/0.0211	6368/0.0287	15517/0.0222
wR_2 (all data, on F^2)[a)]	0.0600	0.0669	0.0766
R_1 (*I* > 2σ(*I*)) [a)]	0.0240	0.0285	0.0369
S [b)]	1.087	0.932	1.250
Res. dens./e·Å^{-3}	0.384/-0.304	0.441/-0.303	0.684/-0.563
absorpt method	multi-scan	multi-scan	multi-scan
absorpt corr $T_{min}/_{max}$	0.6578/0.7654	0.5948/0.9533	0.7211/0.7456
CCDC No.	1028091	1028775	1028092

Table S3: Crystal data and refinement details for the X-ray structure determinations of the compounds **9**, **9a**, 1**2** and **12a.**

Compound	**9**	**9a**	**12**	**12a**
formula	$C_{20}H_{12}Fe_2O_7S_2Si$	$C_{37}H_{27}Fe_2O_6PS_2Si$	$C_{20}H_{12}Fe_2O_6S_3Si$	$C_{37}H_{27}Fe_2O_5PS3Si$
fw ($g \cdot mol^{-1}$)	568.21	802.47	584.27	818.53
T/°C	-140(2)	-140(2)	-140(2)	-140(2)
crystal system	triclinic	monoclinic	triclinic	triclinic
space group	P $\bar{1}$	P 2_1/c	P $\bar{1}$	P $\bar{1}$
a/ Å	7.4982(2)	12.8289(3)	7.8110(2)	12.5266(4)
b/ Å	20.3948(6)	23.9902(5)	12.2886(3)	12.7723(5)
c/ Å	23.4037(7)	12.0117(2)	13.3607(3)	13.2791(5)
α/°	114.635(2)	90	114.026(1)	82.853(2)
β/°	90.822(2)	109.099(1)	91.707(1)	65.387(2)
γ/°	92.164(2)	90	101.525(1)	66.719(2)
V/Å^3	3249.13(16)	3493.32(12)	1138.83(5)	1772.21(11)
Z	6	4	2	2
ρ ($g \cdot cm^{-3}$)	1.742	1.526	1.704	1.534
μ (cm^{-1})	16.29	10.76	16.36	11.17
measured data	18474	20528	7157	10219
data with I > 2σ(I)	11245	6583	4771	7085
unique data (R_{int})	13620/0.0373	7974/0.0415	5130/0.0177	7660/0.0222
wR_2 (all data, on F^2)[a)]	0.1682	0.0832	0.0663	0.0867
R_1 (*I* > 2σ(*I*)) [a)]	0.0817	0.0420	0.0296	0.0347
S [b)]	1.223	1.091	1.081	1.086
Res. dens./e·Å^{-3}	0.899/-0.658	0.429/-0.328	0.390/-0.398	0.439/-0.502
absorpt method	multi-scan	multi-scan	multi-scan	multi-scan
absorpt corr $T_{min}/_{max}$	0.6213/0.7456	0.6839/0.7456	0.6743/0.7456	0.6982/0.7564
CCDC No.	1028093	1028094	1028094	1028096

[a)] Definition of the *R* indices: $R_1 = (\Sigma || F_o| - |F_c ||)/\Sigma |F_o|$;
$wR_2 = \{\Sigma[w(F_o^2-F_c^2)^2]/\Sigma[w(F_o^2)^2]\}^{1/2}$ with $w^{-1} = \sigma^2(F_o^2) + (aP)^2+bP$; $P = [2F_c^2 + Max(F_O^2]/3$;
[b)] $s = \{\Sigma[w(F_o^2-F_c^2)^2]/(N_o-N_p)\}^{1/2}$.

TableS4: Selected bond lengths (Å) and angles (°) for 3a.

Fe1-Fe2	2.5939(3)	C15-Fe1-Fe2	142.91(5)
Fe1-S1	2.2488(4)	C19-Fe2-Fe1	148.35(4)
Fe1-S2	2.2479(4)	S1-C1-Si1	122.33(8)
Fe2-S1	2.2510(4)	S2-C2-Si1	122.49(8)
Fe2-S2	2.2382(4)	C1-Si1-C3	110.66(6)
Fe2-P1	2.2393(4)	C2-Si1-C14	114.43(7)
P1-C20	1.8341(14)	C2-Si1-C3	109.57(7)
P1-C26	1.8386(14)	C1-Si1-C14	116.07(7)
P1-C32	1.8258(14)	C1-Si1-C2	112.48(7)
S1-C1	1.8204(14)	C3-Si1-C14	91.62(7)
S2-C2	1.8236(15)		
C1-Si1	1.8732(15)		
C2-Si1	1.8702(15)		

TableS5: Selected bond lengths (Å) and angles (°) for 7.

Fe1-Fe2	2.5003(3)	C16-Fe1-Fe2	146.55(3)
Fe1-S1	2.2583(4)	C19-Fe2-Fe1	160.03(5)
Fe1-S2	2.2631(4)	S1-C14-C13	121.35(10)
Fe2-S1	2.2712(4)	S2-C15-C13	123.72(11)
Fe2-S2	2.2465(4)	C14-C13-C15	114.56(12)
S1-C14	1.8350(15)	C1-C13-C14	110.17(12)
S2-C15	1.8322(15)	C12-C13-C15	113.24(12)
C14-C13	1.525(2)	C12-C13-C14	112.96(12)
C13-C15	1.556(2)	C1-C13-C15	104.27(12)

TableS6: Selected bond lengths (Å) and angles (°) for 7a.

Fe1A-Fe2A	2.5693(4)	C34A-Fe1A-Fe2A	153.01(7)
Fe1A-S1A	2.2447(6)	C38A-Fe2A-Fe1A	144.57(8)
Fe1A-S2A	2.2473(6)	S1A-C1A-C2A	123.00(15)
Fe2A-S1A	2.2507(6)	S2A-C3A-C2A	124.08(16)
Fe2A-S2A	2.2626(6)	C1A-C2A-C3A	115.04(18)
Fe1A-P1A	2.2442(6)	C1A-C2A-C15A	111.51(19)
P1A-C16A	1.837(2)	C1A-C2A-C4A	106.75(18)
P1A-C22A	1.839(2)	C15A-C2A-C4A	100.78(19)
P1A-C28A	1.824(2)	C15A-C2A-C3A	113.43(19)
S1A-C1A	1.830(2)	C4A-C2A-C3A	108.03(19)
S2A-C3A	1.837(2)		
C1A-C2A	1.548(3)		
C2A-C3A	1.559(3)		

TableS7: Selected bond lengths (Å) and angles (°) for 9.

Fe1A-Fe2A	2.5204(14)	C15A-Fe1A-Fe2A	149.3(2)
Fe1A-S1A	2.2521(18)	C20A-Fe2A-Fe1A	151.3(2)
Fe1A-S2A	2.2478(19)	S1A-C1A-Si1A	124.0(4)
Fe2A-S1A	2.2525(19)	S2A-C2A-Si1A	123.8(4)
Fe2A-S2A	2.2562(18)	C1A-Si1A-C3A	111.5(3)
S1A-C1A	1.820(7)	C2A-Si1A-C14A	112.5(3)
S2A-C2A	1.832(7)	C2A-Si1A-C3A	109.6(3)
C1A-Si1A	1.884(7)	C1A-Si1A-C14A	110.2(3)
C2A-Si1A	1.886(7)	C1A-Si1A-C2A	111.6(3)
		C3A-Si1A-C14A	101.0(3)

TableS8: Selected bond lengths (Å) and angles (°) for 9a.

Fe1-Fe2	2.5807(5)	C15-Fe1-Fe2	141.01(9)
Fe1-S1	2.2530(7)	C19-Fe2-Fe1	148.44(8)
Fe1-S2	2.2451(8)	S1-C1-Si1	122.53(15)
Fe2-S1	2.2316(7)	S2-C2-Si1	120.27(15)
Fe2-S2	2.2595(7)	C1-Si1-C3	116.11(13)
Fe2-P1	2.2490(7)	C2-Si1-C14	111.01(12)
P1-C20	1.836(3)	C2-Si1-C3	108.92(13)
P1-C26	1.843(3)	C1-Si1-C14	108.43(13)
P1-C32	1.829(3)	C1-Si1-C2	111.92(13)
S1-C1	1.824(3)	C3-Si1-C14	99.81(13)
S2-C2	1.832(3)		
C1-Si1	1.874(3)		
C2-Si1	1.874(3)		

TableS9: Selected bond lengths (Å) and angles (°) for 12.

Fe1-Fe2	2.5124(4)	C15-Fe1-Fe2	146.28(8)
Fe1-S1	2.2542(6)	C20-Fe2-Fe1	151.68(7)
Fe1-S2	2.2659(6)	S1-C1-Si1	113.66(11)
Fe2-S1	2.2885(6)	S2-C2-Si1	122.90(12)
Fe2-S2	2.2455(6)	C1-Si1-C3	110.46(10)
S1-C1	1.835(2)	C2-Si1-C14	104.60(9)
S2-C2	1.823(2)	C2-Si1-C3	115.47(10)
C1-Si1	1.858(2)	C1-Si1-C14	114.16(9)
C2-Si1	1.872(2)	C1-Si1-C2	108.09(10)
		C3-Si1-C14	104.07(9)

TableS10: Selected bond lengths (Å) and angles (°) for 12a.

Fe1-Fe2	2.5012(4)	C15-Fe1-Fe2	146.88(7)
Fe1-S1	2.2960(6)	P1-Fe2-Fe1	156.62(2)
Fe1-S2	2.2603(6)	S1-C1-Si1	114.62(12)
Fe2-S1	2.2591(6)	S2-C2-Si1	121.14(12)
Fe2-S2	2.2884(5)	C1-Si1-C3	111.25(10)
Fe2-P1	2.2434(6)	C2-Si1-C14	113.31(10)
P1-C20	1.830(2)	C2-Si1-C3	106.92(10)
P1-C26	1.839(2)	C1-Si1-C14	112.00(11)
P1-C32	1.831(2)	C1-Si1-C2	108.98(10)
S1-C1	1.829(2)	C3-Si1-C14	104.22(10)
S2-C2	1.828(2)		
C1-Si1	1.863(2)		
C2-Si1	1.876(2)		

4.4 **[RG4]**

Enhanced Photocatalytic Hydrogen Evolution by Silicon-Containing [FeFe] Hydrogenase Models

Roman Goy[1], Luca Bertini[2], Tobias Rudolph[3], Martin Schulz[4], Giuseppe Zampella[2], Benjamin Dietzek[4], Felix H. Schacher[3], Luca De Gioia[2], Wolfgang Weigand[5]

In preparation

Comprehensive photocatalytic hydrogen evolution experiments were performed for the small and compact [FeFe] hydrogenase model complexes, which were reported in the publication "Silicon-Heteroaromatic [FeFe] Hydrogenase Model Complexes: Insight into Protonation, Electrochemical Properties and Molecular Structures" [RG3]. Optical properties for all reported compounds were investigated in detail for a better understanding of possible photocatalytic hydrogen generation mechanisms as well as further theoretical studies to rationalize the obtained results. By this way, a complete H_2 photocatalytic mechanism could be established as well as the formation pathway of the η^2-H_2 complex.

Photochemical H_2 evolution experiments were carried out with the *1*-silafluorene *all*-CO model complex as the reference under different conditions, which affects the catalytic efficiency dramatically. After establishment of optimized conditions, experiments were performed with the *10,10'*-phenoxsilane, *10,10'*-phenothiasilane as well as the 9-fluorene containing *all*-CO complexes. The catalysis experiments were run in an organic environment as well as in pure aqueous solutions by effectively introduction of hydrophilicity *via* micelle solutions of SDS and CTAB, respectively, resulting in the highest catalytic efficiency reported so far for micellar systems utilizing photoactive [FeFe] hydrogenase model complexes.

Within this work a turn-over number of 539 were reached under optimized conditions after 7 h irradiation, what represents an exceptionally turn-over frequency of 77 molecules H_2/h. The approach of creating such small and compact [FeFe] hydrogenase model complexes makes this design to a powerful platform for proton reduction catalysts.

Enhanced Photocatalytic Hydrogen Evolution by Silicon-containing [FeFe] Hydrogenase models

Roman Goy,[a] Luca Bertini,[b] Tobias Rudolph,[c] Martin Schulz,[d] Giuseppe Zampella,[b] Benjamin Dietzek,[d] Felix H. Schacher,[c] Luca De Gioia,[b] Wolfgang Weigand[a*]

[a] Institut für Anorganische und Analytische Chemie, Friedrich-Schiller-Universität, Humboldtstraße 8, 07743 Jena, Germany, E-mail: wolfgang.weigand@uni-jena.de
[b] Department of Biotechnology and Biosciences, University of Milano-Bicocca, 20126 Milan, Italy
[c] Laboratory of Organic and Macromolecular Chemistry, Friedrich Schiller University Jena, Humboldtstraße 10, 07743 Jena, Germany
[d] Institut für Physikalische Chemie, Friedrich-Schiller-Universität, Helmholtzweg 4, 07743 Jena, Germany

Keywords: Hydrogen/Photocatalysis/Micelle/Hydrogenase/TDDFT

Abstract

Light-induced hydrogen evolution experiments for small and compact catalysts, in which the photosensitizer is directly attached to the dithiolate bridge of [FeFe] hydrogenase model complexes, were successfully performed. The recently published silicon-containing photoactive [FeFe]-H_2ase mimics **1a**-**4a** showed remarkable and promising catalytic activities as well as stabilities during photocatalytic hydrogen generation experiments. The catalysis was run in an organic environment as well as in pure aqueous solutions by effectively introduction of hydrophilicity *via* micelle solutions of sodium dodecyl sulfate (SDS) and cetrimonium bromide (CTAB), respectively. In this study a turn-over number of 539 was reached under optimized conditions, what represents an exceptionally turn-over frequency of 77 molecules H_2/h. Extensive theoretical investigations were performed in order to rationalize the catalytic experiments and to elucidate possible catalytic mechanisms.

Introduction

The production of hydrogen as a promising post-oil energy carrier appears as a sustainable solution owing to his remarkable properties.[1–4] Producing H_2 allows for the conversion of renewable energy sources, like *e.g.* solar power, into a storable form. However, the development of efficient and noble-metal-free catalysts is required if we want this process to be sustainable.[5–11] Much attention is paid to proteins called hydrogenases, which are highly capable systems for H_2 evolution in nature.[12–14] In the last 15 years a wide range of simple bioinspired model systems for hydrogenases, which are mimicking the structure or function of their active site and powered by photosensitizers are published. Multicomponent systems with commonly used organometallic complexes as sensitizers containing Ru, Re, Rh or Ir are often reported[15–19] as well as systems, in which the light harvester is covalently linked to the catalytic active site revealing moderate turn-over-numbers (TON < 127).[20–25] Further adaptations including complete hybrid artificial photosynthetic systems,[26], dendrimer-based systems,[27], ZnS-nanoparticles[28] or quantum dots[29] as light harvester were reported. An entire spectrum of [FeFe] hydrogenase mimics have been established, but most of them are just soluble in organic solvents or mixtures of organic solvents and H_2O because of their insolubility. In order to force a photocatalytic H_2 generation under aqueous conditions, the hydrophobic catalysts were incorporated into supramolecular systems like micelles[30] and cyclodextrins.[31] Even the inclusion into metal-organic frameworks,[32,33] molecular thieves[34] or hydrogels[35] as solid supported molecular catalysts seems to be feasible approaches.

We address these issues by an extensive and substantial characterization of the recently published silicon-containing photoactive [FeFe]-H_2ase mimics **1a**-**4b** (Scheme 9)[22,36]. Photocatalytic hydrogen evolution experiments were performed in an organic environment and in pure aqueous solutions by introduction of hydrophilicity *via* micelle solutions of SDS (sodium dodecyl sulfate) and CTAB (cetrimonium bromide), respectively. Comparison of these conditions will promote the understanding of hydrogen production by hydrophobic [FeFe] H_2ase model complexes. To explore possible catalytic mechanisms, several experimental results were addressed to DFT calculations. A splendid catalytic activity and efficiency in organic solvents as well as aqueous solutions is reported by small, compact,

favorable and good accessible [FeFe] hydrogenase mimics with the photosensitizer directly imbedded into the bridging dithiolate unit (Scheme 9).

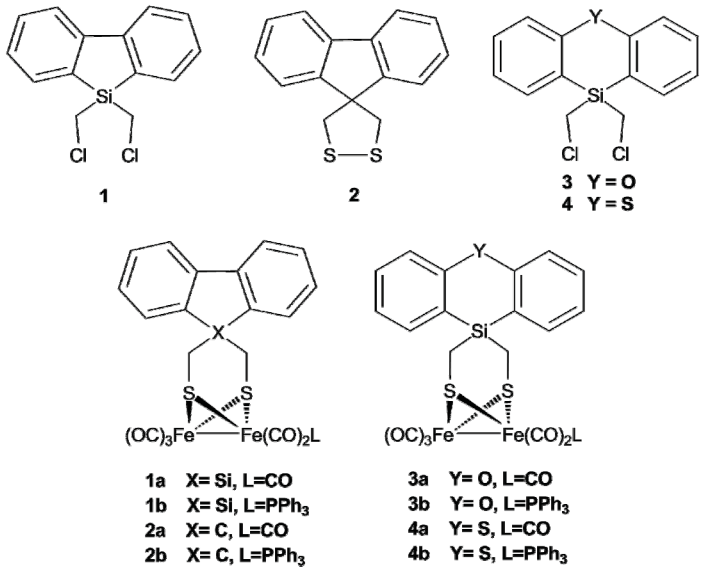

Scheme 9. Herein studied [FeFe] hydrogenase model complexes and precursors **1-4b**.

Results and Discussion

Photophysically Properties

The UV-vis absorption spectra for the compounds **1**, **2**, **3** and **4** are shown in Figure 29. The 1-silafluorene moiety of **1** shows intense bands between 220-245 nm and 260-290 nm. Compared with the fluorene moiety of **2** a hypsochromically shift by 7 nm of these bands is observed, which is related to the substitution of the silicon by a carbon atom while the intense band around 210 nm is similar in both systems. The phenoxsilane moiety of **3** exhibits weak bands between 260-300 nm and intense bands at 247 nm and 210 nm. Compared to the phenothiasilane moiety of **4** these intense bands are shifted bathochromically by 8 nm and the weaker bands at 265-330 nm are broader. In contrast to their *all*-CO complexes ([FeFe] hydrogenase mimics coordinated by six CO ligands at the two iron atoms) **1a**, **2a**, **3a** and **4a** and *mono*-PPh_3 complexes ([FeFe] hydrogenase mimics coordinated by five CO ligands and one PPh_3 ligand at the two iron atoms) **1b**, **2b**, **3b** and **4b** (Figures S1-S4), higher intensities of all absorption bands are observed for the complexes. New absorption bands between 300 and 400 nm were observed, which are related to the σ-σ* of the

Fe-Fe unit. In the *mono*-PPh_3 complexes these bands are shifted bathochromically compared to their *all*-CO analogues due to the higher electron density at the Fe-Fe unit caused by the better donating of the PPh_3-group compared to carbon monoxide.

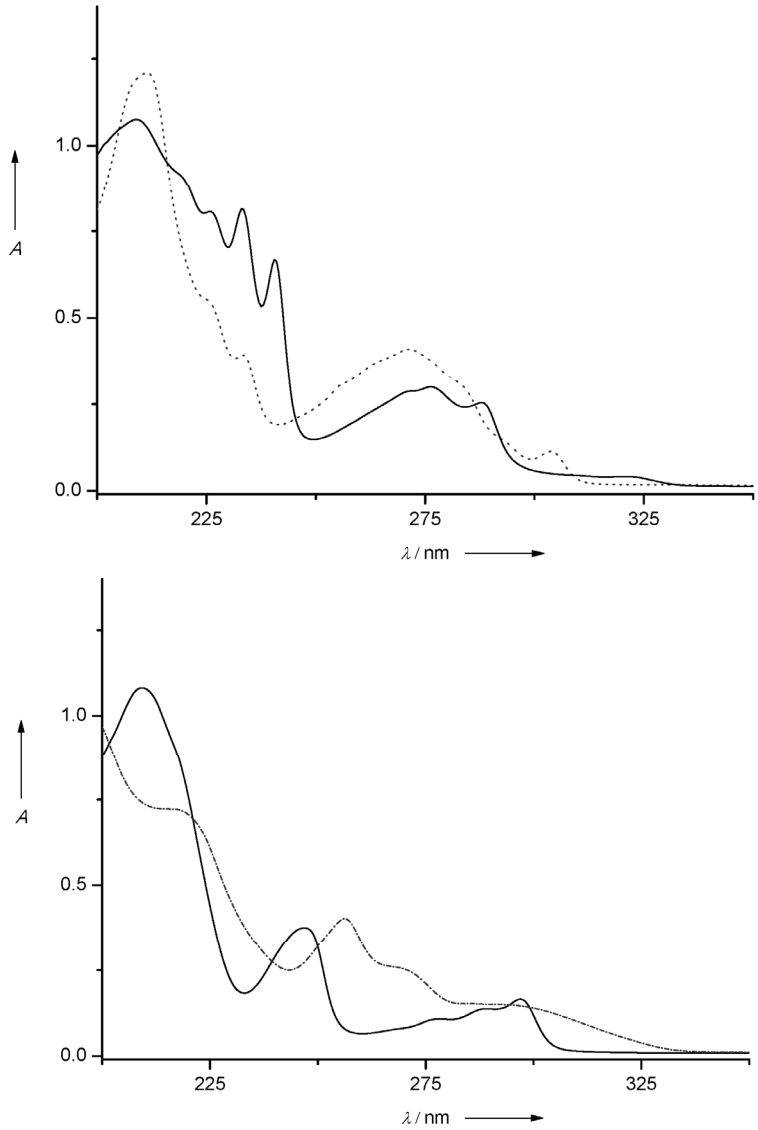

Figure 29. UV-vis spectra for compound **1** (black line, top), **2** (grey dotted, top), **3** (black line, bottom) and **4** (grey dash dotted, bottom), 27 µM in acetonitrile in comparison.

To gain more insights into the photophysical properties of the complexes, the absorption spectra of the series **1a**-**4a** have been computed at TDDFT BP86 level (Figures S5/S6, Tables S1/S2). The band assignments can be made at first instance on the basis of the comparison between the computed spectra of the systems and of the heteroaromatic rings as isolated molecules, considering the observed transitions as localized on the Fe_2S_2 core, on the heteroaromatic rings or as charge transfer band

between the two parts of the system. The most intense bands are essentially the results of the superposition of a large number of transitions that mainly involve the aromatic rings, while the very weak features are due to the transitions that involve the Fe_2S_2 core.

In the following the TDDFT investigation on the photophysically and photochemical properties will be focused on the **1a** and **2a** systems. Therefore the features of the lower energy parts of their absorption spectra were considered into detail, which are more relevant in their photodynamic behavior (Tables S3/S4, Figures S7/S8). The ground state HOMOs of **1a** and **2a** are characterized by the π-system orbital contribution of the phenyl rings. The HOMO of **2a** has also a small Fe-Fe σ-bonding contribution that is not observed for the HOMO of **1a**. The HOMO-1 for both systems is the fully Fe-Fe σ-bonding molecule orbital. The two LUMOs are very similar and characterized by the contributions of the Fe-Fe σ*-antibonding orbitals and sulfur *p*-orbitals. These FMO-features imply the elongation of the Fe-Fe bond upon population of the LUMO as well as a charge transfer toward the sulfur atoms at the same time. As already figured out for simpler [FeFe] hydrogenase models,[37] these facts support the stabilization of the rotated isomers with respect to the all terminal CO ligand forms and/or favoring the weakening/dissociation of a Fe-S bond. A second interesting aspect in the MO composition is related to the higher molecular symmetry of **1a** compared to **2a**, which implies a lower mixing of the Fe_2S_2 and heteroaromatic ring orbital contributions (Figures S7/S8).

Focusing the different properties of **1a** and **2a** regarding their photoluminescence properties, calculations at TDDFT PBE0 level has been performed to better reproduce excitation energies. To focus on the effect of the Si substitution, **1a** and **2a** were reduced to their simplified silafluorene and fluorene aromatic systems, respectively (black molecules in Scheme 2). In Scheme 2 are reported the computed excitation energies for the first singlet and the first two triplet states, which correspond to the π→π* transitions. The HOMO-LUMO gaps are 5.36 eV and 5.21 eV for fluorene and silafluorene, respectively.

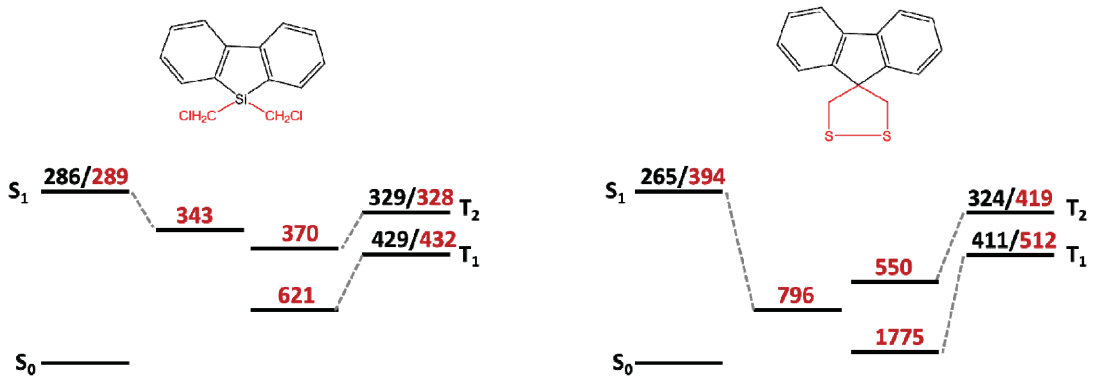

Scheme 2. PBE0 vertical excitation energies (in nm) for their simplified silafluorene and fluorene systems (black molecules and numbers) and compounds **1** and **2** (red molecules and numbers) computed at the corresponding ground state minimum structures. Excitation energies are also computed at the S_1, T_1 and T_2 TDDFT optimized structures.

The S_1 and T_1 excited states correspond to the HOMO→LUMO one-electron transition and in T_2 to the HOMO-1→LUMO+1. Interestingly, for both systems T_1 and T_2 states lie below S_1.[38] As expected, the silicon substitution of the carbon atom implies the lowering of the excitation energies of the three considered states. If compounds **1** and **2** are supposed, the effect of the 5-membered disulfide ring in **2** results in a significant excitation energy lowering with respect to **1**. By TDDFT geometry optimization of S_1 and T_1 the photoluminescence wavelength for **1** can be evaluated at 343 nm (S_1) and 621 nm (T_1). Switching back to the [FeFe] hydrogenase models **1a** and **2a**, nine (**2a**) and ten (**1a**) triplet states below the lowest singlet S_1 state (Figure S9) can be found. Focusing on the first singlet state S_1 and the first two triplet states T_1 and T_2 (Scheme 3), the excitation energy of T_1 is much lower in energy than that of S_1.

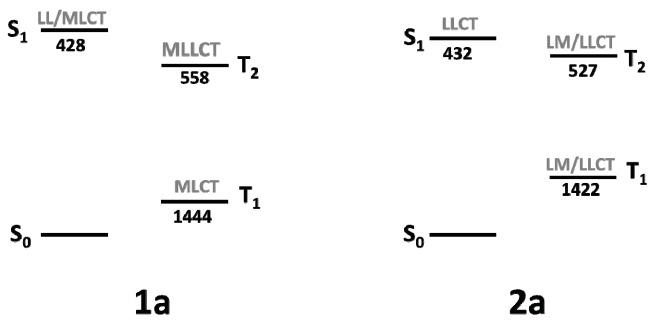

Scheme 3. PBE0 vertical excitation energies (in nm) for **1a** and **2a** computed at the corresponding ground state minimum structures.

By computing the differential MO Mulliken populations for each excited state computed according to the TDDFT single-electronic transitions (Table 1), the S_1 and T_1 states of **1a** are matching to metal-to-ligand (MLCT) and ligand-to-ligand (LLCT) bands characterized by Fe→CO and S→CO charge transfers (CT), respectively, with no involvement of the heteroaromatic ring. Contrary T_2 is a MLCT with a significant FeS→ring transfer involving the LUMO+1 MO (π* orbital combinations of the heteroaromatic ring) as presented in Figure S8. The first excitation of **1a** similar to the π→π* triplet excitations in **1** is the LM/LLCT T_8 excitation, in which the main mono-electronic transition is HOMO→LUMO+1. Due to the similar photoluminescence spectra of **1** and **1a**, the higher excited states might contribute significantly the photophysically properties of **1a**. Contrary, the lower energy states of **2a** are all characterized by LLCTs of the aromatic ring to the CO ligands, in line with the π→π* triplet excitations in **2.**

Table 1. **1a** and **2a** differential PBE0 Mulliken MO populations computed according to the TDDFT main one-electron excitations.

	1a				**2a**		
	S_1	**T_1**	**T_2**	**T_8**	**S_1**	**T_1**	**T_2**
Ring	0.00	0.02	1.24	-0.77	−0.36	−1.38	−0.55
2·S	−0.16	0.27	−0.27	0.18	0.24	0.23	0.21
2·Fe	−0.14	−0.24	−1.08	0.28	−0.02	0.71	0.14
6·CO	0.38	0.01	0.12	0.34	0.17	0.43	0.21

To compare the efficiency of a photoinduced electron transfer (PET) from an electron donor into the S_0 orbital after excitation into S_n for compound **2**, **3** and **4**, the spectral change in the presence of triethylamine (TEA) as sacrificial electron donor was studied, whereas experiments for compound **1** were recently published.[22] In Figure 2 are shown the Stern-Volmer plots for compounds **2**-**4**. Iterative addition of TEA to a solution of compound **2** leads to luminescence quenching with a rate constant K_{SV} of 21.54 ± 0.59 L/mol for **2** (27 μM in acetonitrile) at an excitation wavelength of λ_{ex} = 245 nm. Similar results were obtained for compound **3** (27 μM in acetonitrile) with K_{SV} = 10.28 ± 0.14 L/mol at λ_{ex} = 247 nm and compound **4** (27 μM in acetonitrile) with K_{SV} = 4.36 ± 0.10 L/mol at λ_{ex} = 256 nm (K_{SV} = 80.0 ± 2.2 L/mol

for **1**, 27 µM in acetonitrile, excitation at 255 nm)[22]. The decrease of the emission intensity at λ_{max} (Figures S10-S12) under these conditions is reasonable as TEA acts as sacrificial electron donor to fill the hole generated in the π-orbital (S_0 state) upon photoexcitation. Comparison of the Stern-Volmer rate constants for the different aromatic systems **1-4** affords the highest quenching efficiency for the silafluorene-system **1** (not shown here). The fluorene-system **2** with K_{SV} = 21.54 ± 0.59 L/mol is four-times less efficient than the silafluorene-system **1**, which clearly demonstrates the influence of the substitution of a carbon by a silicon atom regarding the lowering of involved orbitals. Comparison of compound **3** and **4** reveals a higher efficiency for the phenoxsilane-system **3** rather than the phenothiasilane one **4**, but compared with compound **1** just a moderate quenching efficiency for both compounds **3** and **4**.

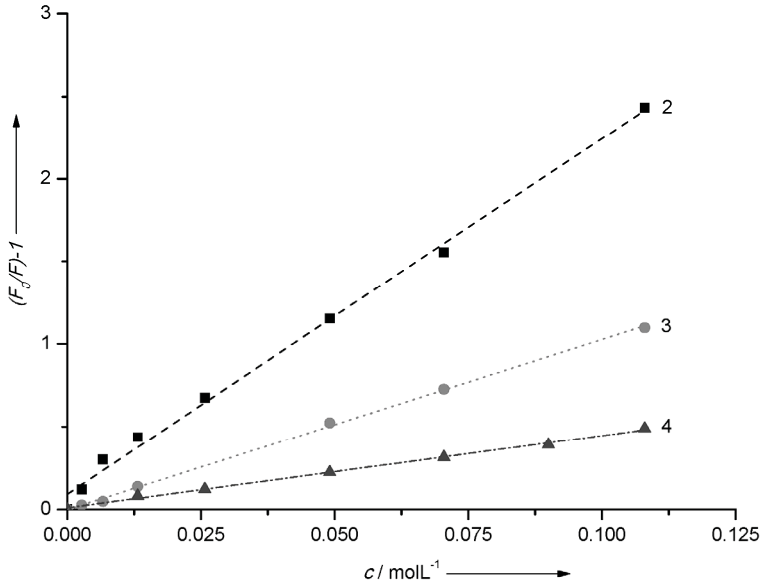

Figure 30. Stern-Volmer plot for the emission quenching of compound **2** (K_{SV} = 21.54 L/mol), **3** (K_{SV} = 10.28 L/mol) and **4** (K_{SV} = 4.36 L/mol) by triethylamine.

Excitation at the characteristic absorptions of compounds **1-4b** results in a maximum luminescence (based on a 0.01 mm pyrene solution in cyclohexane as reference) as highlighted in Table 2 and Figures S13-S16. As reported recently for the compounds **1** and **1a,** complex **1b** shows a maximum luminescence at 387 nm with a quantum yield of 18.3 ± 0.3 % for **1** and much lower values for **1a** (0 % ± 0.03 %) and **1b** (0 % ± 0.03 %). The fluorene-based compounds show a bathochromic shift of the luminescence maximum of 18 nm to 405 nm for compound **2** with a quantum yield of 3.2 ± 0.6 %. A further bathochromic shift by 12 nm to 413 nm is observed for the

all-CO complex **2a** (1.8 ± 0.6 %) as well as a shift by 9 nm to 422 nm for **2b** (2.4 ± 0.6 %). A similar observation is obtained for the phenoxsilane system **3**. A maximum luminescence of 413 nm for compound **3** with a quantum yield of 7.3 ± 0.4 % shifts by 2 nm for **3a** (4.6 ± 0.6 %) and further by 7 nm for **3b** (3.3 ± 0.6 %). The phenothiasilane system behaves like the silafluorene one, with a consistent maximum luminescence for **4**, **4a** and **4b** at 436 nm. This value is the most bathochromic λ_{max} for all investigated compounds. Compared to **1** this value is shifted by 49 nm to higher wavelength with an almost same absorption spectrum. Therefore a higher gap between the HOMO and LUMO for **4** is assumed, which is also observed for **2** and **3**. The quantum yield of 12.1 ± 0.4 % for compound **4** is satisfying compared to those for the phenoxsilane system. As observed for the silafluorene system **1**, the quantum yields of **4**, **4a** (2.7 ± 0.6 %) and **4b** (0.7 ± 0.6 %) decrease in the same manner.

Table 2. Maximal luminescence and quantum yields of all herein investigated compounds **1**-**4b**.[22]

compound	λ_{max} / nm	*quantum yield / %*
1	387	18.3 ± 0.3
1a	387	0 ± 0.03
1b	387	0 ± 0.03
2	405	3.2 ± 0.6
2a	413	1.8 ± 0.6
2b	422	2.4 ± 0.6
3	413	7.3 ± 0.4
3a	415	4.6 ± 0.6
3b	422	3.3 ± 0.6
4	436	12.1 ± 0.4
4a	436	2.7 ± 0.6
4b	436	0.7 ± 0.6

Photocatalytic Investigations

Photochemical hydrogen evolution experiments were carried out for compound **1a** under different conditions, affecting dramatically the catalytic efficiency.

Subsequently, complexes **2a**, **3a** and **4a** were investigated under optimized conditions. Since it was shown, that compounds **1b**, **2b**, **3b** and **4b** reveal a lack of stability under reductive conditions,[36] these complexes were not investigated under photocatalytic conditions. The samples (solution volume 3 mL) were stirred under inert conditions in a sealed vial (V = 5.6 mL) and irradiated with a 15 W mercury vapor lamp (254 nm emission) at room temperature. Hydrogen was detected by manual injection of a 100 µL sample from the headspace of the sealed vial into a gas chromatograph (GC) equipped with a thermal conductivity detector (TCD) and nitrogen as carrier gas. The hydrogen was quantified by a calibration curve obtained from known concentrations of H_2 and the turn-over numbers (TONs) were calculated based on the amount of hydrogen molecules generated *versus* the number of catalyst molecules. As a reference system, every measurement was also performed without the utilization of the relevant catalyst **1a**, **2a**, **3a** or **4a** and was subtracted from the measurements run with catalyst to maintain the catalytic process as represented graphically. Further stability tests (irradiation experiments monitored by GC and UV-vis spectrometry, respectively, NMR and IR spectroscopic studies) of such [FeFe] hydrogenase mimics as well as of iron carbonyls [$Fe_3(CO)_{12}$] and [$Fe_2(CO)_9$] under irradiation with UV light were already carried out to a large extent and described in previous publications.[22,39–41]

The optimized environment for hydrogen evolution was found by use of acetonitrile as solvent and a catalyst concentration of 10 µM (Figure 31). Triethylamine (TEA) was used as electron donor in 10,000 times excess (100 mM) and 5000 equivalents trifluoroacetic acid (TFA, 50 mM) were added (TEA/TFA 2:1). Under irradiation a TON of 539 molecules H_2 (16.18 µmol) within 7 h could be reached for complex **1a,** representing the highest reported turn-over number for such small, compact systems without the use of noble metal containing photosensitizers. This TON corresponds to a turn over frequency (TOF) of 77 molecules H_2/h calculated for the catalysis time of 7 hours with an initial TOF of 242 molecules H_2 in the first hour. Direct comparison with the carbon analogue complex **2a** reveals a positive influence of the substitution of the carbon atom by a silicon atom. The TON for **2a** was 458 after 7 h (13.73 µmol, Figure 31) with a TOF of 65.4 molecules H_2/h and an initial TOF of 186 molecules H_2 in the first hour. This represents also an excellent value but compared to that of **1a** a lower catalytic efficiency. The phenothiasilane complex **4a** reached a TON of 389 after 7 h (11.67 µmol) compared to 267 molecules H_2 for **3a**

after 5 hours (8.01 µmol, Figure 31) revealing a lower stability for compound **3a** under catalytic conditions. In contrast, the TOFs show almost similar catalytic efficiencies with a TOF of 53.4 molecules H_2/h calculated for 5 h for **3a** and 55.6 calculated for 7 h for **4a**. Also the initial TOFs calculated for the first hour are comparable with 153 molecules H_2 for **3a** and 136 for **4a**.

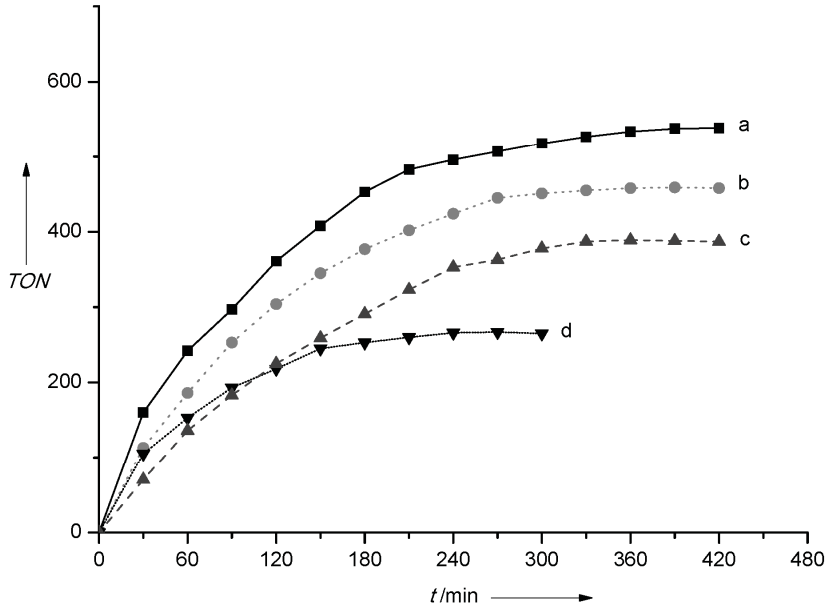

Figure 31. Time dependence of photocatalytic H_2 evolution under optimized conditions (TEA (100 mM), TFA (50 mM) in acetonitrile) of (a) **1a** (10 µM), (b) **2a** (10 µM), (c) **4a** (10 µM) and(d) **3a** (10 µM). Total solution volume 3 mL, Hg vapor lamp (12 W).

Further photocatalytic experiments under different conditions using complex **1a** (Table 3) were performed. Changing the volume ratio of TEA and TFA during the hydrogen catalysis experiments (10:1, 1:1 and 1:2, respectively) revealed just moderate TONs and TOFs < 2/h (Figure 32, run e and f). The same results were obtained changing TFA to acetic acid or H_2O. No results have been obtained using acetic acid. The use of TEA/water in acetonitrile (both 100 mM) results in a TON of 93 molecules H_2 (2.80 µmol) within four hours, albeit the stability of the catalyst under these aqueous conditions is reduced remarkably. Nevertheless, a turn-over-frequency of 23 molecules H_2/h is calculated and an initial TOF of 43 molecules H_2 in the first hour could be obtained (Figure 32, run c). Using ascorbic acid as sacrificial electron donor as well as proton source in 10,000 times excess (100 mM) in acetonitrile/water 7:1 mixture reveals moderate TONs, too (Figure 32, run g).

After 7 hours a TON of 43 molecules H_2 (1.3 µmol) could be received, which corresponds to a TOF of 6 molecules H_2/h.

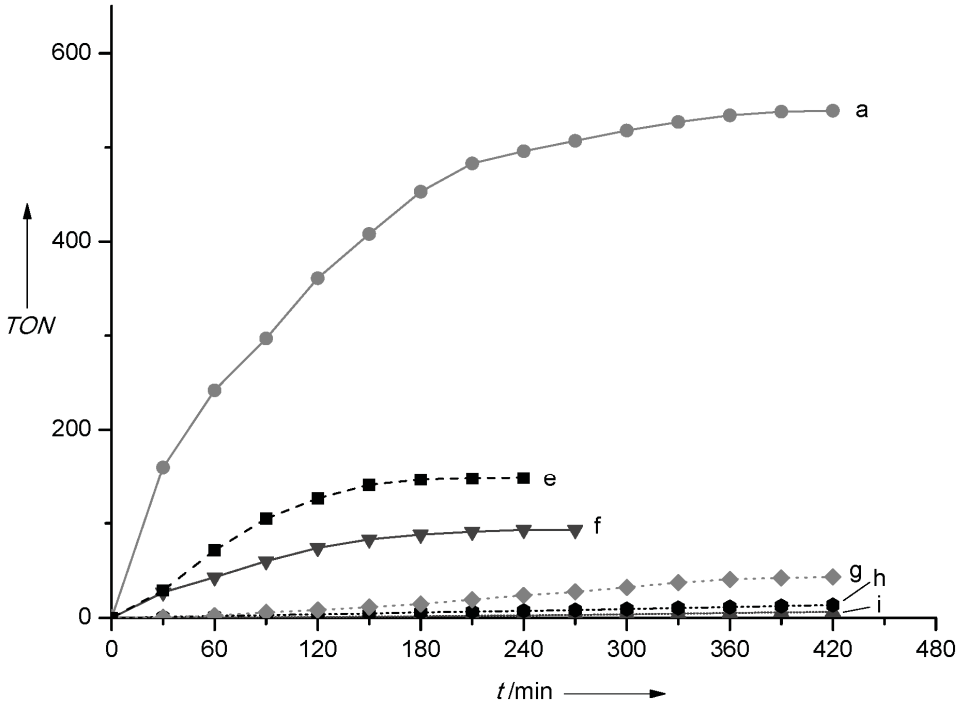

Figure 32. Time dependence of photocatalytic H_2 evolution of **1a** (10 µM) in (a) TEA (100 mM), TFA (50 mM) in acetonitrile, (e) TEA (100 mM), TFA (50 mM) in aqueous CTAB solution, (f) TEA (100 mM), H_2O (100 mM) in acetonitrile, (g) ascorbic acid (100 mM) in acetonitrile/H_2O 7:1, (h) TEA (100 mM), TFA (100 mM) and (i) TEA (50 mM), TFA (100 mM) in acetonitrile. Total solution volume 3 mL, Hg vapor lamp (12 W).

In order to force a photocatalytic H_2 generation in pure aqueous solution, the hydrophobic catalyst **1a** has been successfully incorporated into an aqueous SDS or CTAB solution as represented in Scheme 4 and TEA/TFA 2:1 (100 mM/ 50 mM) as well as ascorbic acid (100 mM) were used as sacrificial donors. Studies on the catalytic hydrogen evolution at pH = 10 for TEA/TFA 2:1 mixture revealed a higher efficiency for the aqueous micelle solution compared to experiments at pH = 2 using ascorbic acid as sacrificial agent.

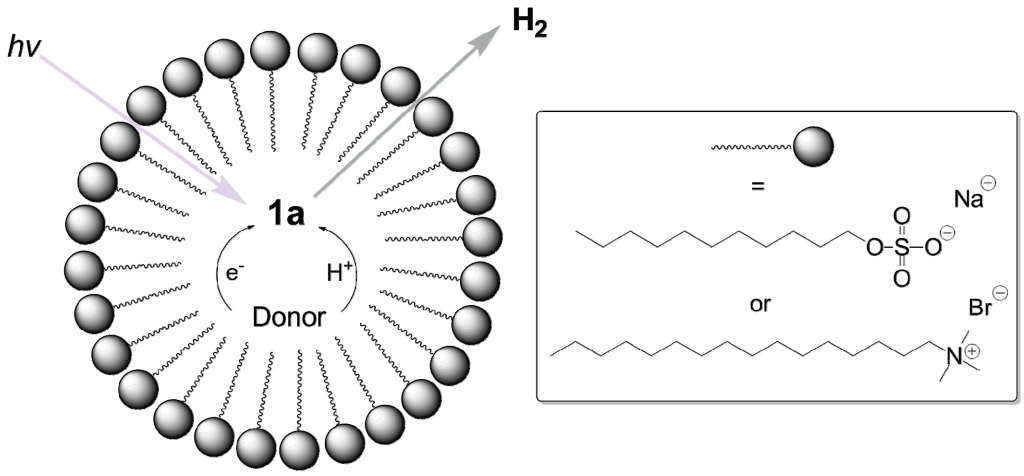

Scheme 4. Photocatalytic hydrogen evolution using **1a** in aqueous SDS and CTAB micelle solutions, respectively.

After an irradiation time of four hours, a TON of 148 could be reached for the aqueous CTAB solution of **1a** using TEA/TFA 2:1 (100 mM/ 50 mM) at pH = 10 as the most efficient micellar system (Figure 33). Using SDS under same conditions as well as the same irradiation time a TON of 139 was obtained, which is similar to that obtained in a CTAB solution. Using ascorbic acid (100 mM) as the sacrificial donor (instead of TEA) as well as the proton source at pH = 2, different results have been received: A similar initial TOF for the CTAB as well as the SDS solution is observed with a TOF of 10.4 molecules H_2 and 9.7 molecules H_2, respectively. After 90 min the SDS solution began to reach a plateau with a TON of 19 after four hours of irradiation with a TOF of 4.8 H_2/h. In comparison, the amount of hydrogen for the catalysis using CTAB solution is increasing linear during four hours. This is detectable by the small difference between the initial TOF of 10.4 molecules H_2 and the overall TOF of 9.8 molecules H_2/h. After four hours a TON of 39 was observed, which represents the double efficiency compared to that of the SDS solution under same conditions. This is reasonable due to the charge of the surfactant heads (SDS micelles are negatively charged and the CTAB micelles positive). At pH = 2 the ascorbic acid occurs deprotonated in aqueous solution which gives a repulsive effect with the negatively charged SDS micelles and thus an inhibited sacrificial donation of electrons and protons to the catalyst **1a**. With positively charged CTAB micelles such repulsive effects are not very conceivable. Also by use of TEA/TFA 2:1 (100 mM/ 50 mM) at pH = 10 such interactions are not feasible due to the neutral charge of TEA and the protonated form of TFA at pH = 10.

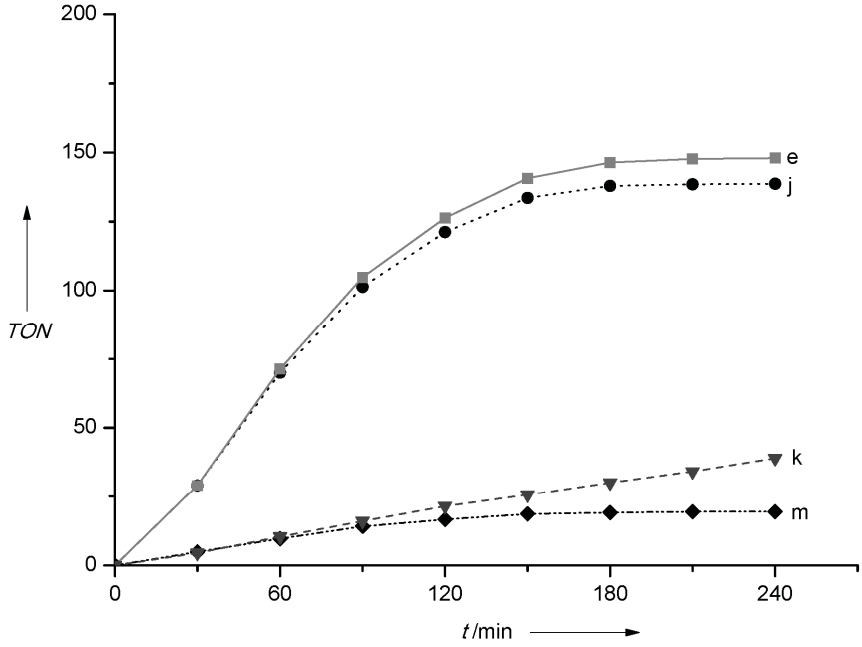

Figure 33. Time dependence of photocatalytic H_2 evolution of (e) **1a** (10 μM), TEA (100 mM), TFA (50 mM), (k) **1a** (10 μM), ascorbic acid (100 mM) in an aqueous CTAB solution and (j) **1a** (10 μM), TEA (100 mM), TFA (50 mM) and (m) **1a** (10 μM), ascorbic acid (100 mM) in an aqueous SDS solution. Total solution volume 3 mL, Hg vapor lamp (12 W).

Table 3. Influence of catalytic conditions on photoinduced hydrogen evolution experiments.

Run (conditions written in Figure 3, 4 and 5)	***Irradiation time / h***	***TON***	***TOF / h^{-1}***	***Initial TOF (after 1h) / h^{-1}***
a	7	539	77	242
b	7	459	65.6	186
c	5	267	53.4	153
d	7	389	55.6	136
e	4	148	37	71.4
f	4.5	93	23.2	43
g	7	43	6.1	2.4
h	7	6.4	0.9	0.4
i	7	13.6	1.9	2.1
j	4	139	34.8	70
k	4	39	9.8	10.4
m	4	19	4.8	9.7

Theoretical investigation of the photocatalytic properties

DFT and TDDFT characterization of the excited state properties of the heteroaromatic models is focused on **1a** and **2a**. The typical modeling of the sensitization process can be resumed as following: the system is first irradiated with UV light (254 nm), a number of singlet excited states (S_n) are populated and successively undergo internal conversion (IC) to the S_1 first singlet state and then to intersystem crossing (ISC) to the corresponding T_1 triplet state. This latter is supposed to have a longer lifetime with respect to S_1 and can be reduced more easily to the anionic form S_0^-.

The ground state structures of **1a** and **2a** have been already discussed in a previous paper.[36] Briefly, the C-Si bond distances (1.9 Å on average) between the central Si atom of the silafluorene pendant allow **1a** to adopt an almost C_{2v} configuration, while corresponding C-C bonds distances (1.5 Å on average) in **2a** induce the stabilization of the typical tilted conformation of the [FeFe] hydrogenase models. While discussing the nature of the structural differences of the neutral and anionic ground states, as well as the lowest singlet and triplet excited states of **1a** and **2a**, also the analysis of the LUMOs is crucial. The structure of the anionic forms can be discussed on the basis of the Fe-Fe σ* nature of the LUMO of the neutral species. As already figured out for simpler [FeFe] hydrogenase models, these facts support the stabilization of the rotated isomers with respect to the all terminal CO ligand form and/or favoring the weakening/dissociation of a Fe-S bond.

In Figure 5 are resumed the main features of the structures of **1a** and **2a** in their ground state as well as their lowest singlet and triplet state and anionic form along with the corresponding energy differences. The lowest singlet state S_1 is computed at TDDFT level while T_1 is computed at ΔSCF level.

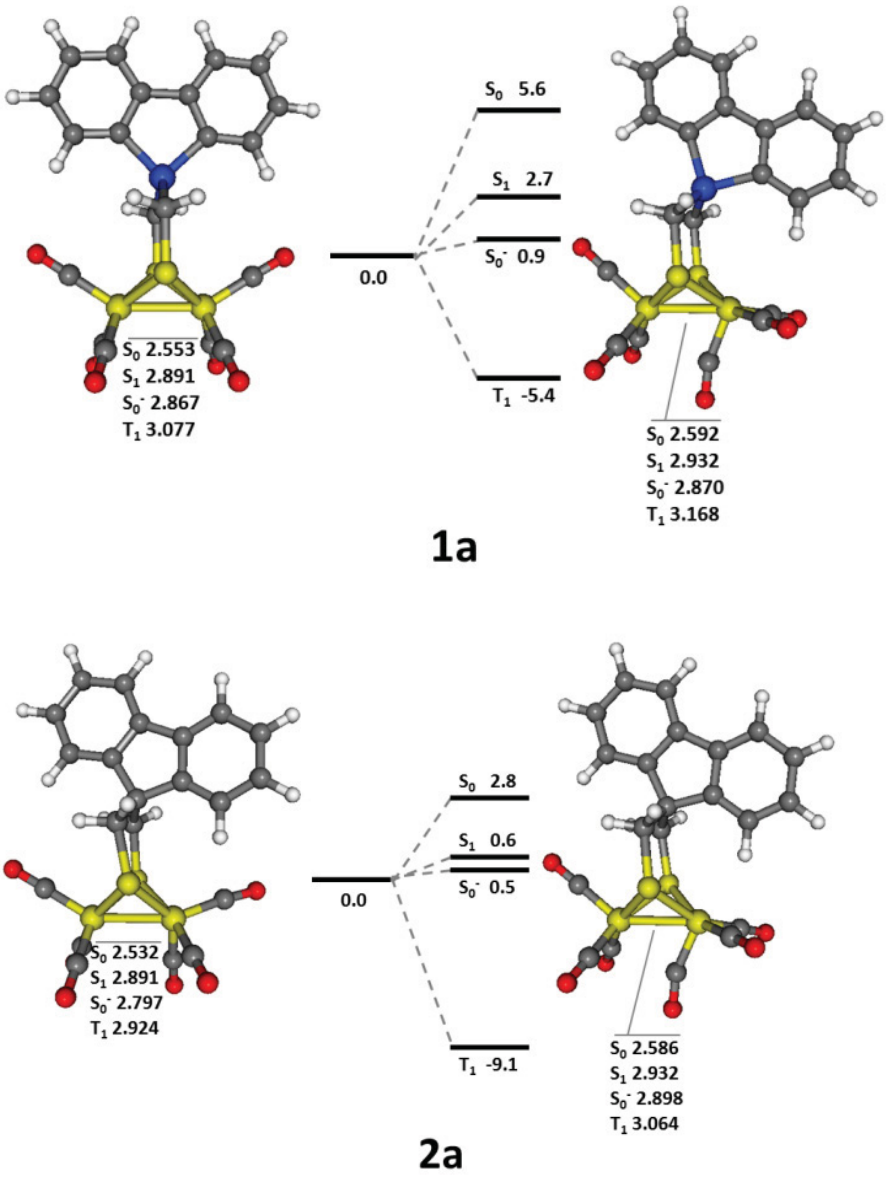

Figure 5. Structures of the ground state (S_0) of **1a** and **2a**, first singlet (S_1) and triplet (T_1) exicted states and anionic form (S_0^-). Fe-Fe bond distances in Å. Energy differences (in kcal/mol) are computed with respect to the corresponding all terminal CO ligand form.

The ground state global minimum structure of **1a** is very symmetric (almost C_{2v}) with the peculiar half-chair conformation adopted by the bridging dithiolate ligand. The rotated form is a transition state (one imaginary normal mode frequency at 20.6i cm^{-1}, which describes the $Fe(CO)_3$ moiety rotation) 5.6 kcal/mol higher in energy in which the bridging dithiolate is tilted toward the $Fe(CO)_3$ group as observed in many [FeFe] hydrogenase models. The lowest energy form of **2a** is already partially rotated (C-Fe-Fe-C dihedral angle δ between carbon atom that belong to the apical CO ligands and the two Fe atoms is 47.7°), while the fully all terminal CO ligand form (δ=2.12°) is 0.5 kcal/mol higher in energy and the fully rotated form (δ=103.5°) 2.8 kcal/mol. The anionic species of **1a** is stable in the all

terminal CO ligand coordination with a Fe-Fe distance elongated by 0.317 Å, whereas the corresponding rotated form is only 0.1 kcal/mol higher in energy. In the case of **2a**, the semirotated form is the lowest energy isomer with δ=49.5°. Both anionic species are characterized by the elongation of the four Fe-S bonds (the longest Fe-S bond length in **2a** is 2.340 Å (+0.050 Å with respect to **1a**) and 2.356 Å in **1a** (+0.036 Å with respect to **2a**)). The lowest T_1 energy forms of **1a** and **2a** are rotated with a Fe-Fe bond particularly elongated (+0.524 and +0.532 Å, respectively), while on S_1 PES the rotated isomer is the lowest energy form (**2a**) or is stabilized (**1a**) with respect to the all terminal ligand species. In the latter case, the main mono-electronic excitation is the HOMO→LUMO translation, while for **2a** the HOMO becomes the bridging Fe-CO bonding MO. It is important to underline that all the excited state minimum species are characterized by the elongation of the Fe-S bonds, in particular for the S_1 of **2a** (two Fe-S bonds at 2.537 Å, + 0.239 Å compared with the ground state form). This fact is due to the Fe-S non-bonding/antibonding orbital contributions due to the non-occupied frontier MOs, as TDDFT computations already suggested for other [FeFe] hydrogenase models.[37,42] The stabilization of the rotated form and the partial Fe-S bond dissociation upon excitation is also confirmed by exploring the excited state PES along the Fe-S bond dissociation and of $Fe(CO)_3$ group rotation reported in Figure 6. The scan along the rotated coordinate has been carried out only for **1a**, since the ground state structure of **2a** is already partially rotated.

Most of the computed excited state curves result partially dissociative with respect to the Fe-S bond weakening, in particular for **2a**. Similarly, the curves along the $Fe(CO)_3$ rotation of **1a** suggest a stabilization of the rotated form over the all terminal CO ligand form for many excited states. It is relevant to the present theoretical investigation to understand which structural type represents the stabilized excited state PES. The lowest energy structures of the dianionic form of $\mathbf{1a}^{2-}$ and $\mathbf{2a}^{2-}$ are reported in Figure 7.

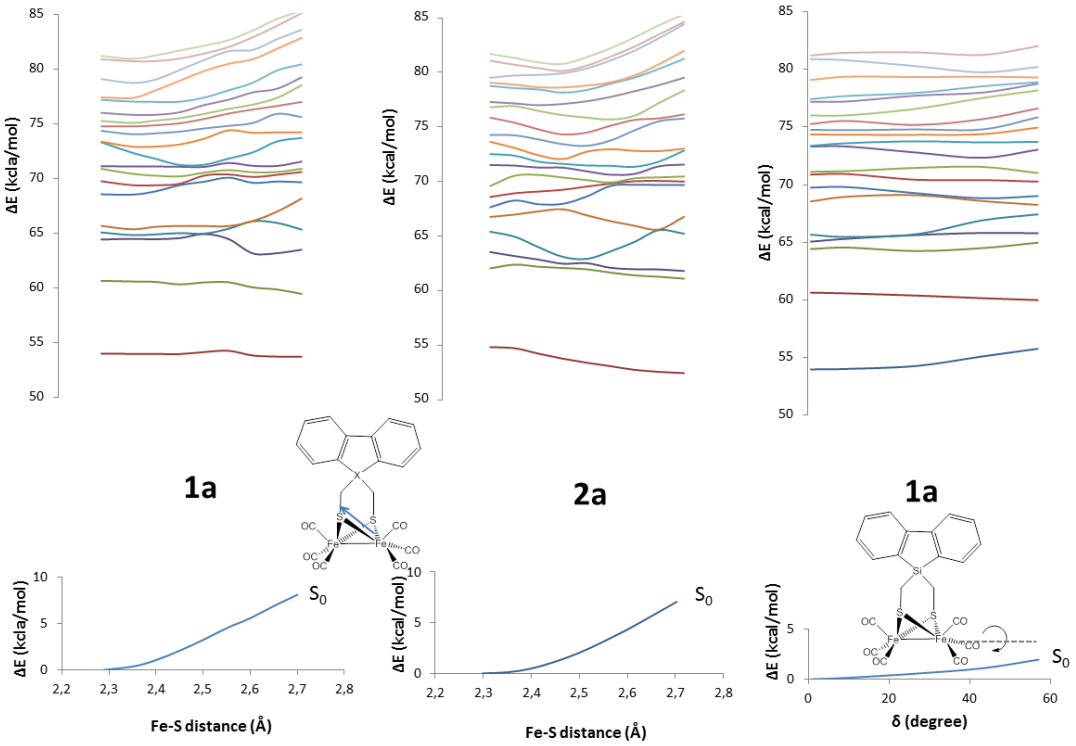

Figure 6. Potential energy surfaces of the ground state and the first 20 singlet excited states of **1a** and **2a** along the Fe-S bond elongation coordinate. For **1a** is also reported the scan of the excited surfaces along the pathway that connects the all terminal CO ligand form to the rotated form. Energy differences in kcal/mol computed with respect to the minimum ground state energy.

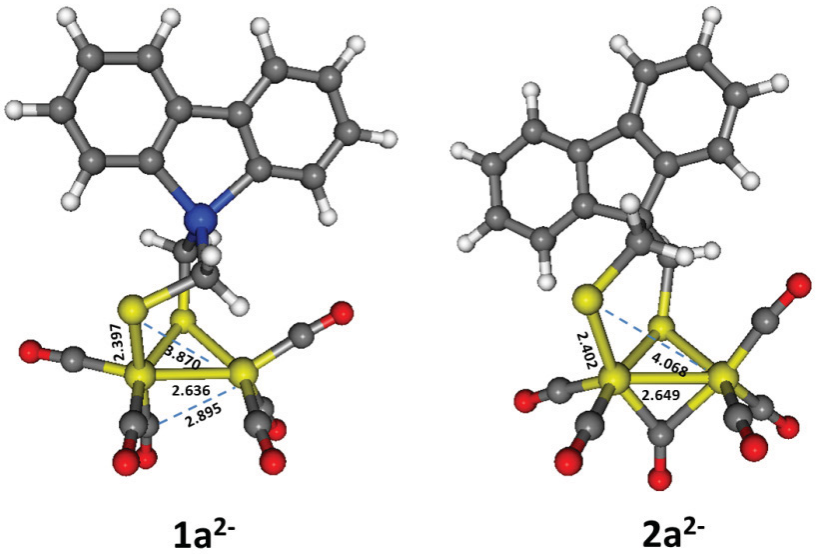

Figure 7. Structures of the lowest energy isomers of $\mathbf{1a}^{2-}$ and $\mathbf{2a}^{2-}$ (S_0^{-2}). Bond distances in Å.

Both structures feature the complete dissociation of one Fe-S bond of the Fe_2S_2 core and the partial ($\mathbf{1a}^{2-}$) or full ($\mathbf{2a}^{2-}$) bridging character of one CO ligand. These two species are very low in energy compared to the other isomers and they can be considered as the prevalent species in solution. The structure of $\mathbf{1a}^{2-}$ with one fully

bridging CO ligand is a local minimum 11.6 kcal/mol higher in energy with respect to that reported in Figure 7. Finally, it was figured out that the structures and energetics of all species considered before do not change significantly if implicit CH_3CN solvatation with COSMO approach[43–45] is adopted (Table S5). The computation of the differential NBO atomic and group charges between the lowest energy dianionic and neutral ground state forms evidence that extra electron density is delocalized at the ligands but not on the iron atoms (Scheme 5). In particular we observe a significant charge accumulation on the sulfur atom that belongs to the dissociated Fe-S bond, making the latter electrophilic and thus susceptible for protonation during a catalytic process.

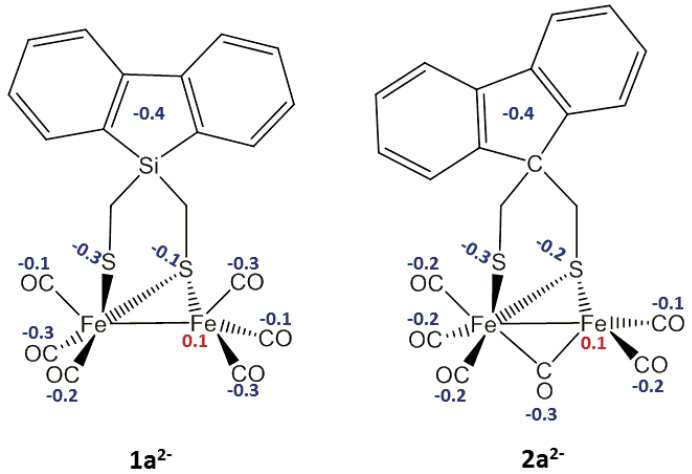

$1a^{2-}$ **$2a^{2-}$**

Scheme 5. NBO atomic or group charge differences computed between the lowest energy isomers of **$1a^{2-}$** and **$2a^{2-}$** and the corresponding neutral lowest energy forms of **1a** and **2a**. Positive values and negative values indicate increasing of the positive and negative charges, respectively.

Possible photocatalytically H_2 evolution mechanism

In Scheme 6 are resumed the suggested general possible mechanism for light induced H_2 production by the *all*-CO complex subscribed with **1a**. The first common step for both pathways (cycle **A** and **B**) is the sensitization process in which the system is first excited and then reduced to **$1a^-$** with TEA. Successively the anionic form **$1a^-$** could undergo a further reduction promoted by a second molecule of TEA or by the formed radical cation $TEA^{+\bullet}$[46], or by a second photoreduction to the dianionic form **$1a^{2-}$**, respectively, followed by double protonation to **$1aH_2$** and final H_2 detach closing the cycle (cycle **A**). Another possibility is a protonation step of **$1a^-$** by formation of the single-protonated **1aH** form, followed by a second reduction or

photoreduction, respectively, and a second protonation to **1aH$_2$** and finally H_2 detach (cycle **B**).

However, on the basis of some reasonable assumptions we can rule out the second proposed mechanism (cycle **B**): first of all, we recall that the process of photoinduced electron transfer can be very fast (sub picoseconds time scale) while ground state reactivity has a time scale, which is much longer. Starting from this point and observing in electrochemical experiments that the reduction of **1a** is an one-step two-electron reduction process that occurs at -1.55 (first reduction) and -1.48 V (second reduction, thermodynamically favoured by structural change after first electron transfer),[22,36] respectively, we can reasonably exclude that **1a**$^-$ undergoes protonation before the second reduction occurs.

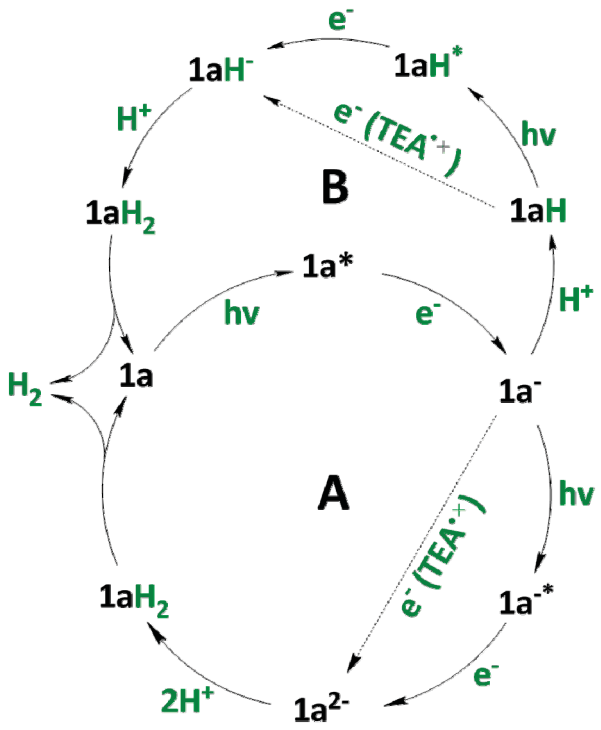

Scheme 6. Possible general pathways for the light-induced H_2 production for **1a**.

Starting from the dianionic species (**1a**$^{2-}$ and **2a**$^{2-}$) we explore the possible single (**1aH**$^-$ and **2aH**$^-$) and doubly-protonated forms (**1aH$_2$** and **2aH$_2$**). The structures of the most stable isomers are reported in Scheme 7. As NBO atomic charges suggest (Scheme 5), protonation at the dissociated sulfur atom yields the most stable **1aH**$^-$ and **2aH**$^-$ isomers which also feature one bridging carbonyl ligand, while in the lowest energy structures of **1aH$_2$** and **2aH$_2$** the second proton is forming a hydride, occupying the bridging coordination position.

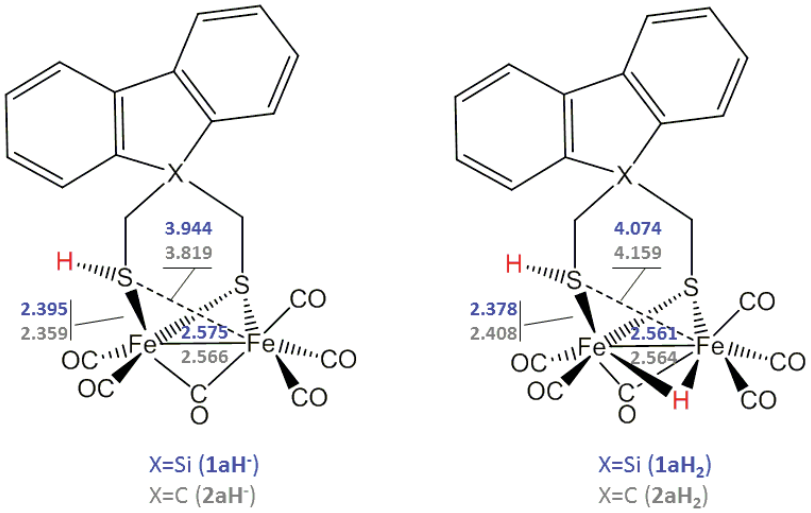

Scheme 7. Structure of single (**1aH**$^-$ and **2aH**$^-$) and doubly-protonated forms (**1aH$_2$** and **2aH$_2$**). Distances in Å.

In Figure 8 are reported the computed mechanisms for the H_2 formation starting from the lowest energy structures of **1aH$_2$** and **2aH$_2$**. For both complexes the computed free energy profile is similar and consists of two steps. In the first step the isomerization of the doubly-protonated species occurs obtaining the η^2-H_2 complex. The transition state is much closer to the η^2-H_2 species, with the concomitant displacement of the proton bound to the sulfur atom and of the bridging hydride towards the terminal coordination at the iron atom that belongs to the Fe-S dissociated bond. Successively the H_2 release take place with the isomerization of the Fe-S bond dissociated species to the all terminal CO ligand ground state form. The two energy profiles are similar, but the free energy barrier of the **2aH$_2$** isomerization to the η^2-H_2 species is 6.9 kcal/mol higher in energy compared to that computed for **1aH2**, suggesting a higher propensity of **1a** in the H_2 photoproduction as observed in the experiments.

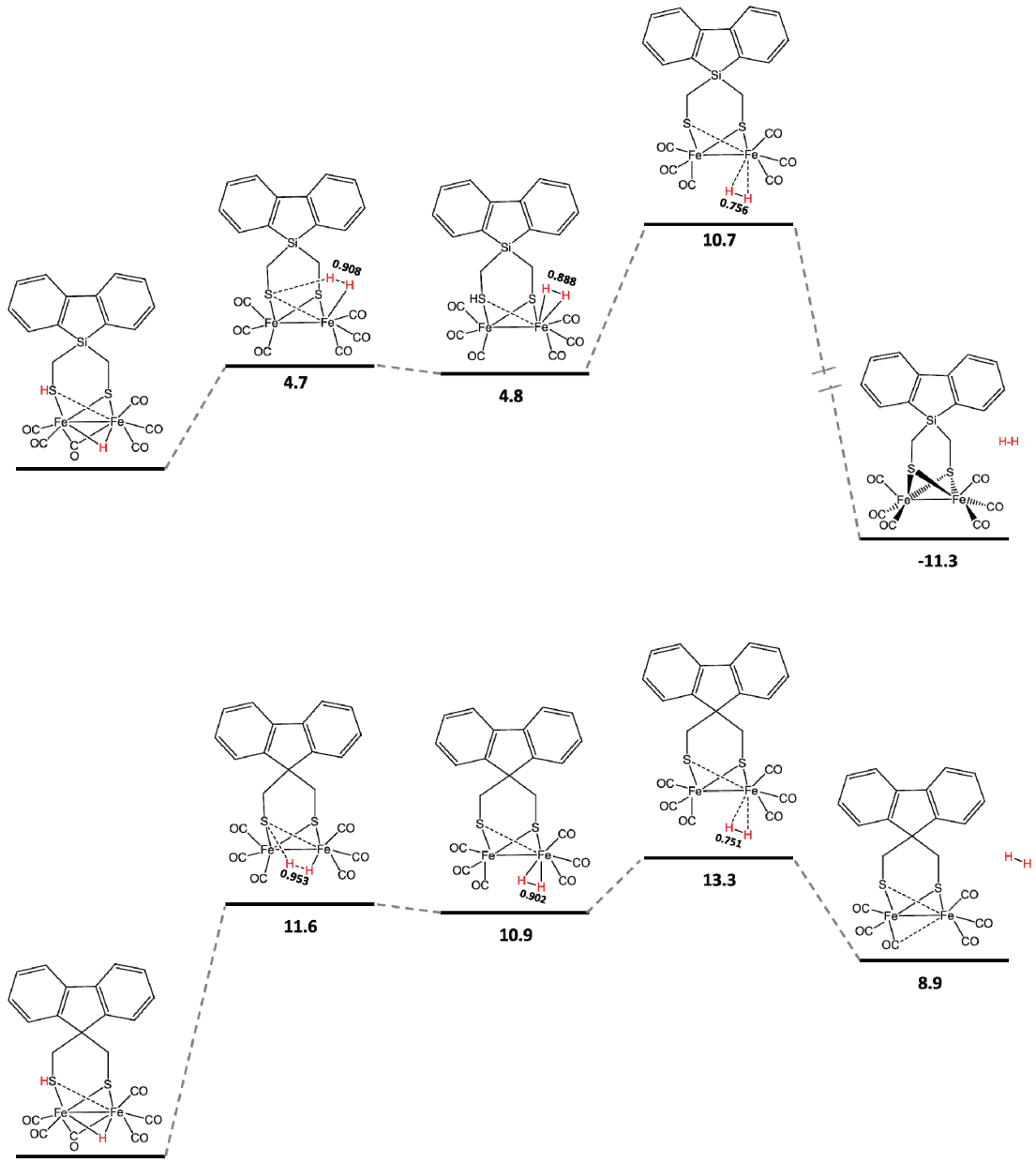

Figure 8. H_2 production pathwahs of **1aH$_2$** and **2aH$_2$**. Energy differences in kcal/mol.

Conclusion

Within this work the complete photophysical characterization of the [FeFe]-H_2ase mimic series **1a-4b** as well as their precursors **1-4** were described and investigated. One of the most interesting aspects is the comparison of the *1*-silafluorene with the carbon analogue *9*-fluorene containing complexes **1a** and **2a**. As expected, the substitution of carbon by a silicon atom offered a constructive influence on the photophysical properties as well as on the catalytic efficiencies. Focusing the different properties of **1a** and **2a** regarding their photoluminescence properties,

substantial DFT as well as TDDFT calculations has been performed, suggesting a higher propensity of **1a** in the photocatalytically H_2 production as observed in the experiments. For this purpose photochemical H_2 evolution experiments were carried out with **1a** as reference under different conditions (Figure 4). After establishing optimized conditions, experiments were performed with the 9-fluorene, *10,10'*-phenoxsilane as well as the *10,10'*-phenothiasilane containing complexes **2a**, **3a** and **4a**, respectively, yielding complex **1a** as the most efficient catalyst within the investigated series. A turn-over number of 539 was reached after 7 h irradiation under optimized conditions by use of acetonitrile as solvent and a catalyst concentration of 10 μM, TEA as electron donor in 10,000 times excess (100 mM) and 5,000 equivalents of trifluoroacetic acid (50 mM) (TEA/TFA 2:1), representing an exceptionally high TOF of 77 molecules H_2/h. The observed TONs are the highest reported values by far for such small, compact systems, in which the photosensitizer is covalently linked to the catalytic active center. Furthermore, photocatalytic H_2 generation was forced to takes place in aqueous solution by successfully incorporation of complex **1a** into an aqueous SDS or CTAB micelle solution. A mixture of TEA/TFA in a 2:1 ratio (100 mM/ 50 mM) at pH = 10 was established as optimized conditions, too. After an irradiation time of four hours, a TON of 148 could be reached for the aqueous CTAB solution of **1a** offering the most efficient micellar system reported so far utilizing [FeFe] hydrogenase model complexes.[30] Using SDS under same conditions and irradiation time a TON of 139 was obtained, which offers an almost negligible influence of the used tenside under the investigated conditions.

Supported by theoretical calculations, electrochemical experiments[22] as well as photocatalytic investigations a general possible mechanism for light induced H_2 production could be established figuring out some key intermediates after recognizing the common steps for the cycle **A** in Scheme 6. Starting from the dianionic species $\mathbf{1a^{2-}}$, protonation at the lower coordinated thiolato sulfur atom (Scheme 7)[36] yields the most stable $\mathbf{1aH^-}$ isomer featuring a bridging CO ligand, while in $\mathbf{1aH_2}$ the second proton forms a bridging hydride.

The reported systems are much more efficient than comparable model complexes using noble metal containing photosensitizers. The short linker with a CH_2-group between the silicon and the sulfur atoms makes the design of the herein reported [FeFe] hydrogenase model complexes to a powerful platform for the further

development of hydrogen generating catalysts. The synthetic pathway to carbon bridged, photocatalytic active model complexes should be also feasible and opened a whole new spectrum of approaches and possibilities, in particular the aspect of shifting the absorbance wavelength of the currently used photosensitizers into the visible light region.

Experimental part

General Procedures: UV/Vis spectra were recorded with a Specord S600 spectrometer, and fluorescence spectra were recorded with a Perkin–Elmer LS50B spectrometer.

Procedure for photocatalytic H_2 evolution: Photochemical hydrogen evolution experiments were performed by irradiating samples with a solution volume of 3 mL under inert conditions in a sealed quartz glass precision cell (V = 5.6 mL) with a 15 W mercury vapor lamp (254 nm main radiation) at room temperature. Hydrogen was detected by manual injection of a 100 µL sample from the headspace of the sealed cell into an Agilent 7820A gas chromatograph equipped with a mol. sieve column 5A, a TCD and nitrogen as carrier gas. The hydrogen was quantified by a calibration curve obtained from known concentrations of H_2 and the turn-over numbers (TONs) were calculated based on the amount of hydrogen molecules generated *versus* the number of catalyst molecules. Every measurement was also performed without the utilization of the relevant catalyst **1a**, **2a**, **3a** or **4a** and was subtracted from the measurements run with catalyst.

Computational setting: Computations were performed using pure Gradient Generalized Approximation pure BP86[47,48] and PBE0[49] hydride DFT functionals. Basis sets of triple-ζ plus polarization[50] split valence quality were adopted for all atoms in the complex. All the computations presented have been carried out using the TURBOMOLE[51] suite of programs. DFT grid-size was set to standard m3 value. The optimization of transition state (TS) structures on the ground state PES was carried out according to a procedure based on a pseudo-Newton-Raphson method. Analytic excited state energy gradients were recently implemented[52] within TURBOMOLE. Ground state and excited state geometry optimizations were carried

out with convergence criteria fixed to 10^{-6} hartree for the energy and 0.001 hartree·bohr^{-1} for the gradient norm vector. This computational setting[53] provides ground state geometry parameters in good agreement with experimental X-ray values, and a reasonable picture for excited state PES properties. The explorations of the excited state PES were carried out using the following protocol. Starting from the ground state structure, a given bond was elongated from its equilibrium distance in a number of steps with constant increment (0.05Å). For each step, first the geometry parameters were optimized on the ground state PES imposing the constraint on the elongated distance and then the TDDFT excitation energies were computed. All TDDFT optimizations were carried out removing all symmetry constrains and when convergence criteria could not be met, we report the lowest energy structure obtained as the final structure. Excited state PES explorations have been carried out by computation of the excitation energies along a given path previously computed on the ground state PES and by TDDFT geometry optimization starting from the ground state minimum structure.[37]

Preparation of SDS and CTAB micelles for inclusion of the compounds: For the preparation of the micelles for the complexation of compound **1a**, sodium dodecyl sulfate (SDS) or cetyl trimethylammonium bromide (CTAB, 3.47 mmol) were dissolved in water (10 mL, 347 mM), far above the CMC of the tensides (SDS 8.2 mM,[54] CTAB 6 mM[55]), respectively. 500 µL of the complex solution (acetone, 1 mg/mL) was added under vigorous stirring directly to the aqueous solution. The solution was stirred overnight and the acetone was allowed to evaporate. Afterwards, the solutions were centrifuged for 8 minutes at 3,000 rpm to remove the non-encapsulated complex from the solution (orange precipitate).

For the determination of the complex concentration of **1a** in solution, the concentration of the complex solution in comparison to the constant SDS concentration (347 mM) was varied and iteratively increased until no further precipitation of the complex was observed after centrifugation. This saturation was reached between 0.015-0.02 mg/mL of the complex.

Acknowledgments

Financial support for this work was provided by the Deutsche Bundesstiftung Umwelt (to R. Goy). The University of Milano Biccoca is acknowledged for

financial support. T. R. acknowledges the Carl-Zeiss foundation for a PhD-scholarship.

[1] M. Momirlan, T. Veziroglu, *Renew. Sustain. Energy Rev.* **2002**, *6*, 141–179.
[2] C. Koroneos, *Int. J. Hydrog. Energy* **2004**, *29*, 1443–1450.
[3] C. L. Aardahl, S. D. Rassat, *Int. J. Hydrog. Energy* **2009**, *34*, 6676–6683.
[4] A. Thapper, S. Styring, G. Saracco, A. W. Rutherford, B. Robert, A. Magnuson, W. Lubitz, A. Llobet, P. Kurz, A. Holzwarth *et al.*, *Green* **2013**, *3*, 43–57.
[5] J.-F. Capon, F. Gloaguen, F. Y. Pétillon, P. Schollhammer, J. Talarmin, *Coord. Chem. Rev.* **2009**, *253*, 1476–1494.
[6] M. Beyler, S. Ezzaher, M. Karnahl, M.-P. Santoni, R. Lomoth, S. Ott, *Chem. Commun.* **2011**, *47*, 11662–11664.
[7] G. F. Moore, I. D. Sharp, *J. Phys. Chem. Lett.* **2013**, *4*, 568–572.
[8] A. Hijazi, J. C. Kemmegne-Mbouguen, S. Floquet, J. Marrot, J. Fize, V. Artero, O. David, E. Magnier, B. Pégot, E. Cadot, *Dalton Trans.* **2013**, *42*, 4848–4858.
[9] J. R. McKone, S. C. Marinescu, B. S. Brunschwig, J. R. Winkler, H. B. Gray, *Chem. Sci.* **2014**, *5*, 865–878.
[10] D. L. DuBois, *Inorg. Chem.* **2014**, *53*, 3935–3960.
[11] T. R. Simmons, G. Berggren, M. Bacchi, M. Fontecave, V. Artero, *Coord. Chem. Rev.* **2014**, *270-271*, 127–150.
[12] D. J. Evans, C. J. Pickett, *Chem. Soc. Rev.* **2003**, *32*, 268–275.
[13] A. Volbeda, J. Fontecillacamps, *Coord. Chem. Rev.* **2005**, *249*, 1609–1619.
[14] C. Madden, M. D. Vaughn, I. Díez-Pérez, K. A. Brown, P. W. King, D. Gust, A. L. Moore, T. A. Moore, *J. Am. Chem. Soc.* **2012**, *134*, 1577–1582.
[15] C. Tard, C. J. Pickett, *Chem. Rev.* **2009**, *109*, 2245–2274.
[16] A. Roy, C. Madden, G. Ghirlanda, *Chem. Commun.* **2012**, *48*, 9816–9818.
[17] W.-N. Cao, F. Wang, H.-Y. Wang, B. Chen, K. Feng, C.-H. Tung, L.-Z. Wu, *Chem. Commun.* **2012**, *48*, 8081–8083.
[18] Y. Shim, R. M. Young, A. P. Douvalis, S. M. Dyar, B. D. Yuhas, T. Bakas, M. R. Wasielewski, M. G. Kanatzidis, *J. Am. Chem. Soc.* **2014**, *136*, 13371–13380.
[19] A. Onoda, Y. Kihara, K. Fukumoto, Y. Sano, T. Hayashi, *ACS Catal.* **2014**, *4*, 2645–2648.
[20] J. Liu, W. Jiang, *Dalton Trans.* **2012**, *41*, 9700–9707.
[21] H. Cui, M. Hu, H. Wen, G. Chai, C. Ma, H. Chen, C. Chen, *Dalton Trans.* **2012**, *41*, 13899–13907.
[22] R. Goy, U.-P. Apfel, C. Elleouet, D. Escudero, M. Elstner, H. Görls, J. Talarmin, P. Schollhammer, L. González, W. Weigand, *Eur. J. Inorg. Chem.* **2013**, 4466–4472.
[23] S. Gao, S. Huang, Q. Duan, J. Hou, D. Jiang, Q. Liang, J. Zhao, *Int. J. Hydrog. Energy* **2014**, *39*, 10434–10444.
[24] P. W. J. M. Frederix, K. Adamczyk, J. A. Wright, T. Tuttle, R. V. Ulijn, C. J. Pickett, N. T. Hunt, *Organometallics* **2014**, *33*, 5888–5896.
[25] L.-Z. Wu, B. Chen, Z.-J. Li, C.-H. Tung, *Acc. Chem. Res.* **2014**, *47*, 2177–2185.
[26] F. Wen, C. Li, *Acc. Chem. Res.* **2013**, *46*, 2355–2364.
[27] T. Yu, Y. Zeng, J. Chen, Y.-Y. Li, G. Yang, Y. Li, *Angew. Chem. Int. Ed.* **2013**, *52*, 5631–5635.

[28] F. Wen, X. Wang, L. Huang, G. Ma, J. Yang, C. Li, *ChemSusChem* **2012**, *5*, 849–853.
[29] Y. Li, C. Nie, H. Wang, X. Li, F. Verpoort, C. Duan, *Eur. J. Org. Chem.* **2011**, *2011*, 7331–7338.
[30] H.-Y. Wang, W.-G. Wang, G. Si, F. Wang, C.-H. Tung, L.-Z. Wu, *Langmuir* **2010**, *26*, 9766–9771.
[31] X. Li, M. Wang, D. Zheng, K. Han, J. Dong, L. Sun, *Energy Environ. Sci.* **2012**, *5*, 8220–8224.
[32] S. Pullen, H. Fei, A. Orthaber, S. M. Cohen, S. Ott, *J. Am. Chem. Soc.* **2013**, *135*, 16997–17003.
[33] K. Sasan, Q. Lin, C. Mao, P. Feng, *Chem. Commun.* **2014**, *50*, 10390–10393.
[34] W. Wang, T. Yu, Y. Zeng, J. Chen, Y. Li, *Chin. J. Chem.* **2014**, *32*, 479–484.
[35] T. Yu, Y. Zeng, J. Chen, X. Zhang, G. Yang, Y. Li, *J Mater Chem A* **2014**, 20500–20505.
[36] R. Goy, L. Bertini, H. Görls, L. De Gioia, J. Talarmin, G. Zampella, P. Schollhammer, W. Weigand, *Chem. - Eur. J.* **2015**, *21*, 5061–5073.
[37] L. Bertini, C. Greco, P. Fantucci, L. De Gioia, *Int. J. Quantum Chem.* **2014**, *114*, 851–861.
[38] M. E. Alberto, G. Mazzone, A. D. Quartarolo, F. F. R. Sousa, E. Sicilia, N. Russo, *J. Comput. Chem.* **2014**, *35*, 2107–2113.
[39] F. Gärtner, B. Sundararaju, A.-E. Surkus, A. Boddien, B. Loges, H. Junge, P. H. Dixneuf, M. Beller, *Angew. Chem.* **2009**, *121*, 10147–10150.
[40] F. Gärtner, B. Sundararaju, A.-E. Surkus, A. Boddien, B. Loges, H. Junge, P. Dixneuf, M. Beller, *Angew. Chem. Int. Ed.* **2009**, *48*, 9962–9965.
[41] F. Gärtner, A. Boddien, E. Barsch, K. Fumino, S. Losse, H. Junge, D. Hollmann, A. Brückner, R. Ludwig, M. Beller, *Chem. - Eur. J.* **2011**, *17*, 6425–6436.
[42] L. Bertini, P. Fantucci, L. De Gioia, G. Zampella, *Inorg. Chem.* **2013**, *52*, 9826–9841.
[43] A. Klamt, G. Schüürmann, *J. Chem. Soc. Perkin Trans. 2* **1993**, 799–805.
[44] A. Klamt, *J. Phys. Chem.* **1995**, *99*, 2224–2235.
[45] A. Klamt, *J. Phys. Chem.* **1996**, *100*, 3349–3353.
[46] A. J. Esswein, D. G. Nocera, *Chem. Rev.* **2007**, *107*, 4022–4047.
[47] A. Becke, *Phys. Rev. A* **1988**, *38*, 3098–3100.
[48] J. Perdew, *Phys. Rev. B Condens. Matter* **1986**, *33*, 8822–8824.
[49] C. Adamo, G. E. Scuseria, V. Barone, *J. Chem. Phys.* **1999**, *111*, 2889–2899.
[50] A. Schäfer, C. Huber, R. Ahlrichs, *J. Chem. Phys.* **1994**, *100*, 5829–5835.
[51] R. Ahlrichs, M. Bär, M. Häser, H. Horn, C. Kölmel, *Chem. Phys. Lett.* **1989**, *162*, 165–169.
[52] F. Furche, R. Ahlrichs, *J. Chem. Phys.* **2002**, *117*, 7433–7447.
[53] L. Bertini, C. Greco, L. De Gioia, P. Fantucci, *J. Phys. Chem. A* **2006**, *110*, 12900–12907.
[54] N. J. Turro, A. Yekta, *J. Am. Chem. Soc.* **1978**, *100*, 5951-5952.
[55] A. B. Mandal, B. U. Nair, *J. Phys. Chem.* **1991**, *95*, 9008-9013.

Supporting Information

Enhanced Photocatalytic Hydrogen Evolution by Silicon-containing [FeFe] Hydrogenase models

Roman Goy,[a] Luca Bertini,[b] Tobias Rudolph,[c] Martin Schulz,[d] Giuseppe Zampella,[b] Benjamin Dietzek,[d] Felix H. Schacher,[c] Luca De Gioia,[c] Wolfgang Weigand[a]

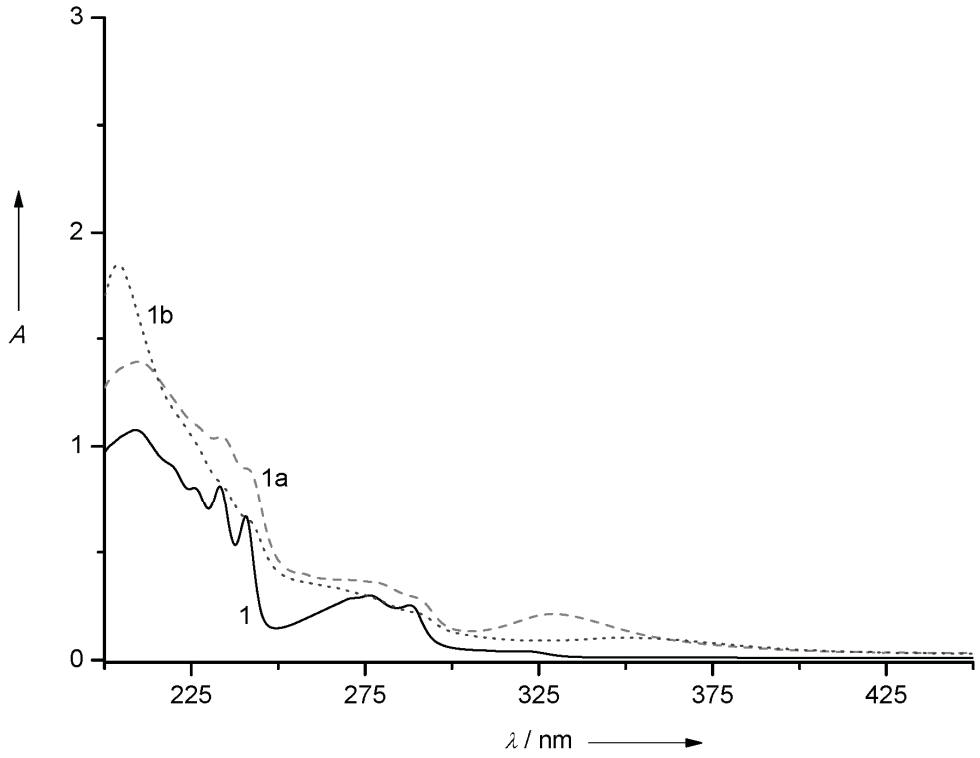

Figure S1: UV-vis spectra for compound **1-1b** (27 μM in acetonitrile).

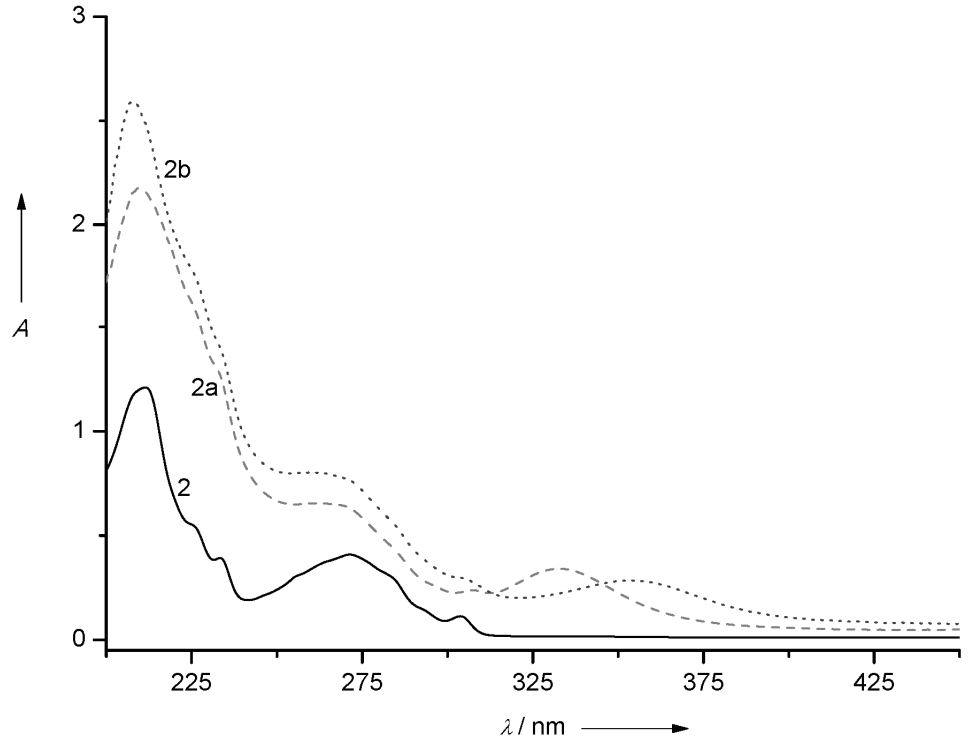

Figure S2: UV-vis spectra for compound **2-2b** (27 μM in acetonitrile).

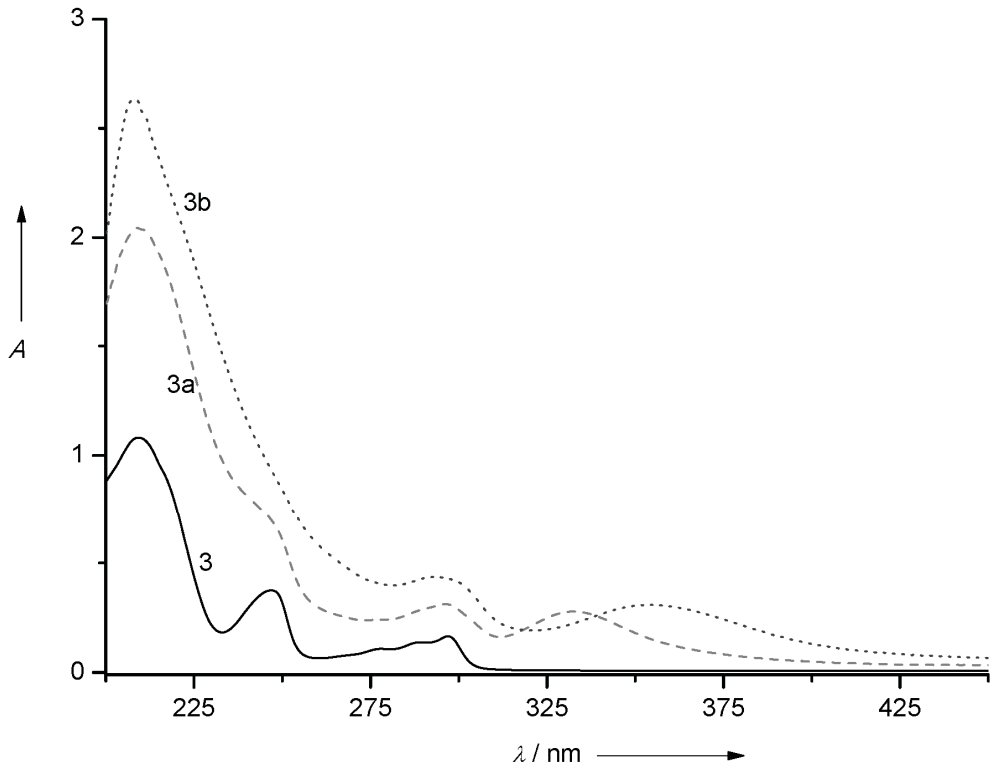

Figure S3: UV-vis spectra for compound **3-3b** (27 μM in acetonitrile).

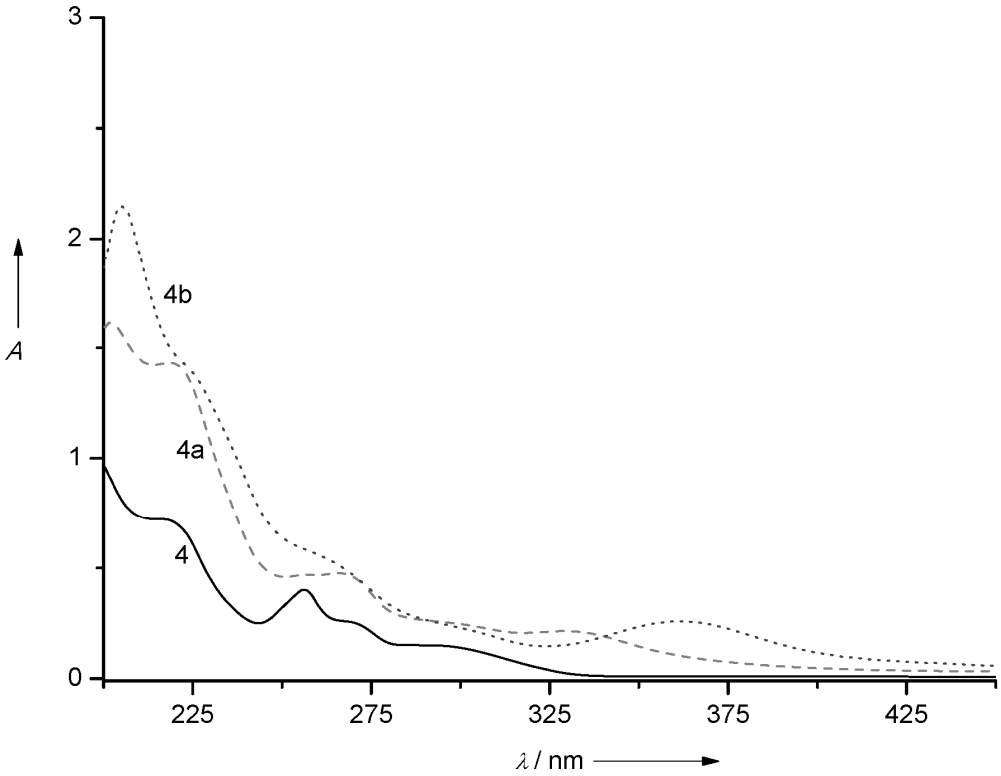

Figure S4: UV-vis spectra for compound **4-4b** (27 μM in acetonitrile).

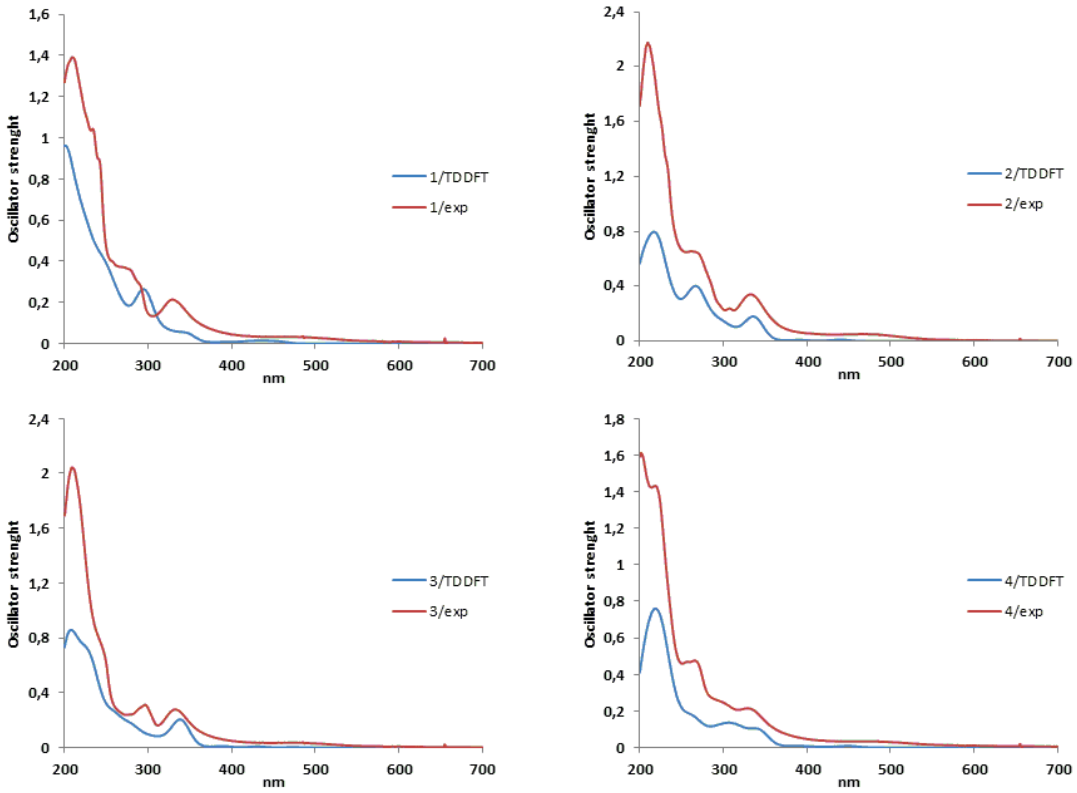

Figure S5. TDDFT spectra of **1a-4a** in gas phase at BP86/TZVP level. In red are also over imposed the experimental spectra for sake of comparison. The spectra are computed by superposition of Gaussian function centered on the computed TDDFT excitation energies with the proper intensities computed on the basis of the corresponding oscillator strength the first 300 (**1a-3a** spectra)/310 (**4a**) computed transitions.

Each experimental spectrum is characterized by i) a very weak shoulder around 500 nm; ii) Aa weak band around 350 nm; iii) two intense bands around 250-300 nm and around 200-250 nm. In the table below are reported the position (in nm) of the spectral features of each spectrum.

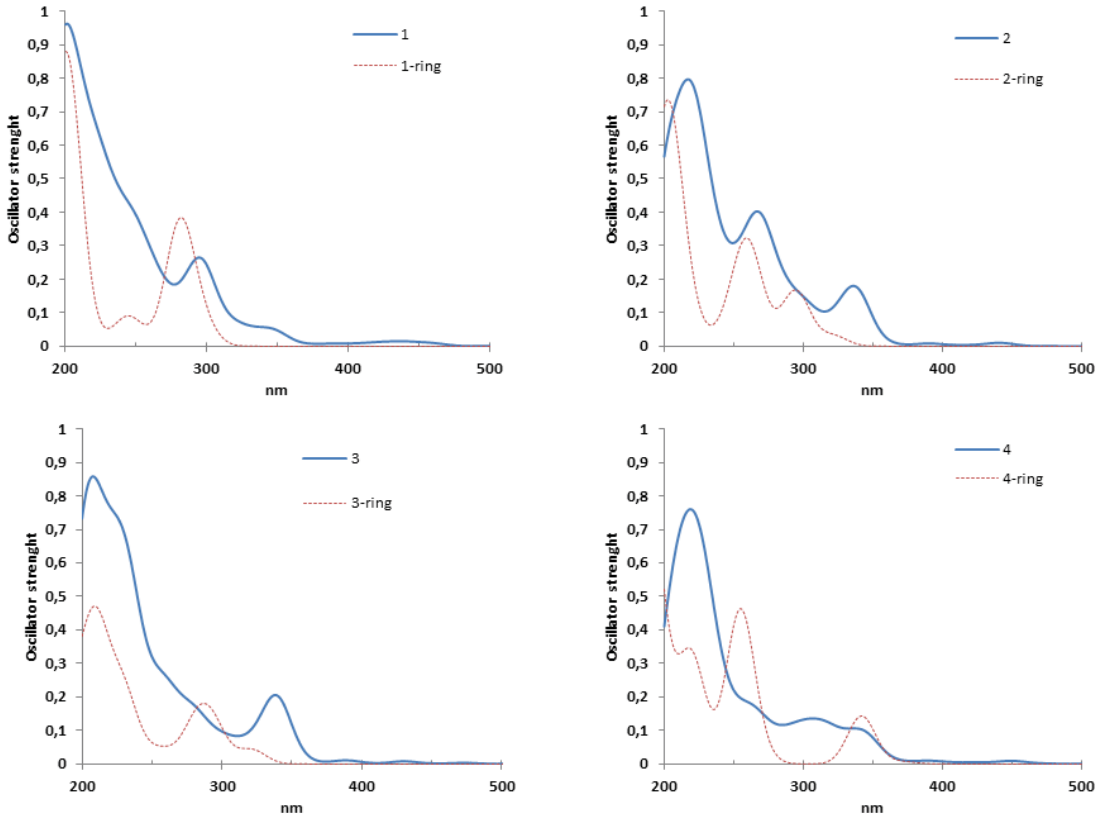

Figure S6. BP86/TZVP gas phase TDDFT spectra of the **1a-4a** and the corresponding heteroaromatic system as isolated molecule (dashed lines). See caption of Figure S5 for details.

Table S1.

complex	1a		2a		3a		4a	
	exp	TDDFT	exp	TDDFT	exp	TDDFT	exp	TDDFT
Feature 1	490	440	470	450	480	430	480	450
Feature 2	330	340	335	340	335	340	335	One broad band
Feature 3	280	250	265	270	250	230	270	
Feature 4	210	200	210	220	210	210	220	220
							205	

Table S2. Results of the band assignments. For each excitation are reported i) the excitation energy in nm (and the excitation order number); ii) the main mono-electronic transition; iii) the assignment according to the localization of the MO involved.

	1a		2a	
Very weak band	444 nm (3) HOMO-2→LUMO	Fe_2S_2→ Fe_2S_2	437 nm (4) HOMO-2→LUMO	Fe_2S_2→ Fe_2S_2
Band ~ 350 nm	338 nm (27) HOMO→LUMO+4	Ring→ Fe_2S_2	346 nm (23) HOMO-5→LUMO+3	Ring→ Fe_2S_2
Band ~280 nm	252 nm (132) HOMO-6→LUMO+8	Ring→ Fe_2S_2	294 nm (51) HOMO→LUMO+3	Ring→Ring
	3a		4a	
Very weak band	429 nm (6) HOMO-4→LUMO	Fe_2S_2→ Fe_2S_2	450 nm (5) HOMO-2→LUMO	Fe_2S_2→ Fe_2S_2
Band ~ 350 nm	340 nm (25) HOMO→LUMO+4	Ring→Ring	343 nm (24) HOMO-11→LUMO	Fe_2S_2→ Fe_2S_2
Band ~280 nm	258 nm (112) HOMO-7→LUMO+4	Ring→Ring Ring→Fe_2	261 nm (117) HOMO-4→LUMO	Ring→Ring Ring→Fe_2

The main result here is the fact that the four complexes share similar spectral features, in particular for lower energy transitions. Going form **1a-2a** to **3a-4a**, the excitation energies seem not significantly affected by the change of the nature of the heteroaromatic ligand.

Table S3. BP86 and PBE0 excitation energy, the oscillator strength and the main one-electron excitations for the first 10 singlet excited states and for the triplet states lower in energy compared with the first singlet state. The shape of the main FMOs involved are reported in Figure S14.

1a	nm	f	1e	2a	nm	f	1e
1^1A	529.6	$3\cdot10^{-7}$	HOMO→LUMO	1^1A	521	$3\cdot10^{-4}$	HOMO→LUMO (83%) HOMO-1→LUMO (17%)
1^3A	654.7		HOMO-1→ LUMO+1 (87%)	1^3A	664.8		HOMO-1→LUMO (73%) HOMO→LUMO (18%)
2^3A	529.9		HOMO→ LUMO	2^3A	522.9		HOMO→LUMO (80%) HOMO-1→LUMO (18%)
2^1A	471	$2\cdot10^{-5}$	HOMO-3→LUMO	2^1A	461	$6\cdot10^{-3}$	HOMO-3→LUMO (55%) HOMO-1→LUMO (29%)
3^1A	444	$6\cdot10^{-3}$	HOMO-1→LUMO (43%) HOMO-3→LUMO (30%) HOMO-4→LUMO (23%)	3^1A	450	$5\cdot10^{-3}$	HOMO→LUMO+1 (85%) HOMO-1→LUMO+1 (15%)
4^1A	439	$2\cdot10^{-4}$	HOMO→ LUMO+1	4^1A	437	$1\cdot10^{-2}$	HOMO-2→LUMO+1 (27%) HOMO-1→LUMO+2 (26%) HOMO-1→LUMO (23%)
5^1A	435	$4\cdot10^{-3}$	HOMO-3→LUMO (62%) HOMO-4→LUMO (24%) HOMO-1→LUMO (10%)	5^1A	428	$7\cdot10^{-4}$	HOMO→LUMO+2 (82%) HOMO-1→LUMO+2 (15%)
6^1A	417	$2\cdot10^{-3}$	HOMO→LUMO+2	6^1A	423	$5\cdot10^{-3}$	HOMO-1→LUMO+1 (51%) HOMO-2→LUMO+1 (14%)
7^1A	410	$4\cdot10^{-4}$	HOMO-5→LUMO (57%) HOMO-1→LUMO+1 (40%)	7^1A	417	$3\cdot10^{-3}$	HOMO-3→LUMO (69%) HOMO-1→LUMO+2 (17%)
8^1A	403	$7\cdot10^{-4}$	HOMO-1→LUMO+1 (53%) HOMO-5→LUMO (38%)	8^1A	411	$3\cdot10^{-3}$	HOMO-1→LUMO+2 (62%) HOMO→LUMO+2 (12%)
9^1A	402	$3\cdot10^{-5}$	HOMO-6→LUMO	9^1A	400	$2\cdot10^{-3}$	HOMO-5→LUMO (73%)
10^1A	390	$7\cdot10^{-3}$	HOMO-2→LUMO+2 (40%) HOMO-4→LUMO (23%) HOMO-1→LUMO (10%)	10^1A	394	$2\cdot10^{-3}$	HOMO-6→LUMO (80%) HOMO-7→LUMO (11%)

Table S4. BP86 and PBE0 excitation energy, the oscillator strength and the main one-electron excitations for the first 10 singlet excited states and for the triplet states lower in energy compared with the first singlet state. The shape of the main FMOs involved are reported in Figure S14.

1a	nm	f	1e	2a	nm	f	1e
1^3A	1444.1		HOMO-1→LUMO (84%)	1^3A	1422.9		HOMO→LUMO (83%) HOMO-1→LUMO (17%)
2^3A	558.2		HOMO-3→ LUMO+1 (78%)	2^3A	526.7		HOMO-1→LUMO (73%) HOMO→LUMO (18%)
3^3A	503.9		HOMO-7→ LUMO (56%) HOMO-3→ LUMO+3 (17%)	3^3A	510.7		HOMO→LUMO (80%) HOMO-1→LUMO (18%)
4^3A	484.6		HOMO-4→LUMO+3 (23%) HOMO-3→LUMO+3 (16%)	4^3A	493.2		HOMO-7→LUMO (37%)
5^3A	480.3		HOMO-1→LUMO+3 (26%) HOMO-8→LUMO (25%)	5^3A	474.6		HOMO-3→LUMO (55%) HOMO-1→LUMO (29%)
6^3A	457.3		HOMO-1→ LUMO (51%)	6^3A	473.0		HOMO→LUMO+1 (85%) HOMO-1→LUMO+1 (15%)
7^3A	442.3		HOMO-4→LUMO (66%)	7^3A	458.2		HOMO-2→LUMO+1 (27%) HOMO-1→LUMO+2 (26%) HOMO-1→LUMO (23%)
8^3A	435.7		HOMO→LUMO+1 (43%) HOMO→LUMO+2 (27%)	8^3A	446.9		HOMO→LUMO+2 (82%) HOMO-1→LUMO+2 (15%)
9^3A	430.8		HOMO-8→LUMO (41%) HOMO-7→LUMO (15%)	9^3A	427.6		HOMO-1→LUMO+1 (51%) HOMO-2→LUMO+1 (14%)
10^3A	428.4		HOMO-9→LUMO (18%) HOMO-7→LUMO+2 (16%)	1^1A	432.1	$3\cdot10^{-2}$	HOMO-1→LUMO (30%) HOMO-7→LUMO (16%)
1^1A	427.6	$3\cdot10^{-3}$	HOMO-3→LUMO (73%) HOMO-8→LUMO (12%)	10^3A	423.0		HOMO-3→LUMO (69%) HOMO-1→LUMO+2 (17%)
2^1A	401.8	$7\cdot10^{-3}$	HOMO-7→LUMO (79%)	2^1A	405.7	$3\cdot10^{-3}$	HOMO-3→LUMO (36%) HOMO-7→LUMO (18%)

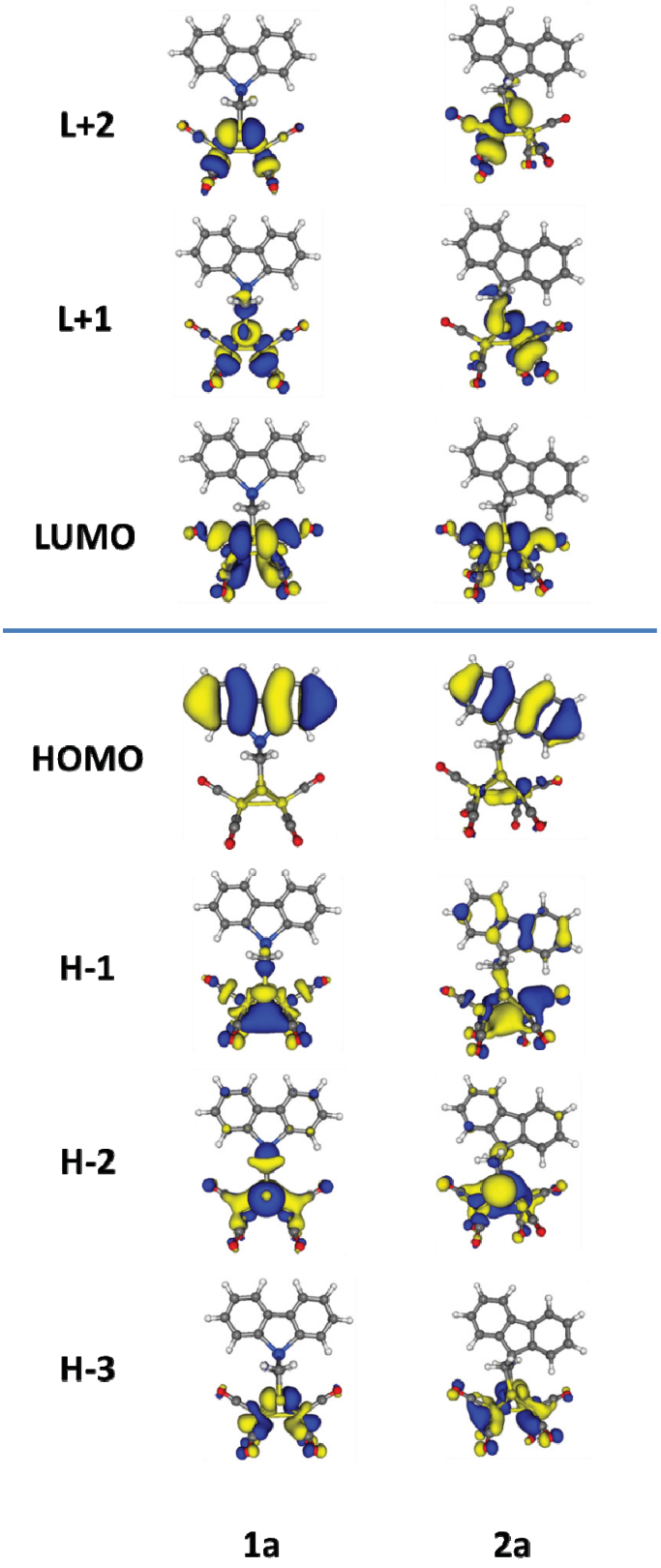

Figure S7. Shape of the **1a** and **2a** BP86 FMOs involved in the lower energy excited states. Isosurface computed at 0.05 au.

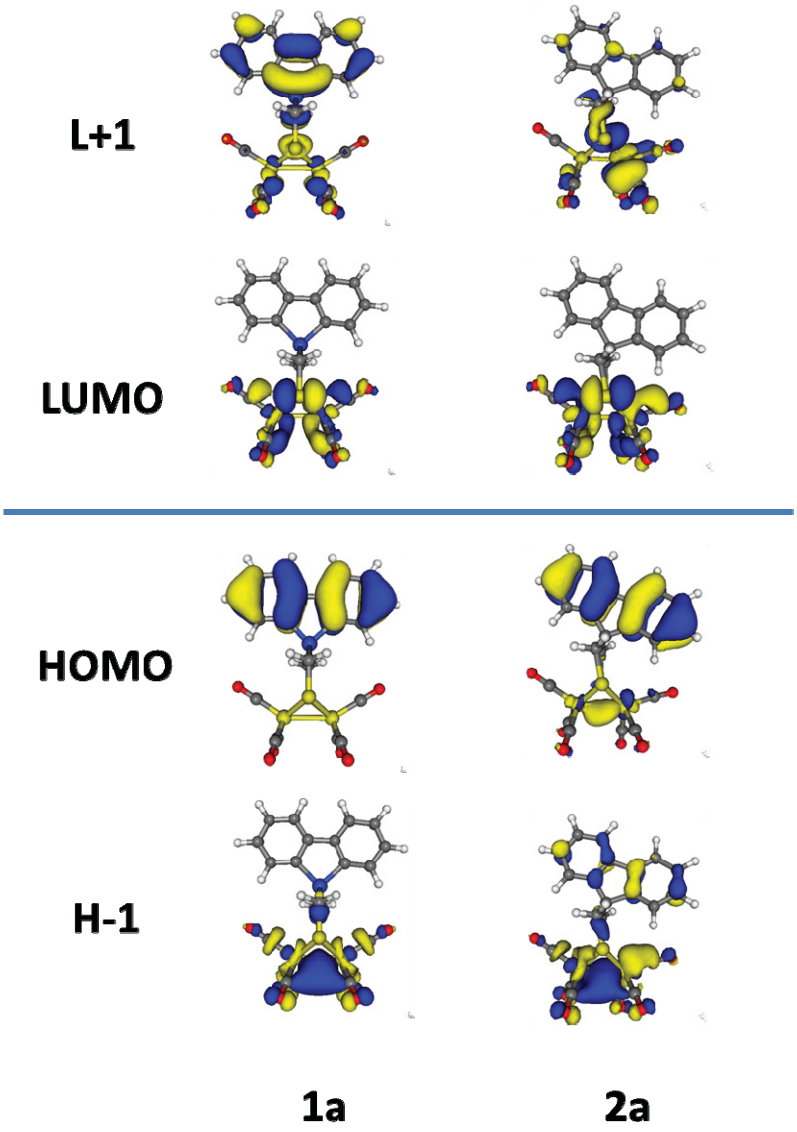

Figure S8. Shape of the **1a** and **2a** PBE0FMOs involved in the lower energy excited states. Isosurface computed at 0.05 au.

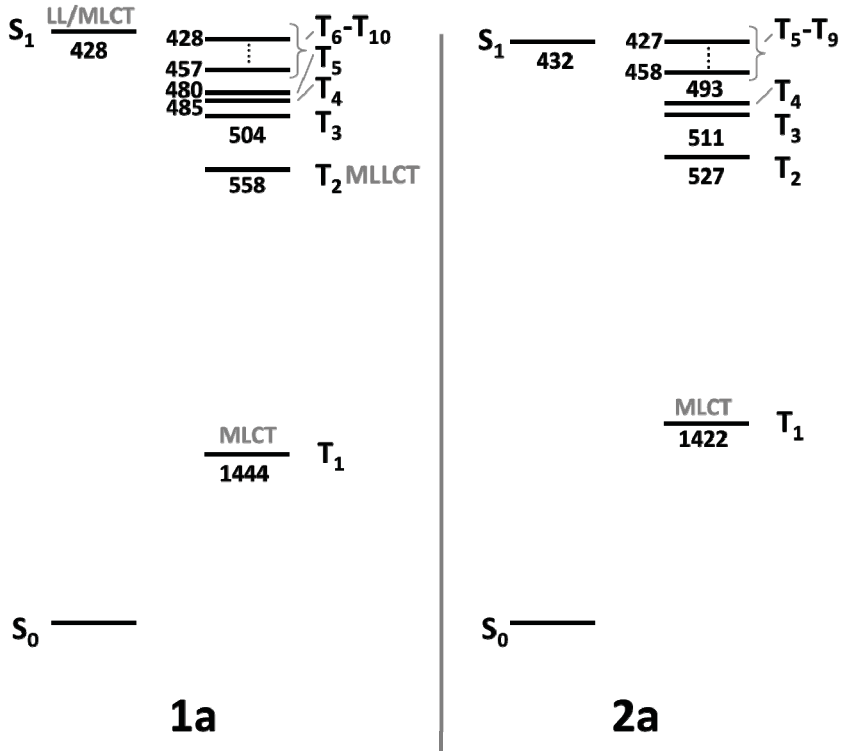

Figure S9. PBE0 vertical excitation energies (in nm) for **1a** and **2a** computed at the corresponding ground state minimum structures.

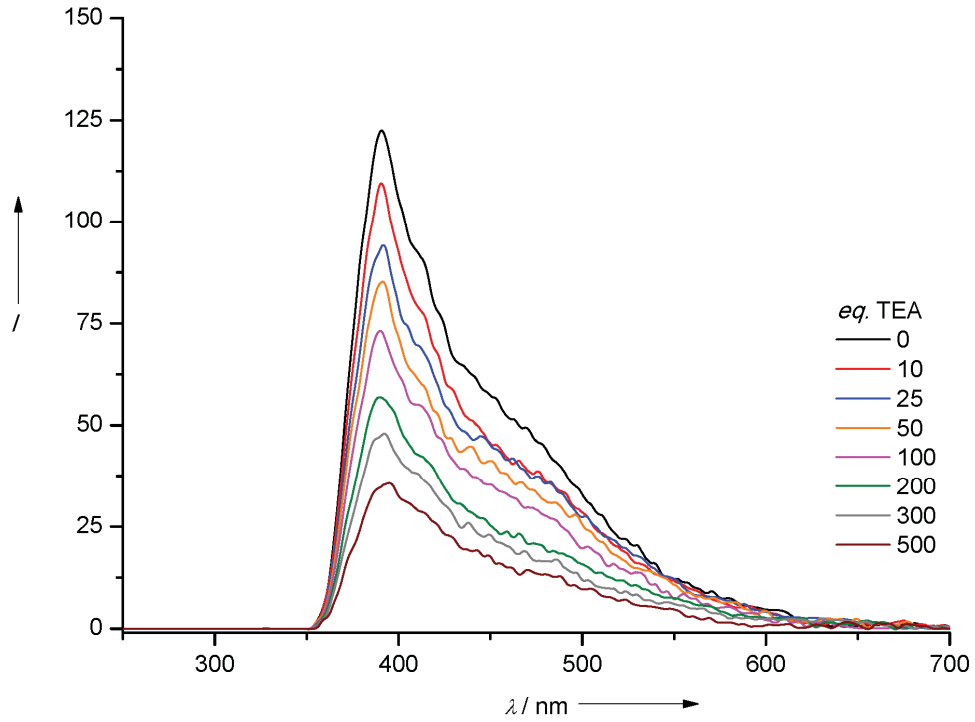

Figure S10. Photoluminescence spectra of **2** (0.27 μM) in acetonitrile in the presence of various amounts of triethylamine (excitation wavelength 245 nm).

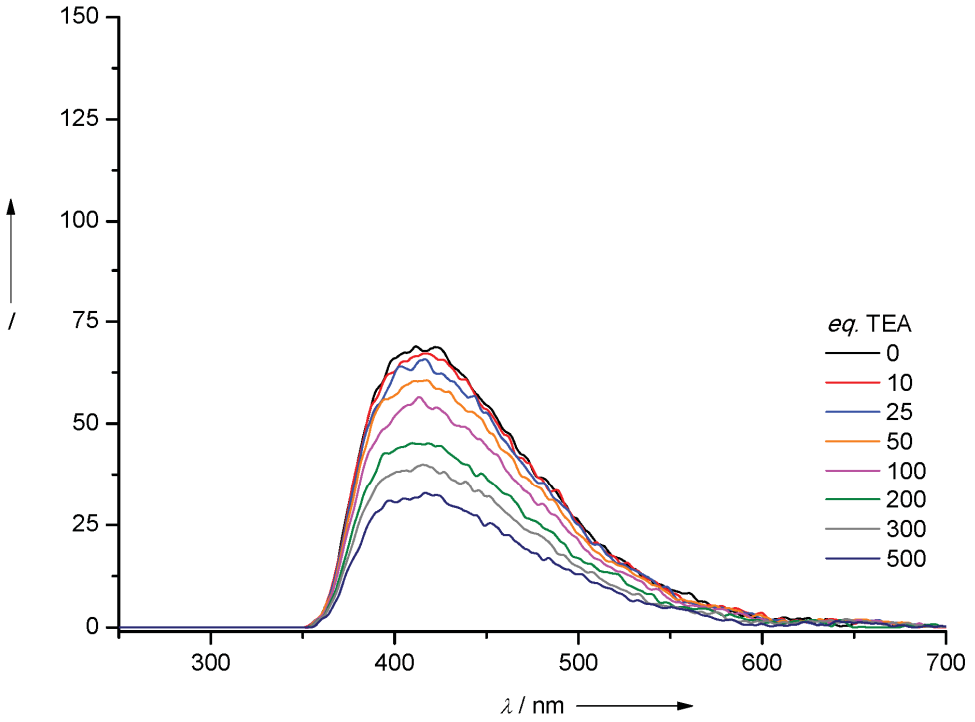

Figure S11. Photoluminescence spectra of **3** (0.27 μM) in acetonitrile in the presence of various amounts of triethylamine (excitation wavelength 247 nm).

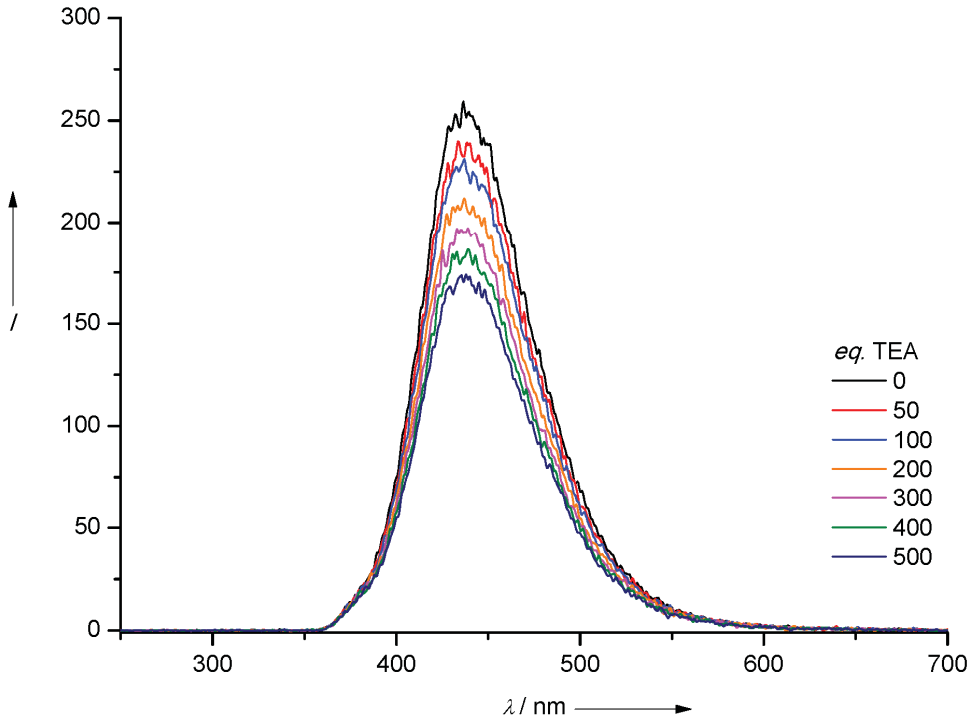

Figure S12. Photoluminescence spectra of **4** (0.27 μM) in acetonitrile in the presence of various amounts of triethylamine (excitation wavelength 256 nm).

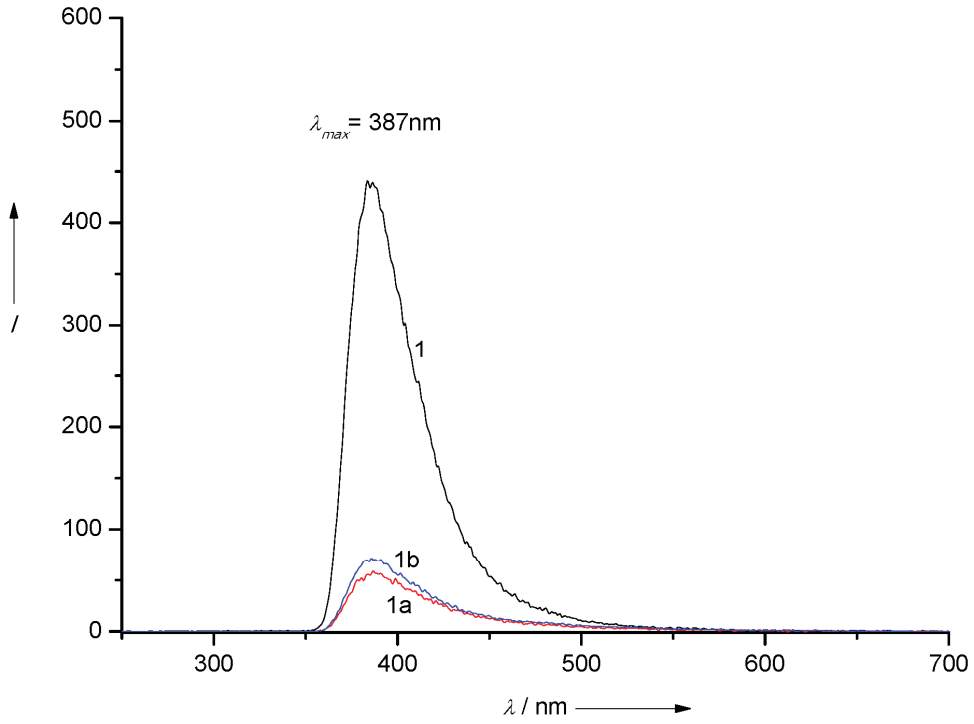

Figure S13. Photoluminescence spectra of **1-1b** 0.27 μM in acetonitrile (excitation wavelength 256 nm).

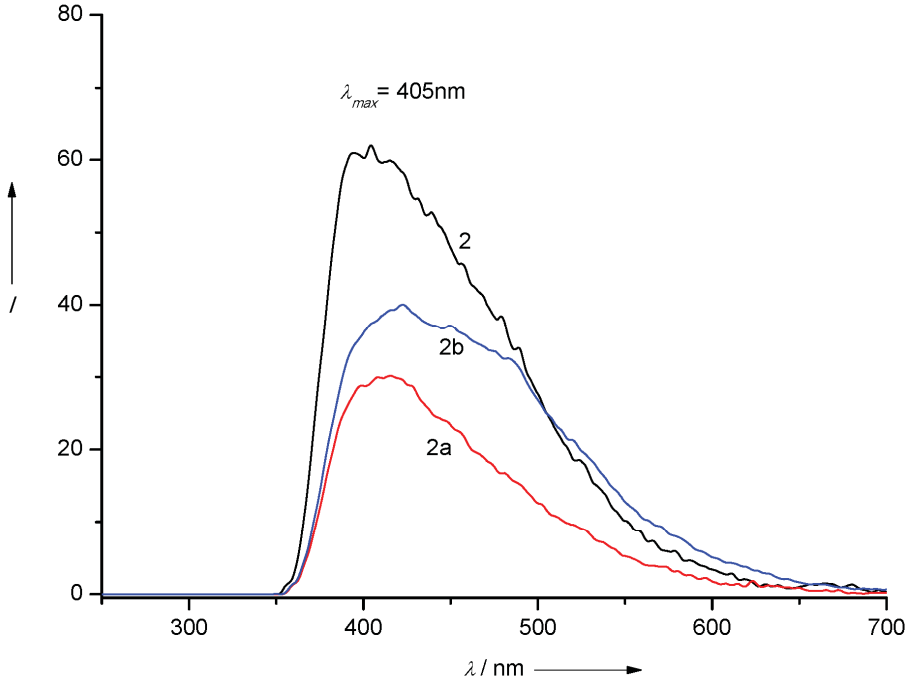

Figure S14. Photoluminescence spectra of **2-2b** 0.27 μM in acetonitrile (excitation wavelength 245 nm).

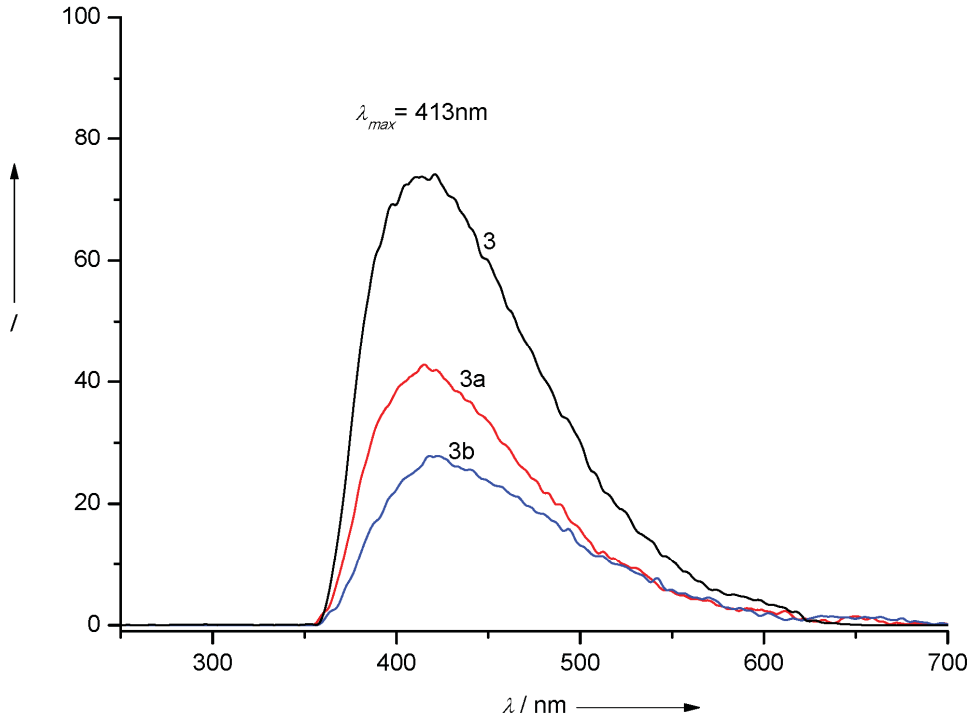

Figure S15. Photoluminescence spectra of **3-3b** 0.27 μM in acetonitrile (excitation wavelength 247 nm).

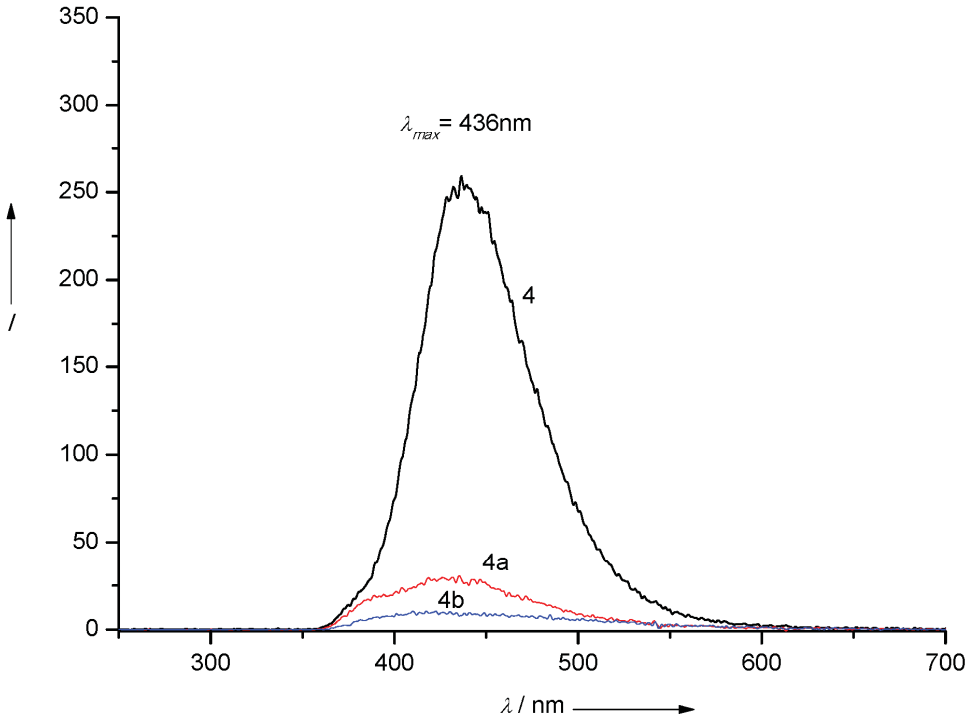

Figure S16. Photoluminescence spectra of **4-4b** 0.27 μM in acetonitrile (excitation wavelength 256 nm).

Table S5. Energy differences (in kcal/mol) among **1a** and **2a** all terminal ligand (**All**), rotated (**Rot**) and Fe-S dissociated (**Fe-S**) isomers in their neutral (S_0), anionic (S_0^-) and bianionic (S_0^{2-}) ground states, the first singlet excited state (S_1) computed at TDDFT level and the first triplet state (T_1) computed at ΔSCF level. Implicit CH_3CN solvent is also considered at DFT and ΔSCF levels.

	1a			**2a**		
	All	**Rot**	**Fe-S**	**All**	**Rot**	**Fe-S**
$\mathbf{S_0}$	0.0	5.6	→all	0.0	2.8	→rot
$\mathbf{S_0^-}$	0.0	0.9	3.1	0.0	0.5	0.4
$\mathbf{S_0^-}$ (CH_3CN)	0.0	0.1	3.7	→semirot	0.6	0.0
$\mathbf{S_1}$	0.0	2.7	→all	→semirot	0.0	6.6
$\mathbf{T_1}$	5.4	0.0	6.4	8.9	0.0	3.6
$\mathbf{T_1}$ (CH_3CN)	→rot	0.0	6.5	9.1	0.0	3.6
$\mathbf{S_0^{2-}}$	→semirot	19.1	0.0	14.6	16.6	0.0
$\mathbf{S_0^{2-}}$ (CH_3CN)	→semirot	9.0	0.0	17.2	18.8	0.0

5 Summary

In the present thesis a new approach was established with feasible synthetic pathways towards small and compact photocatalytic active [FeFe] hydrogenase model complexes with silicon containing heteroaromatic systems as the photosensitizer as well as one carbon analogue system directly imbedded into the bridging dithiolate unit (Figure 34). The synthesized model complexes as well as all other compounds were fully characterized by NMR and IR spectroscopy, mass spectrometry, elemental analysis, UV-vis and fluorescence spectroscopy, XRD analysis as well as cyclovoltammetry. Further theoretical studies were performed for a better understanding of these systems. Finally, comprehensive photocatalytic investigations were carried out with these systems, whereas an extraordinary activity was found for the *all*-CO complexes **65a**-**68a**. A possible filled-filled interaction between the σ(Si-C)-orbital and the *3p*(S)-orbital, allowing a direct communication between the photosensitizer and the [2Fe2S] cluster must be assumed.

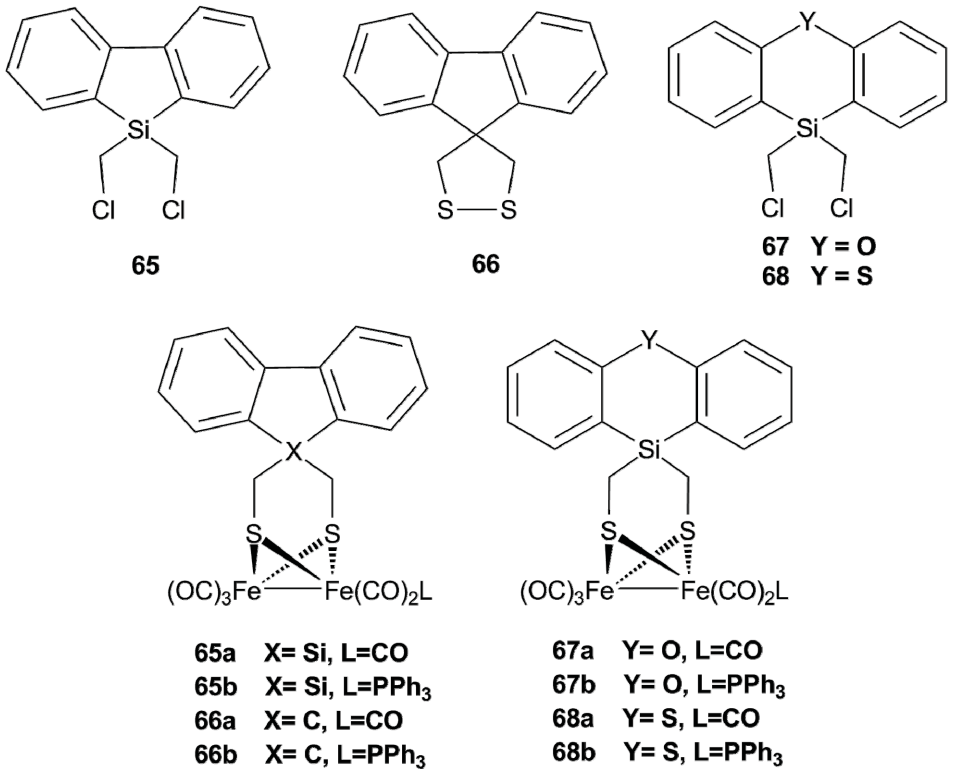

Figure 34: Synthesized photoactive [FeFe] hydrogenase model complexes and their precursors.

The mono-chelating PPh_3 ligand in the substituted model complexes **65b**-**68b** increases the steric hindrance in proximity of the Fe-Fe bond region and thus favors different protonation sites and concomitantly increases the basicity of the diiron cluster. Extensive CV experiments coupled with IR spectroscopy offered the μ-S atoms in these complexes as possible protonation sites, whereas a stable μ-S protonated species could be obtained just with **65b**. Advanced theoretical calculations are in line with these protonation experiments and further elucidate the different structural characteristics of the complex series by the different sterical bulk of the dithiolate bridgeheads.

The most interesting aspect is the comparison of the *1*-silafluorene with the carbon analogue *9*-fluorene containing complexes **65a** and **66a**. As expected, the introduction of silicon instead of a carbon atom offered a positive influence on the optical properties as well as on the catalytic efficiencies. The UV-vis absorption spectra for compounds **65/65a** and **66/66a** offered intense bands between 220-245 nm and 260-290 nm for the *1*-silafluorene moiety. Compared with the fluorene moiety of **66/66a** a hypsochromically shift by 7 nm of these bands is observed, while the intense band at around 210 nm is similar in both systems. Further comparison of the Stern-Volmer rate constants for the two aromatic systems affords a four-time higher quenching efficiency for the *1*-silafluorene-system, which clearly demonstrates the influence of the substitution of a carbon by a silicon atom regarding the lowering of involved orbitals.

Optimized conditions for photocatalytic hydrogen evolution experiments (Figure 35, Table 3) were found by use of acetonitrile as solvent and a catalyst concentration of 10 µM. Triethylamine was used as electron donor in 10,000 times excess (100 mM) and 5,000 equivalents trifluoroacetic acid (50 mM) were added (TEA/TFA 2:1). Under these catalytic environment a turn-over-number of 539 molecules H_2 (16.18 µmol) in 7 h could be reached for complex **65a,** what represents the highest reported turn-over-number by far for such small, compact systems, in which the photosensitizer is covalently linked to the catalytic active center. The reported systems are much more efficient than comparable model complexes using noble-metal-containing photosensitizers. The TON of 539 corresponds to a turn-over-frequency of 77 molecules H_2/h calculated for the catalysis time of 7 hours with an initial TOF of 242 molecules H_2 in the first hour. Direct comparison with the carbon analogue complex **66a** reveals a positive influence of the substitution of the

carbon atom by a silicon atom. The turn-over-number for **66a** was 458 after 7 h (13.73 µmol) with a TOF of 65.4 molecules H_2/h and an initial TOF of 186 molecules H_2 in the first hour. This represents also an excellent value but compared to that of **65a** a minor catalytic efficiency. Nevertheless, also carbon analogue complexes represent an efficient possibility for photocatalytic hydrogen generation and should not be neglected. It seems that the key issue of these systems is the close proximity of the photosensitizer to the catalytic active [2Fe2S] cluster. The short linker of just one CH_2-group makes the design of the herein reported [FeFe] hydrogenase model complexes to a powerful platform for the further development of hydrogen generating catalysts. The synthetic pathway to carbon bridged model complexes should be also feasible and opened a whole new spectrum of approaches and possibilities, in particular the aspect of shifting the absorbance wavelength of the currently used photosensitizers into the visible light region.

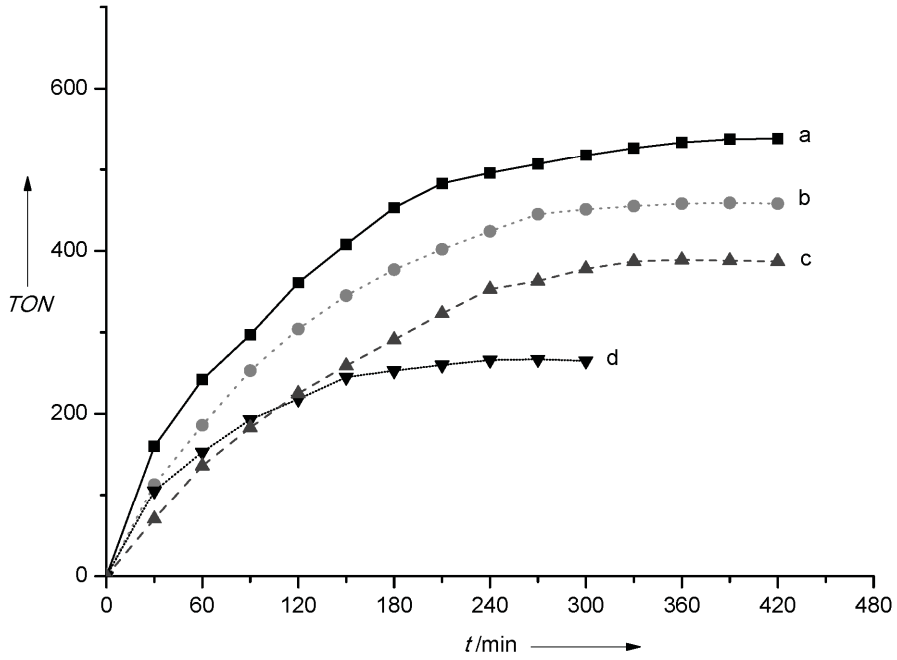

Figure 35: Time dependence of photocatalytic H_2 evolution under optimized conditions (TEA (100 mM), TFA (50 mM) in acetonitrile) of (a) **65a** (10 µM), (b) **66a** (10 µM), (c) **68a** (10 µM) and (d) **67a** (10 µM). Total solution volume 3 mL, Hg vapor lamp (12 W).

Furthermore, photocatalytic H_2 generation was forced to takes place in aqueous solution. For this reason the hydrophobic catalyst **65a** have been successfully incorporated into an aqueous SDS or CTAB solution and TEA/TFA 2:1 (100 mM/ 50 mM) at pH = 10 were established as optimized conditions, too. After an

irradiation time of four hours, a TON of 148 could be reached for the aqueous CTAB solution of **65a** offering the most efficient micellar system reported so far utilizing [FeFe] hydrogenase model complexes.[167] Using SDS under same conditions and irradiation time a TON of 139 was obtained, which offers an almost negligible influence of the used tenside under the investigated conditions.

Table 3: Photocatalytic hydrogen evolution experiments under optimized conditions.

Run	***Irradiation time / h***	***TON***	***TOF / h^{-1}***	***Initial TOF (after 1h) / h^{-1}***
a	7	539	77	242
b	7	459	65.6	186
c	5	267	53.4	153
d	7	389	55.6	136

In consideration of performed experiments and characterization methods like *e.g.* electrochemical studies as well as photocatalytic investigations and comprehensive theoretical calculations, a possible photocatalytic pathway for the H_2 generation (Figure 36) was elucidated. By this way some key intermediates could be figured out. The first common step is the sensitization process, in which the system is first excited and then reduced to **65a**$^-$ by an photoinduced electron transfer from TEA to the excited **65***. Furthermore, the mono-anionic **65a**$^-$ undergo a second reduction process promoted either by the formed radical cation $TEA^{+\bullet}$ or a second photoreduction process to the dianionic form **65a**$^{2-}$, followed by a doubly protonation to **65aH$_2$** and final H_2 detach closing the catalytic cycle. Starting from the dianionic species **65a**$^{2-}$, protonation at the dissociated sulfur atom yields the most stable **65aH**$^-$ isomer featuring a bridging CO ligand, while in **65aH$_2$** the second proton forms a bridging hydride.

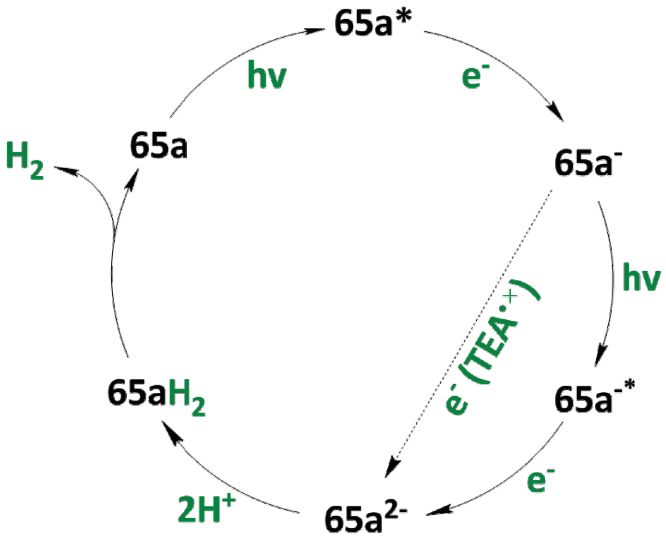

Figure 36: Established pathway for the light-induced hydrogen evolution by [FeFe] hydrogenase model complex **65a**.

A different aspect of this work was the utilization of the sterically bulky and silicon containing dithiolate *meso*-bis(benzylthio)diphenylsilane as linker in a [FeFe] hydrogenase model compound **69** for the investigation of the rotated state species of [$Fe^{I}Fe^{I}$] subsite models. Inspired by the recently published results of Schollhammer *et al*.[148,149] and the established cooperation to this group complex **69** was reacted with dmpe (Schema 11), which affords [FeFe] H_2ase mimic **71** as an example with the highest degree of rotation so far (87,1°) reported for [$Fe^{I}Fe^{I}$] hydrogenase models without any agostic interactions ($Fe^{\cdots}H$-C)[145] and enabling new approaches for the design of dithiolate bridgeheads to achieve a full-rotated geometry related to the active site of [FeFe] hydrogenases without any type of H-bond interaction.

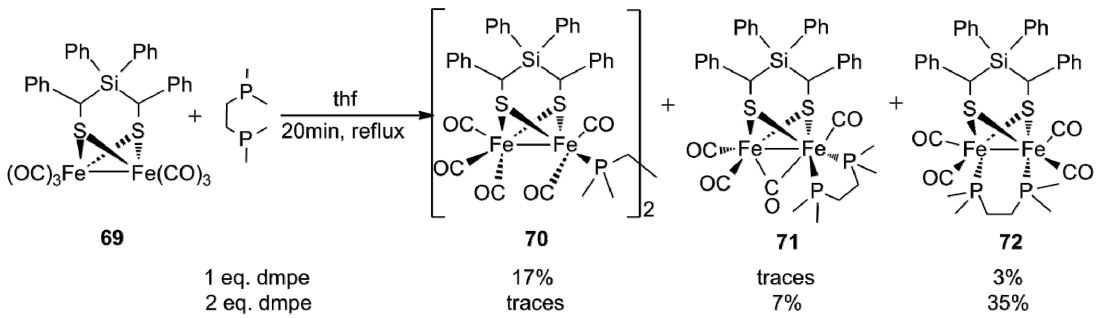

Scheme 10: Reaction of [FeFe] hydrogenase model complex **69** with different equivalents of dmpe.

6 Zusammenfassung

In der vorliegenden Dissertationsschrift wurde ein neuartiger Ansatz für biomimetische [FeFe]-H_2ase-Modelle gewählt und durchführbare Synthesemethoden etabliert, um kleine und kompakte fotoaktive Modellkomplexe mit Silizium-haltigen heteroaromatischen Systemen als auch das entsprechende Kohlenstoff-analoge System herzustellen, in welchem der Fotosensibilisator direkt mit dem verbrückendem Dithiolato-Ligand verknüpft ist (Figure 34). Die synthetisierten Modellkomplexe als auch alle weiteren hergestellten Verbindungen wurden vollständig mit NMR- und IR-Spektroskopie, Massenspektrometrie, Elementaranalyse, UV-vis- und Fluoreszenzspektroskopie, Einkristall-Röntgenstrukturanalyse als auch Zyklovoltammetrie charakterisiert. Weiterführende DFT-Rechnungen wurden durchgeführt, um die untersuchten Systeme und ihre strukturellen als auch chemischen Unterschiede bzw. Gemeinsamkeiten besser zu verstehen. Schließlich wurden mit diesen [FeFe]-Hydrogenase Modellkomplexen umfassende photokatalytische Untersuchungen unternommen, wobei eine ausordentlich hohe katalytische Aktivität für die *all*-CO Komplexe **65a**-**68a** gemessen wurde. Hierzu sollte eine mögliche "filled-filled" Wechselwirkung zwischen dem σ(Si-C)-Orbital und dem *3p*(S)-Orbital in Betracht gezogen werden, welche eine direkte Kommunikation zwischen dem Fotosensibilisator und dem katalytisch aktivem [2Fe2S]-Cluster erlaubt.

Der mono-dentate Triphenylphosphan-Ligand in den Komplexen **65b**-**68b** erhöht den sterischen Anspruch in der Nähe der Eisen-Eisen-Bindung und favorisiert dadurch andere mögliche Protonierungsstellen. Gleichzeitig stellt er einen besseren σ-Donor als CO dar und erhöht damit die ohnehin hohe Basizität des Eisenzentrums in Silizium-haltigen Modellkomplexen. Umfassende CV-Experimente gekoppelt mit IR-spektroskopischen Untersuchungen offenbarten die μ-S Atome dieser Komplexe als mögliche Protonierungsstellen, wobei eine stabile protonierte μ-S-Spezies nur bei Komplex **65b** beobachtet werden konnte. Weiterführende theoretische Betrachtungen stimmen mit den experimentellen Daten diesbezüglich überein und führen die unterschiedlichen strukturellen Eigenschaften dieser Komplexserie auf den unterschiedlichen sterischen Anspruch der Dithiolato-Liganden zurück.

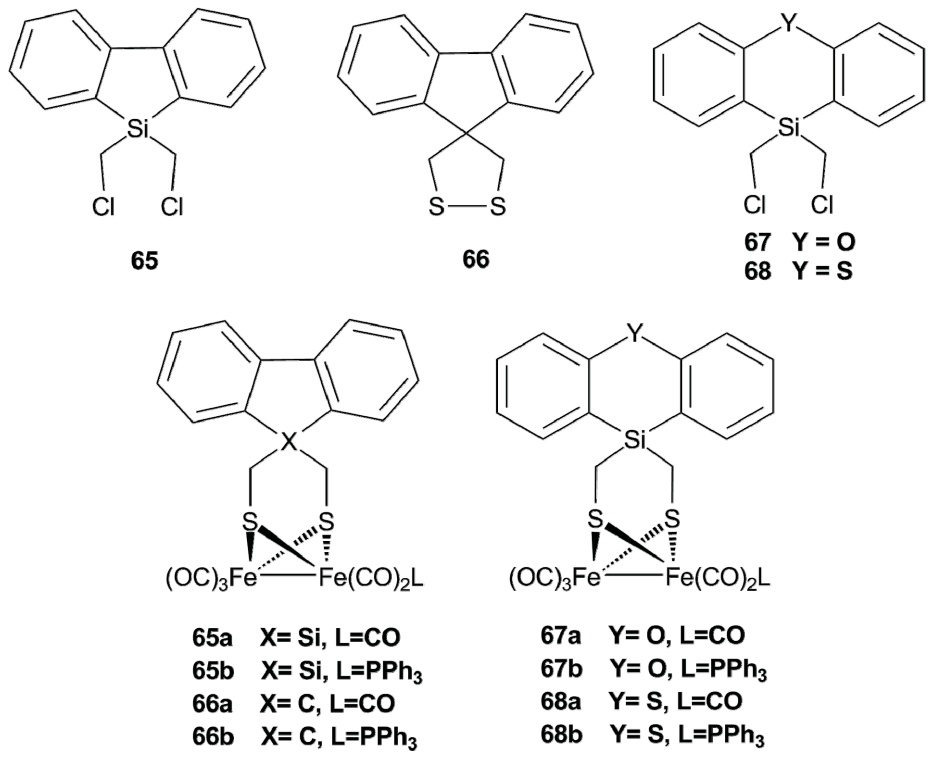

Abbildung 37: Synthetisierte fotoaktive [FeFe]-Hydrogenase Modellkomplexe und ihre Vorstufen.

Der interessanteste Aspekt jedoch ist der direkte Vergleich zwischen dem *1*-Silafluoren- und dem Kohlenstoff-analogen *9*-Fluoren-Liganden bzw. der Vergleich der *all*-CO Komplexe **65a** und **66a**. Wie erwartet zeigt die Substitution eines Kohlenstoffatoms mit einem Silizium einen positiven Einfluss auf die optischen als auch katalytischen Eigenschaften. Die UV-vis-Absorptionsspektren der Verbindungen **65/65a** und **66/66a** zeigen Banden hoher Intensität zwischen 220-245 nm und 260-290 nm für das *1*-Silafluoren-System. Bei dem Vergleich mit dem *9*-Fluoren-System der Verbindungen **66/66a** ist ein hypsochromer Shift von 7 nm bei diesen Banden zu beobachten, während eine weitere Bande mit hoher Intensität bei 210 nm bei beiden Systemen gleich bleibt. Ein Vergleich der Stern-Volmer Konstanten für diese beiden aromatischen Systeme offenbart eine 4-fach höhere Effizienz der Fotolumineszenzlöschung für das *1*-Silafluoren-System, was nochmals deutlich den Einfluss der durch die Silizium-Substitution verursachte energetische Absenkung der beteiligten Orbitale aufzeigt.

Bei der Durchführung von Experimenten zur fotokatalytischen Wasserstoff-generierung wurden verschiedene Bedingungen untersucht (Figure 35, Table 3) und die Verwendung von Acetonitril als Lösungsmittel und eine Katalysatorkonzentration von 10 µM als optimale Bedingungen etabliert.

Triethylamin wurde als Elektronendonor in 10.000-fachen Überschuss (100 mM) zugesetzt und 5.000 Äquivalente Trifluoressigsäure (50 mM) verwendet (TEA/TFA 2:1). Unter diesen katalytischen Bedingungen konnte eine TON von 539 Molekülen H_2 (16,18 µmol) bei einer Belichtungsdauer von 7 h für Komplex **65a** gemessen werden, was die bei Weitem höchste bekannte Umsatzzahl für solche kleinen und kompakten Systeme, in dem der Fotosensibilisator mit dem katalytischen Zentrum kovalent verbunden ist, darstellt. Die hier untersuchten Modellsysteme sind sehr viel effizienter als vergleichbare Systeme, welche teure Edelmetall-haltige Fotosensibilisatoren verwenden. Die TON von 539 entspricht einer Frequenz von 77 Molekülen H_2 pro Stunde mit einer anfänglichen TOF von 242 Molekülen H_2 in der ersten Stunde der Katalyse. Der direkte Vergleich mit dem Kohlenstoff-analogen Komplex **66a** offenbart auch hier einen positiven Einfluss der Substitution eines Kohlenstoffatoms mit einem Silizium. Die TON für **66a** beträgt 458 nach ebenfalls 7 h Belichtungszeit (13,73 µmol), was einer TOF von 65,4 Molekülen H_2/h und einer anfänglichen TOF von 186 Molekülen H_2 innerhalb der ersten Katalysestunde entspricht. Dies ist ebenfalls ein hervorragender Wert, zeigt aber im Vergleich mit **65a** eine geringer katalytische Effizienz. Trotzdem stellen die Kohlenstoff-analogen Komplexe eine effiziente Möglichkeit für fotokatalytische Wasserstoffgenerierung dar und sollten deshalb nicht vernachlässigt werden. Der Schlüsselaspekt dieser Systeme scheint dabei die doch sehr große Nähe des Fotosensibilisators zum katalytisch aktivem [2Fe2S]-Cluster zu sein. Der kurze Linker, welcher nur eine einfache CH_2-Gruppe darstellt, macht den Aufbau der in dieser Arbeit untersuchten [FeFe]-Hydrogenase Modellkomplexe zu einer vielversprechenden Plattform für die weitere Entwicklung von Wasserstoff-produzierenden Katalysatoren. Die Synthese

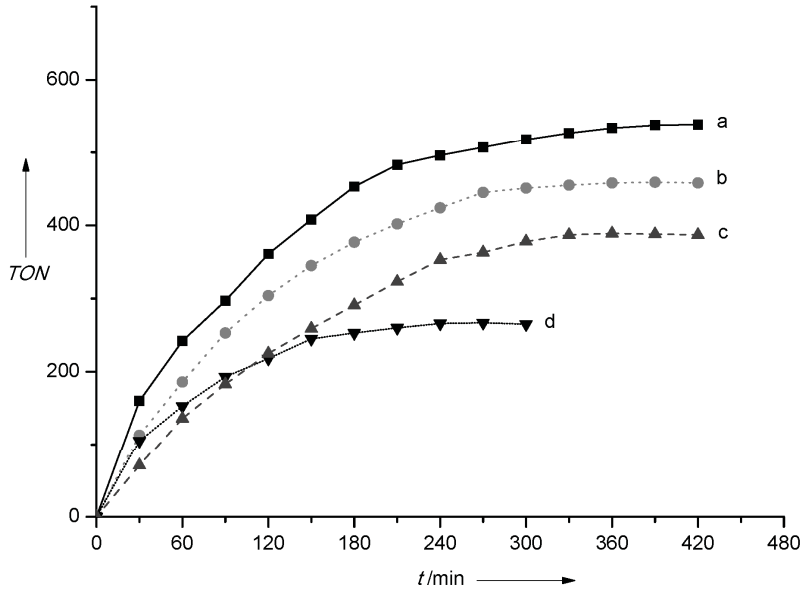

Abbildung 38: Zeit-abhängige photokatalytische H_2 Generierung unter optimierten Bedingungen (TEA (100 mM), TFA (50 mM) in Acetonitril) von (a) **65a** (10 µM), (b) **66a** (10 µM), (c) **68a** (10 µM) und (d) **67a** (10 µM). V = 3 mL, Hg-Dampflampe (12 W).

der Kohlenstoff-verbrückten Modellkomplexe sollte ähnlich der Synthesen der Si-Modellkomplexe etablierbar sein und öffnet ein ganz neues Spektrum von Möglichkeiten, wie z.B. die Lage der Absorptionsbanden der hier untersuchten Fotosensibilisatoren in den sichtbaren Wellenlängenbereich zu verschieben.

Weiterhin wurden Experimente durchgeführt, um eine fotokatalytische H_2 Generierung in wässrigen Medien zu gewährleisten. Aus diesem Grund wurde der hydrophobe Katalysator **65a** erfolgreich in wässrige SDS- bzw. CTAB-Micellensysteme eingeschlossen und ebenfalls TEA/TFA 2:1 (100 mM/ 50 mM) bei pH = 10 als optimale Katalysebedingungen etabliert. Nach einer Belichtungsdauer von vier Stunden konnte eine TON von 148 für das wässrige **65a**-CTAB-System ermittelt werden. Dieses System stellt damit das bisher effizienteste Micellensystem, welches [FeFe]-Hydrogenase Modellkomplexe als Katalysatoren verwendet, dar.[167] Unter gleichen Bedingungen ergab das **65a**-SDS-System eine TON von 139, was nur einen geringen Einfluss des verwendeten Tensids unter diesen Bedingungen offenbart.

Tabelle 4: Fotokatalytische Wasserstoffgenerierung unter optimierten Bedingungen.

Lauf	*Belichtungszeit / h*	*TON*	*TOF / h^{-1}*	*TOF (nach 1h) / h^{-1}*
a	7	539	77	242
b	7	459	65.6	186
c	5	267	53.4	153
d	7	389	55.6	136

Im Bezug auf die durchgeführten Experimente wie zum Beispiel den elektrochemischen Untersuchungen und auch den fotochemischen Katalysen wurden umfangreiche theoretische Rechnungen durchgeführt, um einen möglichen fotokatalytischen Mechanismus für die H_2-Generation zu formulieren (Abbildung 34). Dadurch konnten in Übereinstimmung mit durchgeführten Experimenten einige wichtige Zwischenstufen herausgestellt werden. In einem ersten Schritt kommt es zur Lichtanregung des Komplexes **65a**, welcher direkt durch einen fotoinduzierten Elektronentransfer vom TEA zum angeregten **65*** zum **65a**$^-$ reduziert wird. Diese monoanionische Spezies **65a**$^-$ unterzieht sich einer weiteren Reduktion, welche entweder durch das gebildete Radikalkation $TEA^{+\bullet}$ oder einem weiteren fotochemischen Prozess begünstigt ist, wodurch sich die dianionische Form **65a**$^{2-}$ bildet. Dieser Schritt ist von einer zweifachen Protonierung zum **65aH$_2$** gefolgt, welcher anschließend H_2 entlässt und so den katalytischen Kreislauf schließt.

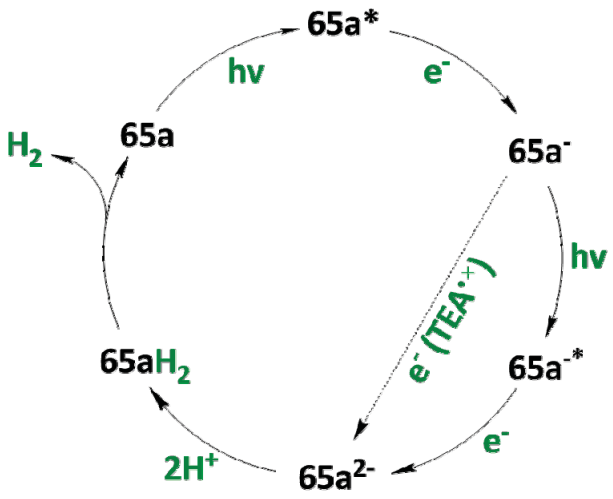

Abbildung 34: Etablierter Mechanismus für eine lichtinduzierte Wasserstoffgenerierung durch den [FeFe]-Hydrogenase Modelkomplex **65a**.

Ein weiterer Aspekt der hier vorliegenden Dissertationsschrift war die Verwendung des sterisch sehr anspruchsvollen und Silizium-haltigen Dithiolato-Liganden *meso*-Bis(benzylthio)diphenylsilan in einem [FeFe]-Hydrogenase Modellkomplex **69** für die Untersuchung einer möglichen Ausbildung der sogenannten „rotated state“ in $[Fe^{I}Fe^{I}]$-Systemen. Inspiriert durch kürzlich veröffentlichte Arbeiten von Schollhammer *et al*.[148,149] und der mit dieser Gruppe etablierten Kooperation wurde Komplex **69** mit DMPE umgesetzt (Schema 11), wobei das [FeFe]-H_2ase Modell **71** erhalten werden konnte. Diese Verbindung stellt ein Beispiel seiner Verbindungsklasse dar, welches den bisher höchsten Grad einer Rotation für $[Fe^{I}Fe^{I}]$-Hydrogenase Modelle aufweist, ohne dabei durch irgendeine Art und Weise von einer agostischen Wechselwirkung ($Fe^{\cdots}H$-C)[145] stabilisiert zu werden. Diese Ergebnisse ermöglichen neue Ansätze für das Design von Dithiolato-Liganden, um eine vollständige “rotated-state“ bezogen auf das aktive Zentrum der [FeFe]-Hydrogenase ohne jegliche agostische Wechselwirkung zu erhalten.

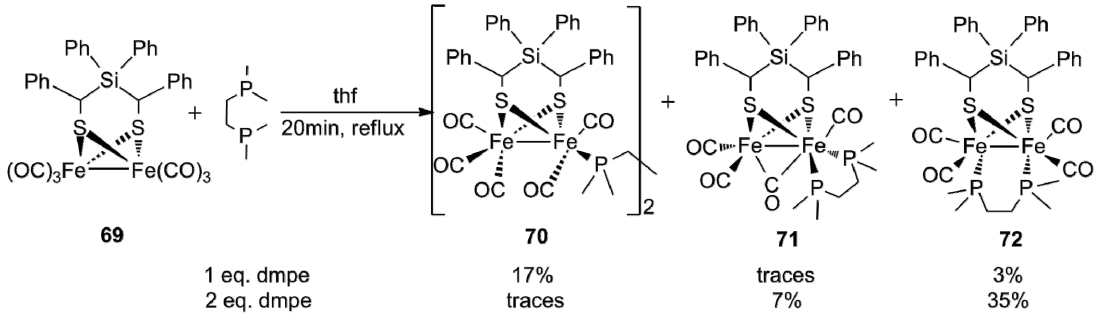

Schema 11: Umsetzung des [FeFe]-Hydrogenase Modellkomplexes **69** mit verschiedenen Äquivalenten DMPE.

7 References

[1] A. Grübler, N. Nakićenović, *Technol. Forecast. Soc. Change* **1996**, *53*, 97–110.

[2] D. M. Etheridge, L. P. Steele, R. L. Langenfelds, R. J. Francey, J.-M. Barnola, V. I. Morgan, *J. Geophys. Res.* **1996**, *101*, 4115–4128.

[3] J. G. Canadell, C. Le Quere, M. R. Raupach, C. B. Field, E. T. Buitenhuis, P. Ciais, T. J. Conway, N. P. Gillett, R. A. Houghton, G. Marland, *Proc. Natl. Acad. Sci.* **2007**, *104*, 18866–18870.

[4] R. Keeling, S. Piper, A. Bollenbacher, S. Walker, "The Keeling Curve | A daily record of atmospheric carbon dioxide from Scripps Institution of Oceanography at UC San Diego," can be found under https://scripps.ucsd.edu/programs/keelingcurve/, **n.d.**

[5] R. Camilli, C. M. Reddy, D. R. Yoerger, B. A. S. Van Mooy, M. V. Jakuba, J. C. Kinsey, C. P. McIntyre, S. P. Sylva, J. V. Maloney, *Science* **2010**, *330*, 201–204.

[6] P. Bossew, G. Kirchner, M. De Cort, G. de Vries, A. Nishev, L. de Felice, *J. Environ. Radioact.* **2012**, *114*, 22–34.

[7] C. Koroneos, *Int. J. Hydrog. Energy* **2004**, *29*, 1443–1450.

[8] D. Cecere, E. Giacomazzi, A. Ingenito, *Int. J. Hydrog. Energy* **2014**, *39*, 10731–10747.

[9] L. Schlapbach, A. Zuttel, *Nature* **2001**, *414*, 353–358.

[10] C. L. Aardahl, S. D. Rassat, *Int. J. Hydrog. Energy* **2009**, *34*, 6676–6683.

[11] W. Osborn, T. Markmaitree, L. L. Shaw, R. Ren, J. Hu, J. H. Kwak, Z. Yang, *JOM* **2009**, *61*, 45–51.

[12] R. M. Navarro, M. A. Peña, J. L. G. Fierro, *Chem. Rev.* **2007**, *107*, 3952–3991.

[13] D. R. Palo, R. A. Dagle, J. D. Holladay, *Chem. Rev.* **2007**, *107*, 3992–4021.

[14] J. M. Ogden, *Annu. Rev. Energy Environ.* **1999**, *24*, 227–279.

[15] R. K. Thauer, *Eur. J. Inorg. Chem.* **2011**, *2011*, 919–921.

[16] M. W. W. Adams, *Science* **1998**, *282*, 1842–1843.

[17] E. C. Hatchikian, N. Forget, V. M. Fernandez, R. Williams, R. Cammack, *Eur. J. Biochem.* **1992**, *209*, 357–365.

[18] J. R. Lancaster Jr., *The Bioinorganic Chemistry of Nickel*, John Wiley & Sons, **1988**.

[19] E. Garcin, X. Vernede, E. Hatchikian, A. Volbeda, M. Frey, J. Fontecilla-Camps, *Structure* **1999**, *7*, 557–566.

[20] C. Zirngibl, W. Dongen, B. Schworer, R. Bunau, M. Richter, A. Klein, R. K. Thauer, *Eur. J. Biochem.* **1992**, *208*, 511–520.

[21] E. J. Lyon, S. Shima, G. Buurman, S. Chowdhuri, A. Batschauer, K. Steinbach, R. K. Thauer, *Eur. J. Biochem.* **2003**, *271*, 195–204.

[22] X. Wang, Z. Li, X. Zeng, Q. Luo, D. J. Evans, C. J. Pickett, X. Liu, *Chem. Commun.* **2008**, 3555–3557.

[23] S. Shima, R. K. Thauer, *Chem. Rec.* **2007**, *7*, 37–46.

[24] D. Das, T. Dutta, K. Nath, S. M. Kotay, A. K. Das, T. N. Veziroglu, *Curr. Sci.* **2006**, *90*, 1627–1637.

[25] M. W. W. Adams, *Biochim. Biophys. Acta BBA - Bioenerg.* **1990**, *1020*, 115–145.

[26] Y. Nicolet, C. Piras, P. Legrand, C. E. Hatchikian, J. C. Fontecilla-Camps, *Structure* **1999**, *7*, 13–23.

[27] J. W. Peters, W. N. Lanzilotta, B. J. Lemon, L. C. Seefeldt, *Science* **1998**, *282*, 1853–1858.
[28] Y. Nicolet, A. L. de Lacey, X. Vernède, V. M. Fernandez, E. C. Hatchikian, J. C. Fontecilla-Camps, *J. Am. Chem. Soc.* **2001**, *123*, 1596–1601.
[29] A. Silakov, B. Wenk, E. Reijerse, W. Lubitz, *Phys. Chem. Chem. Phys.* **2009**, *11*, 6592–6599.
[30] T. M. Spek, A. F. Arendsen, R. P. Happe, S. Yun, K. A. Bagley, D. J. Stufkens, W. R. Hagen, S. P. J. Albracht, *Eur. J. Biochem.* **1996**, *237*, 629–634.
[31] P. J. Stephens, F. Devlin, M. C. McKenna, T. V. Morgan, M. Czechowski, D. V. DerVartanian, H. D. Peck, J. LeGall, *FEBS Lett.* **1985**, *180*, 24–28.
[32] H. Thomann, M. Bernardo, M. W. W. Adams, *J. Am. Chem. Soc.* **1991**, *113*, 7044–7046.
[33] P. J. van Dam, E. J. Reijerse, W. R. Hagen, *Eur. J. Biochem. FEBS* **1997**, *248*, 355–361.
[34] A. L. de Lacey, E. C. Hatchikian, A. Volbeda, M. Frey, J. C. Fontecilla-Camps, V. M. Fernandez, *J. Am. Chem. Soc.* **1997**, *119*, 7181–7189.
[35] A. J. Pierik, M. Hulstein, W. R. Hagen, S. P. Albracht, *Eur. J. Biochem. FEBS* **1998**, *258*, 572–578.
[36] A. Silakov, E. J. Reijerse, S. P. J. Albracht, E. C. Hatchikian, W. Lubitz, *J. Am. Chem. Soc.* **2007**, *129*, 11447–11458.
[37] Y. Montet, P. Amara, A. Volbeda, X. Vernede, E. C. Hatchikian, M. J. Field, M. Frey, J. C. Fontecilla-Camps, *Nat. Struct. Biol.* **1997**, *4*, 523–526.
[38] B. Ginovska-Pangovska, M.-H. Ho, J. C. Linehan, Y. Cheng, M. Dupuis, S. Raugei, W. J. Shaw, *Biochim. Biophys. Acta BBA - Bioenerg.* **2014**, *1837*, 131–138.
[39] O. Sode, G. A. Voth, *J. Chem. Phys.* **2014**, *141*, 22D527.
[40] B. J. Lemon, J. W. Peters, *Biochemistry (Mosc.)* **1999**, *38*, 12969–12973.
[41] A. S. Pandey, T. V. Harris, L. J. Giles, J. W. Peters, R. K. Szilagyi, *J. Am. Chem. Soc.* **2008**, *130*, 4533–4540.
[42] A. L. De Lacey, V. M. Fernández, M. Rousset, R. Cammack, *Chem. Rev.* **2007**, *107*, 4304–4330.
[43] A. Adamska, A. Silakov, C. Lambertz, O. Rüdiger, T. Happe, E. Reijerse, W. Lubitz, *Angew. Chem. Int. Ed.* **2012**, *51*, 11458–11462.
[44] A. Adamska-Venkatesh, D. Krawietz, J. Siebel, K. Weber, T. Happe, E. Reijerse, W. Lubitz, *J. Am. Chem. Soc.* **2014**, 11339–11346.
[45] W. Roseboom, A. L. Lacey, V. M. Fernandez, E. C. Hatchikian, S. P. J. Albracht, *JBIC J. Biol. Inorg. Chem.* **2006**, *11*, 102–118.
[46] A. S. Pereira, P. Tavares, I. Moura, J. J. G. Moura, B. H. Huynh, *J. Am. Chem. Soc.* **2001**, *123*, 2771–2782.
[47] Z. Cao, M. B. Hall, *J. Am. Chem. Soc.* **2001**, *123*, 3734–3742.
[48] Z.-P. Liu, P. Hu, *J. Am. Chem. Soc.* **2002**, *124*, 5175–5182.
[49] C. V. Popescu, E. Münck, *J. Am. Chem. Soc.* **1999**, *121*, 7877–7884.
[50] G. Fritz, D. Griesshaber, O. Seth, P. M. H. Kroneck, *Biochemistry (Mosc.)* **2001**, *40*, 1317–1324.
[51] A. L. De Lacey, C. Stadler, C. Cavazza, E. C. Hatchikian, V. M. Fernandez, *J. Am. Chem. Soc.* **2000**, *122*, 11232–11233.
[52] W. Lubitz, E. Reijerse, M. van Gastel, *Chem. Rev.* **2007**, *107*, 4331–4365.
[53] J. Telser, M. J. Benecky, M. W. Adams, L. E. Mortenson, B. M. Hoffman, *J. Biol. Chem.* **1986**, *261*, 13536–13541.

[54] F. M. Rusnak, M. W. Adams, L. E. Mortenson, E. Münck, *J. Biol. Chem.* **1987**, *262*, 38–41.
[55] P. Chernev, C. Lambertz, A. Brünje, N. Leidel, K. G. V. Sigfridsson, R. Kositzki, C.-H. Hsieh, S. Yao, R. Schiwon, M. Driess, et al., *Inorg. Chem.* **2014**, *53*, 12164–12177.
[56] L. Yu, C. Greco, M. Bruschi, U. Ryde, L. De Gioia, M. Reiher, *Inorg. Chem.* **2011**, *50*, 3888–3900.
[57] S. P. J. Albracht, W. Roseboom, E. C. Hatchikian, *J. Biol. Inorg. Chem. JBIC Publ. Soc. Biol. Inorg. Chem.* **2006**, *11*, 88–101.
[58] E. Drobner, H. Huber, G. Wächtershäuser, D. Rose, K. O. Stetter, *Nature* **1990**, *346*, 742–744.
[59] M. Dörr, J. Käßbohrer, R. Grunert, G. Kreisel, W. A. Brand, R. A. Werner, H. Geilmann, C. Apfel, C. Robl, W. Weigand, *Angew. Chem. Int. Ed.* **2003**, *42*, 1540–1543.
[60] M. Y. Darensbourg, E. J. Lyon, X. Zhao, I. P. Georgakaki, *Proc. Natl. Acad. Sci.* **2003**, *100*, 3683–3688.
[61] H. Reihlen, A. Gruhl, G. v. Hessling, *Justus Liebigs Ann. Chem.* **1929**, *472*, 268–287.
[62] W. Hieber, P. Spacu, *Z. Für Anorg. Allg. Chem.* **1937**, *233*, 353–364.
[63] W. Hieber, J. Gruber, *Z. Für Anorg. Allg. Chem.* **1958**, *296*, 91–103.
[64] W. Hieber, C. Scharfenberg, *Berichte Dtsch. Chem. Ges. B Ser.* **1940**, *73*, 1012–1021.
[65] W. Hieber, W. Beck, *Z. Für Anorg. Allg. Chem.* **1960**, *305*, 265–273.
[66] A. Winter, L. Zsolnai, G. Huttner, *Chem. Ber.* **1982**, *115*, 1286–1304.
[67] A. Winter, L. Zsolnai, G. Huttner, *Z Naturforschung 37b* **1982**, 1430–1436.
[68] D. Seyferth, G. B. Womack, J. C. Dewan, *Organometallics* **1985**, *4*, 398–400.
[69] M. Cowie, R. L. DeKock, T. R. Wagenmaker, D. Seyferth, R. S. Henderson, M. K. Gallagher, *Organometallics* **1989**, *8*, 119–132.
[70] D. Seyferth, R. S. Henderson, *J. Am. Chem. Soc.* **1979**, *101*, 508–509.
[71] D. Seyferth, R. S. Henderson, M. K. Gallagher, *J. Organomet. Chem.* **1980**, *193*, C75–C78.
[72] D. Seyferth, L.-C. Song, R. S. Henderson, *J. Am. Chem. Soc.* **1981**, *103*, 5103–5107.
[73] C. Chieh, D. Seyferth, L. C. Song, *Organometallics* **1982**, *1*, 473–476.
[74] D. Seyferth, R. S. Henderson, L. C. Song, *Organometallics* **1982**, *1*, 125–133.
[75] T. C. W. Mak, L. Book, C. Chieh, M. K. Gallagher, L.-C. Song, D. Seyferth, *Inorganica Chim. Acta* **1983**, *73*, 159–164.
[76] D. Seyferth, G. B. Womack, L. C. Song, M. Cowie, B. W. Hames, *Organometallics* **1983**, *2*, 928–930.
[77] D. Seyferth, G. B. Womack, M. Cowie, B. W. Hames, *Organometallics* **1984**, *3*, 1891–1897.
[78] D. Seyferth, R. S. Henderson, L.-C. Song, G. B. Womack, *J. Organomet. Chem.* **1985**, *292*, 9–17.
[79] D. Seyferth, A. M. Kiwan, *J. Organomet. Chem.* **1985**, *286*, 219–223.
[80] D. Seyferth, A. M. Kiwan, E. Sinn, *J. Organomet. Chem.* **1985**, *281*, 111–118.
[81] D. Seyferth, C. M. Archer, *Organometallics* **1986**, *5*, 2572–2574.
[82] D. Seyferth, G. B. Womack, R. S. Henderson, M. Cowie, B. W. Hames, *Organometallics* **1986**, *5*, 1568–1575.
[83] J. B. Hoke, J. C. Dewan, D. Seyferth, *Organometallics* **1987**, *6*, 1816–1819.
[84] D. Seyferth, J. B. Hoke, J. C. Dewan, *Organometallics* **1987**, *6*, 895–897.

[85] D. Seyferth, J. B. Hoke, A. L. Rheingold, M. Cowie, A. D. Hunter, *Organometallics* **1988**, *7*, 2163–2172.
[86] D. Seyferth, G. B. Womack, C. M. Archer, J. C. Dewan, *Organometallics* **1989**, *8*, 430–442.
[87] D. Seyferth, G. B. Womack, C. M. Archer, J. P. Fackler, D. O. Marler, *Organometallics* **1989**, *8*, 443–450.
[88] D. Seyferth, C. M. Archer, D. P. Ruschke, M. Cowie, R. W. Hilts, *Organometallics* **1991**, *10*, 3363–3380.
[89] D. Seyferth, L. L. Anderson, F. Villafane, M. Cowie, R. W. Hilts, *Organometallics* **1992**, *11*, 3262–3271.
[90] D. Seyferth, L. L. Anderson, W. M. Davis, *J. Organomet. Chem.* **1993**, *459*, 271–281.
[91] D. Seyferth, J. B. Hoke, J. C. Dewan, P. Hofmann, M. Schnellbach, *Organometallics* **1994**, *13*, 3452–3464.
[92] D. Seyferth, D. P. Ruschke, W. M. Davis, *Organometallics* **1994**, *13*, 4695–4703.
[93] L. F. Dahl, C.-H. Wei, *Inorg. Chem.* **1963**, *2*, 328–333.
[94] M. Stephenson, L. H. Stickland, *Biochem. J.* **1931**, *25*, 205–214.
[95] A. L. Cloirec, S. C. Davies, D. J. Evans, D. L. Hughes, C. J. Pickett, S. P. Best, S. Borg, *Chem. Commun.* **1999**, 2285–2286.
[96] M. Schmidt, S. M. Contakes, T. B. Rauchfuss, *J. Am. Chem. Soc.* **1999**, *121*, 9736–9737.
[97] E. J. Lyon, I. P. Georgakaki, J. H. Reibenspies, M. Y. Darensbourg, *Angew. Chem. Int. Ed.* **1999**, *38*, 3178–3180.
[98] T. R. Simmons, G. Berggren, M. Bacchi, M. Fontecave, V. Artero, *Coord. Chem. Rev.* **2014**, *270-271*, 127–150.
[99] J. D. Lawrence, H. Li, T. B. Rauchfuss, M. Bénard, M.-M. Rohmer, *Angew. Chem. Int. Ed.* **2001**, *40*, 1768–1771.
[100] L.-C. Song, Z.-Y. Yang, H.-Z. Bian, Q.-M. Hu, *Organometallics* **2004**, *23*, 3082–3084.
[101] L.-C. Song, Z.-Y. Yang, H.-Z. Bian, Y. Liu, H.-T. Wang, X.-F. Liu, Q.-M. Hu, *Organometallics* **2005**, *24*, 6126–6135.
[102] J. Windhager, H. Görls, H. Petzold, G. Mloston, G. Linti, W. Weigand, *Eur. J. Inorg. Chem.* **2007**, *2007*, 4462–4471.
[103] L.-C. Song, Z.-Y. Yang, Y.-J. Hua, H.-T. Wang, Y. Liu, Q.-M. Hu, *Organometallics* **2007**, *26*, 2106–2110.
[104] T. R. Simmons, G. Berggren, M. Bacchi, M. Fontecave, V. Artero, *Coord. Chem. Rev.* **2014**, *270-271*, 127–150.
[105] U.-P. Apfel, Y. Halpin, H. Görls, J. G. Vos, W. Weigand, *Eur. J. Inorg. Chem.* **2011**, *2011*, 581–588.
[106] U.-P. Apfel, H. Görls, G. A. N. Felton, D. H. Evans, R. S. Glass, D. L. Lichtenberger, W. Weigand, *Helv. Chim. Acta* **2012**, *95*, 2168–2175.
[107] U.-P. Apfel, D. Troegel, Y. Halpin, S. Tschierlei, U. Uhlemann, H. Görls, M. Schmitt, J. Popp, P. Dunne, M. Venkatesan, et al., *Inorg. Chem.* **2010**, *49*, 10117–10132.
[108] R. S. Glass, N. E. Gruhn, E. Lorance, M. S. Singh, N. Y. T. Stessman, U. I. Zakai, *Inorg. Chem.* **2005**, *44*, 5728–5737.
[109] L. R. Almazahreh, U.-P. Apfel, W. Imhof, M. Rudolph, H. Görls, J. Talarmin, P. Schollhammer, M. El-khateeb, W. Weigand, *Organometallics* **2013**, *32*, 4523–4530.

[110] M. K. Harb, T. Niksch, J. Windhager, H. Görls, R. Holze, L. T. Lockett, N. Okumura, D. H. Evans, R. S. Glass, D. L. Lichtenberger, et al., *Organometallics* **2009**, *28*, 1039–1048.
[111] M. K. Harb, U.-P. Apfel, J. Kübel, H. Görls, G. A. N. Felton, T. Sakamoto, D. H. Evans, R. S. Glass, D. L. Lichtenberger, M. El-khateeb, et al., *Organometallics* **2009**, *28*, 6666–6675.
[112] L. Schwartz, P. S. Singh, L. Eriksson, R. Lomoth, S. Ott, *Comptes Rendus Chim.* **2008**, *11*, 875–889.
[113] E. S. Donovan, J. J. McCormick, G. S. Nichol, G. A. N. Felton, *Organometallics* **2012**, *31*, 8067–8070.
[114] S. Pullen, H. Fei, A. Orthaber, S. M. Cohen, S. Ott, *J. Am. Chem. Soc.* **2013**, *135*, 16997–17003.
[115] C. Tard, C. J. Pickett, *Chem. Rev.* **2009**, *109*, 2245–2274.
[116] R. Zaffaroni, T. B. Rauchfuss, D. L. Gray, L. De Gioia, G. Zampella, *J. Am. Chem. Soc.* **2012**, *134*, 19260–19269.
[117] S. Ezzaher, A. Gogoll, C. Bruhn, S. Ott, *Chem. Commun.* **2010**, *46*, 5775–5777.
[118] W. Dong, M. Wang, X. Liu, K. Jin, G. Li, F. Wang, L. Sun, *Chem. Commun.* **2006**, 305–307.
[119] C. Liu, J. N. T. Peck, J. A. Wright, C. J. Pickett, M. B. Hall, *Eur. J. Inorg. Chem.* **2011**, *2011*, 1080–1093.
[120] S. Tschierlei, S. Ott, R. Lomoth, *Energy Environ. Sci.* **2011**, *4*, 2340–2352.
[121] B. E. Barton, M. T. Olsen, T. B. Rauchfuss, *J. Am. Chem. Soc.* **2008**, *130*, 16834–16835.
[122] B. E. Barton, T. B. Rauchfuss, *Inorg. Chem.* **2008**, *47*, 2261–2263.
[123] M. T. Olsen, B. E. Barton, T. B. Rauchfuss, *Inorg. Chem.* **2009**, *48*, 7507–7509.
[124] J. L. Stanley, Z. M. Heiden, T. B. Rauchfuss, S. R. Wilson, L. De Gioia, G. Zampella, *Organometallics* **2008**, *27*, 119–125.
[125] W. Gao, J. Sun, T. Åkermark, M. Li, L. Eriksson, L. Sun, B. Åkermark, *Chem. - Eur. J.* **2010**, *16*, 2537–2546.
[126] S. Ezzaher, J.-F. Capon, F. Gloaguen, F. Y. Pétillon, P. Schollhammer, J. Talarmin, N. Kervarec, *Inorg. Chem.* **2009**, *48*, 2–4.
[127] Y. Wang, Z. Li, X. Zeng, X. Wang, C. Zhan, Y. Liu, X. Zeng, Q. Luo, X. Liu, *New J. Chem.* **2009**, *33*, 1780–1789.
[128] P. Li, M. Wang, L. Chen, J. Liu, Z. Zhao, L. Sun, *Dalton Trans.* **2009**, 1919–1926.
[129] M. Bruschi, P. Fantucci, L. De Gioia, *Inorg. Chem.* **2002**, *41*, 1421–1429.
[130] K.-T. Chu, Y.-C. Liu, Y.-L. Huang, C.-H. Hsu, G.-H. Lee, M.-H. Chiang, *Chem. - Eur. J.* **2015**, DOI 10.1002/chem.201501114.
[131] J. I. van der Vlugt, T. B. Rauchfuss, C. M. Whaley, S. R. Wilson, *J. Am. Chem. Soc.* **2005**, *127*, 16012–16013.
[132] S. Ezzaher, J.-F. Capon, F. Gloaguen, F. Y. Pétillon, P. Schollhammer, J. Talarmin, R. Pichon, N. Kervarec, *Inorg. Chem.* **2007**, *46*, 3426–3428.
[133] F. I. Adam, G. Hogarth, S. E. Kabir, I. Richards, *Comptes Rendus Chim.* **2008**, *11*, 890–905.
[134] M. E. Carroll, B. E. Barton, T. B. Rauchfuss, P. J. Carroll, *J. Am. Chem. Soc.* **2012**, *134*, 18843–18852.
[135] B. E. Barton, M. T. Olsen, T. B. Rauchfuss, *Curr. Opin. Biotechnol.* **2010**, *21*, 292–297.

[136] M. Razavet, S. C. Davies, D. L. Hughes, C. J. Pickett, *Chem. Commun.* **2001**, 847–848.
[137] M. Razavet, S. J. Borg, S. J. George, S. P. Best, S. A. Fairhurst, C. J. Pickett, *Chem. Commun.* **2002**, 700–701.
[138] S. J. George, Z. Cui, M. Razavet, C. J. Pickett, *Chem. - Eur. J.* **2002**, *8*, 4037–4046.
[139] C. A. Boyke, T. B. Rauchfuss, S. R. Wilson, M.-M. Rohmer, M. Bénard, *J. Am. Chem. Soc.* **2004**, *126*, 15151–15160.
[140] C. A. Boyke, J. I. van der Vlugt, T. B. Rauchfuss, S. R. Wilson, G. Zampella, L. De Gioia, *J. Am. Chem. Soc.* **2005**, *127*, 11010–11018.
[141] J. I. van der Vlugt, T. B. Rauchfuss, S. R. Wilson, *Chem. - Eur. J.* **2006**, *12*, 90–98.
[142] T. Liu, M. Y. Darensbourg, *J. Am. Chem. Soc.* **2007**, *129*, 7008–7009.
[143] A. K. Justice, T. B. Rauchfuss, S. R. Wilson, *Angew. Chem. Int. Ed.* **2007**, *46*, 6152–6154.
[144] M. L. Singleton, N. Bhuvanesh, J. H. Reibenspies, M. Y. Darensbourg, *Angew. Chem. Int. Ed.* **2008**, *47*, 9492–9495.
[145] C.-H. Hsieh, Ö. F. Erdem, S. D. Harman, M. L. Singleton, E. Reijerse, W. Lubitz, C. V. Popescu, J. H. Reibenspies, S. M. Brothers, M. B. Hall, et al., *J. Am. Chem. Soc.* **2012**, *134*, 13089–13102.
[146] M. T. Olsen, M. Bruschi, L. De Gioia, T. B. Rauchfuss, S. R. Wilson, *J. Am. Chem. Soc.* **2008**, *130*, 12021–12030.
[147] D. Zheng, M. Wang, L. Chen, N. Wang, L. Sun, *Inorg. Chem.* **2014**, *53*, 1555–1561.
[148] S. Munery, J.-F. Capon, L. De Gioia, C. Elleouet, C. Greco, F. Y. Pétillon, P. Schollhammer, J. Talarmin, G. Zampella, *Chem. - Eur. J.* **2013**, *19*, 15458–15461.
[149] L. De Gioia, C. Elleouet, S. Munery, F. Y. Pétillon, P. Schollhammer, J. Talarmin, G. Zampella, *Eur. J. Inorg. Chem.* **2014**, *22*, 3456–3461.
[150] W. Wang, T. B. Rauchfuss, C. E. Moore, A. L. Rheingold, L. De Gioia, G. Zampella, *Chem. - Eur. J.* **2013**, *19*, 15476–15479.
[151] A. R. Finkelmann, M. T. Stiebritz, M. Reiher, *Chem. Sci.* **2014**, *5*, 215.
[152] R. D. Bethel, D. J. Crouthers, C.-H. Hsieh, J. A. Denny, M. B. Hall, M. Y. Darensbourg, *Inorg. Chem.* **2015**, 150313095220003.
[153] L.-Z. Wu, B. Chen, Z.-J. Li, C.-H. Tung, *Acc. Chem. Res.* **2014**, *47*, 2177–2185.
[154] K. A. Brown, M. B. Wilker, M. Boehm, G. Dukovic, P. W. King, *J. Am. Chem. Soc.* **2012**, *134*, 5627–5636.
[155] A. Das, Z. Han, M. G. Haghighi, R. Eisenberg, *Proc. Natl. Acad. Sci.* **2013**, *110*, 16716–16723.
[156] Z. Han, F. Qiu, R. Eisenberg, P. L. Holland, T. D. Krauss, *Science* **2012**, *338*, 1321–1324.
[157] Z. Han, L. Shen, W. W. Brennessel, P. L. Holland, R. Eisenberg, *J. Am. Chem. Soc.* **2013**, *135*, 14659–14669.
[158] J. Huang, K. L. Mulfort, P. Du, L. X. Chen, *J. Am. Chem. Soc.* **2012**, *134*, 16472–16475.
[159] T. Yu, Y. Zeng, J. Chen, Y.-Y. Li, G. Yang, Y. Li, *Angew. Chem. Int. Ed.* **2013**, *52*, 5631–5635.
[160] W. Zhang, J. Hong, J. Zheng, Z. Huang, J. (Steve) Zhou, R. Xu, *J. Am. Chem. Soc.* **2011**, *133*, 20680–20683.

[161] H. Zhu, N. Song, H. Lv, C. L. Hill, T. Lian, *J. Am. Chem. Soc.* **2012**, *134*, 11701–11708.
[162] A. Roy, C. Madden, G. Ghirlanda, *Chem. Commun.* **2012**, *48*, 9816–9818.
[163] W.-N. Cao, F. Wang, H.-Y. Wang, B. Chen, K. Feng, C.-H. Tung, L.-Z. Wu, *Chem. Commun.* **2012**, *48*, 8081–8083.
[164] A. Onoda, Y. Kihara, K. Fukumoto, Y. Sano, T. Hayashi, *ACS Catal.* **2014**, *4*, 2645–2648.
[165] T. Yu, Y. Zeng, J. Chen, Y.-Y. Li, G. Yang, Y. Li, *Angew. Chem. Int. Ed.* **2013**, *52*, 5631–5635.
[166] D. Streich, Y. Astuti, M. Orlandi, L. Schwartz, R. Lomoth, L. Hammarström, S. Ott, *Chem. - Eur. J.* **2010**, *16*, 60–63.
[167] H.-Y. Wang, W.-G. Wang, G. Si, F. Wang, C.-H. Tung, L.-Z. Wu, *Langmuir* **2010**, *26*, 9766–9771.
[168] W. Wang, T. Yu, Y. Zeng, J. Chen, Y. Li, *Chin. J. Chem.* **2014**, *32*, 479–484.
[169] T. Yu, Y. Zeng, J. Chen, X. Zhang, G. Yang, Y. Li, *J Mater Chem A* **2014**, 20500–20505.
[170] W. W. Yu, L. Qu, W. Guo, X. Peng, *Chem. Mater.* **2003**, *15*, 2854–2860.
[171] N. Ikuta, S. Takizawa, S. Murata, *Photochem. Photobiol. Sci.* **2014**, *13*, 691–702.
[172] A. J. Esswein, D. G. Nocera, *Chem. Rev.* **2007**, *107*, 4022–4047.
[173] D. J. Evans, C. J. Pickett, *Chem. Soc. Rev.* **2003**, *32*, 268–275.
[174] A. Volbeda, J. Fontecillacamps, *Coord. Chem. Rev.* **2005**, *249*, 1609–1619.
[175] C. Madden, M. D. Vaughn, I. Díez-Pérez, K. A. Brown, P. W. King, D. Gust, A. L. Moore, T. A. Moore, *J. Am. Chem. Soc.* **2012**, *134*, 1577–1582.
[176] J. Liu, W. Jiang, *Dalton Trans.* **2012**, *41*, 9700–9707.
[177] H. Cui, M. Hu, H. Wen, G. Chai, C. Ma, H. Chen, C. Chen, *Dalton Trans.* **2012**, *41*, 13899–13907.
[178] S. Gao, S. Huang, Q. Duan, J. Hou, D. Jiang, Q. Liang, J. Zhao, *Int. J. Hydrog. Energy* **2014**, *39*, 10434–10444.
[179] P. W. J. M. Frederix, K. Adamczyk, J. A. Wright, T. Tuttle, R. V. Ulijn, C. J. Pickett, N. T. Hunt, *Organometallics* **2014**, *33*, 5888–5896.
[180] F. Wen, C. Li, *Acc. Chem. Res.* **2013**, *46*, 2355–2364.
[181] T. Nann, S. K. Ibrahim, P.-M. Woi, S. Xu, J. Ziegler, C. J. Pickett, *Angew. Chem. Int. Ed.* **2010**, *49*, 1574–1577.
[182] F. Wen, X. Wang, L. Huang, G. Ma, J. Yang, C. Li, *ChemSusChem* **2012**, *5*, 849–853.
[183] F. Wang, W.-G. Wang, X.-J. Wang, H.-Y. Wang, C.-H. Tung, L.-Z. Wu, *Angew. Chem. Int. Ed.* **2011**, *50*, 3193–3197.
[184] C. Orain, F. Quentel, F. Gloaguen, *ChemSusChem* **2014**, *7*, 638–643.
[185] X. Li, M. Wang, D. Zheng, K. Han, J. Dong, L. Sun, *Energy Environ. Sci.* **2012**, *5*, 8220–8224.
[186] K. Sasan, Q. Lin, C. Mao, P. Feng, *Chem. Commun.* **2014**, *50*, 10390–10393.
[187] S. Ott, M. Kritikos, B. Åkermark, L. Sun, *Angew. Chem. Int. Ed.* **2003**, *42*, 3285–3288.
[188] S. Ott, M. Borgström, M. Kritikos, R. Lomoth, J. Bergquist, B. Åkermark, L. Hammarström, L. Sun, *Inorg. Chem.* **2004**, *43*, 4683–4692.
[189] H. Wolpher, M. Borgström, L. Hammarström, J. Bergquist, V. Sundström, S. Styring, L. Sun, B. Åkermark, *Inorg. Chem. Commun.* **2003**, *6*, 989–991.
[190] J. Ekström, M. Abrahamsson, C. Olson, J. Bergquist, F. B. Kaynak, L. Eriksson, L. Sun, H.-C. Becker, B. ?kermark, L. Hammarstr?m, et al., *Dalton Trans.* **2006**, 4599–4606.

[191] W. Gao, J. Liu, W. Jiang, M. Wang, L. Weng, B. Åkermark, L. Sun, *Comptes Rendus Chim.* **2008**, *11*, 915–921.
[192] L.-C. Song, M.-Y. Tang, F.-H. Su, Q.-M. Hu, *Angew. Chem. Int. Ed.* **2006**, *45*, 1130–1133.
[193] A. P. S. Samuel, D. T. Co, C. L. Stern, M. R. Wasielewski, *J. Am. Chem. Soc.* **2010**, *132*, 8813–8815.
[194] L.-C. Song, F.-X. Luo, H. Tan, X.-J. Sun, Z.-J. Xie, H.-B. Song, *Eur. J. Inorg. Chem.* **2013**, *2013*, 2549–2557.
[195] Y. Na, M. Wang, J. Pan, P. Zhang, B. Åkermark, L. Sun, *Inorg. Chem.* **2008**, *47*, 2805–2810.
[196] Y. Na, J. Pan, M. Wang, L. Sun, *Inorg. Chem.* **2007**, *46*, 3813–3815.
[197] B. Kumar, M. Beyler, C. P. Kubiak, S. Ott, *Chem. - Eur. J.* **2012**, *18*, 1295–1298.
[198] C.-B. Li, Z.-J. Li, S. Yu, G.-X. Wang, F. Wang, Q.-Y. Meng, B. Chen, K. Feng, C.-H. Tung, L.-Z. Wu, *Energy Environ. Sci.* **2013**, *6*, 2597–2602.
[199] F. Wang, W.-J. Liang, J.-X. Jian, C.-B. Li, B. Chen, C.-H. Tung, L.-Z. Wu, *Angew. Chem. Int. Ed.* **2013**, *52*, 8134–8138.
[200] J.-X. Jian, Q. Liu, Z.-J. Li, F. Wang, X.-B. Li, C.-B. Li, B. Liu, Q.-Y. Meng, B. Chen, K. Feng, et al., *Nat. Commun.* **2013**, *4*, 2695.
[201] M. W. Büttner, C. Burschka, J. O. Daiss, D. Ivanova, N. Rochel, S. Kammerer, C. Peluso-Iltis, A. Bindler, C. Gaudon, P. Germain, et al., *Chembiochem Eur. J. Chem. Biol.* **2007**, *8*, 1688–1699.
[202] M. W. Büttner, C. Burschka, J. O. Daiss, D. Ivanova, N. Rochel, S. Kammerer, C. Peluso-Iltis, A. Bindler, C. Gaudon, P. Germain, et al., *Chembiochem Eur. J. Chem. Biol.* **2007**, *8*, 1688–1699.
[203] R. Ilg, C. Burschka, D. Schepmann, B. Wünsch, R. Tacke, *Organometallics* **2006**, *25*, 5396–5408.
[204] T. Johansson, L. Weidolf, F. Popp, R. Tacke, U. Jurva, *Drug Metab. Dispos. Biol. Fate Chem.* **2010**, *38*, 73–83.
[205] W. P. Lippert, C. Burschka, K. Götz, M. Kaupp, D. Ivanova, C. Gaudon, Y. Sato, P. Antony, N. Rochel, D. Moras, et al., *ChemMedChem* **2009**, *4*, 1143–1152.
[206] R. Tacke, V. Müller, M. W. Büttner, W. P. Lippert, R. Bertermann, J. O. Daiss, H. Khanwalkar, A. Furst, C. Gaudon, H. Gronemeyer, *ChemMedChem* **2009**, *4*, 1797–1802.
[207] R. Tacke, B. Nguyen, C. Burschka, W. P. Lippert, A. Hamacher, C. Urban, M. U. Kassack, *Organometallics* **2010**, *29*, 1652–1660.
[208] R. Tacke, F. Popp, B. Müller, B. Theis, C. Burschka, A. Hamacher, M. U. Kassack, D. Schepmann, B. Wünsch, U. Jurva, et al., *ChemMedChem* **2008**, *3*, 152–164.
[209] J. B. Warneck, F. H. M. Cheng, M. J. Barnes, J. S. Mills, J. G. Montana, R. J. Naylor, M.-P. Ngan, M.-K. Wai, J. O. Daiss, R. Tacke, et al., *Toxicol. Appl. Pharmacol.* **2008**, *232*, 369–375.
[210] A. C. Grimsdale, K. Leok Chan, R. E. Martin, P. G. Jokisz, A. B. Holmes, *Chem. Rev.* **2009**, *109*, 897–1091.
[211] M. Hissler, P. W. Dyer, R. Réau, *Coord. Chem. Rev.* **2003**, *244*, 1–44.
[212] L. Ilies, H. Tsuji, Y. Sato, E. Nakamura, *J. Am. Chem. Soc.* **2008**, *130*, 4240–4241.
[213] T. Matsuda, S. Kadowaki, T. Goya, M. Murakami, *Org. Lett.* **2007**, *9*, 133–136.

[214] M. Shimizu, K. Mochida, T. Hiyama, *Angew. Chem. Int. Ed.* **2008**, *47*, 9760–9764.
[215] M. Shimizu, H. Tatsumi, K. Mochida, K. Oda, T. Hiyama, *Chem. - Asian J.* **2008**, *3*, 1238–1247.
[216] K. Tamao, S. Yamaguchi, *J. Organomet. Chem.* **2000**, *611*, 5–11.
[217] E. Wang, C. Li, W. Zhuang, J. Peng, Y. Cao, *J. Mater. Chem.* **2008**, *18*, 797–801.
[218] S. Yamaguchi, K. Tamao, *Chem. Lett.* **2005**, *34*, 2–7.
[219] S. Yamaguchi, C. Xu, T. Okamoto, *Pure Appl. Chem.* **2006**, *78*, 721–730.
[220] G. Yu, S. Yin, Y. Liu, J. Chen, X. Xu, X. Sun, D. Ma, X. Zhan, Q. Peng, Z. Shuai, et al., *J. Am. Chem. Soc.* **2005**, *127*, 6335–6346.
[221] E. Wiberg, N. Wiberg, *Lehrbuch der anorganischen Chemie*, Walter De Gruyter, Berlin, **1995**.
[222] U.-P. Apfel, **2010**.
[223] G. Frapper, M. Kertesz, *Organometallics* **1992**, *11*, 3178–3184.
[224] S. Grigoras, G. C. Lie, T. J. Barton, S. Ijadi-Maghsoodi, Y. Pang, J. Shinar, Z. V. Vardeny, K. S. Wong, S. G. Han, *Synth. Met.* **1992**, *49*, 293–304.
[225] S. Y. Hong, S. J. Kwon, S. C. Kim, *J. Chem. Phys.* **1995**, *103*, 1871–1877.
[226] S. Y. Hong, D. S. Marynick, *Macromolecules* **1995**, *28*, 4991–4995.
[227] S. Y. Hong, J. M. Song, *Synth. Met.* **1997**, *85*, 1113–1114.
[228] S. Y. Hong, S. J. Kwon, S. C. Kim, D. S. Marynick, *Synth. Met.* **1995**, *69*, 701–702.
[229] J. Kürti, P. R. Surján, M. Kertész, G. Frapper, *Synth. Met.* **1993**, *57*, 4338–4343.
[230] R. A. Loomis, R. L. Schwartz, M. I. Lester, *J. Chem. Phys.* **1996**, *104*, 6984–6996.
[231] Y. Matsuzaki, M. Nakano, K. Yamaguchi, K. Tanaka, T. Yamabe, *Chem. Phys. Lett.* **1996**, *263*, 119–125.
[232] Y. Yamaguchi, J. Shioya, *Mol. Eng.* **1993**, *2*, 339–347.
[233] Y. Yamaguchi, T. Yamabe, *Int. J. Quantum Chem.* **1996**, *57*, 73–78.
[234] Y. Yamaguchi, *Mol. Eng.* **1994**, *3*, 311–320.
[235] S. Yamaguchi, K. Tamao, *J. Chem. Soc. Dalton Trans.* **1998**, 3693–3702.

8 Acknowledgements

I would like to thank Prof. Dr. Wolfgang Weigand for giving me the opportunity to work on this very intersting field. I have to thank him for the possibility to use his collaborations for research stays and to establish new collaborations, which were fruitful to fulfill and to complement my thesis, respectively. He always gave me the possibility to follow my own research strategies and supported me on my way.

Furthermore, I have to thank the Deutsche Bundesstiftung Umwelt (DBU) for their financial support during my time as a PhD student and for the interesting fellows' seminars at fantastic places. Also for their financial support I have to thank the Deutscher akademischer Austauschdienst (DAAD) during the research stays at the Université de Bretagne Occidentale Brest, France and to the European cooperation in science and technology (COST) during my research stay at the Laboratoire de Chimie et Biologie des Métaux at the CEA/Université Grenoble-Alpes/CNRS, France.

I also thank Prof. Dr. Philippe Schollhammer, who granted together with Prof. Dr. Weigand for the procope program of the DAAD and gave me the opportunity to stay with his working group at the Université de Bretagne Occidentale Brest, France. During the period of in summary almost three months, he supported me very much. I also have to thank him, Dr. Jean Talarmin and Dr. Catherine Elleouet for introducing me into the topic of cyclic voltammetry, for carrying out a lot of measurements, for the fruitful scientific discussions of results and for the nice working atmosphere in their laboratories. I am grateful to further members of the UBO Brest: Dr. Jean-François Capon, Dr. Franck Thetiot for their help, discussions and the nice atmosphere as well as Dr. François Michaud for his explanation on XRD measurements and for the measuring of my compounds.

I am grateful to Dr. Vincent Artero, who gave me the opportunity to work in his labs at the CEA/Université Grenoble-Alpes/CNRS, France. I have to thank him, Dr. Murielle Chavarot-Kerlidou and Dr. Souvik Roy for the scientific discussions and the nice atmosphere during my two weeks in Grenoble. Although the planned works could not be carried out, we found an interesting research topic to afford a lot of results.

Many thanks to Dr. Ulf-Peter Apfel for the introduction into the interesting hydrogenase chemistry and the nice atmosphere during my undergraduate studies. I have to thank him for the scientific discussions as well as many manuscript discussions.

I am also in deep gratitude to Dr. Luca Bertini, Dr. Giuseppe Zampella and Prof. Dr. Luca De Gioia for their collaboration and theoretical calculations dealing with my compounds. It was a big pleasure for me to discuss and work with them. I further thank Dr. Daniel Escudero as well as Prof. Dr. Leticia Gonzalez for DFT calculations performed for [**RG1**].

Furthermore, I thank Lin Shu and Prof. Dr. Ken Sakai for performing the emission decay experiments for my compound **63a** to clarify the photocatalytic process. I thank Prof. Dr. Benjamin Dietzek for the possibility to perform the photocatalytic experiments in his laboratories. The results of [**RG4**] were not feasible without his analytical facilities. Therefore I have to thank Dr. Martin Schulz for his guidance, the scientific discussions and the nice atmosphere during the work in his lab. I also have to thank Dr. Kristina Dubnack for the experimental support regarding the GC measurements for [**RG1**]. Many thanks to Tobias Rudolph and Prof. Dr. Felix Schacher for the successful preparation of the micelle solutions, which were necessary to perform photocatalytic experiments of [**RG4**] in aqueous solutions.

I moreover thank all technical assistants of the IAAC. Dr. Poppitz, Mrs. Schönau and Mrs. Heineck (MS), Mrs. Rambach, Mr. Reinhardt and Dr. Friedrich (NMR), Mrs. Lentvogt and Mrs. Schönfeld (elemental analysis). I am especially pleased to acknowledge Dr. Helmar Görls for the XRD measurements and Dr. Sven Krieck for the possibility to perform light induced reactions and reactions under argon-atmosphere in his lab.

Many thanks to my colleagues and members of the AG Weigand for the nice atmosphere as well as the constructive working climate and to my students, which were in practical training, Dominique Gampe and Martin Obst, whose works leads to good results.

Finally, I would like to thank my friends, family and beloved wife Caro for their support and patience in every situation in life.

9 Curriculum Vitae

Personal Information

Name	Roman Goy
Date of birth	2th June 1987
Place of birth	Eisenach
Martial status	married
Nationality	German

Education

08.1993 - 07.1997	Haineck-Grundschule (elementary school) Nazza
08.1997 - 06.2005	Elisabeth-Gymnasium (secondary school) in Eisenach

Academic Achievments

01.10.2006 - 28.09.2011	Study of chemistry at the Friedrich-Schiller-University in Jena
26.10.2010 - 28.09.2011	Title of diploma thesis: „Siliciumhaltige photoaktive Modelle für das aktive Zentrum der [FeFe]-Hydrogenase“
01.10.2011 – 31.07.2015	PhD thesis in chemistry at the Friedrich-Schiller-University in Jena Title of PhD thesis: „Synthesis and Characterization of Photocatalytically Active [FeFe] Hydrogenase Subsite Models”
01.08.2015 -	PostDoc position at DSM Nutritional Products GmbH, Kaiseraugst (Switzerland)

Research Experience

11.2012 - 12.2012	Guest researcher at the Université de Bretagne Occidentale Brest, France; Group of Prof. Schollhammer

06.2013 - 07.2013	Guest researcher at the Université de Bretagne Occidentale Brest, France; Group of Prof. Schollhammer
12.01.2014 - 25.01.2014	Guest researcher at the Université de Bretagne Occidentale Brest, France; Group of Prof. Schollhammer
07.2014 - 07.2014	Guest researcher at the Laboratoire de Chimie et Biologie des Métaux at the CEA/Université Grenoble-Alpes/CNRS, France; Group of Prof. Dr. Artero

Training / Fellowships

09.2005 – 07.2006	Training to chemistry lab assistant in the Heraeus Kulzer GmbH, Wehrheim (development prosthetics and techniques)
01.2012 – 12.2014	PhD fellowship of the Deutschen Bundesstiftung Umwelt (DBU)

Skills

Languages	German (mother tongue) English (fluently) Latin (school) French (A1)

Conferences

24.02. -26.02.2013	9. Coordination chemistry meeting 2013 Bayreuth, Germany *Oral presentation*
09.03. - 11.03.2014	COST Symposium on Current Challenges in Supramolecular Artificial Photosynthesis, young-researcher meeting Jena, Germany *Oral and poster presentation*

12.03. - 13.03.2014	COST Symposium on Current Challenges in Supramolecular Artificial Photosynthesis Jena, Germany *Oral presentation*
29.01. – 30.01.2015	20. Seminar day of the GRK "chemical photocatalysis" DBU-Symposium University of Regensburg, Germany *Oral presentation*

Additional

2003-2005	School and Training for Tolerance and Democracy („XENOS – Leben und Arbeiten in Vielfalt")
01.10.2005 – 01.01.2012	Member of the Union IG-BCE (mining, chemistry, energy) to represent the interests of the employees
01.10.2007 – 30.09.2009	Committee work at the student's council of chemistry (elected member, voluntarily and free of charge to help and represent the interests of the students)

Jena,

Roman Goy

10 Declaration of authorship/Selbstständigkeitserklärung

I declare that this thesis and the work presented herewith are my own and have been generated by me as the result of my own original research.

Ich erkläre, dass ich die vorliegende Arbeit selbstständig und unter Verwendung der angegebenen Hilfsmittel, persönlichen Mitteilungen und Quellen angefertigt habe.

Jena, _____

Roman Goy